



HAL
open science

Spatialized study of the coupling between extended defects and mobile species in the nuclear fuel

Lokesh Verma

► **To cite this version:**

Lokesh Verma. Spatialized study of the coupling between extended defects and mobile species in the nuclear fuel. Condensed Matter [cond-mat]. Aix Marseille Université, 2019. English. NNT : . tel-02479378

HAL Id: tel-02479378

<https://theses.hal.science/tel-02479378>

Submitted on 14 Feb 2020

HAL is a multi-disciplinary open access archive for the deposit and dissemination of scientific research documents, whether they are published or not. The documents may come from teaching and research institutions in France or abroad, or from public or private research centers.

L'archive ouverte pluridisciplinaire **HAL**, est destinée au dépôt et à la diffusion de documents scientifiques de niveau recherche, publiés ou non, émanant des établissements d'enseignement et de recherche français ou étrangers, des laboratoires publics ou privés.

AIX-MARSEILLE UNIVERSITÉ

Ecole Doctorale 352 : Physique et Sciences de la
Matière

Thèse présentée pour obtenir le grade de
DOCTORAT de l'UNIVERSITE AIX-MARSEILLE

Discipline: Physique et Sciences de la Matière
Spécialité: Matière Condensée et Nanosciences
par

Lokesh VERMA

Spatialized study of the coupling between extended defects and mobile species in the nuclear fuel

Soutenue le 11/12/2019 devant le jury composé de:

Mme Veena TIKARE	Sr. Researcher, SNL (USA)	Rapporteur
M. Thomas JOURDAN	Sr. Researcher, CEA Saclay	Rapporteur
M. Jean-Marc DEBIERRE	Professeur, Aix-Marseille Université	Examineur
M. Roland DUBOURG	Sr. Researcher, IRSN	Examineur
Mme Laurence NOIROT	Research Engineer, CEA Cadarache	Encadrante de thèse
M. Philippe MAUGIS	Professeur, Aix-Marseille Université	Directeur de thèse



Cette oeuvre est mise à disposition selon les termes de la [Licence Creative Commons Attribution - Pas d'Utilisation Commerciale - Pas de Modification 4.0 International](#).

“The beauty of a living thing is not the atoms that go into it, but the way those atoms are put together.”

Carl Sagan

Abstract

Spatialized study of the coupling between extended defects and mobile species in the nuclear fuel

by Lokesh VERMA

Fission gases (Xe, Kr) produced during irradiation in a nuclear fuel can contribute to significant effects such as swelling and fission gas release which may affect the overall performance of the fuel. The effective diffusion theory, which is generally used in the modelling of base-irradiation of nuclear fuel, cannot predict the intra-granular fission gas release during post-irradiation annealing tests. From the several scenarios proposed, we discuss and analyze three such mechanisms: the directed movement of pressurized intra-granular gas bubbles in a vacancy concentration gradient towards the grain surface, the Brownian movement of these intra-granular bubbles via volume and surface diffusion mechanisms, a scenario of gas bubble movement along with the dislocations via the mechanism of dislocation climb. A new spatially resolved model, BEEP Model, has been developed for gas bubble migration and its interaction with point defects. Analyses done using the BEEP model show that neither of the directed or random movement, nor their combination, could explain the large fission gas release obtained during post-irradiation annealing in our reference experiment. The dislocation climb mechanism has been demonstrated as a prominent gas release mechanism, however, the values for diffusion of vacancies on the dislocations are not known and were chosen to allow gas release. The work carried out in this thesis has provided a better insight to the transport of intra-granular gas bubbles and its impact on fission gas release. This work also emphasized the questions that need to be answered at the lower scales.

Acknowledgements

The experiences gained in the three years working on this thesis have made me realise that the decision to pursue a doctoral degree was really worth it. Apart from the scientific knowledge, it is the all round exposure that I got during these years that has shaped me into a better researcher. It is impossible to embark on a journey so demanding without the support of people around you. The support I received from several people throughout the duration of my thesis is the reason that I am in a position to complete this manuscript. Words cannot express the gratitude I feel towards these people but I would like to acknowledge them here.

First and foremost, I take this opportunity to thank Mme Laurence NOIROT, my thesis supervisor at CEA Cadarache. This document would have no scientific worth, had it not been for her. She taught me the basic physics needed to understand the subject. She was just a door knock away from discussions and was always available to help me with my problems. Her constructive criticism always motivated me to out-perform my own capabilities.

Next, I would like to thank Prof. Philippe MAUGIS, my thesis director at Aix Marseille University. He has been the pillar supporting the basis of this thesis. His experience and deep understanding of the subject provided insights that helped build this thesis on a strong foundation.

I would like to acknowledge AMU, CEA, EdF and Framatome for the financial support provided for this thesis in the framework of the PLEIADES project.

I cannot thank enough the members of the jury, Mme Veena TIKARE, M. Thomas JOURDAN, M. Roland DUBOURG and Prof. Jean-Marc DEBIERRE for accepting to be a part of the jury for the thesis defense.

I thank Mme Veena TIKARE and M. Thomas JOURDAN for reviewing this manuscript and providing their valuable feedback and recommendations which have helped to shape this manuscript into a complete document.

I would also like to extend my gratitude to the people of LSC and LM2C labs in CEA Cadarache. M. Gérald JOMARD, head of lab LM2C, provided constant motivation and feedback throughout the thesis and made sure that the thesis was going in the right direction and in the right time to meet the deadlines. I am also thankful to the researchers from the labs, M. Serge MAILLARD, Mme Isabelle RAMIERE, M. Bruno MICHEL, M. Stephane BERNAUD, M. Emeric BOURASSEAU, Mme Marcelle IBRAHIM and M. Jean-Marie GATT for their suggestions during the 'advancement of thesis' meetings.

Special mention goes to Mme Regine BOUSQUET at CEA Cadarache and Mme Delphine STURMA at IM2NP, Aix-Marseille University, for taking care of

all my administrative requirements. I would also like to thank the thesis follow-up committee set up at IM2NP lab at AMU for their analysis of my thesis at the end of each year.

A shout-out to all the wonderful friends I made at work, Mourad, Luc, Piotr, Daria, who kept my social life alive and did not let me wonder into loneliness in this foreign land.

My friends outside of work, supported me throughout this journey. Ravi, Lav, Mohit, back at home and specially Rakhi, being a PhD student herself, kept motivating me, not letting me ever lose hope. Thank you, Rakhi, for being a motivation and for leading by example. This would not have been possible without you by my side.

No work can be deemed successful without the blessings of our parents and elders. Thank you Mumma, Papa for showering your blessings and love that made me keep going. I consider this journey a success if I have made you proud. My elder brothers have been a real support system, not only during this thesis, but throughout my life. Thank you for your love.

Lastly, I thank God for giving me the strength and will to keep moving forward in life and for providing me with such wonderful and supportive people who guided me, loved me and motivated me throughout this journey.

A handwritten signature in black ink, appearing to read 'Lokesh Verma', with a long horizontal stroke underneath.

Lokesh VERMA

Contents

Abstract	v
Acknowledgements	vii
List of Figures	xiii
List of Tables	xvii
General Introduction	1
1 Context and Literature review	5
1.1 Introduction and Context	5
1.1.1 Pressurized Water reactor (PWR)	5
1.2 Description of the UO ₂ nuclear fuel	7
1.2.1 Chemical composition of Uranium dioxide	8
1.2.2 Fission and fission products	9
1.2.3 Fission gases	11
1.3 Defects in nuclear fuel	11
1.3.1 Point Defects	11
1.3.2 Extended Defects	13
1.4 Fission gas behaviour	14
1.5 Mechanisms of FGR	16
1.5.1 Recoil and Knock-out	16
1.5.2 Single gas atom transport	17
1.5.3 Trapping of gas atoms	18
1.5.4 Irradiation induced re-resolution of gas atoms	19
1.5.5 Thermal re-resolution of gas atoms	20
1.5.6 Diffusion in the temperature gradient	23
1.5.7 Grain boundary diffusion	25
1.5.8 Intra-granular bubble migration	25
1.5.9 Grain boundary sweeping	26
1.5.10 Inter-granular bubble interconnection	27
1.5.11 Burst release	27
1.6 Mechanisms associated with intra-granular gas release during PIA tests	28
1.7 Experimental observations during post-irradiation annealing (PIA)	29
1.7.1 Microstructure evolution during PIA tests	29
1.7.2 FGR during PIA tests	32
1.8 Modelling approaches for FGR	34
1.8.1 Booth Model	35

1.8.2	Improving the Booth Model	36
1.8.3	Speight's Model for effective diffusion	37
1.8.4	Beyond Speight's Model	38
1.8.5	FGR modules in Fuel performance codes	38
1.9	Detailed modelling of intra-granular bubbles	40
1.9.1	Different scales of modelling	40
1.9.2	Meso-scale modelling	41
1.9.3	Prominent meso-scale methods	42
	Cluster Dynamics	42
	Kinetic Monte Carlo (kMC)	43
	Phase Field Model (PF)	45
1.9.4	Application of meso-scale modelling for intra-granular bubbles	46
	Conclusions from the application of meso-scale models for intra-granular bubbles	52
1.10	In Closing	53
2	A new spatialized meso-scale model: BEEP Model	55
2.1	BEEP Model: Introduction	55
2.1.1	Assumptions used in the model	55
2.2	Modelling methodology	56
2.2.1	Representation	56
2.2.2	Physical properties used in the model	59
2.3	Methodology adopted in the model	59
2.3.1	Initialization	60
2.3.2	Diffusion of point defects and crystal atoms	60
2.3.3	Space and Time Discretization	62
2.3.4	Bubble volume calculation	63
2.3.5	Determining the next center ("Target center") of bubble	64
2.3.6	Re-drawing the bubble keeping the atom and volume balance	64
2.3.7	Random movement of the bubbles	67
2.4	Parallelizing the BEEP Model	67
2.4.1	Using OpenMP	68
2.4.2	Implementing sub-domains	68
2.4.3	Message Passing Interface (MPI)	70
2.5	Testing the Model	73
2.5.1	Crystal atom balance	73
2.5.2	Verification for calculation of solid ratio "RS"	73
2.5.3	Verification for diffusion calculation	74
2.5.4	Verification of particular functionalities of BEEP Model	76
	Coalescence of two bubbles	76
	Vanishing of a bubble in the presence of a large bubble	77
2.5.5	Verification for bubble movement	78
2.6	Technical note on the exterior region ("Flat bubble")	81
2.7	In Closing	82

3	FGR due to bubble migration in a vacancy gradient	85
3.1	Directed movement of intra-granular bubbles in a vacancy gradient	85
3.1.1	Evans' model for directed movement of bubbles	87
3.1.2	Testing the movement and growth of bubbles in the BEEP Model	88
3.1.3	Grid size and Coalescence	92
3.2	Analysis of FGR via Directed Movement Mechanism	93
3.2.1	FGR values from experiments for comparison	93
3.2.2	Conditions for numerical analyses	94
3.2.3	FGR analysis	95
3.3	FGR analysis until vacancy gradient lasts	97
3.4	Uncertainty analysis of parameters	101
3.4.1	Uncertainty analysis of D_v	101
3.4.2	Uncertainty analysis of C_v^{eq}	101
3.5	In Closing	103
4	Brownian motion of bubbles and impact on FGR	105
4.1	Random (Brownian) movement of bubbles	105
4.1.1	Bubble diffusion by volume diffusion mechanism	105
4.1.2	Bubble diffusion by surface diffusion mechanism	107
4.2	Influence of random bubble movement without vacancy diffusion	108
4.2.1	Random movement of bubbles due to volume diffusion mechanism	109
4.2.2	Random movement of bubbles due to surface diffusion mechanism	109
4.3	FGR due to combined random and directed bubble movement in a vacancy concentration gradient	110
4.4	Dependence of bubble diffusion coefficient via surface diffusion mechanism on the bubble radius	113
4.5	FGR due to combined movement until vacancy gradient lasts	115
4.6	Parametric investigation of Mikhlin's suppression term	118
4.7	In Closing	121
5	Bubble movement via Dislocations	123
5.1	Introduction to Dislocations	123
5.1.1	Mechanisms of Dislocation movement	124
	Dislocation glide	124
	Dislocation climb	124
5.2	Scenario of bubble movement with dislocation climb	125
5.3	Implementation of Dislocations in BEEP Model	127
5.3.1	Assumptions	127
5.3.2	Formulation	128
5.3.3	Methodology	132
	Initialization	133
	Visualization	133
	Calculating the volume of pinned bubbles	134
	Equilibrating bubbles on a dislocation	135

Center targets for bubbles pinned on dislocations	135
Updating dislocations	136
Calculating the new dislocation velocities	136
Choosing an acceptable Δt for dislocation evolution . . .	136
5.4 First 3D Test Case for Dislocation and bubble movement	136
5.5 Scenario of FGR via bubble movement with Dislocations	140
5.5.1 Conditions for analysis	140
5.5.2 FGR analysis without any diffusion of vacancies from free surface	142
5.5.3 Factors influencing the velocity of dislocations	147
5.6 In Closing	151
General Conclusion	153
A Fuel Performance Codes	157
B Multi-scale modelling	161
C Von Neuman stability condition for Explicit scheme	163
D RS Calculation for six different cases	167
E Checking the order of convergence for space and time discretiza- tion	171
F Demonstration for the bubble velocity in a vacancy gradient	173
G Grid Sensitivity and impact on the coalescence process	179
G.1 Grid sensitivity analysis	179
G.2 Perspective for coalescence and space discretization in the model	180
H Target value of FGR (From spherical to planar geometry)	183
I Problems with classical rate theory in predicting FGR in anneal- ing condition with the random movement of bubbles	185
J Chemical potential in terms of vacancy formation energy	187
Bibliography	191
Résumé en français	211

List of Figures

1.1	A typical PWR design. [2]	6
1.2	A PWR fuel assembly with fuel rod. [3]	7
1.3	Fuel pellets used in the fuel rod. <i>Source:</i> [4]	8
1.4	The arrangement of uranium and oxygen ions in UO_2 .	8
1.5	Distribution of fission products during fission of U-235.	9
1.6	Different point defects in a crystal lattice.	12
1.7	Different types of dislocations (a) Edge dislocation, (b) Screw dislocation, (c) Mixed dislocation.[12]	13
1.8	Different types of planar defects: (a) Grain boundary, (b) Stacking fault	14
1.9	Bulk (3-D) defects in UO_2 fuels (a) SEM image of an as-fabricated UO_2 disk showing the presence of pores (b) TEM image indicating the presence of gas bubbles in a UO_2 thin film implanted with Xe ions after annealing at up to 1500°C during 2 hours.	15
1.10	Pellet-Cladding Interaction due to swelling of the nuclear fuel (taken from [15]).	16
1.11	Scanning electron micrographs of polished surface of 3 cycle specimens (burnup: 23 GWd/t)[96].	30
1.12	Scanning electron micrographs of fracture surface of 1 cycle specimen and 3 cycle specimen (a,c) as-irradiated, and (b,d) isothermal annealing at 1800°C for 5 h, respectively [96].	31
1.13	Variation in fraction of Kr-85 released during isothermal annealing of UO_2 sample [8].	34
1.14	Methods used for materials model development and computer simulations at different scales (taken from [175]).	41
1.15	(a) Diffuse-interface; continuous variation of properties at the interface. (b) Sharp-interface; discontinuous properties at the interface [187].	46
1.16	Potts-kMC Model used by ORNL for the benchmark study.	51
2.1	A regular 2-D mesh representing the fuel matrix and a cavity with spins designated to each cell.	57
2.2	General algorithm adopted in the model	60
2.3	An example of a visualization in terms of RS using the PAR-AVIEW application.	61
2.4	5-point stencil scheme in 2-D for space discretization.	62
2.5	Schematic explanation of the algorithm adopted in Explicit Method	64
2.6	Description of cell division for calculating RS with the error generated in the atom balance	65

2.7	Division of a large domain into smaller sub-domains	69
2.8	Speed-up (Time Ratio) using sub-domains.	69
2.9	Sub-domains and ghost slices.	70
2.10	Algorithm for MPI Parallelization.	71
2.11	Speed up for different number of processors using MPI Parallelization.	73
2.12	Numerical vs Analytical values for vacancy concentration.	75
2.13	Coalescence of 2 bubbles, at time $t = 0$ and after annealing at $t = 12$ s of simulation time.	77
2.14	Vanishing of a bubble in the presence of a larger bubble, at time $t=0$ and after diffusion at $t=10$ min of experiment time	79
2.15	Evolution of volume of the small and big bubble with the experiment time.	80
2.16	Bubble movement and growth in a vacancy concentration gradient.	81
2.17	Theoretical vs Numerical value of bubble velocity.	82
3.1	Vacancy concentration gradient existing between surfaces.	86
3.2	Directed movement of a bubble in a vacancy concentration gradient.	86
3.3	Evans model description.	87
3.4	Schematic representation of domain for bubble movement and growth.	88
3.5	Movement and growth of bubbles in a vacancy gradient.	89
3.6	Equilibrium concentration of vacancies at the vicinity of bubbles as a function of time.	90
3.7	Distribution of bubbles in the domain after equilibrium concentration was reached and the mean radius of the bubbles.	91
3.8	Directed motion of smaller bubbles towards the big bubble.	91
3.9	Domain used for the analyses with various conditions.	94
3.10	Dashed box representing the enlarged region of the actual domain presented in the results.	95
3.11	Bubble distribution in the domain during 3 hours of simulated time.	95
3.12	Bubble movement in a vacancy concentration gradient for 110 hours of simulated time.	96
3.13	Mean bubble radius along the domain for directed movement case.	97
3.14	Vacancy concentration values along the grain at different times.	98
3.15	Bubble distribution in the domain until vacancy gradient lasts.	99
3.16	Bubble distribution in the entire domain at the end of the simulation.	99
3.17	Mean bubble radius along the domain at the times $t = 110$ h and at the end of the simulation at $t = 8569$ h.	100
3.18	Evolution of FGR and mean radius of the bubbles during the simulation.	100

4.1	Random movement of bubbles by volume and surface diffusion mechanism.	106
4.2	Random bubble distribution at time $t = 0$	108
4.3	Random movement of bubbles at time = 3 hours by volume diffusion mechanism.	109
4.4	Random movement of bubbles at time = 3 hours by surface diffusion mechanism with Mikhlin's suppression term.	110
4.5	Bubble movement in a vacancy concentration gradient with random movement of bubble by surface diffusion for 110 hours of simulated time.	111
4.6	Bubble diffusion coefficient via surface mechanism with and without the diffusion of vacancies in 3 hours of simulated time.	111
4.7	Mean Bubble radius along the domain for combined movement case.	112
4.8	Mean of first term in D_b^{surf} along the domain up to time $t = 110$ h.	113
4.9	Mean Mikhlin Suppression Factor for bubbles along the domain up to time $t = 110$ h.	114
4.10	Mean Bubble diffusion coefficient for bubbles along the domain.	115
4.11	Vacancy concentration values along the grain at different times.	116
4.12	Bubble distribution in the domain until vacancy gradient lasts.	117
4.13	Bubble distribution in the entire domain at the end of the simulation.	117
4.14	Mean Bubble diffusion coefficient for bubbles along the domain until simulation lasts.	118
4.15	Bubble distribution due to random movement by surface diffusion mechanism at time = 3 hr.	119
4.16	Random movement of bubbles via surface diffusion in the new domain at time $t = 0$, $t = 110$ h and $t = 5500$ h, after the first 3 hours.	120
5.1	Dislocation movement via glide mechanism.	124
5.2	Dislocation movement via climb mechanism: (a) Positive climb by vacancy annihilation, (b) Negative climb by vacancy generation.	125
5.3	Scenario of bubble movement via dislocation climb mechanism.	127
5.4	Pinned bubbles on dislocation.	130
5.5	Net work done on the solid.	131
5.6	Incorporation of dislocations into BEEP Model.	133
5.7	Visualization of 3D cases in the BEEP Model.	134
5.8	Calculating the volume of bubble pinned on a dislocation.	134
5.9	Correction of target center for pinned bubble.	136
5.10	Schematic representation of the initial condition of the domain.	137
5.11	Bubble movement via Dislocation climb mechanism.	138
5.12	Evolution of the velocity of the dislocation and pinned bubble gas content with time.	139
5.13	Volume of the pinned bubble on dislocation.	140
5.14	Schematic representation of domain with boundary and initial conditions.	141

5.15	Bubble movement via Dislocation climb mechanism for 3 hours of annealing simulation.	144
5.16	Bubbles pinned on dislocation move via dislocation climb mechanism.	145
5.17	FGR in 3h hours via dislocation climb mechanism.	146
5.18	FGR in the first 386 s via dislocation climb mechanism.	146
5.19	Radius evolution of the 6 pinned bubbles on the remaining dislocations after 1122 s.	148
5.20	Effective pressure of the 6 pinned bubbles on the remaining dislocations after 1122 s.	149
5.21	Velocity of the six dislocations remaining after 1122 s.	150
5.22	FGR in 3 hours with the different mechanisms of bubble movement adopted in the 2-D analysis.	154
D.1	Different bubble configurations in the 1-cells to verify numerical calculation of RS with the theoretical.	168
D.2	Calculating the area of bubble outside the cell.	169
D.3	Calculating the RS of cells.	170
E.1	Determining the order of convergence in space.	171
E.2	Determining the order of convergence in time.	172
F.1	Spherical coordinates in 3D.	174
F.2	Polar coordinates in 2D.	176
G.1	Grid sensitivity analysis: Plot for mean bubble radius with time for 3 different grids.	180
G.2	Grid sensitivity analysis: bubble distribution after 1 hour for large (Grid 1), medium (Grid 2) and small (Grid 3) grids.	181
H.1	Target value of FGR from spherical to Planar geometry.	183
I.1	FGR from the grain during the annealing simulation at 1600°C from rate theory without Mikhlin's suppression term.	186
I.2	Bubble density and radius during the annealing simulation at 1600°C from the rate theory without Mikhlin's suppression term.	186
J.1	Box containing vacancies and normal (crystal atom) sites.	187
FR1	Domaine utilisé pour les analyses en 2-D avec les différentes conditions.	213
FR2	RGF en 3 heures avec les différents mécanismes de mouvement des bulles adoptés dans les analyses 2D.	218
FR3	Représentation schématique du domaine en 3-D avec conditions limites et initiales.	219
FR4	RGF en 3h via un mécanisme de montée disloqué.	220

List of Tables

1.1	Rate of creation of the main fission products in PWR for enriched UO_2 fuel calculated using the CATACOMB module [9].	10
1.2	Literature on thermal re-solution.	24
1.3	Literature on experiments of PIA tests for FGR.	35
1.4	Fuel Performance Codes and FGR modules.	39
1.5	Initial conditions for the intra-granular bubbles and the thermodynamic properties of defects used for benchmark problem [176].	48
1.6	Computational efforts made in the different models used in the benchmark demonstration [176].	49
1.7	Computational efforts made in the different models used in the benchmark demonstration [176, Table 6].	49
2.1	Physical parameters used in the model.	59
2.2	Computation time and speed up for test case using MPI and communications between sub-domains.	72
2.3	Analytical vs Numerical calculation of RS.	74
2.4	Quantities used in the model for the cases of coalescence and vanishing of bubbles at $T = 1800^\circ\text{C}$	76
2.5	Properties of bubbles for coalescence test.	76
2.6	Properties of bubbles for vanishing test.	78
2.7	Conditions used in the model.	81
3.1	Properties of the five bubbles with respect to the big bubble at $t = 0$ and $t = 60$ min.	92
3.2	Evolution of quantities from $t = 0$ to $t = 60$ min.	92
3.3	Initial conditions used for the analyses.	95
3.4	Evolution of various parameters with time for the directed movement case.	96
3.5	Evolution of various parameters with time for the directed movement case continued until possible	98
3.6	FGR during uncertainty analysis of C_v^{eq}	102
3.7	C_v^{eq} values at the rightmost and leftmost end of the domain.	102
4.1	Values of surface diffusion coefficient, D_s from literature.	107
4.2	Evolution of various quantities with time for the combined directed and random movement case.	113
5.1	Physical parameters used for the analysis.	142
5.2	Characteristics of the dislocations and the pinned bubbles at time $t = 1122$ s.	148

List of Abbreviations

°C	degree C elsius or C entigrade
2-D	two- D imensional
3-D	three- D imensional
CASL	C onsortium for A dvanced S imulation of L ight W atre R eactors
CFL	C ourant- F riedrichs- L ewy
CMSNF	C enter for M aterial S cience of N uclear F uels
DFT	D ensity F unctional T heory
eV	electron V olt
FCC	F ace C entered C ube
FFTW	F ast F ourier T ransform in the W est
FGR	F ission G as R elease
INL	I dhao N ational L aboratory
KMC	kinetic M onte C arlo
LWR	L ight W ater R eactor
MD	M olecular D ynamics
MOOSE	M ulti-physics O bject O riented S imulation E nvironment
MPI	M essage P assing I nterface
NEAMS	N uclear E nergy A dvanced M odelling and S imulation
ODE	O rdinary D ifferential E quation
ORNL	O ak R idge N ational L aboratory
PF	P hase F ield
PIA	P ost I rradiation A nneling
PKA	P rimary K nock- O n A toms
PNNL	P acific N orthwest N ational L aboratory
PWR	P ressurized W ater R eactor
RS	R atio S olide (Solid Ratio/Fraction)
SEM	S canning E lectron M icroscope
SMA	S tandard M etropolis A lgorithm
SNL	S andia N ational L aboratory
TDS	T hermal D esorption S pectroscopy
TEM	T ransmission E lectron M icroscopy

List of Symbols

Δa	excess of atoms numerically introduced	-
ΔH	activation enthalpy	J
ΔS	local fractional swelling	-
Δt	time step for the calculation	s
∇C_v	vacancy concentration gradient	fraction of site. m^{-1}
∇T	temperature gradient	K m^{-1}
ΔV_{comp}	complimentary volume added numerically	m^3
b	re-resolution rate	s^{-1}
C_a	concentration of crystalline atoms	fraction of site
C_g	concentration of gas atoms	fraction of site
C_v	concentration of vacancies	fraction of site
$C_v^{analytic}$	analytically calculated C_v	fraction of site
C_v^{num}	numerically calculated C_v	fraction of site
$C_v^{eq}(bubble)$	equilibrium conc of vacancy in the vicinity of a bubble	fraction of site
C_v^{ini}	initial concentration of vacancies in the solid	fraction of site
C_{Xe}^{eq}	concentration of equilibrium of Xe	fraction of site
d	most probable distance	m
$diam$	hard sphere diameter (Buckingham potential)	m
D^*	vacancy diffusion coefficient on the dislocation multiplied by $x_{v,d}^{eq}$	$\text{m}^2 \text{s}^{-1}$
D_b	bubble diffusion coefficient	$\text{m}^2 \text{s}^{-1}$
D_b^{surf}	bubble diffusion coefficient via surface diffusion	$\text{m}^2 \text{s}^{-1}$
D_b^{vol}	bubble diffusion coefficient via volume diffusion	$\text{m}^2 \text{s}^{-1}$
D_{eff}	effective diffusion coefficient	$\text{m}^2 \text{s}^{-1}$
D_s	surface diffusion coefficient	$\text{m}^2 \text{s}^{-1}$
D_U	uranium self-diffusion coefficient	$\text{m}^2 \text{s}^{-1}$
D_v	vacancy diffusion coefficient	$\text{m}^2 \text{s}^{-1}$
D_v^*	non-dimensional vacancy diffusion coefficient	-
D_{Xe}	single Xe gas atom diffusion coefficient	$\text{m}^2 \text{s}^{-1}$
f	correlation factor	-
f_{FGR}	fractional FGR in Booth's Model	-
g	trapping rate	s^{-1}
h	grid size	m
k	Boltzmann constant	J K^{-1}
l^*	non-dimensional length	-
L_i	length of the segment of the dislocation	m
L_{tot}	total length of the segment	m
N	number of cells in the domain	-

N_b	bubble number density	bubbles/m ³
$N_{b,2D}$	bubble number density in 2-D	bubbles/m ²
P_b	bubble inner pressure	Pa
P_{eff}	effective pressure	Pa
P_{ext}	external pressure on the system	Pa
P_i	internal pressure of the pinned bubble	Pa
q	volume of the region with no gas atoms	m ³
r_b	radius of bubble	m
R_{booth}	Booth radius	m
R_g	radius of the grain	m
S/V	surface-to-volume ratio	m ⁻¹
s_v	excess entropy of vacancy formation	J K ⁻¹
t	simulation time	s
t^*	non-dimensional time	-
T	absolute temperature	K
T_m	Monte Carlo temperature	K
$V_{add.}$	additional volume due to dislocation climb	m ³
V_{at}	volume per atom of gas	m ³
$V_b^{0-cells}$	volume in the 0-cells of the bubble	m ³
v_b	bubble velocity in a vacancy gradient	m s ⁻¹
V_{cell}	volume of one cell	m ³
v_d	dislocation velocity	m s ⁻¹
V_{flux_disloc}	volume added due to flux of vacancies	m ³
w	width of dislocation	m
W_b	Mikhlin's suppression factor	-
w_{ext}	width of external region	m
$x_{v_d}^{eq}$	equilibrium vacancy concentration on the dislocation	fraction of site
β	vacancy source term	vac m ⁻³ s ⁻¹
ϵ_v	vacancy formation energy	J
γ_b	surface tension at the solid-bubble interface	J m ⁻²
κ	curvature of the surface	m ⁻¹
Ω	atomic volume of UO ₂	m ³
ϕ	random angle	rad
ϕ_a	flux of crystal atoms	atoms m ⁻² s ⁻¹
ϕ_v	flux of vacancies	vac m ⁻² s ⁻¹
μ	chemical potential	J
η	packing fraction	-

Dedicated to my grandfather, Late Mr. K.L. VERMA

General Introduction

When fission takes place in a nuclear reactor, the nuclear reactions lead to the generation of fission products, including inert gas atoms, and point defects such as vacancies, self-interstitials and gas in substitution. Fission gases (Xe, Kr) generated during the irradiation have a fission yield of about 0.3 and are mostly insoluble in the fuel matrix and often precipitate into bubbles. The point defects interact with these bubbles and other microstructural features like as-fabricated pores and grain boundaries in the fuel. These interactions between the mobile point defects and the extended defects like gas bubble, grain boundary or free surface can lead to macroscopic phenomena like Fission Gas Release (FGR) and swelling in the fuel. These phenomena affect the proper functioning of the fuel rod and must be considered in any fuel performance code. FGR from the fuel increases the pressure in the fuel rod plenum, subjecting the cladding to additional stress and also reduces the thermal conductivity of the fuel-cladding gap causing the fuel operating temperature to increase. Due to their low solubility in UO_2 , fission gases also precipitate into highly pressurized bubbles causing the swelling of the fuel. Swelling contributes to the fuel-cladding interaction, again exposing the cladding to higher stress and ultimately hampering its lifetime. So, understanding fission gas behaviour is very important for optimal utilization of fuel rod during nuclear reactor operation.

In order to understand fission gas behaviour, in-pile as well as out-of-pile measurements are carried out in the nuclear fuel. It is, however, difficult to carry out measurements in a fuel under irradiation (in-pile) due to uncontrollable environment variables. Post-irradiation annealing (out-of-pile) tests are carried out to obtain data on FGR under controlled and monitored environment. One of the interesting issues during post-irradiation annealing tests has been the transport of intra-granular gas to the grain surface, as it is found to be very rapid as compared to the values predicted from effective diffusion theory. The fission gas bubbles can be either nanobubbles within the grain (intra-granular) or larger bubbles on grain boundaries (inter-granular). The mechanism of fission gas release out of the fuel can be understood as a two step process: the transfer of gas atoms from the grain to the grain boundaries, and then the coalescence and interlinkage of grain-boundary bubbles to give pathways to outside the fuel. While the latter is clearly observed at high temperatures ($T \geq 1400^\circ\text{C}$), the former step of gas atoms transfer within the grain has been a topic of debate for the past few decades. If the gas bubbles are considered as perfect traps for gas atoms and according to the

effective diffusion theory, the gas should be trapped in the large number of intra-granular bubbles during annealing at high temperatures and should not escape the grain within the duration of annealing. However, it has been long observed that, in practice, the fission gas release from the grain to the grain boundaries may reach large values.

Several mechanisms have been proposed for the explanation of such behaviour in the past. For a few years, spatially resolved models have been developed at the mesoscale to understand the microstructure in greater detail. The advantage of using the mesoscale is that material characteristics at the microstructure-level such as bubbles can be represented explicitly. Moreover, mesoscale allows us to study the microstructure at larger time and length scales than the atomic scale (Molecular Dynamics). Within the framework of this thesis, we present a new spatially resolved model, called the BEEP Model, for the interactions between point defects and extended defects like fission gas bubbles and free surfaces. The aim of the thesis is to model and analyze some of the mechanisms of intra-granular gas bubble transport during post-irradiation annealing and their impact on the FGR using the BEEP Model. The mechanisms discussed in the thesis include:

- Directed movement of gas bubbles up the vacancy concentration gradient caused by the arrival of thermal vacancies from grain boundaries.
- Brownian movement of gas bubbles via volume and surface diffusion mechanisms.
- Movement of gas bubbles along with the dislocations via the dislocation climb mechanism.

In order to present the relevant information in a continuous manner, this manuscript is structured into five main chapters. The first two chapters aim to present a detailed literature review and the methodology adopted in the modelling of BEEP. The findings obtained from the numerical analyses carried out using BEEP are presented in the last three chapters. The organization of this manuscript in the form of different chapters is as follows:

Chapter 1 provides an overview of the works present in the literature to provide a context to the physics related to the subject. It gathers essential data for a good understanding of the work done during the thesis. The description of the nuclear fuel used in Light Water Reactors (LWR) is presented and its microstructure explained. In addition, a non-exhaustive summary of the different studies focused on the mechanisms of gas bubble transport within the grain during post-irradiation annealing tests and the modelling approaches used to study the fuel behaviour is provided. Experimental data on FGR and bubble movement available in literature is also discussed.

Chapter 2 presents the methodology adopted for the development of the BEEP Model. This chapter discusses the various physical phenomena implemented into the model and describes in detail the mathematical and numerical

aspects of these physical phenomena. The verification tests are presented for the credibility of the BEEP Model to carry out further studies.

Chapter 3 aims to present the first mechanism of intra-granular gas transport during post-irradiation annealing tests. This mechanism is the directed movement of intra-granular gas bubbles in a vacancy concentration gradient that exists between the pressurized bubbles and the free surface. First the BEEP Model is tested for bubble movement and then the entire domain is simulated using the BEEP Model. The results from the simulations are analyzed and presented in this chapter.

Chapter 4 presents the next mechanism of intra-granular gas transport during post-irradiation annealing tests. This mechanism is the Brownian movement of bubbles via the volume and surface diffusion mechanisms. First, the impact of random movement of bubbles is studied without the diffusion of vacancies in the domain. Later, FGR estimates are also studied using the combined movement of gas bubbles via the directed movement in a vacancy gradient and their random movement.

Lastly, Chapter 5 presents a simple approach to incorporate dislocations into the BEEP Model. A scenario is then studied for the FGR by the movement of intra-granular gas bubbles pinned on the dislocations along with the dislocations via the mechanism of dislocation climb. The methods adopted in the BEEP modelling to incorporate this phenomenon are also described.

Finally, the conclusions and perspectives of the thesis are presented in the final section of this manuscript.

Chapter 1

Context and Literature review

1.1 Introduction and Context

A nuclear reactor produces energy from the process of splitting of atoms of certain elements, called fission. In a nuclear power reactor, the energy released during fission (200 MeV) is used as heat to make steam to generate electricity. Over the years, there have been many designs of nuclear reactors in the world. The principles for using nuclear power to produce electricity are usually the same for most types of reactors. The energy released from the fission of the atoms of the fuel is harnessed in the form of heat in either a gas or water coolant, and is used to produce steam. This steam is then used for rotating the turbines which produce electricity. The various designs of nuclear power reactors operational at present are Pressurised Water Reactor (PWR), Boiling Water Reactor (BWR), Pressurised Heavy Water Reactor (PHWR), Advanced Gas-cooled Reactor (AGR), Fast Breeder Reactor (FBR), among others.

The most common type of power reactors are the PWRs, with 301 operational reactors in the world, generating 287 GW of net electrical capacity as of September, 2019 [1].

1.1.1 Pressurized Water reactor (PWR)

A PWR has water at over 300°C under pressure in its primary cooling/heat transfer circuit, and generates steam in a secondary circuit. Ordinary water is used both as coolant and moderator in PWRs. The design is distinguished by having a primary cooling circuit which flows through the core of the reactor under very high pressure, and a secondary circuit in which steam is generated to drive the turbine. A typical PWR with its primary and secondary circuits is depicted in Fig.1.1.

The various components of a PWR are as follows:

- Fuel and Reactor Core

The reactor core contains the fissile elements (mainly U-235 and Pu-239) in the form of fuel pellets. Uranium dioxide (UO₂) enriched to 3-5%

A Pressurized Water Reactor (PWR)

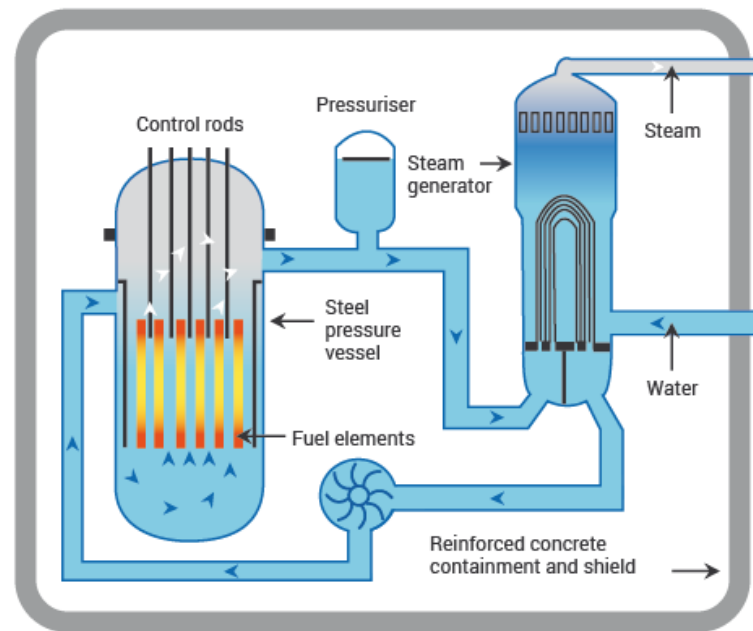


FIGURE 1.1: A typical PWR design. [2]

in U-235 is used as the fuel. After enrichment, UO_2 powder is fired in a high-temperature, sintering furnace to create hard, ceramic pellets. The cylindrical pellets are then clad in a corrosion-resistant zirconium metal alloy Zircaloy which are backfilled with helium to aid heat conduction and detect leakages. The finished fuel rods are grouped in fuel assemblies, called fuel bundles, that are then used to build the core of the reactor. Generally, the fuel bundles consist of fuel rods bundled 14×14 to 17×17 . A PWR fuel bundle is about 4 meters in length and about 20 cm across and weighs about half a tonne. The assembly has vacant rod positions left for the vertical insertion of a control rod. A fuel assembly consisting of fuel rods is depicted in Fig.1.2.

- **Moderator**
 A moderator is needed in a thermal nuclear reactor to slow down the fast fission neutrons (about 2 MeV) to thermal values (few eV) in order to interact with the nuclear fuel and sustain the chain reaction. In PWRs the coolant water is used as a moderator by letting the neutrons undergo multiple collisions with light hydrogen atoms in the water, losing speed in the process.
- **Control Rods**
 Control rods are used in nuclear reactors to control the fission rate of uranium and plutonium. They are composed of chemical elements that are capable of absorbing many neutrons without themselves undergoing fission. Control rods are usually used in assemblies of typically 20 rods for a commercial PWR and inserted into guide tubes within a fuel element. The candidates for materials of control rods for PWRs include

silver, indium, cadmium, boron, cobalt, hafnium, among others. Alloys such as high-boron steel, silver-indium-cadmium alloy or boron carbide are other potential candidates. Borated water is also used to control the reactivity.

- Coolant and cooling circuit

Coolant is a heat transfer fluid, which transfers the heat produced in the fuel. In PWRs, light water under high pressure (~ 150 bar) is used as the primary coolant. Water entering through the bottom of the reactor's core is heated as it flows upwards through the reactor core to a temperature of about 315°C . The water remains liquid despite the high temperature due to the high pressure in the primary coolant loop which is maintained by a pressurizer. The primary coolant then transfers heat in a steam generator to water in a lower pressure secondary circuit, evaporating the secondary coolant to saturated steam. The cooled primary coolant is then returned to the reactor vessel to be heated again.

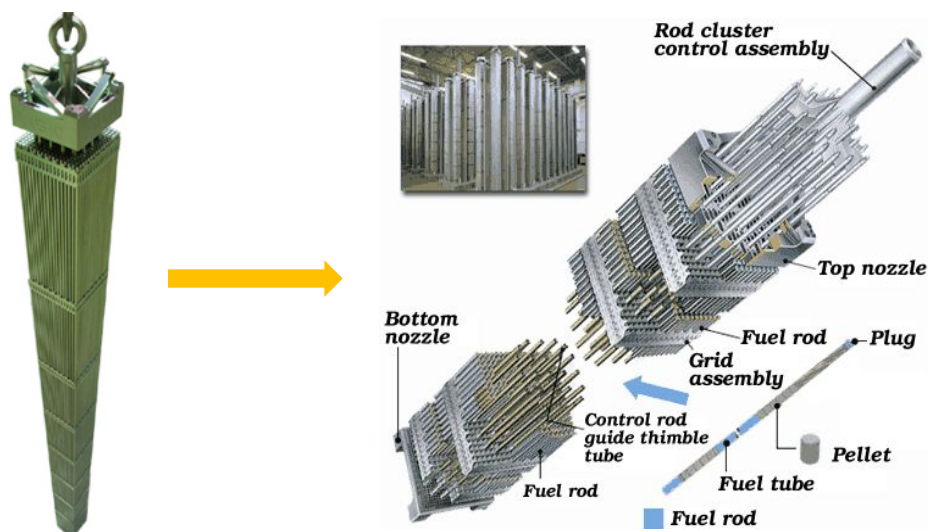


FIGURE 1.2: A PWR fuel assembly with fuel rod. [3]

1.2 Description of the UO_2 nuclear fuel

As mentioned earlier, usually the material constituting the PWR fuel is enriched uranium dioxide. Typically, the PWR fuel is in the form of pellets of height = 13 mm and diameter = 8 mm, which are created by pressing and then sintering at 1700°C . Fig.1.3 shows a picture of fuel pellets used in the fuel rod. The target stoichiometry (oxygen / uranium ratio) of the industrial UO_2 pellets is equal to 2.00 ± 0.01 , and the targeted density is close to $95\% \pm 0.5\%$ of the theoretical density (for both guaranteeing a low re-densification, and accommodate the swelling of the pellet under irradiation). The pellets are stacked and held in zirconium alloy sheaths. The most commonly used alloy in PWRs today has been Zircaloy-4, but is currently being replaced by new

zirconium-niobium alloys, also known as M5, which are more resistant to corrosion. The sheath acts as the first barrier to prevent the spread of fission products and uranium oxide. Depending on the fuel management, the fuel remains in a reactor for several years divided into 3 to 5 cycles. At the end of each cycle of operation, the arrangement of the fuel assemblies is modified.



FIGURE 1.3: Fuel pellets used in the fuel rod. *Source: [4]*

1.2.1 Chemical composition of Uranium dioxide

Uranium dioxide (UO_2) also known as urania or uranous oxide, is an oxide of uranium, and is a black, radioactive, crystalline powder that naturally occurs in the mineral uraninite. It is a preferred material for nuclear fuels because of its intrinsic properties. First of all, it has a crystalline structure of fluorine type (see Fig.1.4) which is stable under the effect of the radiation emitted during reactor operation. The uranium atoms are arranged in a face-centered cubic

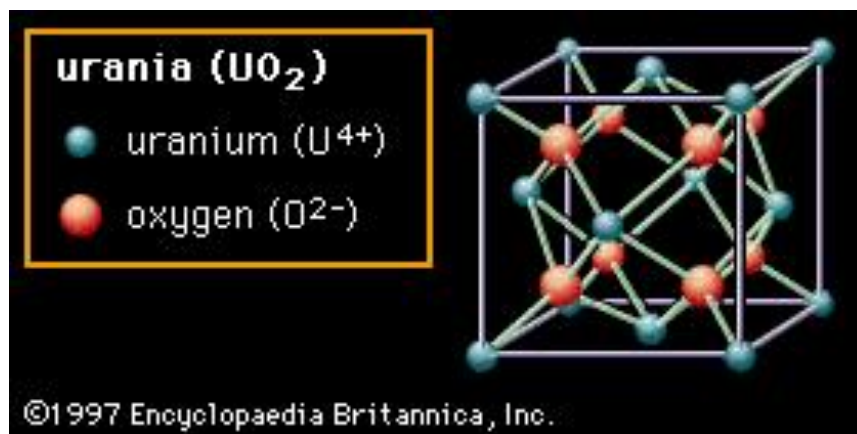


FIGURE 1.4: The arrangement of uranium and oxygen ions in UO_2 .

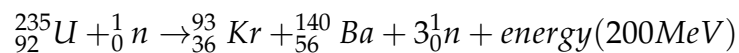
(FCC) lattice, whose 8 tetrahedral sites are occupied by the oxygen atoms. The octahedral sites, i.e., the middle of the edges and the center of the cube, are vacant and can be occupied by the fission products. Oxygen atoms form

a simple cubic network in which the uranium atoms occupy the center of one cube in two, having no common face.

Moreover, UO_2 has a high melting point of 2847°C , a fairly high chemical inertia, with respect to metal alloys commonly used as cladding materials and heat transfer fluids (water under pressure for PWRs). The non-irradiated stoichiometric UO_2 cell parameter is 0.5471 nm [5] and has a theoretical density of 10.952 g.cm^{-3} . However, UO_2 has a low thermal conductivity, of the order of $4.5\text{ W.m}^{-1}\text{.K}^{-1}$ at 450°C , and of $3\text{ W.m}^{-1}\text{.K}^{-1}$ at 1000°C [6]. This low thermal conductivity gives rise to a strong thermal gradient in the reactor. Typical surface temperatures of the fuel pellet are in the order of 500°C , while the fuel centerline temperatures are about 1000°C .

1.2.2 Fission and fission products

In a nuclear reactor, the fission of fissile heavy nuclei (U-235, Pu-239, Pu-241) gives rise to radionuclides called fission products. The fission process is accompanied by a release of energy of 200 MeV: 80% of this energy is found in the form of kinetic energy of neutrons and fission products, on average 65 MeV for the heavier fission product and 95 MeV for the lighter. The rest is dissipated as β and γ radiations. An example of a typical fission reaction of a U-235 atom is shown below:



The distribution of the fission products created during the fission of uranium 235 is given by the fission yield (%)¹ curve as a function of the mass number (A) as shown in Fig.1.5. 15% of the fission products generated are

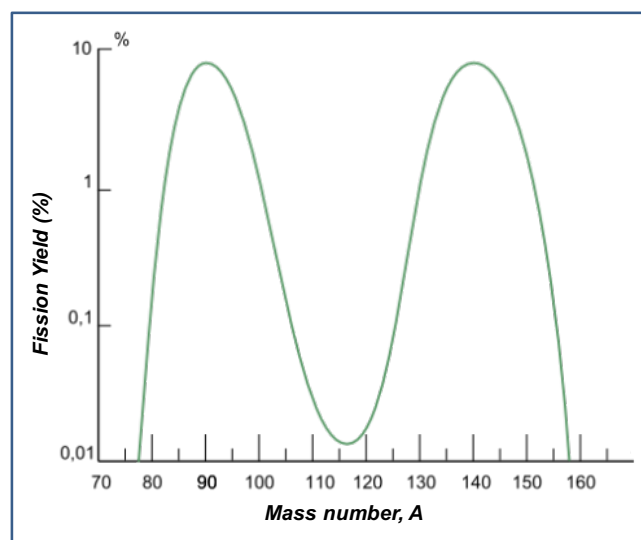


FIGURE 1.5: Distribution of fission products during fission of U-235.

¹Note that the total of the fission yields is 200%, as 2 fission products are generated per fission.

in gaseous form and the remaining are in volatile or solid form. The fission products are classified into the following groups [7]:

- gaseous fission products: these are the rare gases Xenon and Krypton;
- volatile fission products: cesium, iodine, tellurium, rubidium;
- solid fission products: metallic precipitates, elements forming insoluble oxides in the UO_2 matrix, elements in substitution of Uranium in the lattice of UO_2 (lanthanides).

The rate of creation of these different fission products depends on the neutron energy spectrum (thermal, epithermal or fast) and the nature of the fissile atoms which changes with time in the reactor. Table 1.1 [8] gives a calculation of the rate of creation of the fission products in PWR for a UO_2 fuel enriched in U-235 at 3.7% and a burnup of $10.5 \text{ GWd}/t_U$ using the CATACOMB module of the CATHARE code [9]. At the end of this cycle, about a third of the U-235 atoms disappeared by fission.

Type of Fission Product	Element	Number of atoms per 10^3 atoms of U present initially	Total fraction of atoms of fission product
Rare gases	Krypton	0.39	1.8%
	Xenon	2.96	13.4%
Volatile elements	Cesium	1.59	7.2%
	Tellurium	0.26	1.2%
	Rubidium	0.35	1.6%
Metals (inclusions)	Ruthenium	1.62	7.4%
	Palladium	0.38	1.7%
	Technetium	0.64	2.9%
	Rhodium	0.29	1.3%
	Molybdenum	2.34	10.6%
Insoluble oxides	Barium	0.79	3.6%
	Strontium	1.02	4.6%
	Zirconium	3.23	14.7%
Dissolved oxides	Yttrium	1.76	8.0%
Lanthanides	Cerium	0.52	2.4%
	Neodymium	1.76	8.0%
	Praseodymium	0.57	2.6%
	Lanthanum	0.68	3.1%
	Samarium	0.26	1.2%

TABLE 1.1: Rate of creation of the main fission products in PWR for enriched UO_2 fuel calculated using the CATACOMB module [9].

1.2.3 Fission gases

Fission products generated in the gaseous state are essentially rare gases:

- Xenon in the isotopic forms: Xe-129, Xe-131, Xe-132, Xe-134 and Xe-136;
- Krypton: Kr-83, Kr-84, Kr-85 and Kr-86;

The set of stable gases created in PWR is of the order of 0.31 at/fission. As can be seen from Table 1.1, the gases thus formed, especially Xenon, represent significant amounts. These fission gases are mostly insoluble in bulk UO_2 and can lead to macroscopic phenomena like swelling and gas release. These phenomena directly affect the thermo-mechanics of the fuel rods and may shorten their lifetime. Due to their characteristics, the fission gas behaviour needs to be understood properly as it concerns the safety of the nuclear reactors. The fission gas behaviour will be discussed further in Section 1.4.

1.3 Defects in nuclear fuel

No material existing in nature is a perfect crystal. Atom arrangements in real materials do not completely follow perfect crystalline patterns. The imperfections in the materials are called defects. These defects are best described in terms of their dimensions. The 0-dimensional defects affect isolated sites in the crystal structure, and are hence called "point defects". The defects other than the point defects are extended in space and are referred to as "extended defects". The 1-dimensional defects are lines along which the crystal pattern is broken and are called dislocations. The 2-dimensional defects are surfaces, such as the external surface and the grain boundaries along which the different crystallites are joined. The 3-dimensional defects are those which change the crystal pattern over a volume. These defects are discussed below.

1.3.1 Point Defects

Point defects are defects that occur only at or around a single lattice point. They are not extended in space in any dimension. During elastic collisions, if the energy transferred by the projectile is greater than the binding energy of the atoms in their lattice sites, the lattice atoms are displaced from their original positions. The displaced atoms, also known as Primary Knock-On atoms (PKA), can cause an avalanche of other atomic collisions if they have enough kinetic energy resulting in a succession of cascade displacement to form point defects. Point defects typically involve at most a few extra or missing atoms. Slightly larger defects in an ordered structure are usually dislocation loops (discussed later). The different point defects are shown in Fig.1.6 and are described below.

- **Vacancy**
Vacancy defects are lattice sites which would be occupied in a perfect crystal, but are vacant. If a neighboring atom moves to occupy the vacant site, the vacancy moves in the opposite direction to the site which used to be occupied by the moving atom. The stability of the surrounding crystal structure guarantees that the neighboring atoms will not simply collapse around the vacancy.
- **Interstitials**
Interstitial defects are atoms that occupy a site in the crystal structure at which there is usually not an atom. They are generally high energy configurations, but small atoms in some crystals can occupy interstices without high energy. They may be the same type of atom as the others (self interstitial) or an impurity atom.

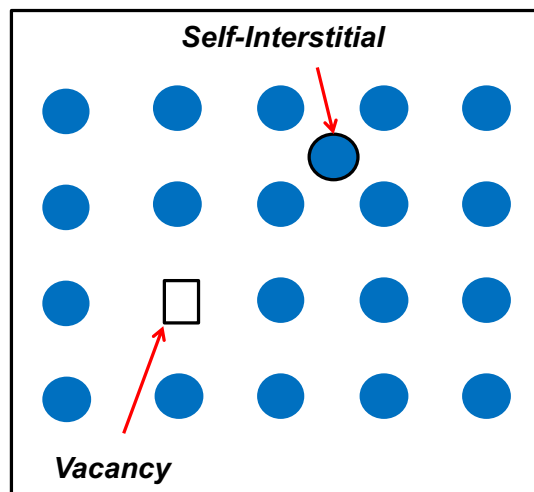


FIGURE 1.6: Different point defects in a crystal lattice.

- **Frenkel Pairs**
A Frenkel pair defect arises when a lattice atom is pushed to an interstitial site as a result of ballistic collision with an energetic particle or when the crystal is heated at sufficiently high temperature, provided that the energy absorbed by the atom is higher than its displacement energy. According to Olander [10], Frenkel pair defects are most commonly observed in UO_2 under irradiation.
- **Schottky Defect and other defects including a U vacancy in $\text{UO}_{2\pm x}$**
The Schottky defect is characterized by one uranium vacancy and two oxygen vacancies. For stoichiometric UO_2 , the Schottky defect is the most probable defect including a U vacancy [11].

1.3.2 Extended Defects

As the name suggests, these defects are extended in space. These can be categorized as one-dimensional line defects, two-dimensional planar defects and three-dimensional bulk defects.

- Line defects

One-dimensional defects refer mainly to dislocation linear defects. The atoms of the crystal lattice around a dislocation are misaligned. Dislocation networks are likely to be formed in nuclear fuels due to the slowing down of fission fragments in high temperature conditions during in-reactor operations. There are two basic types of dislocations, the edge dislocation and the screw dislocation. "Mixed" dislocations, combining aspects of both types, are also common. Fig.1.7 depicts a schematic representation of the different types of dislocations. Edge dislocations are caused by the termination of a plane of atoms in the middle of a crystal. Screw dislocations result from shear distortion such that the atoms over the cut surface are shifted in a direction parallel to the dislocation line. For the mixed dislocations the shift is neither parallel nor perpendicular to the dislocation line.

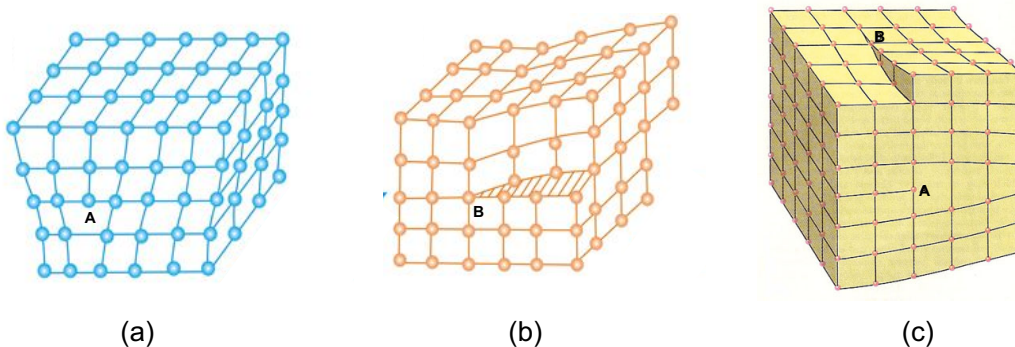


FIGURE 1.7: Different types of dislocations (a) Edge dislocation, (b) Screw dislocation, (c) Mixed dislocation.[12]

- Planar Defects

Two-dimensional defects include surfaces, grain boundaries and stacking faults. These defects act as the internal interfaces that separate neighboring regions within the same crystal structure but with different orientations. Solids are made of a number of small crystallites which are also known as "grains". All the grains are separated by boundaries which are called "grain boundaries" and the atoms in this region are not in perfect arrangement. Grain boundaries occur where the crystallographic direction of the lattice changes abruptly. This usually occurs when two crystals begin growing separately and then meet. Fig.1.8(a) represents a grain boundary.

Stacking faults occur most commonly in close-packed structures. They are formed by a local deviation of the stacking sequence of layers in a

crystal. An example would be the ABCABCBCABCA stacking sequence as shown in Fig.1.8(b).

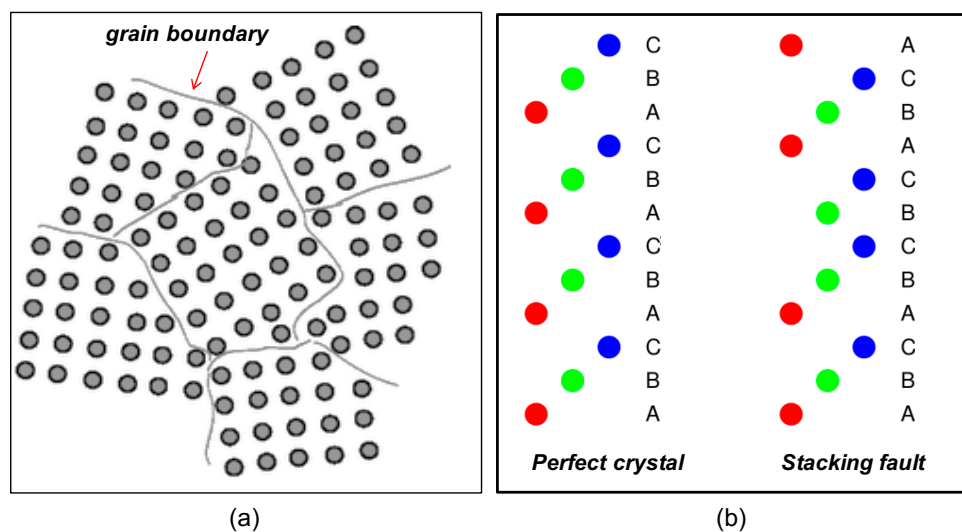


FIGURE 1.8: Different types of planar defects: (a) Grain boundary, (b) Stacking fault

- Bulk defects

Three-dimensional defects, also referred as volume or bulk defects, include pores (voids), cracks and bubbles. Voids are small regions where there are no atoms, and which can be thought of as clusters of vacancies. In the nuclear fuels, voids are produced during the fuel fabrication process. The porosity of sintered UO_2 can be classified either as open pores associated to the pellet surface or closed pores isolated from the surface. Fig.1.9(a) indicates the pores presented in as-fabricated UO_2 disk sintered at 1400°C during 4 hours.

During nuclear operations, a large amount of insoluble gases (mainly Xe and Kr) precipitate as bubbles and start to agglomerate in the fuel matrix. The behaviour of these gaseous bubbles needs to be considered as they can significantly alter the physical and mechanical properties of the fuel. As an illustration in Fig.1.9(b), Michel et al. [13] presented the formation of a multimodal bubble population during the implantation of UO_2 thin film with Xe ions which was then followed by an annealing at 1500°C .

1.4 Fission gas behaviour

Under irradiation, the crystallographic network of UO_2 undergoes changes that have an effect on its physio-chemical properties. Fission gases play a significant part in this evolution and their behaviour needs to be understood. About 15% of the generated fission products consist of the noble gases, xenon and krypton. The solubility of these noble gases in the UO_2 matrix is extremely

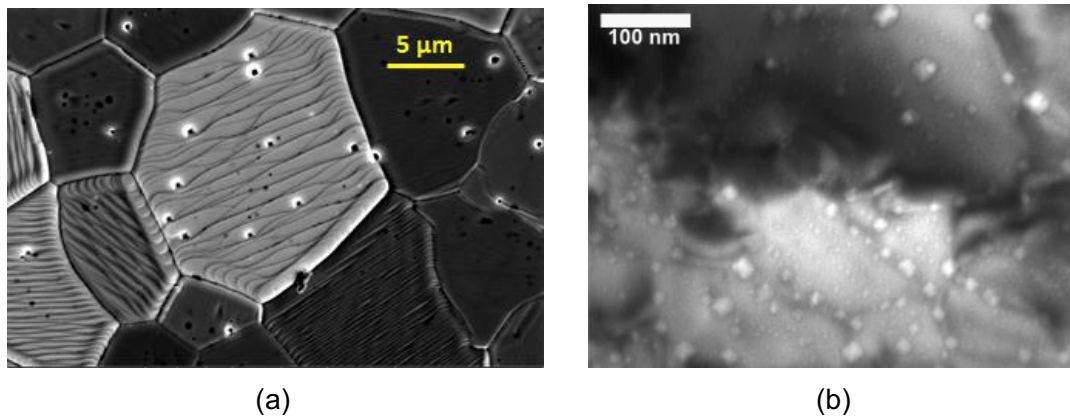


FIGURE 1.9: Bulk (3-D) defects in UO₂ fuels (a) SEM image of an as-fabricated UO₂ disk showing the presence of pores (b) TEM image indicating the presence of gas bubbles in a UO₂ thin film implanted with Xe ions after annealing at up to 1500°C during 2 hours.

low [14] and they either tend to be released from the fuel or precipitate in the form of small nanometer size clusters leading to macroscopic phenomena like Fission Gas Release (FGR) and swelling in the fuel. Both swelling and FGR are detrimental to fuel safety.

If the gas is released from the fuel, the pressure within the fuel rod is correspondingly increased, subjecting the cladding to additional stress. The thermal conductivity of the gap is lowered, since xenon has a lower conductivity than the cover gas, helium. This further increases the temperature which accelerates gas release and, eventually, the cladding is subjected to further stresses that can ultimately result in failure.

On the other hand, if the fission gases are retained in the fuel, they significantly precipitate as bubbles. As the density of the gas in such bubbles may be considerably lower than that of the gas in the solid fuel (especially for inter-granular bubbles, or at high temperature), gas atoms residing in bubbles occupy more volume than either the fissile atoms they replaced or fission-product atoms that segregate as solid phases. The precipitation of fission gases thus leads to swelling of the fuel to a larger degree than the volume expansion that would occur if the xenon and krypton had remained dispersed on an atomic scale in the fuel matrix. Swelling contributes to the pellet-cladding interaction, again exposing the cladding to higher stress and ultimately limiting the life time of the fuel rod. Pellet-cladding interaction due to swelling of fuel in the fuel rod is depicted in Fig.1.10.

To better understand the evolution and release of gaseous fission products, numerous studies have been conducted for several decades on the diffusion of Xe and Kr atoms in UO₂, as well as nucleation and growth of bubbles/cavities. The mechanism of FGR out of the fuel can be understood as a two step process. The first and basic step is the transfer of gas atoms from within the grain to the grain boundaries (intra-granular fission gas release). The second step is the coalescence and inter-connection of grain-boundary

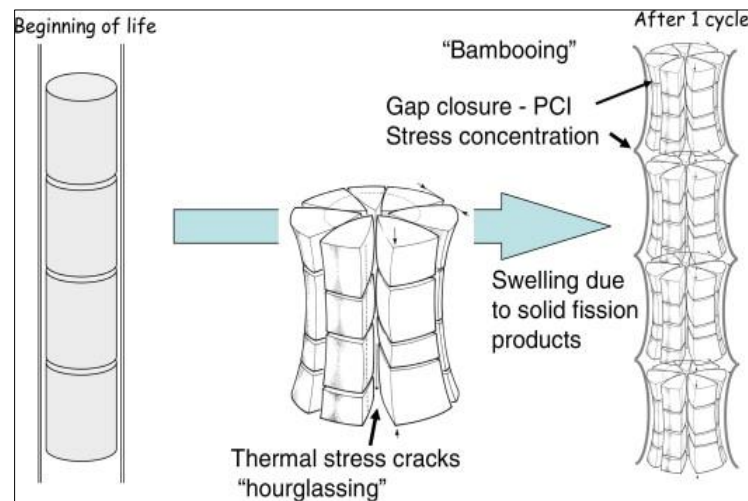


FIGURE 1.10: Pellet-Cladding Interaction due to swelling of the nuclear fuel (taken from [15]).

bubbles to give pathways to gas atoms at the grain boundaries to go outside the fuel (inter-granular fission gas release). The latter is clearly observed in high temperature conditions (ramp tests or annealing tests). We will be discussing the different mechanisms associated with these two steps in the following sections.

1.5 Mechanisms of FGR

1.5.1 Recoil and Knock-out

At temperatures below 1000°C , where the thermally activated processes do not dominate, the fission products formed at the external surface of the UO_2 pellets can escape by the direct recoil or knock-out mechanisms. The fission fragments having large kinetic energies (60 to 100 MeV) can dissipate their energy to the fuel lattice, primarily by interaction with the electrons of the material. However, a fission fragment close enough to a free surface (< 6 to $7 \mu\text{m}$), can escape from the fuel due to its high kinetic energy. This mechanism of release is known as (direct) recoil release.

Similarly, when the fission fragments make elastic collisions with the nuclei of atoms of the lattice, these atoms can also become energetic particles, called primary knock-ons with mean energy of $\sim 100 \text{ keV}$. These can then be released, or transfer part of their energy to neighbouring atoms, thereby, creating higher order knock-ons with mean energy of $\sim 200 \text{ eV}$ [16]. The interaction of a fission fragment, a collision cascade or a fission spike with a stationary gas atom near the surface can cause the latter to leave the fuel. This mechanism of release is known as knock-out release.

These release mechanisms in fuel operating at low powers were studied by Olander [10], Wise [17], and Lewis [18]. Recoil release can contribute

significantly in the release of short-lived radioactive nuclides in failed rods and in experiments [19] on low temperature fission product release in which high density gas surrounds the fuel [17, 18]. The release by knock-out is negligible compared with that of recoil for short-lived isotopes. These release mechanisms, active at low burn-ups, contribute less than 1% to the release of generated gas [17, 18].

1.5.2 Single gas atom transport

The transport of single gas atoms in the bulk UO_2 is determined by the diffusion rate of fission gas atoms and by the interaction with the fuel microstructure, in particular, the trapping and re-resolution of gas atoms by and from intragranular bubbles, respectively [10, 20, 21]. In this section, the transport refers to the unperturbed diffusion of gas atoms (mainly Xe) in the bulk lattice without the interaction with the fuel microstructure. The interactions with the fuel microstructure like trapping and re-resolution are discussed in the next sections.

Several studies based on density functional theory (DFT) [22, 23, 24, 25, 26, 27] and molecular dynamics (MD) with empirical potentials [28, 29, 30, 31, 32] show that Xe gas atoms prefer uranium vacancy trap sites. There is a general agreement between DFT and empirical potential calculations for the most favourable sites for Xe atoms in the UO_2 lattice, with regard to thermodynamics. These are the divacancies (one uranium vacancy and one oxygen vacancy) in stoichiometric (UO_2) matrices; a bound Schottky defect (one uranium vacancy and two oxygen vacancies) for hypostoichiometric (UO_{2-x}) matrices; and single Uranium vacancies for hyperstoichiometric (UO_{2+x}) matrices [33]. The computational study of Nicoll et al. [34] showed a shift of the most probable site for Xe atoms from di- to tri-vacancies when the fuel becomes hypostoichiometric. As a consequence, the lattice diffusion coefficient for inert gas atoms in UO_2 is influenced not only by the temperature, but also by the stoichiometry.

Above 1000 K, the single gas atom diffusion coefficient in UO_2 can be expressed by the Arrhenius law suggested by Matzke [35] as:

$$D_{\text{UO}_2}^{\text{Xe}} = D_0 \exp\left(\frac{-\Delta H}{kT}\right)$$

where D_0 is the pre-exponential factor ($= 5 \cdot 10^{-4}$ to $2.90 \cdot 10^{-12}$ m^2/s [27]), ΔH represents the activation enthalpy ($= 2.87$ to 3.95 eV/atom [27]), and k is the Boltzmann constant ($= 8.6173$ eV/K).

Depending on the stoichiometry of uranium oxide fuel, although there is general agreement that Xe-release from UO_{2+x} is faster than release from UO_2 , and, conversely that the Xe-release is inhibited in UO_{2-x} , there is essential disagreement on the details [36, 35, 37, 38].

Several kinds of doping are added to the UO_2 fuel in order to improve different aspects of fuel performance [39, 40, 41, 42]. Doping of UO_2 with foreign cations can simulate the non-stoichiometry, hence it affects the defect structure as well.

During irradiation, Xe atom mobility is increased due to the fission that creates more vacancies (irradiation enhanced diffusion) or by directly moving the Xe atoms in the displacement cascades (athermal diffusion).

1.5.3 Trapping of gas atoms

The migration of gas atoms in nuclear fuels involves more than simple lattice diffusion. The solubility of noble gases in the UO_2 matrix is extremely low (See Section 1.5.5). A direct consequence of the low solubility is the tendency of the moving gas atoms to be easily trapped in more stable configurations in various clusters or sinks, such as closed pores, vacancy clusters, precipitation of gases into bubbles, as well as trapping on dislocations or at grain boundaries [43, 44]. Experiments suggest that for burn-ups reached in power reactors, gas atom trapping by fission produced defects should be more important than trapping at natural defects in the as-manufactured fuel [10]. TEM observations have shown that the most possible trap is the population of fission gas bubbles [45]. Experiments on single crystals and sinters of stoichiometric UO_2 indicate that the apparent diffusion coefficient of Xe is dramatically decreased for fission doses exceeding 10^{15} fissions/cm³ [36, 46]. The strong tendency of the gas atoms to precipitate into bubbles has been demonstrated for samples implanted with Kr and Xe ions, even at temperatures as low as 300-350°C [47]. Volatile fission products such as Cs, I, and Rb can also form bubble-like structures in the bulk depending on the temperature and the chemical nature of the impurity [48]. The factors affecting the trapping of migrating fission products by bubbles are the diffusion coefficient of the fission product and the bubble number density and size.

Other significant trapping sites for fission gas atoms are the dislocations. Nerikar et al. [49] investigated Xe segregation to edge and screw dislocations in UO_2 and the segregation trends were found to be significantly dependent on the dislocation characteristics. Xe prefers to segregate to screw dislocation rather than to edge. The Xe segregation to dislocations is found to be thermodynamically favorable. Furthermore, MD simulations using empirical potentials of Xe diffusion around edge dislocations in UO_2 were performed by Murphy et al. [50] to analyze the scenario for FGR via this pathway. The results suggest that the activation energy for Xe diffusion is dramatically reduced for free gas atoms in the vicinity of a dislocation as compared to the bulk. However, Xe atoms diffusing along the dislocation aggregate to form small bubbles, which incorporate all of the isolated mobile Xe atoms and inhibits fast diffusion of Xe along the dislocation core.

During irradiation, an irradiation-induced re-resolution mechanism is also operational (see section 1.5.4), hence the trapping and the re-resolution rates can be balanced. Accordingly, the migrating atoms are at equilibrium between the lattice and the traps. Speight [51] has shown that saturation of the intra-granular bubbles occurs relatively fast and many FGR models define an effective diffusion coefficient, considering the trapping and re-resolution of gas atoms. Practically, the free, untrapped gas atoms still diffuse with their intrinsic diffusion coefficient, but the fraction of them reduces. The re-resolution

of gas atoms from the bubble to the bulk UO_2 is discussed in the upcoming sections.

1.5.4 Irradiation induced re-solution of gas atoms

The low solubility of rare gas atoms in UO_2 provides a strong driving force for the precipitation of gas atoms in bubbles. The trapped gas atoms can, however, simultaneously be freed from the traps during irradiation. Early experiments [52, 53, 54, 55, 56, 57] have shown that the population of gas in the matrix significantly increases due to irradiation induced re-solution of the gas, which thus, remains capable of diffusing out of the grains. The trapping effect can saturate either if there is no more gas in the solid or if there is re-solution of gas into the bulk. This saturation of the trapping effect has been demonstrated in experiments [36], which is in accordance with the conclusions of Lawrence [58].

Among γ -rays, neutrons and fission fragments, which can all cause the re-solution of fission gases from bubbles, only the fission fragments are efficient as observed experimentally. The reason for this being that the fission fragments have a higher kinetic energy (50-100 MeV) than fast neutrons (2 MeV), and they are also charged, thus, having a higher cross-section for transferring energy to the lattice, or to the gas atoms. The plausible mechanisms of irradiation induced re-solution have been reviewed by Turnbull [57] and Olander [10]. Olander and Wongsawaeng [59] have reviewed the re-solution of fission gas bubbles by two radiation induced mechanisms: heterogeneous mechanism, based on the work of Turnbull [55] and homogeneous mechanism, based on the work of Nelson [54].

Homogeneous mechanism involves the re-solution of individual fission gas atoms, one by one, from the bubble by direct elastic collisions with fission fragments or energetic primary knock-on atoms (PKA). Heterogeneous mechanism, on the other hand, involves instantaneous complete or partial re-solution of the fission gas contained in a bubble by a fission fragment passing through the bubble due to the energy lost by it through electronic excitation. These energetic ions first heat the electrons, then part of the energy is transferred from the hot electrons to the lattice through electron–phonon coupling. This produces a cylindrical thermal spike which can easily reach temperatures above the melting point of the material, and if the spike intersects a gas bubble, a purely thermally-driven re-solution may occur [60].

MD simulations using Monte Carlo were done by Schwen et al. [61] to study the homogeneous re-solution from a bubble of radius 1 nm. They obtained a re-solution parameter that was lower than previous estimates [54] by a factor of fifty and found that five xenon atoms were re-solved on average per bubble per fission fragment. They further combined MD simulation with a two temperature model to study the effect of fission track damage on a similar Xe bubble in UO_2 and to see whether the electronic energy loss can cause heterogeneous Xe bubble re-solution [62]. They did not observe complete bubble destruction and concluded that heterogeneous re-solution is likely to be insignificant compared to homogeneous re-solution of fission gas. On the

contrary, MD simulations of lower energy recoils and higher energy thermal spikes by Govers et al. [63] showed that thermal spikes destroy Xe bubbles completely in UO_2 and they are more effective at gas re-resolution than primary knock on atoms. Pastore et al. [64] have performed a sensitivity analysis of fission gas behavior by considering variation of the re-resolution parameter over two orders of magnitude. The study showed that engineering scale modeling of fission gas behavior is limited by large uncertainties, which limit the improvement of predictive power by the incorporation of more physical details or the increase of model complexity.

1.5.5 Thermal re-resolution of gas atoms

In order for a trapped gas atom to be redissolved into the bulk, a potential barrier is needed to be crossed. The thermally activated re-resolution of an atom of a precipitate or bubble, within a matrix, depends on both its solubility (or solution energy) in the bulk solid and the binding energy of the migrating atom to the trap. Another way to calculate the equilibrium concentration of a defect such as Xe in substitution position at the vicinity of a bubble is to minimize the free energy of the system composed by a bubble in a fixed volume and temperature box of UO_2 admitting a concentration of such defects. The concentration that corresponds to the minimum free energy is the equilibrium concentration at this temperature and for the characteristics of the bubble [65]. Following this procedure, the factors influencing the thermal re-resolution are the temperature, the internal gas pressure, the surface energy and the curvature of the bubble, as well as the formation energy of the defect "Xe in substitution position". An entropy term should also appear in the formula for $C_v^{eq}(bubble)$, but has been taken as 1 in [65] by lack of information. The probability of thermal re-resolution of gas is higher from small bubbles with a high internal pressure, as is also noted from the computations of Jackson et al. [66, 67]. Though there is agreement on the latter statement, there has been a debate over the magnitude of the phenomenon and its contribution to the release process.

In 1964, based on the shape of release curves from a powder of monocrystals irradiated at $8.5 \cdot 10^{20}$ fission/ m^3 , MacEwan and Stevens [46] proposed a solubility of Xe between 0 and $3 \cdot 10^{-9}$ Xenon atoms/site/atm. As there were many hypotheses done (such as every grain of the powder has the same fabrication porosity), the authors were themselves quite cautious with this value. Moreover, from the article, a concentration of one xenon for every $6.8 \cdot 10^9$ uranium would be in equilibrium with a partial pressure of ~ 130 mm (Hg) at 1400°C . So, at 1400°C , the solubility would be $8.6 \cdot 10^{-10}$ Xenon atoms/site/atm, and the origin of the value $3 \cdot 10^{-9}$ remains unclear. Olander [10, p.310], on the basis of [68] presented the same analysis and compared the mean delay time of gas in traps at 1400°C (estimated to 13 days) to the mean re-resolution time under reactor irradiation which is 4 to 40 hours.

MacInnes and Brearley [69] through a model for FGR during transient heating of irradiated fuel showed that with selected materials properties (e.g., gas atom solution energy), the high gas releases observed could be due to

thermal re-solution from bubbles together with single gas atom diffusion to the grain boundaries. In another publication, Brearley and MacInnes [70] also modelled the high release rates observed during isothermal transient heating of fuel.

However in 1985, thermal dissolution of gas from under-pressurised bubbles was ruled out by molecular statics calculations studying single Xe atom trapping and migration, since the predicted solution energy was very high (10 eV) [66].

In 1987, Ronchi [71] proposed an alternative theory which considers the precipitation of gas into highly pressurized bubbles and predicts that the elastic strain field produced increases with gas precipitation and finally leads to a lowering of the precipitation rate. Ronchi [71] further showed, in an analogous fashion to the thermal re-solution model, that a lowering of the gas precipitation rate combined with single gas atom diffusion to the grain boundaries qualitatively explained the high gas releases observed in Post-Irradiation Annealing (PIA) experiments. However, in order to take into account the stress field in the vicinity of an over pressurized bubble, one has to use the gradient of chemical potential to calculate the Xe flux:

$$\mu(Xe) = \mu(Xe, \sigma = 0, C_{Xe}) - \Omega\eta \sum_k \sigma_{kk}$$

where $\mu(Xe, \sigma = 0, C_{Xe})$ is the chemical potential without taking the stress field into account, Ω is the volume of the site, η is the size effect, supposed spherical, per atom of gas, (η tells how the solid is strained due to the presence of 1 atom of Xe in substitution) and $\sum_k \sigma_{kk}$ is the trace of the stress tensor at the considered location. Around a spherical bubble at very high pressure, the trace of the stress tensor is constant, radial compression being counter-balanced by the tensile stresses in the tangential directions. This is why, Ronchi's approach does not seem convincing and will not be used in the following of the thesis.

In 1992, Evans et al. [47] carried out an experiment with Kr ion-implantation in UO_2 , followed by TEM observation before and after annealing tests. The loss of gas was monitored using TDS (thermal desorption spectroscopy) during the annealing. The goal of the experiment was explicitly to find evidence of thermal re-solution of gas. As the implanted foils were very thin (for TEM observations), thermal re-solution of gas from bubble near the surface would have led to FGR and the shrinking of those bubbles. Such a shrinkage without any change in the bubble population during the FGR peak would have proved the existence of thermal re-solution of gas. However, this was not observed in the experiment. Instead, clear evidence of bubble movement and coalescence was seen as well as an impact of thermal vacancies coming from the surface: the bubbles near the surface were bigger after the annealing. The results of the experiment disregarded the realism of thermal re-solution mechanism.

In 2000, a series of tests were performed and analyzed by White et al. [72] to address specifically the issue of thermal re-solution of fission gas atoms from intra-granular bubbles. Bubble size distribution was obtained from SEM

observations after annealing tests (out-of-pile) and compared to bubble size distribution after in-pile test at the same temperature. First, vacancy starvation was noted for the out-of-pile test. The bubble total volume was less out-of-pile than in-pile. Consequently, the analysis of bubble distribution, if it is supposed to be governed by thermal re-solution, namely Ostwald Ripening, may be done using $C_v^{eq}(bubble) = Constant * e^{\frac{2\gamma\Omega}{kTR_b}}$, like for precipitates. Note here that the bubbles observed by White were inside the grains, probably far from the surface, unlike in the experiment by Evans et al. [47]. White then invoked the theory of [73] that gives the shape of the size distribution of a bubble population governed by Ostwald Ripening. Comparison of theoretical size distribution and experimental ones shows that Ostwald Ripening cannot be invoked. Instead, the experimental size distribution exhibits long exponential tails in which the largest bubbles are present in concentrations of four or five orders of magnitude lower than the average bubble radius, as if certain bubbles benefited of a selected growth for some reason. So, from that second experimental attempt, gas thermal re-solution could not be shown to operate as well.

In the same year (2000), however, Veshchunov [74] used the concept of thermal re-solution at high temperature in modelling. The justification for thermal re-solution was that, at 1200°C visible bubbles appeared at burnup of $3*10^{25}$ fission/m³, which corresponds to the gas concentration of $3*10^{-4}$ atoms/site. Then, a reasoning involving several hypotheses followed and arrived to a Henry constant $= \frac{c_s}{p_s} = (3*10^{13})^{-1} \text{ Pa}^{-1} = 3.3*10^{-9} \text{ atoms/site/bar}$. The fact that visible bubbles appeared at burnup of $3*10^{25}$ fission/m³ was taken from the reference [56]. However, in [56], the lowest burnup of the 4 samples examined was $3*10^{25}$ fission/m³ and no examination was performed at burnup lower than that. So, there is no indication that there was no bubble at burnup lower than $3*10^{25}$ fission/m³ and it seems excessive to say that the bubbles "appeared" at this particular burnup. Consequently, the argument of Veshchunov for thermal re-solution seems weak. The limit for the presence of bubbles is rather 10^{21} fission/m³ as noticed by those who tried to measure diffusion coefficients of Xenon [75, 46]. Finally, the absence of bubbles below 10^{21} fission/m³, which corresponds to a concentration of $1.2*10^{-8}$ atoms/site $= C_g$ does not mean that $C_g = \text{Henry constant} * P_c$, P_c being the inner pressure of a critical nucleus of bubble. Kinetics also plays a part. In that case, bubbles are absent probably because the gas atoms just have low probability to meet.

In 2012, molecular dynamics simulations were performed by Murphy et al. [31]. They calculated the average Xe free energy of Xe atoms situated 1) on a Schottky defect, 2) in a nano-cluster of 4 Schottky defects, 3) in a small bubble of diameter 1.2 nm, and 4) in a large bubble of diameter 2 nm. The ratio Xe/Schottky was varied in different simulations of bubbles. It appeared that for $\text{Xe/Schottky} \leq 1$, the Xe free energy decreased with the size of the bubble and was lower than the one for the Xenon in a Schottky defect. The conclusion was that there is a clear thermodynamic driving force to bubble nucleation and growing.

In 2014, Noirot [65] presented a method to calculate the equilibrium concentration of a defect in the vicinity of a bubble containing gas. A box at

volume and temperature constant and containing a bubble and defects in the solid is considered as the system. The free energy of this system is calculated analytically as a function of the characteristics of the bubble and the concentration of defects. Then the free energy is minimized. The concentration of defects corresponding to the minimum is the equilibrium concentration for that bubble. For Xenon, the defect considered is a Xenon in a Schottky defect. The method gives the formula relating C_{Xe}^{eq} to the characteristics of the bubble and the formation energy of this defect calculated from DFT (= 4.36 eV [76]). At 1600°C, for a bubble of 1 nm radius and for Xe/Schottky equal to 1 in the bubble ($V_{at} = \Omega$), the concentration of equilibrium of Xe, $C_{Xe}^{eq} \approx 2 \cdot 10^{-6} \text{ mol/m}^3 = 5 \cdot 10^{-11} \text{ atom/site}$, which is virtually 0 in terms of impact on gas release in bubble evolution.

To summarize this 50 years of recurrent controversy over thermal re-resolution of gas atoms, we can say that no experimental procedure could prove that thermal re-resolution of gas from bubbles into the bulk exists during out-of-pile annealing tests. Instead, proofs of bubble movement (coalescence, for instance) or proof of vacancy starvation in the bulk, and influence of thermal vacancy supply near the surface are available. Moreover, theoretical arguments, based on MD calculations, seem to rule out thermal re-resolution. It is always more difficult to prove that a phenomenon does not exist than the contrary, and theory may also be improved. For example, in [65], the fact that the atoms in the vicinity of the defect, Xe in a Schottky, would vibrate in a different way than in the bulk is neglected (see Appendix of [65]). The impact of such a simplification could not be assessed. That is why, interest for this subject should be continued. The different and contrasting literature on thermal re-resolution has also been summarized in Table 1.2.

1.5.6 Diffusion in the temperature gradient

If a homogeneous mixture of two or more species is placed in a temperature gradient, a thermal force is exerted on all the molecules in the mixture, such that all particles are forced to move in the direction of the heat flow. This is the diffusion in a temperature gradient and is also called the Soret effect. The simplified flux equation can be obtained as [77]:

$$J_i = -D_i \left(\nabla c_i + \frac{Q_i c_i}{RT^2} \nabla T \right)$$

where J_i corresponds to the flux of atoms of type i , D_i is the diffusion coefficient of the species, c_i represents the concentration of the species i , Q_i is the heat of transport for the considered species and R is the universal gas constant.

The flux of atoms is proportional to the diffusion coefficient, D_i and the heat of transport, Q_i . Diffusion in a temperature gradient of oxygen in $\text{UO}_{2\pm x}$ is very pronounced [35] but there is a minimum in the heat of transport in the vicinity of the stoichiometric composition [78]. Several studies on the diffusion of Xe at various temperature ranges, following the concept of Turnbull et al. [79], are present, however, we did not find any mention of the Soret effect for

Author	Year	Thermal re-solution yes/no	Modelling/ Experiment	Summary (Comment)
MacEwan and Stevens [46]	1964	yes	Experiment	thermal re-solution invoked for the first time, with caution from the authors
MacInnes and Brearley [69]	1982	yes	Modelling	high FGR during transient heating attributed to thermal re-solution
Brearley and MacInnes [70]	1983	yes	Modelling	high FGR during isothermal annealing attributed to thermal re-solution
Jackson and Catlow [66]	1985	no	Modelling	atomistic calculations rule out the thermal re-solution
Ronchi [71]	1987	no	Modelling	strain field produced hinders the precipitation of gas into bubbles (not convincing as $\sum \sigma_{kk}$ is constant around a bubble)
Evans et al. [47]	1992	no	Experiment	TEM and TDS study of ion implantation overrule thermal re-solution
White et al. [72]	2000	no	Experiment	Bubble size distribution during PIA rule out thermal re-solution
Veshchunov [74]	2000	yes	Modelling	thermal re-solution is used as an important phenomenon at high temperatures (the justification is not convincing)
Murphy et al. [31]	2012	no	Modelling	MD simulation showed thermodynamic driving force to bubble nucleation and growth
Noiroot [65]	2014	no	Modelling	thermal re-solution around bubbles found to be extremely low and cannot play a role for FGR. However, entropy terms should be precised

TABLE 1.2: Literature on thermal re-solution.

the diffusion of Xe in the literature. The diffusion in a temperature gradient of Xe is, however, out of scope for this thesis, which is focused on annealing tests ($\nabla T = 0$).

1.5.7 Grain boundary diffusion

Grain boundary diffusion is the most commonly observed pathway for solute migration in polycrystalline materials. It is a commonly accepted fact that diffusion in crystalline solids occurs more rapidly along grain boundaries as compared to through the lattice [80, 81]. This is due to the fact that the atomic jump frequency in these planar defects is drastically greater than that of regular lattice atoms in stoichiometric materials. The dominant atomic jump mechanism by which the atoms move along grain boundaries appears to be the vacancy mechanism [81, 82]. Analysis for grain boundary diffusion for in-pile release of volatile fission gas atoms in trace irradiated UO_2 fuels was done in [83, 84, 85]. Olander et al. [86, 87] followed the same idea in post-irradiation analysis of low burnup UO_2 samples.

The majority of experimental investigations regarding grain boundary diffusion mechanisms have been performed on metals [81, 88]. Unfortunately, there is a scarcity of experimental data available for the grain boundary diffusion coefficient of inert gas atoms in the UO_2 fuel. It is noted that the energy to form a vacancy or move an atom into a vacancy near a grain boundary is less than that in the lattice [49, 89]. Considering a vacancy mechanism for self-diffusion of U, the activation energy in the boundary will be appreciably less than that in the lattice and, therefore, grain-boundary diffusion will be more important at lower temperatures (below 1800°C for UO_2). The role of the grain boundaries in FGR has been debated, with some authors advocating that it serves as a high diffusivity pathway for the release of fission products in trace irradiated fuel [83, 84, 85, 86, 87], while present day models in high burnup UO_2 [20, 90, 91, 92] consider it to be a perfect sink where gas atoms are almost immobile and precipitate to form bubbles, which eventually will interconnect and form a tunnel network. This is mainly based on the presence of grain bubbles in high burnup fuel [93, 94, 95, 96] which appears to be inconsistent with rapid grain boundary diffusion unless irradiation-induced or thermal re-resolution from inter-granular bubbles to the grain boundary occurs. To our knowledge, these last subjects have not been addressed in the literature so far.

1.5.8 Intra-granular bubble migration

The different types of inclusions that are present in the fuel are the fission gas bubbles, the as-fabrication pores and the solid inclusions of fission products. The fission gas bubbles result from the precipitation of fission gases, mainly xenon and some krypton, and are highly pressurized and quite small (radius $< 1\mu\text{m}$) due to re-resolution effects. The as-fabrication pores result from incomplete densification of the fuel during manufacture. These pores are usually large (radius $> 1\mu\text{m}$) and contain a low-pressure gas, primarily the gas used

during fuel-pellet sintering. The solid inclusions of fission products are mainly composed of metallic precipitates (Mo, Tc, Ru, Rh, Pd) or oxide precipitates (Rb, Cs, Ba, Zr, Nb, Mo, Te) [7]. The migration of fission gas bubbles and solid inclusions provides an additional mechanism for fission product release from nuclear fuels [97, 98, 99, 100]. Apart from the gas release, the migration of fission gas bubbles has another important consequence which is the coalescence of the bubbles entailing fuel swelling [10, 99].

During PIA experiments, the atoms that cause the bubble motion, move about randomly. As a result, the bubble performs a form of random (Brownian) motion in three dimensions. When the individual atoms are moving under the influence of a potential gradient, the bubbles move in the direction of that gradient. Nichols [101, 99] has developed a general analysis of bubble mobility that can be applied to any force acting on a bubble or to any microscopic mechanism by which bubble motion occurs. Different forces may affect the bubble motion [99], such as the thermal gradient, the stress gradient, the electric potential gradient in ionic crystals, moving dislocations and shifting grain boundaries. Evans et al. [47, 100, 102, 103] proposed another driving force which is even operative under thermal annealing conditions. Their approach invokes the presence of a thermal vacancy concentration gradient between a vacancy source (eg. grain boundary) and the pressurized intra-granular bubbles. A directed motion of bubbles up the vacancy gradient will occur by trapping vacancies arriving at the bubble surface from the vacancy source.

Bubble motion through a solid requires the transfer of atoms around the bubble. This can be done by mass transfer (i.e., via vacancies) through the volume of the solid near the bubble, or by direct surface diffusion, or by vapour diffusion (evaporation and condensation) of the matrix material within the bubble volume. The expressions for the bubble diffusivity for each of these mechanisms can be derived [10, 104]. The dominant mechanism for diffusion depends on the temperature, due to the different activation energies required (with Q_{vapour} being the highest and Q_s being the lowest). Thus, with increasing temperature, the dominant mechanism could shift from surface diffusion to volume diffusion to vapour transport. Moreover, surface diffusion dominates at sufficiently small bubble size (radius $< 1\mu\text{m}$), but as the bubble radius increases, either volume diffusion or vapour transport eventually becomes dominant. However, according to Olander [10], the vapor transport mechanism is only likely to be significant for as-fabricated pores with a diameter in the order of $10\mu\text{m}$ but not for fission gas bubble migration. The vapour transport mechanism is prevalent only at high temperatures ($\sim 2000\text{ K}$), which is typical of fast reactor conditions rather than LWR.

The bubble movement via directed motion in a vacancy concentration gradient and via random movement is discussed in detail in chapters 3 and 4, respectively.

1.5.9 Grain boundary sweeping

Grain growth [105] can affect the fission product release as grain boundary sweeping provides another mechanism for the collection of fission gas at

these internal surfaces from which release can occur [106]. This happens because the fission gas is mostly insoluble in the fuel matrix, hence the sweeping grain boundary does not re-deposit any gas in the crystal formed behind it. Speight and Greenwood [107] proposed a grain growth theory that includes the sweeping of entrapped micro-bubbles by the front of an advancing grain boundary. According to their theory, small bubbles, which exert a minimal drag force on an advancing grain surface, are swept along with the moving boundary, whereas large bubbles can detach from the advancing surface due to their higher drag. On the contrary to providing a mechanism for FGR via grain boundary sweeping, grain growth also increases the diffusion distance for the fission products created in the grain. This tends to reduce the release rate.

Grain growth is affected by a variety of parameters like the temperature, grain radius, grain shape and presence of pores and second-phase particles. Grain boundary sweeping occurs at temperatures at which grain growth is significant. Olander [10] suggests that the temperature range for equi-axed grain growth is between 1900 K and 2100 K (1627°C - 1827°C) and consequently, this process is not operative in LWR fuel under normal operating conditions.

1.5.10 Inter-granular bubble interconnection

After a certain burnup, fission gas bubbles appear along grain faces and grain edges [93, 94, 95, 96, 108]. SEM and TEM observations show that FGR in UO₂ fuel takes place through tunnel-type networks formed at grain edges and faces when these bubble interconnect during irradiation [109, 110, 95, 111], at least at high temperatures. While the inter-granular gas release is clearly observed at high temperatures ($T \geq 1400^\circ\text{C}$), it has recently been questioned for base irradiation [112]. The tunnel network can close again under the influence of the surface tension when the outgoing flow of gas atoms outweighs their supply. Diffusion of the gas atoms into the grain boundaries up to the concentration necessary for the formation of tunnels requires a certain "incubation time", which is dependent on burn-up [113, 111].

Bubble interconnection and the onset of "percolation release" is influenced by several factors. The onset of percolation release can be delayed by the resolution of the grain boundary bubbles, as it reduces the build-up of the saturation concentration and thus, increases the "incubation time" for the release. Moreover, the increase in the hydrostatic pressure increases the amount of gas atoms necessary to obtain the saturation or opening of the tunnel network, causing a delay in the onset of release. On the other hand, an increase in temperature will raise the pressure of the gas in the bubbles and boost the interconnection and therefore, the onset of release. Interconnection of gas filled bubbles generally takes place when diffusion-controlled precipitation occurs at the grain boundaries, i.e., when both the temperature and the burnup are high enough.

1.5.11 Burst release

During rapid power transients, a jump in the FGR has been observed [114, 115, 116]. This phenomenon is typically called “burst release”. During post-irradiation annealing, both rapid increases and decreases in temperature have resulted in fission gas burst release. These sudden jumps in FGR have been ascribed to micro-cracking along grain boundaries induced by rapid thermal stresses and gas bubble pressure [114, 117]. Transient-tested UO₂ fuel rods exhibit grain face separations observed using microscopy [115, 94, 118] and it was postulated that all fission gas stored on the cracked grain boundaries was released through these cracks.

Various models have been developed to describe the increase in FGR during transients in fuel performance codes. Some approaches add a contribution of gas release from grain boundaries due to micro-cracking when specific empirical conditions regarding the power occur [119, 120, 121]. A burn-up dependent temperature threshold is also used [120, 121]. Bernard et al. [122] developed a model which reduces the gas concentration at grain boundaries after the beginning of a transient according to an exponential function. Pastore et al. [123] extend an existing diffusion-controlled FGR model by reducing the grain-face gas inventory and storing capacity as the local temperature varies during transients. An empirical temperature-dependent function is developed to represent the micro-cracking mechanism. Chakraborty et al. [124] carried out finite element simulations to determine the bubble pressure required for grain boundary separation.

1.6 Mechanisms associated with intra-granular gas release during PIA tests

The transport of fission gas from within the fuel grains to the grain boundaries is a fundamental controlling mechanism of fission gas release in nuclear fuel. The mechanisms controlling the behaviour of the gas inside the grains must be known if the FGR process is to be modelled successfully. The gas atoms transfer within the grain has been a topic of debate for the past few decades [125, 70]. In-pile fission gas transport to the grain boundaries occurs by thermal, irradiation-enhanced and athermal diffusion of single gas atoms, coupled with trapping in and irradiation-induced re-solution from intra-granular bubbles. However, during PIA tests, the contribution of different mechanisms of FGR due to the intra-granular gas may differ. It has been recognized that the amount of fission gas arriving at grain boundaries through the high density of intra-granular traps would be very small, far below the experimental gas release measurements.

If the gas bubbles are considered as perfect traps for gas atoms then at high temperatures, all the gas atoms would be trapped in the numerous intra-granular bubbles. According to Speight’s effective diffusion theory [51], the effective diffusion of single gas atoms, taking into account the trapping in and

re-resolution from the bubbles is given by:

$$D_{eff} = \frac{b}{b+g} D_{Xe}$$

where b is the re-resolution rate, g is the trapping rate, defined as a probability per unit time and D_{Xe} is the single gas atom diffusion coefficient. Speight's model is described in detail later in Section 1.8.3.

The trapping rate, g , is proportional to the number density of intra-granular bubbles, whereas the re-resolution rate, b , is proportional to the fission rate density. Since the intra-granular bubble density is high and during annealing there is no fission rate, there should be no effective movement of the intra-granular gas atoms and they should not escape the grain within the duration of annealing. However, experimental studies on PIA have shown significant gas release from the grain to the grain boundary.

Among the mechanisms of intra-granular gas release discussed earlier, the single gas atom diffusion is ruled out considering the effective diffusion theory. It has also been noted from studies mentioned beforehand that thermal re-resolution is not a realistic scenario during PIA tests. Trapping of gas atoms in the numerous intra-granular bubbles and eventually the migration of these gas contained bubbles seems to be the most plausible scenario for the intra-granular gas release.

In this thesis, **we have focused our study of fission gas behaviour on the intra-granular release during PIA tests taking into account the different mechanisms of intra-granular bubble migration.** In the next few sections, we will discuss the experimental observations and modelling approaches for intra-granular gas release during PIA tests.

1.7 Experimental observations during post-irradiation annealing (PIA)

1.7.1 Microstructure evolution during PIA tests

Microstructural observation before and after annealing on UO_2 fuels irradiated in a commercial BWR during 1 to 4 cycles with burnup $\sim 6-23$ GWd/ t_U was done by Une and Kashibe [96]. The 4 different specimens (1 to 4 cycles) were annealed at 1800°C for 5 hours. Before and after the annealing experiments, the microstructure of the specimens was examined by an optical microscope and a scanning electron microscope (SEM). Measurements of their grain size and porosity were carried out by an image analysis of micrographs of the specimens' polished surfaces. Scanning electron micrographs of these polished specimens clearly indicated that both inter- and intra-granular bubbles grow on increasing the annealing temperature (See Fig.1.11).

Bubble swelling was evaluated by the difference in total porosity between before and after annealing and was found to be about 7% for the specimens annealed at 1600°C for 5 hours and about 9-10% for the specimens annealed

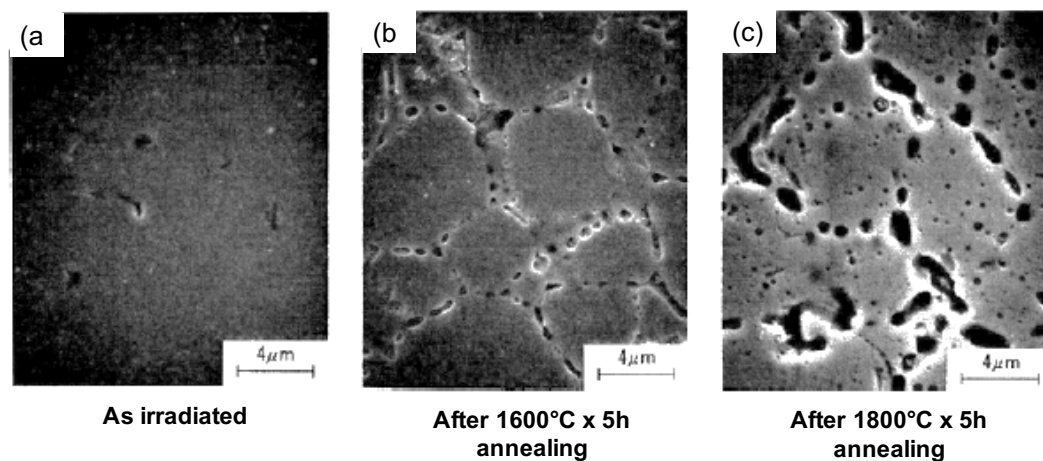
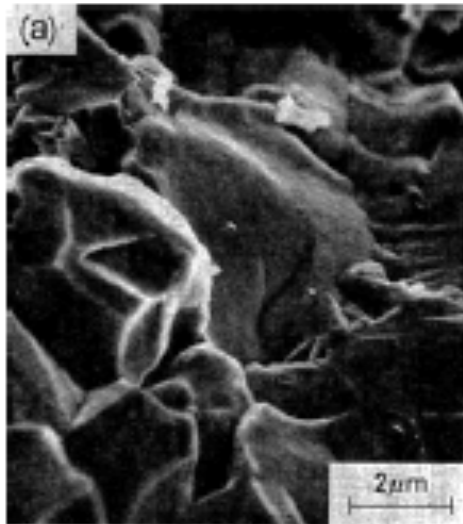


FIGURE 1.11: Scanning electron micrographs of polished surface of 3 cycle specimens (burnup: 23 GWd/t)[96].

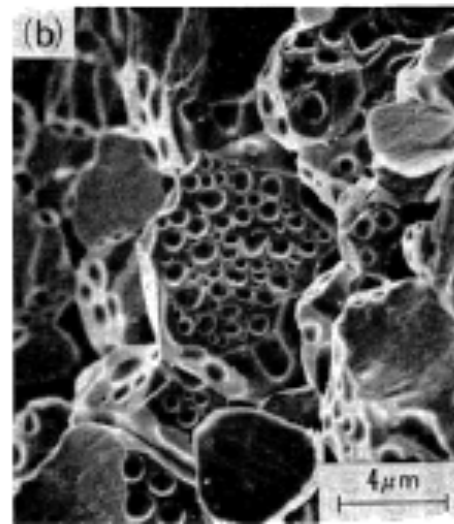
at 1800°C for 5 hours. The morphology of intra- and inter-granular bubbles was observed from the fracture surfaces of the specimens. Fig.1.12 shows the bubble morphology for as-irradiated 1 and 3 cycle specimens and the same after 5 hours of isothermal annealing at 1800°C.

There were no fission gas bubbles on the grain boundaries for the as-irradiated 1 cycle specimen (Fig.1.12(a)). On the other hand, for the 3 cycle specimen (Fig.1.12(c)), many small fission gas bubbles could be seen on the grain faces, which grow with the higher irradiation cycles. After 5 hours of isothermal annealing at 1800°C, the fracture was both trans-granular and inter-granular for the 1 cycle specimen (Fig.1.12(b)), while it was mainly trans-granular for the 3 cycle specimen (Fig.1.12(d)). **The trans-granular faces after annealing showed large intra-granular bubbles (~100 nm), which were not clearly observed for the unannealed specimens.** The intra-granular bubbles for the 3 cycle specimen became larger in comparison with the 1 cycle specimen. Moreover, there was a region of larger bubbles near the grain boundaries, as reported by Baker and Killeen [126] and Small [127]. These results suggested that vacancy diffusion from the grain boundaries could play an important role in the growth of the intra-granular bubbles near the boundaries.

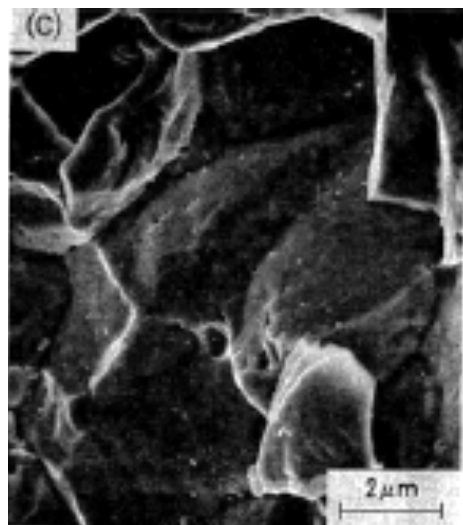
Further, intra-granular gas bubble growth kinetics in irradiated UO₂ during thermal annealing from 800°C to 1800°C was investigated by Kashibe et al. [128]. Their results show a rapid increase in the size of the intra-granular bubbles from a mean radius of ~1 nm to a mean radius of >20 nm in less than 10 minutes after heating to temperatures of ~ 1800°C. The bubble density correspondingly decreased by about 10³. Their results also indicate that gas bubble growth kinetics is dependent more on the burnup and proximity to grain boundaries than on the annealing temperature or heating rate. This implies that structural defects such as dislocations and grain boundaries, which may act as sinks and/or sources of vacancies, interstitials, and gas atoms (which are more numerous with burnup), play an important role in the evolution of the intra-granular bubble size and density.



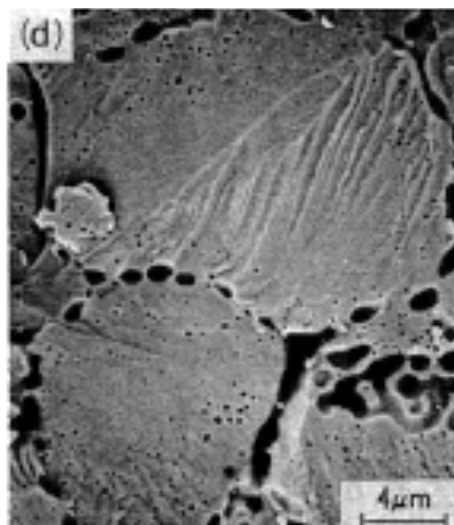
(a) 1 cycle specimen
(As-irradiated)



(b) 1 cycle specimen
(Isothermal annealing: 5 hr)



(c) 3 cycle specimen
(As-irradiated)



(d) 3 cycle specimen
(Isothermal annealing: 5 hr)

FIGURE 1.12: Scanning electron micrographs of fracture surface of 1 cycle specimen and 3 cycle specimen (a,c) as-irradiated, and (b,d) isothermal annealing at 1800°C for 5 h, respectively [96].

Similar intra-granular gas bubble growth kinetics were reported by White et al. [72] during PIA experiments with UO_2 . In their experiments, UO_2 fuel specimens were subjected to transient heating at a ramp rate of 0.5°C/s and 20°C/s in order to target temperatures between 1600°C and 1900°C . They measured the bubble size distribution from 17 specimens. They observed that the bubble densities were three to five orders of magnitude lower than those of the small bubbles at low temperature irradiation condition during annealing, independent of the annealing temperature. Moreover, the bubble size distribution exhibited long exponential tails where the largest bubbles were present in concentrations of 10^4 or 10^5 lower than the concentrations of the average sized bubbles. These results are not consistent with the presence of thermal re-solution from bubbles. They suggested that the bubble growth is driven by competition between vacancy sinks at the bubbles and vacancy sinks at dislocations, and that the bubble growth is severely restricted by vacancy starvation effects under out-of-pile conditions.

1.7.2 FGR during PIA tests

Several experiments have been conducted to analyze the FGR during PIA. Some of these are described below:

- Post-irradiation examinations and high-temperature tests on undoped large-grain UO_2 discs were done by Noirot et al. [129]. Discs made of standard-grain UO_2 and undoped large-grain UO_2 which had been irradiated at 44 GWd/t_{HM} and 42 GWd/t_{HM} , respectively, were subjected to high temperature tests. Both the undoped large-grain UO_2 and the standard-grain UO_2 used in this irradiation were enriched in U-235 by 19.77%. For the standard-grain UO_2 , the pellet fabrication process involved sintering for 4 hours at 1740°C in wet H_2 with an oxygen potential of -380 kJ/mol . The average grain size was $18 \mu\text{m}$ (larger grains of $\sim 22 \mu\text{m}$ were found on the periphery, $26 \mu\text{m}$ on the extreme periphery).

For the undoped large-grain UO_2 , the pellet fabrication process involved sintering for 10 hours at 1740°C in wet H_2 with an oxygen potential of -240 kJ/mol . The average grain size was $51 \mu\text{m}$ in the central part of the pellets and $32 \mu\text{m}$ on their periphery, with $27 \mu\text{m}$ grains at the extreme periphery. The maximum temperature reached during these tests was 1600°C and it was maintained for 20 min. Argon was used as a sweep gas at $\sim 1 \text{ bar}$ to carry the released gases out of the hot cell to be analyzed by gamma spectrometry of Kr-85. During the 1600°C high-temperature tests, the fractional release of fission gases was estimated at 33% of the produced gases for the standard-grain UO_2 and 8% for the large-grain UO_2 .

- Apart from the microstructural observation of UO_2 fuel specimens, Une and Kashibe [96] also carried out the tests for fission gas release via burst release during temperature ramp and diffusional release during isothermal annealing. During the annealing, the specimen was swept

by high purity He/2% H_2 mixed gas at a flow rate of 60 cm^3/min . The released Kr-85 was finally collected in a charcoal trap cooled by liquid nitrogen and its gamma activity was measured by a Ge detector after the annealing tests. A very high release rate at the beginning of the annealing was observed, which is caused by the release of fission gas accumulated at grain boundaries [130]. After the sudden burst release, the cumulative FGR (i.e., including the burst release) in 5 hours, for the 1 cycle specimen (burnup: 6 GWd/t_U) was $\sim 13\%$. The cumulative FGR was $\sim 17\%$ for the 2 cycle specimen (burnup: 16 GWd/t_U), $\sim 24\%$ for the 3 cycle specimen (burnup: 23 GWd/t_U) and $\sim 25\%$ for the 4 cycle specimen (burnup: 28 GWd/t_U).

- Thermal treatment of uranium oxide irradiated in a PWR was done to study the swelling and release of fission gases by Zacharie et al. [131]. Unstressed samples of uranium oxide, a few millimetres in size, recovered when taking a section some 8 mm long, taken from PWR fuel after two normal operating cycles (\sim burn-up of 25 GWd/t_U) were taken. The fuel was enriched to 4.5% with U-235 and the average grain size was 9.3 μm . The samples were placed in a tungsten crucible in vacuum ($<10^{-3}$ mbar) then heated by induction in a high-frequency laboratory furnace at temperatures between 1130°C and 1715°C for durations between 5 min and 10 h. Helium was used as the filling gas at a pressure of 26 bar. The temperatures were accurate within $\pm 20^\circ C$. The samples were loaded and unloaded at room temperature. The fission gas released over time was determined at each temperature. The xenon release show a fast increase in the first 60 min of treatment followed by a slow increase accelerated by temperature. The thermal release of fission gases becomes significant only above 1130°C. The values for FGR at 1630°C are found to be 7.8% in 60 minutes and 9.5% in 5 hours [132].
- Experiments were conducted by the Materials and Chemistry Group of the AEA Technology, UK [133], in which samples of irradiated fuel were heated and retained at high temperatures (1500-1800°C) for 2 to 40 hours. The samples contained fuels with mean grain sizes of 6 μm and 18 μm with the mean burnups as 17.9 GWd/t_U and 17.6 GWd/t_U , respectively. The experiments were conducted to investigate the effective gas atom diffusion coefficient, the holding capacity of the grain-boundary bubbles and the fuel grain size, in order to determine the FGR level. The Kr-85 released was continuously monitored throughout by a beta scintillation counter. The specimens used were in the form of discs of 3 mm diameter and ~ 0.5 mm thickness. Helium with 2% by volume of hydrogen was used as the sweeping gas and the sweep gas flow rate was controlled at 100 ± 5 ml/min. With the larger grain size fuel (18 μm), the temperature was raised to 1650°C at a ramp rate of 0.2°C/s and then held at 1650°C for up to 30 hours. The FGR in 3 hours after the isothermal annealing temperature was reached was found to be $\sim 11.76\%$.

For the smaller grain size fuel ($6 \mu\text{m}$), the temperature was raised to 1600°C at a ramp rate of 0.2°C/s and then held at 1600°C for up to 38 hours. The FGR in 3 hours after the isothermal annealing temperature was reached was found to be $\sim 7.64\%$.

- To study the microstructural mechanisms of FGR in irradiated UO_2 , Valin [8] used a pellet of UO_2 fuel (enriched to 4.5% of U-235) from a PWR which had been irradiated for one cycle. The mean grain size was $11 \mu\text{m}$. At the end of the irradiation, the burnup was 14.2 GWd/t_U and there was nearly no FGR. The fragments of the whole pellet were annealed for 3 hours at 1600°C . During the annealing, the specimen was swept by helium at a flow rate of $60 \text{ cm}^3/\text{min}$. The Kr-85 release was continuously monitored by a spectrometer and the total quantity released was also determined by analyzing cold traps. Fig.1.13 depicts the variation in fraction of Kr-85 released during isothermal annealing at temperature 1400°C , 1500°C and 1600°C . The fraction of FGR was found to be $\sim 65\%$ at 1600°C for 3 hours of annealing.

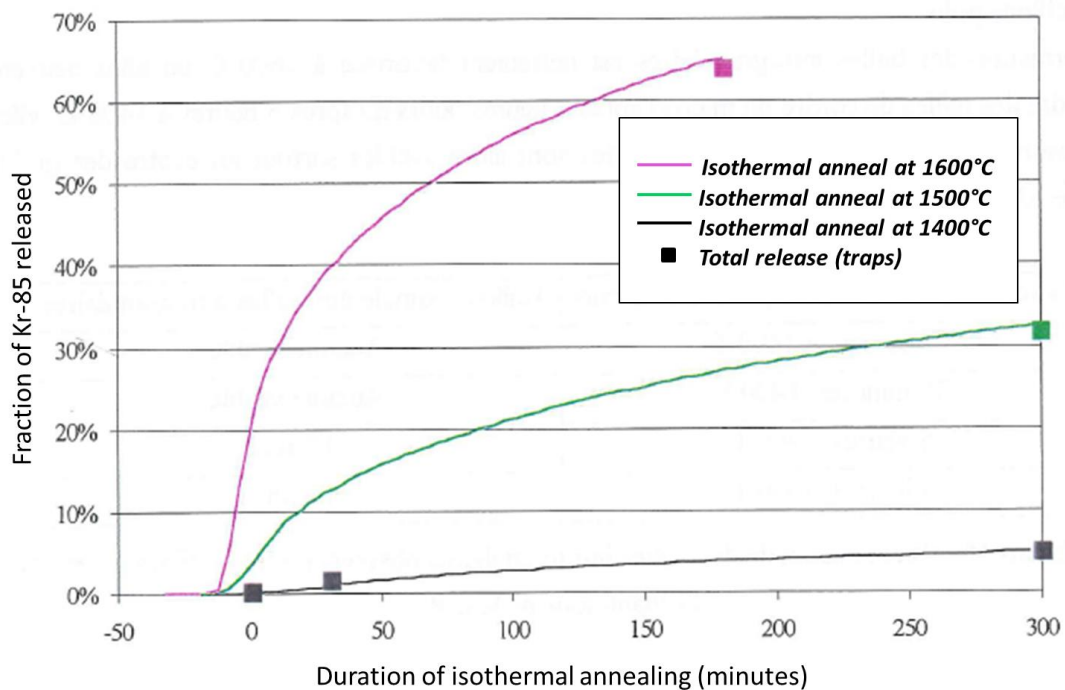


FIGURE 1.13: Variation in fraction of Kr-85 released during isothermal annealing of UO_2 sample [8].

The experiments related to PIA tests for analysing gas release and the conditions used are summarized in Table 1.3.

As can be observed from the Table 1.3, there seems to be no clear correlation among the results from different experiments. For the experiments carried out for more than 3 hours, the FGR value at 3 h is calculated from their respective release curves. From Copeland [133], it is noticed that the FGR in the 3 hours of annealing is lesser (7.64%) from the smaller grain as

Author (Year)	Temperature (°C)	grain diameter	burnup (GWd/t _U)	atmosphere of the sweeper gas	Duration	FGR (%)
Noirot et al. [129] (2015)	1600	51μm	42	Ar at ~1 bar	20 min	8
	1600	18μm	44	Ar at ~1 bar	20 min	33
Une and Kashibe [96] (1990)	1800	18μm	6	He/2%H ₂	3 h	10.8
			16			15.4
			23			21.4
			28			24.5
Zacharie et al. [131, 132] (1998)	1630	9.3 mm	25	He at 26 bar	3 h	8.4
Copeland [133] (1996)	1650	18μm	17.6	He/2%H ₂	3 h	11.76
	1600	6μm	17.9	He/2%H ₂	3 h	7.64
Valin [8] (1999)	1600	11μm	14.2	He at 60 cm ³ /min	3 h	65

TABLE 1.3: Literature on experiments of PIA tests for FGR.

compared to the larger grain. The only reasoning for this can be attributed to a higher temperature (by 50°C) for the larger grain.

1.8 Modelling approaches for FGR

The release of fission gases from UO₂, has been studied extensively since the middle of the 1960's. A number of reviews summarize the previous knowledge [58, 36]. The first and basic step in fission gas release is the diffusion of single gas atoms.

1.8.1 Booth Model

An analytical model to describe the physical process of gas release was first proposed by Booth [134]. Most of the existing mechanistic models for FGR rely on the Booth's model. This model describes the polycrystalline fuel as a collection of uniform spheres with an equivalent radius in order to simplify the mathematical problem. This model is also called the equivalent sphere model. The radius of the hypothetical sphere (R_{booth}) is defined in a way that the effective surface-to-volume ratio of the fuel, (S/V), is preserved:

$$R_{booth} = \frac{3}{(S/V)}$$

As irradiation proceeds, fission gases are generated within the Booth sphere and migrate to the surface, where the concentration is taken to be zero. The concentration of the gas atoms, $C(r,t)$ at the distance r from the center of an equivalent sphere changes as a function of the time t , following the second Fick's law:

$$\frac{\partial C(r,t)}{\partial t} = D\nabla^2 C(r,t) + \beta \quad (1.1)$$

Here β is the rate of creation of gas atoms - for post-irradiation experiments, $\beta = 0$ - and the initial profile of concentration is flat.

For short times and annealing conditions, solving the diffusion equation and integrating the amount passing through the surface, and dividing by the total amount in the sphere initially gives a fraction of released gas, f_{FGR} , proportional to the square root of the annealing time t :

$$f_{FGR} = 6\sqrt{\frac{D't}{\pi}}$$

With $D' = D/R_{booth}^2$, where D is the diffusion coefficient of the gas in the sphere considered as a homogeneous medium without defects. The modeling of the release isotherms obtained at different temperatures makes it possible to obtain the values of diffusion coefficients and then to determine the Arrhenius law controlling this phenomenon, which is given as:

$$D(m^2/s) = D_0 \exp\left(\frac{-E_a}{kT}\right)$$

where T represents the temperature in K, k the Boltzmann constant in $eV.K^{-1}$, D_0 the pre-exponential factor (m^2/s) and E_a the activation energy of the phenomenon in eV.

During reactor operating conditions, the gas generation term, β , comes into play. For such a scenario solving the diffusion equation (Eq.1.1) in the same way as earlier and using the short time approximation, we get the fraction of gas released as:

$$f_{FGR} = 4\sqrt{\frac{D't}{\pi}}$$

where again, $D' = D/R_{booth}^2$.

1.8.2 Improving the Booth Model

The original Booth approach has been improved by several workers to account for some effects neglected in the former model. Some of these improvements have been in terms of the numerical methods applied to solve the problem, such as the finite element method [135, 136], the finite volume method [91], the finite difference method [90] or other approximations [137, 138, 139, 140, 141].

The original Booth approach also disregards the athermal release due to recoil and knockout at open surfaces. Some codes have avoided this restriction by introducing an empirical release term as a function of burnup [142, 143]. Other codes introduced an effective diffusion coefficient depending on the burnup and the local fission rate, and / or an equivalent open porosity fraction resulting from the manufacturing process.

In the Booth model, R_{booth} is the radius of the fragment delimited by the free surfaces. An improvement has been to identify R_{booth} with R_g , the radius of the grain, and model inter-granular behaviour and release as a distinct phenomena. Another major improvement was done in terms of the physical concepts involved in the model. A fine intra-granular dispersion of small nanometric bubbles appears after a short irradiation period and stabilizes rapidly, both in size and in number density. This is a dynamic equilibrium, the gas being trapped and re-solved by fission spikes continuously. These bubbles hinder the diffusion of gas atoms towards the grain faces. The influence of these intra-granular bubbles, acting as efficient trapping sites, on the migration of fission gas atoms in material under irradiation was assessed by Speight [51]. He obtained an expression for the quantity of gas released to the grain boundary, and compared it with the analogous expression derived previously by Booth [134] for the case where there are no intra-granular traps.

1.8.3 Speight's Model for effective diffusion

Booth model contains certain basic assumptions such as the entire gas content of the material exists as single, freely diffusing atoms, and that the fissioning substance can be considered to consist of discrete homogeneous spheres. Since a discontinuity exists at each sphere interface, the surface of each spheroid behaves as a perfect sink for gas atoms. This property defines the boundary condition enabling the solution of the differential equation describing the movement of fission gas within each sphere, and hence, the calculation of the flux of gas atoms through each particle surface. It has been suggested [68] that the original porosity and clusters of irradiation produced defects within the grain (bubbles) are the most effective traps and therefore cannot be neglected in the modelling. Hence, assuming that the trapping sites (bubbles) are effectively immobile, the disposition of gas produced at a rate β per unit volume per second is determined according to the following equations:

$$\frac{\partial c}{\partial t} = D\nabla^2 c - gc + bm + \beta \quad (1.2)$$

$$\frac{\partial m}{\partial t} = gc - bm \quad (1.3)$$

where c is the local average concentration of gas in solution and m is the corresponding amount of gas in bubbles per unit volume of fuel. g is the probability per second of a gas atom in solution being trapped by a bubble and b is the corresponding probability per second of a gas atom within a bubble being re-solved by fission spikes.

Adding Eq.1.2 and Eq.1.3 and denoting the total gas content, $(c+m)$ by c_{tot} , we get the diffusion equation as:

$$\frac{\partial(c_{tot})}{\partial t} = D\nabla^2 c + \beta \quad (1.4)$$

As the phenomenon of local trapping and re-resolution by fission spikes are fast compared to the diffusion of Xe at the grain scale, a dynamic equilibrium is supposed between the dissolved gas and the gas in bubbles. Eq.1.3 can then be considered as near to permanent state,

$$\frac{\partial m}{\partial t} = 0 \Rightarrow gc = bm$$

$$c = \frac{b}{g}m \quad (1.5)$$

Adding m on both sides of Eq.1.5 and rearranging gives us (since $(c+m) = c_{tot}$):

$$c = \frac{b}{b+g}c_{tot} \quad (1.6)$$

Incorporating Eq.1.6 into Eq.1.4, we get the diffusion equation as:

$$\frac{\partial(c_{tot})}{\partial t} = D \left(\frac{b}{b+g} \right) \nabla^2 c_{tot} + \beta \quad (1.7)$$

Thus, Speight [51] provided an analytical solution for the migration problem in the Booth sphere incorporating the effects of both trapping and irradiation induced re-resolution at a fixed number of intra-granular traps. From these expressions he inferred an approximation for the case of saturated traps that enables one to use the Booth-formulas with an effective diffusion coefficient given by:

$$D_{eff} = \frac{b}{b+g}D$$

where again, b is the re-resolution rate and g is the trapping rate, defined as a probability per unit time.

Solving for c and m and integrating over the entire spherical volume of the expressions for c and m gives the total quantity of gas within the grain after an irradiation time t . Comparing this with the total quantity of gas produced since $t = 0$ by fission within this volume, the fraction of gas released to the grain boundary can be calculated. If the concept of effective diffusion coefficient is introduced into the fraction of released gas, the expression becomes completely analogous with that derived previously by Booth [134] for conditions where no gas precipitation occurs.

1.8.4 Beyond Speight's Model

Many models for fission gas release adopt an effective diffusion coefficient [79, 20, 90, 91]. Speight proposed a modified diffusion model incorporating the influence both of a fine dispersion of intra-granular gas bubbles and of a coarser distribution of lenticular inter-granular bubbles decorating the grain faces. The importance of irradiation induced gas-atom re-resolution on grain boundaries was later quantified further by Rest [144] and Dowling et al. [145]. Assuming that re-resolution of gas from these bubbles is irradiation-induced,

Speight demonstrated that the simple gas release model of diffusion from a sphere proposed by Booth was valid only if a lower effective diffusion coefficient and a non-zero gas atom concentration at the surface of the sphere were assumed to account for the effects of re-resolution from intra-granular and grain-boundary gas bubbles, respectively.

1.8.5 FGR modules in Fuel performance codes

Any model which aims to realistically describe the fission gas release and fuel swelling as a function of fuel-fabrication variables and in a wide range of reactor operating conditions, must treat them as coupled phenomena and must incorporate various mechanisms influencing the fission gas behaviour. There are several fuel performance codes that study the different aspects of nuclear fuel behaviour. A review on the fuel performance modelling has been done recently in [146]. Some of these fuel performance codes are discussed in detail in Annex A. Here we focus on the fuel performance codes which incorporate FGR modules or FGR modules which operate as stand alone models. Most prominent among these are tabulated in Table 1.4.

Fuel Performance Code	FGR module	Development Team
ALCYONE [147]	MARGARET [148] CARACAS [149]	CEA, France
BISON [150]	Forsberg–Massih model [138]	INL, USA
TRANURANUS [151]	FROMAS algorithm [138, 152] Physics-based model [153]	ITU, Germany
SFPR [154]	MFPR [155, 156]	IRSN, France IBRAE, Russia

TABLE 1.4: Fuel Performance Codes and FGR modules.

MARGARET [148], in particular, is a comprehensive, mechanistic code for the description of fission gas behavior integrated in the fuel code ALCYONE, co-developed within the PLEIADES software environment by the CEA, EDF and AREVA NP. This same tool can be used for base irradiations up to high burnup, ramp tests and annealing tests. The model is called at each time step and at each node of the mesh to provide inert fission gas swelling strains and inert fission gas release estimates. MARGARET is not a macroscopic model in the sense that there are no connections between the calculations performed at different nodes. It is a local model that describes the behavior of inert fission gas at the grain scale. The grain contains initially two types of cavities: intra-granular gas bubbles and intra-granular fabrication pores which are assumed spherical. The representation of intra-granular or inter-granular bubbles and fabrication pores is highly mechanistic. The partition of fission gas between these cavities and dissolved in the solid allows to determine the

swelling of the fuel. The gas release is obtained by the difference between the created and retained gas in the fuel. A detailed account of the equations and variables associated to the construction of the model can be found [157, 148]. The time evolution of the quantity of dissolved gas in the grain, the change in the number of bubbles (per unit volume of fuel) in the different populations by coalescence and diffusion to grain boundary surface, their increase or decrease in volume (leading to intra-granular and inter-granular gas swelling) are calculated consistently by solving a large Ordinary Differential Equation (ODE) system of equations that describes the coupled behaviour of intra- or inter-granular gas as well as the different kinds of cavities (intra- and inter-granular bubbles, fabrication pores).

CARACAS [149] follows the same principal in a simplified way. For instance, in base irradiation, the characteristics of the bubbles are not calculated as variables but are correlations in function of the temperature.

1.9 Detailed modelling of intra-granular bubbles

Even if the FGR models included in the fuel performance codes have been improved, they are still a very simplified representation of reality. These oversimplifications may be problematic. For example, when FGR models represent bubbles, they generally consider only one class of identical bubbles or at most a few ones. However, the behaviour of bubbles depend on their size and contents, and thus, a spectrum of bubbles with different sizes and content will impact the behaviour of these bubbles. One example for such behaviour is the velocity of a bubble in a thermal gradient. As the velocity depends on the bubble characteristics, it is different for different bubbles, which leads to the coalescence of bubbles among each other. It is impossible to take this effect into account other than by a mere parameter (difficult to relate to reality) in a one class bubble model. Another example of simplification is that most FGR models do not include defect (vacancy) diffusion and interaction with bubbles, or do it in a poor manner. So, the coupling between FGR and swelling is missed.

Due to these reasons, a new type of modelling has emerged that focuses on lower scales. For evident computation time reasons, they are not included in fuel performance codes.

1.9.1 Different scales of modelling

On a broad scope, computational materials models can be categorized into three groups depending on their spatial and temporal scales (Fig.1.14). The first is the atomistic scale, which includes models based on density functional theory (DFT) [28, 29, 30, 24] and molecular dynamics (MD) methods [158, 159, 160, 161, 162, 163]. Modeling within the atomistic scale considers a time scale of at most microseconds and a length scale of up to nanometers (millions of atoms and their motion) in describing atomic or molecular interactions. The next is the mesoscale, including models such as the kinetic Monte

Carlo (kMC) Potts model [164], rate theory (cluster dynamics) [165, 166, 167] and the phase-field (PF) methods [168, 169, 170, 171]. The characteristic length scales in mesoscale modelling generally range from 100s of nanometers to 10s of micrometers and time scales range from 10^{-3} to 10^2 seconds. The last group is the continuum scale, which includes the finite element [172] and finite volume methods [173, 174]. The continuum scale modeling can stretch to years in terms of the time scale and to centimeters for the length scale in the case of nuclear fuel rods or irradiated material. Annex B elaborates on the different scales and the approach towards using multi-scale modelling.

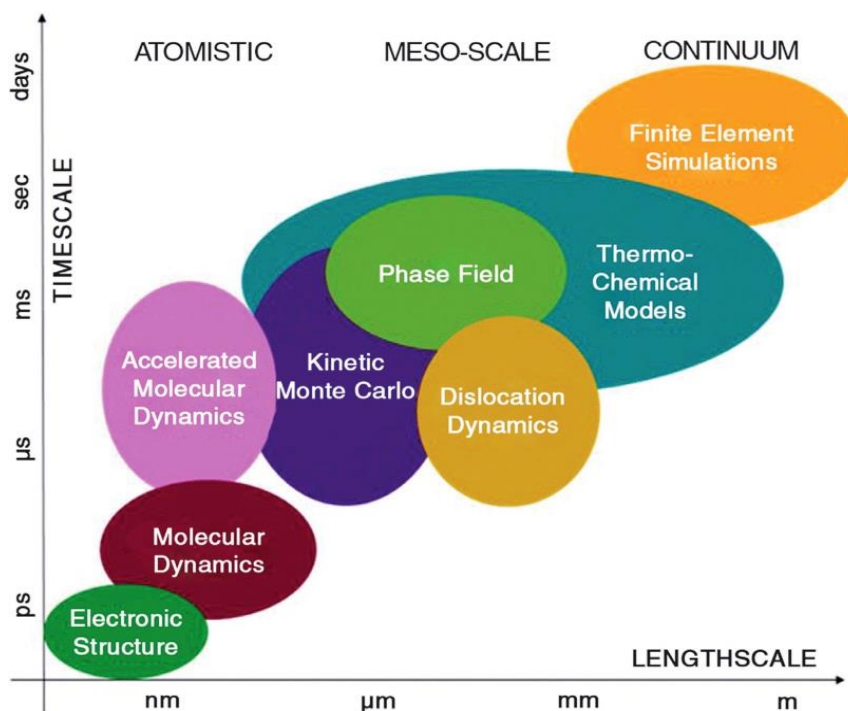


FIGURE 1.14: Methods used for materials model development and computer simulations at different scales (taken from [175]).

In order to model the role of intra-granular bubbles in connection with the FGR for out-of-pile annealing tests, we have to take into account, somehow, the grain radius, which is a key parameter. A model that would represent the bubble individually on the range of a grain radius length would be of great interest to describe the interaction of bubbles with defect (vacancies), their movement and their escape to the free surface. The length and time scales for such mechanisms can only be represented at the meso-scale. So, meso-scale modelling needs to be adopted to model the intra-granular bubbles movement or their interactions with mobile species present in the grain and to analyze the phenomena such as FGR and swelling.

1.9.2 Meso-scale modelling

The interaction of materials with their surroundings inherently occurs at the atomic scale, however, the response is observed at the continuum scale. The ability to describe and model materials from the atomistic to the continuum scales is expected to provide a better understanding of the existing materials. Due to the large disparities in the length and time scales in the atomistic scale and the continuum scale, meso-scale methods can play a key role in bridging the temporal and spatial scales in materials modelling and may provide a more quantitative, mechanistic-based multi-physics representation of the underlying processes controlling the microstructure evolution for predicting the material properties evolution at the continuum scale [176]. As an example, consider the migration of fission gas atoms in nuclear fuel material under irradiation. It is influenced by several important microstructural mechanisms, such as single gas atom diffusion, gas atom or vacancy trapping by defects and dislocations, nucleation and growth of gas bubbles, absorption and re-resolution from gas bubbles, non-equilibrium pressure conditions in gas bubbles, and the elastic interactions between defects and bubbles. Thus, the rate of gas atom diffusion to the grain boundary and its ultimate release from the fuel is dependent on all these mechanisms. Most semi-empirical continuum-level models approximate all of these mechanisms into a single effective diffusivity and have limited predictive capability. The advantage of using the meso-scale is that material characteristics at the microstructure-level such as free surfaces, bubbles or other defects, can be represented explicitly [176]. These microstructural features have a deciding impact on material behavior on the continuum scale. Moreover, meso-scale allows us to study the microstructure at larger time and length scales than the atomic scales.

1.9.3 Prominent meso-scale methods

The most widely used and well-known mesoscale modeling methods are the rate theory (Cluster Dynamics), kinetic Monte Carlo (kMC), and the Phase-Field (PF) approaches. The kMC methods are discrete ensemble representations that use a statistical-mechanical approach to represent the evolution of distinct interfaces in the microstructure. The PF approach, on the other hand, is a thermodynamic model that represents the microstructure using a continuum field with a set of smoothly changing variables that are species concentrations and/or "order parameters". The order parameters are typically used to indicate if a point belongs to one phase or the other. Thus, places where the order parameters change steeply are on the interfaces between different phases [177]. These methods / models are discussed below along with the advantages and limitations of each. The application of these methods for modelling the intra-granular FGR during post-irradiation annealing is also mentioned.

Cluster Dynamics

Cluster dynamics is a rate theory method which is adapted for the simulation of the evolution of point defects and defect clusters in materials [165]. In this method the system investigated is seen as a gas of clusters of various sizes of vacancies, interstitials and solute atoms. The positions of these clusters are not considered so the properties of the system must be considered as averaged values with space. It is not a spatialized model. The evolution of the system can then be described by a set of differential equations of concentrations of clusters of different types. The solution of these equations yields the concentrations of the various defect clusters over time. In practice, a detailed description is only important for the monomers and small clusters while approximations are made for large cluster sizes. The investigation of fission gas release in UO_2 using the rate theory is described in [178, 166].

The advantages associated with cluster dynamics methods are:

- Since the computation cost is low, cluster dynamics can handle long term evolution that cannot be investigated through atomistic methods.
- Cluster dynamics allows us to develop more general and precise models than the standard rate theory models that have previously been applied to nuclear fuels, which rely on the same physics, but make significant and poorly justified approximations on the cluster size distribution.

The disadvantages of cluster dynamics methods are:

- Loss of space correlations of the elements of the material microstructure which is the price paid for the strong decrease of the computational cost compared to atomistic methods. Movement and coalescence of clusters is ignored.
- The improvement compared to earlier rate theory models comes with an increase in the complexity of numerical resolution.

Kinetic Monte Carlo (kMC)

Kinetic Monte Carlo (kMC) methods [179] are stochastic methods enabling the simulation of the time evolution of a system when the processes governing the evolution are known. kMC serves as a powerful tool for modeling materials at the meso-scale. A kMC simulation consists of choosing at every time step an event among all the possible jumps, for instance, and keeping track of the successive positions of the mobile atoms of the system. The transition events are chosen randomly proportional to their transition rates. A large number of steps are simulated so that the average result can be evaluated. At the end of the simulation, various interesting parameters can be extracted, such as diffusion coefficients or thermodynamic constants. Three commonly used kinetic Monte Carlo models are:

- Lattice or atomistic kMC [180, 181]

In this model the system is the atomic lattice with the evolution processes

being the jumps of these atoms from one position to another and the jump rate is due to local environment.

- Object kMC [182, 183, 184]
Only the positions of the “objects” e.g. defects or impurities are taken into consideration, and the positions of atoms on the background lattice are not included in the simulation.
- Event kMC [185]
It is a variant of object kMC where events are related to interactions between objects and not to atomic jumps on the lattice.

Another important model using kMC is the Potts-kMC model discussed below, which will further be discussed in section 1.9.4.

- Potts-kMC [164, 186, 176]
In the Potts-kMC model, a 3D domain is divided in regular voxels. On each of the voxels, integer variables named "spins" (for historical reasons, as the predecessor to the Potts model, the Ising model, was developed for magnetic materials) are defined. These integer variables, for instance, can be:
 - an integer that would label the voxel belonging to the same grain (for grain growth modelling),
 - an integer that would label the "empty" voxels, belonging to pores,
 - an integer that would label voxels containing Xenon

The evolution of the system is done :

- considering the total free energy of the system

In the case of sintering studies, for example, the total free energy, E is

$$E = \frac{1}{2} \sum_{i=1}^N \sum_{j=1}^N J_{ij} (1 - \delta(q_i, q_j))$$

where J_{ij} is the neighbour interaction energy between voxel i and voxel j, q_i and q_j are the spins of voxel i and voxel j, δ is the Kronecker delta (i.e., $\delta(q_i = q_j) = 1$ and $\delta(q_i \neq q_j) = 0$).

- considering every site in turn and trying to switch its spin with one of its neighbours. The energy difference ΔE resulting from this switch is calculated and the switch is effectively done following the Standard Metropolis algorithm (SMA). In SMA, probability for the switch is calculated as:

$$P = \begin{cases} \exp\left(\frac{-\Delta E}{kT_m}\right) & \text{for } \Delta E > 0 \\ 1 & \text{for } \Delta E \leq 0 \end{cases}$$

Then, a random number between 0 and 1 is generated. If it is below P, the switch is effectively done, else the switch is rejected. T_m is the Monte Carlo temperature which is not the real temperature. Raising T_m is a way to render the switches more probable.

The advantages associated with kMC methods are:

- As already discussed, kMC models can span the time scales in between the atomic and continuum scales. It, thus, provides a methodology to overcome the time limitation associated with Molecular Dynamics.
- It tackles the time-scale problem by treating directly the state to state dynamics rather than following the trajectory through every vibrational period. This allows kMC to reach longer time scales, of the order of seconds and even beyond.
- kMC can give the exact dynamical evolution of a system, same as the more expensive Molecular Dynamics, if we can exactly determine the rate constants for every state.
- Systems out of thermodynamic equilibrium can be simulated for microscopic time scales while keeping spatial correlations. In addition, transition events can be turned off or on to separate the effects.

Some disadvantages of KMC methods are:

- The rate catalogs, containing the rate constants for each possible escape pathway must be known beforehand, the method in itself is not predictive. The real dynamical evolution of a system may often surprise us with unexpected and complex reaction pathways. Since these pathways are outside our intuition, they will typically not be included in the rate catalog, and hence cannot occur during the kMC simulation.
- Atomic kMC method is limited to low length scales ($\sim \mu\text{m}$).
- kMC are also computationally expensive, in particular compared to rate theory methods. In the case of plain lattice kMC, calculation time scales linearly with the number of atoms.

Phase Field Model (PF)

The traditional approach used for modeling bubbles, used only the concentration of bubbles, without any consideration to their particular position in space. However, consideration of the particular position of bubbles may be important, for example, when they migrate in a temperature field and can coalesce with other bubbles. To better understand the microstructure evolution, we need spatially resolved models and that is where the phase field (PF) approach has appeared as promising. In the phase field approach, applied to grain growth, for example, the microstructure, which consists of a number of grains, is described by functions called the phase-field variables that are continuous in space and time. These variables have nearly constant values within the grains and vary gradually over the microstructure interface which is defined as a narrow region of finite width. Such a modelling approach is called a diffuse-interface approach. In this approach, the interfaces between domains are defined by a narrow region having continuous variation of properties. It is

different from the more conventional modelling techniques for microstructural evolution in which infinitely sharp interfaces are considered. A schematic representation of the diffuse and sharp interface is shown in Fig. 1.15(a) and (b), respectively. The diffuse-interface approach is advantageous over the sharp interface approach as the need to track the interfaces by means of mathematical equations during microstructural evolution is eliminated. Within the domains, the phase-field variables have the same values as the sharp-interface model, but the transition from one domain to the other is continuous. For example, the evolution of the phase-field variables gives the evolution of the grains or the position of the interface (here, grain boundaries) as a function of time and space.

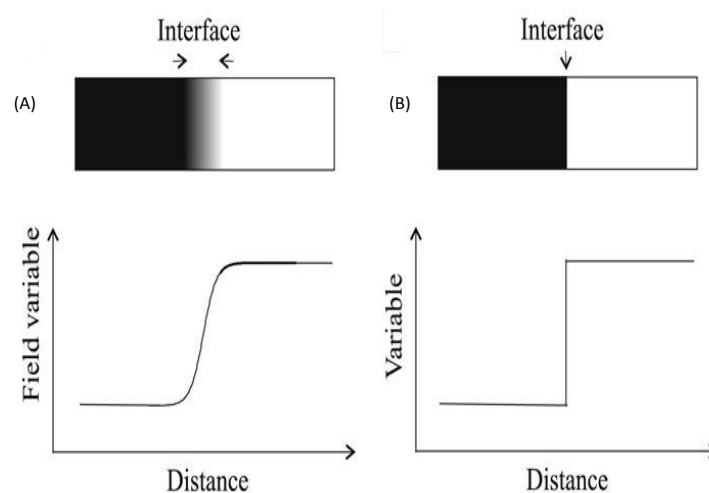


FIGURE 1.15: (a) Diffuse-interface; continuous variation of properties at the interface. (b) Sharp-interface; discontinuous properties at the interface [187].

The evolution of the microstructure is defined in terms of the free energy of the system. In the phase field method, first, the free energy functional of the heterogeneous system is expressed in terms of the free energy of the constituent phases and interfaces. Then, the free energy functional is used to derive the kinetic equations which are partial differential equations that define the evolution of the phase field variables to minimize the overall free energy.

The major advantages of using the phase-field approach are:

- It follows a diffuse-interface description and so no boundary conditions need to be specified at the moving interfaces. Hence, it is able to predict complex morphological evolutions.
- Since the need to track the interfaces is eliminated, the numerical solution and implementation of the phase-field equations is reputed to be simple and straightforward.

Some disadvantages associated with the PF methods are:

- The PF models comprise a large number of phenomenological parameters. These parameters have to be determined to obtain quantitative results. Some of these parameters are related to properties that are difficult to measure or are purely numerical and so it is complicated to determine all the parameters.
- Although the numerical solution and implementation of phase-field equations is relatively straightforward, as there is no need to track the interfaces, the resolution of the numerical technique must be very fine to catch the steep transitions of the phase-field variables at interfaces. Simulations for realistic system sizes and time scales are, therefore, not feasible using the ordinary numerical techniques, because of excessive computation times and insufficient computer memory.

1.9.4 Application of meso-scale modelling for intra-granular bubbles

Despite the intra-granular gas plays an important role in the mechanisms leading to FGR, more often than not, its modelling is based on a simple description through the effective diffusion inside a spherical grain [20, 140, 141, 59]. Post-irradiation annealing (PIA) tests are performed at high temperatures (up to 1600°C - 1800°C) to analyze the FGR mechanisms in such conditions. There is neither irradiation nor high temperature gradient in annealing tests, which allows the study of temperature level effects (separate effects tests) only. It is a well accepted fact that using the effective diffusion coefficient during high temperature and transient conditions leads to an underestimation of the fractional release [141, 140] (inter-granular gas only). High gas releases, observed in a high temperature annealing test, necessarily involve intra-granular gas release. However, gas modeling including gas diffusion and stochastic bubble movement fail to simulate annealing tests. Scenarios involving movement of bubbles in a vacancy gradient have been proposed but are difficult to include in a fuel performance code because vacancies and detailed bubble field within the grain are not modeled in those codes.

In 2009, Rokkam et al. [188] developed a phase-field model to describe voids and vacancy diffusion coupling within a material, however, no gas was involved in the model.

In 2012, a benchmark demonstration was done for the mesoscale simulations of intra-granular fission gas bubbles in UO₂ under post-irradiation thermal annealing [176]. The aim was to evaluate the capabilities of different numerical methods used to represent microstructure behavior at the mesoscale for irradiated material using an idealized benchmark problem. The models used for the benchmark were the phase-field and Potts-kinetic Monte Carlo methods developed by Pacific Northwest National Laboratory (PNNL), Idaho National Laboratory (INL), Sandia National Laboratory (SNL), and Oak Ridge National Laboratory (ORNL). The demonstration was done in order to consider the main mechanisms involved in the process, such as vacancy and gas atom diffusion, vacancy starvation/emission, internal pressure in gas bubbles,

and elastic interactions associated with lattice mismatches of distributed vacancy, gas atoms, and gas bubbles. The initial conditions for the benchmark problem were obtained from the experiments of Kashibe et al. [128]. The gas density and pressure within the bubbles was calculated with the equation of state for Xe given by Ronchi [189]. Another assumption, for simplicity, used in the benchmark demonstration was that periodic boundary conditions were imposed in the all (x-, y-, and z-) directions. The initial conditions for the intra-granular bubbles and the thermodynamic properties of defects used for benchmark problem are presented in Table 1.5. The values were slightly different for the different methods due to the difference in microstructure description in them. Dislocation distribution was only considered by PNNL and was taken into account in the model as a uniform source of vacancies.

Description	Value
Initial bubble density	$9 \times 10^{23} / \text{m}^3$
Initial gas conc. in matrix	0.0042 atom/site
Initial vacancy conc. in matrix	Model parameters
Dislocation density	$2 \times 10^{14} / \text{m}^3$
Initial gas atom conc. in bubbles	0.7 atom/site
Initial bubble distribution	Normal
Mean bubble radius	1 nm
Xe interstitial migration energy in UO_{2-x}	1.6 ~ 6.0 eV
Xe interstitial formation energy	3. ~ 4.35 eV
U vacancy formation energy	2.67 eV
Interfacial energy of gas bubbles	0.6 J/m ²

TABLE 1.5: Initial conditions for the intra-granular bubbles and the thermodynamic properties of defects used for benchmark problem [176].

The computational efforts made in the different models used in the benchmark demonstration are summarized in Table 1.6. The summary of the analysis carried out and the results obtained with the different methods are discussed next.

The mechanisms considered in the different models is listed in Table 1.7.

- **Phase Field model by PNNL**

Having as input the initial gas bubble density, gas bubble size distribution, gas concentration, and the annealing conditions, the phase-field equations for the evolution of the vacancy and Xe concentration and the order parameter were solved by the implicit FFTW (Fast Fourier Transform in the West) method [190]. Here, the order parameter serves to indicate if a point is in the solid or in a bubble. The gas bubble evolution kinetics was simulated in 2-D and 3-D. The PF model describes the mechanisms of diffusion of U vacancies and Xe atoms; absorption and dissolution of vacancies and Xe atoms at gas bubbles; vacancy emission from distributed dislocations; elastic interaction among gas bubbles, vacancies, and Xe atoms; gas bubble growth and gas bubble coalescence.

Description	PNNL Phase-field	INL Phase-field	SNL Potts-kMC	ORNL Potts-kMC
Simulation cell	256x256 (2-D) 128x128x36 (3-D)	Adaptive mesh	500x500x500 (3-D)	300x300x30 (3-D)
Physical domain	256x256 (nm ²) 128x128x36 (nm ³)	300x300 (nm ²) 20x20x20 (nm ³)	100x100x100 (nm ³)	600x600x 60 (nm ³)
No. of bubbles	530	7.2	900	19440
No. of cores	1	64	100	64512
CPU time	260 h	38.5 h	24 h	22.4 h
Simulated time	12 min	9.06 min	0.58 s	40 s

TABLE 1.6: Computational efforts made in the different models used in the benchmark demonstration [176].

Mechanism	PNNL (Phase-field)	INL (Phase-field)	SNL (Potts-kMC)	ORNL (Potts-kMC)
Xe gas diffusion	*	*	*	
Vacancy diffusion	*		*	
Bubble migration			*	*
Gas bubble growth	*	*	*	*
Ostwald ripening	*	*	*	*
Vacancy emission	*			
Dislocation pinning				*
Gas bubble pressure	*		*	*
Elastic interaction	*			

TABLE 1.7: Computational efforts made in the different models used in the benchmark demonstration [176, Table 6].

The phase-field model by PNNL is described more precisely in [191]. An important feature of the model is that the chemical free energy density of the gas bubble phase is assumed to be the sum of two parabolic functions (one in function of C_g and the other in function of C_v). The minimum for the first one is at $C_g = 0.7$, and for the second one at $C_v = 1$. So, the minimum for the sum will be at ($C_g = 0.7$ in fraction of site and $C_v = 1$ in fraction of site). This means that the volume per atom of gas inside the bubble is prescribed to tend to $(0.7)^{-1} * \Omega = 1.4285\Omega$ (Ω is the volume of the UO_2 item). Hence, for a given temperature, the pressure in the bubble is prescribed in the model, as if this corresponds to an equilibrium situation.

However, the only equilibrium state of Xenon and UO_2 is that there is no bubble any more and that the Xenon has completely left the crystal (because of the insolubility of Xe, the surface energy cost of the bubbles,

and the energetic cost of pressurization of the gas inside the bubbles). The problem is only a kinetic one, with local equilibrium of vacancies or Xe atoms at the vicinity of bubbles with evolving characteristics. So, to solve this problem, reaching an equilibrium for the gas in bubbles seems not to adhere to the physics.

Another difficulty that can arise with this model is that it can only be used with periodic conditions. This can be detrimental for the modelling of FGR from a grain.

- **Phase Field model by INL**

At INL, in order to carry out the benchmark demonstration, the simulations were done using the MARMOT FEM-based phase-field modeling framework [192]. MARMOT allows to take advantage of its adaptive mesh capability to discretize the domain. Here again, 2-D as well as 3-D simulation were carried out for bubble evolution with respect to the initial bubble distribution and bubble size distribution. Brownian motion of the bubbles was not considered in the model, therefore, bubble growth was primarily due to Ostwald ripening rather than coalescence. Moreover, the effect of pressure within the bubbles was ignored. Since Xe was considered as the only rate limiting species, the phase-field equations was the one for the evolution of gas concentration. The PF model described the mechanisms of diffusion of Xe atoms; absorption and dissolution of Xe atom at gas bubbles; gas bubble growth and gas bubble coalescence.

As the only species that is taken into account in the model is Xe, the Ostwald Ripening is mandatory due to thermal re-resolution of Xe into the bulk in this model. Yet, it was demonstrated earlier that thermal re-resolution of Xe in UO_2 is highly improbable. The other main hypothesis, about neglecting the inner pressure in the bubble, also seems far from physics for pressures that are of the order of GPa inside the bubbles, and also as there is no vacancy source in the model, it is impossible that this pressure decreases in the model.

- **Potts model by SNL**

The Potts model was used by SNL to carry out the benchmark analysis. In this case, only two spins were used, one for the voxels that belonged to the bulk (or grain), and the other for the voxels filled with Xenon. In this modelling, bubbles would be a gathering of voxels labelled "Xenon". The initial microstructure for the gas bubble coarsening simulation was obtained by a "nucleation and growth" simulation. The concept of nucleation sites is introduced. For those sites, $J(q_{nuc\ site}, q_{Xe}) = 0$ to encourage nucleation. The nucleation sites were placed randomly in the simulation space. The various characteristics were chosen to match the parameters of the benchmarking exercise. The diffusion of Xe atoms was simulated by random walk with no bias. The bubbles coarsen by random walk, coalescence, and the re-resolution of the gas in the bubbles to the lattice and re-precipitating to other bubbles. Both these are simulated

by random walk of the bubble sites. The Potts model could simulate the mechanisms such as the diffusion of Xe atoms, absorption and dissolution of Xe atom at gas bubbles, gas bubble growth, and gas bubble coalescence.

Like in the PF simulation, it seems that the inner pressure of the bubble is not variable and in the case of Potts Model, it does not play a role in bubble evolution. Again, thermal re-resolution is implicitly considered as Xe can detach from the bubbles.

- **kMC model by ORNL**

The simulation domain used in the Potts/kMC model developed at ORNL consists of three "species" on the voxels (or "element") - the matrix (UO_2), "void" (vacancies), and "bubble" (vacancies + gas atoms). The formation of larger "extended bubbles" occurred through a collection of "voids" and "bubble" elements. Three types of Monte Carlo moves are defined which are 1) the exchange of a "void" and a matrix element, 2) exchange of a "void" and a "bubble" element to simulate Xe diffusion inside the bubble, and 3.a) the creation or 3.b) destruction of a "void" element at the bubble-matrix interface. These changes are illustrated in Fig.1.16. In the model, "pinning elements" inside the matrix to account for the drag on the migrating bubbles due to dislocations was also considered. The Potts/kMC model could simulate the mechanisms such as random movement of bubbles, dislocation pinning, gas bubble growth, and gas bubble coalescence.

In the Potts-kMC model of ORNL, Xe remains inside the bubble. The number of Xe atoms per "bubble" element is fixed, but as the number of "void" elements and "bubble" elements may vary in a bubble, the volume per atom and thus the pressure may vary. It is not clear in the description of the model whether a "void" element may detach from a bubble or not, if it is allowed to do so or not, or if it is just very improbable. The fact is that the move 1) is described as "surface diffusion", so voids probably do not detach from bubbles in the model.

Unlike in the Potts model of SNL, switches are not the only allowed events. Moves 3.a) and 3.b), respectively, create or destroy a void element (which is not conservative). This is to simulate the effect of the inner pressure. The more the "bubble" elements are inside a bubble, the more move 3) happens and the bubble grows. However, it is not straightforward that the model represents well the physics. The procedure to link this modelling to the physics is the following: Several simulations were done with a domain containing one bubble, consisting of only "bubble" elements with different T_m . In each simulation, void elements were created by the algorithm at the bubble matrix interface until an equilibrium was reached. At this stage, two pressures can be calculated: $P_{eq} = \frac{2\gamma}{R}$, where γ is the surface energy and R is the radius of the bubble, and P_{EOS} , calculated from the volume per atom obtained in the bubble, the desired true temperature (1800°C) and the Ronchi Equation of State recommended in the benchmark.

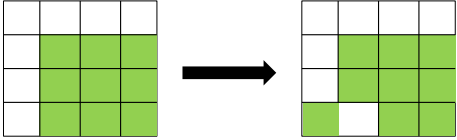
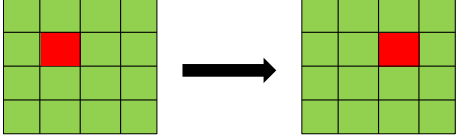
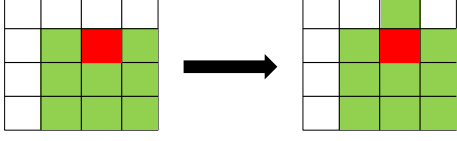
MC Move		
1)		Exchange of void  and matrix element 
2)		Exchange of void  and 'bubble' element 
3.a)		Replacing a matrix element  by a void element  if a 'bubble' element was touching it (<i>non-conservative</i>)
3.b)		Replacing a void element  by a matrix element  (<i>non-conservative</i>)

FIGURE 1.16: Potts-kMC Model used by ORNL for the benchmark study.

T_m is raised until P_{eq} and P_{EOS} fit. So, getting equilibrium bubbles ($P_{eq} = P_{EOS}$) is mandatory in the model because it is the way to feel confident that the algorithm mimics correctly the effect of inner pressure on the bubble growth. In the model, it is like the sources or sinks of vacancies settled at the vicinity of each bubble and guarantee that the bubble is always near the equilibrium.

Random movement and coalescence of bubbles could be observed in the simulation along with the lowering of inner pressure after coalescence, which is impressive. However, non-equilibrium bubbles can not be described with such a model nor the situation of vacancy starvation (that was identified during annealing, far from the vacancy sources). Since the bubbles are in equilibrium in the model, there is no reason to observe the flux of vacancies (void elements here) from one bubble to another. Yet, that is expected between non-equilibrium bubbles or between bubbles and a free surface.

Several other works have been done after the benchmark demonstration of intra-granular behaviour. V. Tikare and her student [193] developed a hybrid approach using concentrations and spins. Concentrations are calculated by resolving the diffusion equations and the spins (used to define the different phases or cavities) were updated though Potts-kMC method. Their work,

however, focused on the inter-granular bubbles. Other works focus on establishing the link between the phase field approach and the sharp interface models [194, 195]. A recent work [196] presented a calculation of intra-granular bubbles by a phase-field method where the minimum for the bubble free energy density as a function of Xe concentration has a better physical base than in [191]. However, the article is about U-Mo fuel and under irradiation. Simulations were done with periodic limit conditions and bubble random movement was not taken into account because it was negligible in the studied conditions.

In 2017, Welland et al. [197] calculated the migration and growing of one intra-granular bubble at the vicinity of a grain boundary that was a source of vacancies and the subsequent capture of the bubble by the grain boundary, using a phase-field approach. The simulation was done in 2-D azimuthally symmetric conditions. The dimension of the domain was 30 nm with a 15 nm radius bubble and the simulation lasted for 2.5 s.

Conclusions from the application of meso-scale models for intra-granular bubbles

The conclusions drawn from the overview of meso-scale modelling for intra-granular bubbles presented in the section 1.9.4 are as follows:

- The relation between the phase-field or Potts-kMC models and the real physics is a subject in itself and is not straightforward.
- None of the models presented in the benchmark demonstration included the whole physical features that are necessary to tackle the problem of FGR out of the grain in annealing conditions. These include:
 - no Xe thermal re-solution,
 - no periodic conditions,
 - vacancy starvation (far from the grain boundary) as well as vacancy flux (coming from the grain boundary),
 - the inner pressure in each bubble may be larger than the equilibrium pressure and may vary in function of the vacancy capture.
- After the 2012 benchmark demonstration, we did not find a new attempt to address this physical problem specifically at the meso-scale.
- Only in 2017, in Welland's article [197], the problem of the interaction of an intra-granular bubble and the grain boundary is addressed. This simulation, however, uses a small domain, only one bubble and spans a duration of 2.5 s.

1.10 In Closing

Fission gas behaviour needs to be understood comprehensively as fission gases, mainly Xenon, cause macroscopic phenomena like swelling and FGR which affect the proper functioning of the nuclear fuel rods. FGR occurs as a two-step process, firstly releasing the gas atoms within the grain to the grain

boundary and secondly by forming pathways in the grain boundaries to outside of the grain and/or diffuse easily on grain boundaries. Several mechanisms of FGR have been described in this chapter. Post-irradiation studies are carried out to analyze the FGR and it has been noticed that the transport of intra-granular gas to the grain boundary is large as compared to the predictions from effective diffusion theory. Experimental observation of FGR during annealing tests have been discussed in the chapter. Due to the low solubility of gas atoms in bulk UO_2 and due to the presence of numerous intra-granular bubbles, which act as traps for the gas atoms, the most plausible mechanism of FGR during post-irradiation annealing seems to be the intra-granular bubble migration. Modelling approaches adopted in the fuel performance codes have also been discussed, which emphasis on the meso-scale methods which are needed to model the intra-granular bubbles behaviour.

In the scope of this thesis, we study the FGR during post-irradiation annealing via the different mechanisms of bubble migration. In this direction, we have developed a new meso-scale model called the "BEEP Model". In the next chapter, we will discuss the methodology adopted in the BEEP Model and its ability to model intra-granular bubbles and their interactions with defects in the nuclear fuel.

Chapter 2

A new spatialized meso-scale model: BEEP Model

2.1 BEEP Model: Introduction

In this chapter, a new spatially resolved model, called the BEEP Model, is presented. In order to model the interactions between point defects (vacancies) and cavities (gas bubbles) or free surfaces, there arises a need to develop a mechanistic model which is capable of explicitly defining the cavities and represent their evolution in space with time. The BEEP Model is a spatialized model focused on modelling such interactions at the meso-scale. Since this model is spatially resolved, it overcomes the limitation of the Cluster Dynamics models. It uses sharp interface approach as compared to the phase-field models and can model bubbles which are even smaller than the individual grid size. The model uses only physical parameters to describe the microstructure and is, therefore, easier to relate to the real physical phenomena. The modelling methodology used in the BEEP Model has been discussed and the cases for the verification of the model are also presented in the following sections in this chapter.

2.1.1 Assumptions used in the model

- The UO_2 fuel is modeled as a mono-crystal containing spherical cavities.
- Each UO_2 is considered as an "atom" and Schottky defects as "vacancies" in the following description of the model.
- Only vacancies are considered as point defects in the model. It is assumed that the simulation starts after the gas has been trapped in the bubbles. So, the Xe gas atoms are present inside the cavities and not in the solid. Self-interstitials (that would be "anti-Schottky" defects) have been included in the model, and can be chosen to be included or not by the user. The calculations carried out in this thesis do not include them.

Indeed, as their energy is very high, their concentration must be much lower than the vacancy concentration.

- Bubbles are assumed to be spherical and remain so. This assumption is justified for the intra-granular bubbles at high temperature.
- Although the model does not explicitly calculate the surface diffusion of bubbles, its effect - a random displacement of the bubbles- has been added in the model.
- No irradiation is considered in the model, i.e. it is applicable for annealing tests.
- In the calculation of FGR, the gas is assumed to be released once it reaches the region outside the free surface. This has been done to focus on the intra-granular gas release.
- The model is developed to function in both 2-D and 3-D, but the major part of the analysis is done in 2-D due to the computation costs.

2.2 Modelling methodology

In the modelling of BEEP, the fuel is modeled as a mono-crystal containing spherical cavities. No grain boundaries or different solid phases are considered in the model. To model the interactions of point defects (vacancies) with the cavity (bubbles), the BEEP model calculates the diffusion of the vacancies between the bubbles and update the bubbles in function of the net vacancy flux that they receive. The changes in the bubble characteristics and their position are updated after each diffusion calculation and the simulation proceeds with the new characteristics of the bubbles and vacancy concentration in the next diffusion calculation.

2.2.1 Representation

In the representation of the model, the solid portion, which is a rectangle in 2-D or a cuboid in 3-D, is discretized on a regular mesh. The limit conditions are either periodic or symmetric along the x-axis and periodic in the other direction(s). The independent variables which are sufficient to represent the model are "spins" and "concentration fields".

- Spins
The first variables, spins, are integer numbers allocated to the cells (pixel in 2-D/voxel in 3-D) to categorize them in the mesh. The spin is 2 for the cells in the solid region, 0 for the cells in a cavity and 1 for the cells at the interface between solid and cavity (Fig.2.1). In the description of the model, "2-cell", "1-cell" and "0-cell" will refer to cells tagged with spin 2, 1 and 0, respectively. A 1-cell will always be between a 2-cell and a 0-cell. The 1-cells are partially solid and partially void.

2	2	2	2	2	2	2	2	2	2	2	2	2
2	2	2	2	1	1	1	1	2	2	2	2	2
2	2	2	1	0	0	0	0	1	2	2	2	2
2	2	1	0	0	0	0	0	0	1	2	2	2
2	2	1	0	0	0	0	0	0	1	2	2	2
2	2	1	0	0	0	0	0	0	1	2	2	2
2	2	1	1	0	0	0	0	1	1	2	2	2
2	2	2	1	1	1	1	1	1	2	2	2	2
2	2	2	2	2	2	2	2	2	2	2	2	2

FIGURE 2.1: A regular 2-D mesh representing the fuel matrix and a cavity with spins designated to each cell.

- Concentration fields

The other variables, the concentration fields, represent the concentrations of different species in the model and are calculated by a system of ordinary differential equations. In theory, several kinds of defects may be modelled, however, in practice, the only defects that have been taken into consideration are vacancies. So, the field for the 2-cell zone is the field "concentration of vacancies", C_v . For the 1-cell zone, the considered field is the "concentration of crystalline atoms", C_a . All the concentrations are expressed in fraction of sites. C_a in particular, is the number of U atoms in the cell divided by the number of U-sites in the cell, itself equal to the volume of the cell divided by Ω (atomic volume). C_a can also be assimilated to the solid fraction (RS) in the interface cell. No fields are required for the 0-cells zone.

The 1-cells have a crucial two-fold usage in the model. Firstly, they contain the C_a variable, which integrates every arrival or removal of U atoms with time. Secondly, the 1-cells are also used to provide a limit condition for the diffusion of vacancies in the 2-cells by imposing that, within the 1-cells, the vacancy concentration C_v is equal to the equilibrium concentration. These equilibrium concentrations of vacancies at the considered temperature in the proximity of a surface with curvature κ and exposed to a pressure P_b are denoted as $C_v^{eq}(\kappa, P_b)$. The method to calculate the equilibrium concentrations of vacancies in the vicinity of over-pressurized bubbles has been presented by Noirod [65] and the expression for this is:

$$C_v^{eq}(bubble) = \exp \left[-\frac{(\epsilon_v - s_v T)}{kT} - \frac{\Omega}{kT} (P_b - \gamma_b \kappa) \right] \quad (2.1)$$

where ϵ_v is the formation energy of vacancies (more precisely, Schottky

defects), s_v is the excess entropy of vacancy formation, T is the annealing temperature in K, Ω is the volume of one UO_2 -site, k is Boltzmann constant and γ_b is the surface tension at the solid-bubble interface (γ_b depends on the temperature by the relation $\gamma_b = 0.41 \cdot (0.85 - 1.4 \cdot 10^{-4} (T - 273))$ in J/m^2 [198]). The excess entropy of vacancy formation, s_v , is assumed purely vibrational:

$$s_v = k \ln \left[\left(\frac{\nu}{\nu'} \right)^\alpha \right]$$

where ν is the perfect crystal vibration frequency, ν' is the vibration frequency of atoms influenced by the vacancies and α is the number of vibrational modes that are altered by the introduction of a single vacancy [10, p.59]. In the analyses carried out using the model, we have taken $s_v = 0$, due to lack of information. The expression for $C_v^{eq}(bubble)$ in Eq.2.1 can be split in two factors where the first factor is the concentration of vacancy at equilibrium in a solid limited by a flat surface (curvature, $\kappa = 0$) and no external pressure ($P_b = 0$) as:

$$C_v^{eq}(bubble) = C_v^{eq}(P_b = 0, \kappa = 0) \exp \left(\frac{-\Omega}{kT} (P_b - \gamma_b \kappa) \right) \quad (2.2)$$

with

$$C_v^{eq}(P_b = 0, \kappa = 0) = \exp \left(-\frac{\epsilon_v - s_v T}{kT} \right) \quad (2.3)$$

The pressure P_b in the bubble is calculated using the Carnahan-Starling Equation of State [199] given as:

$$\frac{P_b V}{NkT} = (1 + \eta + \eta^2 - \eta^3) / (1 - \eta)^3$$

where η is the packing fraction given by the expression:

$$\eta = \frac{\pi N d^3}{6 V}$$

with d being the hard sphere diameter, calculated from the modified Buckingham potential as [200]:

$$diam = 4.45 \cdot 10^{-10} * \left[0.8542 - 0.03996 \ln \left(\frac{T}{231.2} \right) \right]$$

- Bubbles

The bubbles in the model are supposed to be and remain spherical. Each bubble is characterized by the position of its center, the total volume of the 0-cells included in the bubble, the total volume of the bubble, the gas content and the list of 1-cells forming the interface. For the analyses in this manuscript, we have considered the presence of gas in the

bubbles, but we do not consider gas in the solid. We can define a bubble entirely within a cell. For such a bubble, the volume of the 0-cells would be 0 and the spin of the cell containing the bubble would be 1.

2.2.2 Physical properties used in the model

The BEEP Model is formulated such that it explicitly relates to physical parameters and is not dependent on numerical parameters which are hard to relate to physics. Table 2.1 presents the physical parameters considered in the model with their values.

Parameter	Description	Expression/ Value
ϵ_v	Formation energy of vacancy [11, 65]	2.47 eV
k	Boltzmann constant	1.38×10^{-23} J/K
s_v	Excess entropy of vacancy formation	0 J/K
Ω	Volume of one UO ₂ site	40.9×10^{-30} m ³
D_U	Self-diffusion coefficient [201]	$D_U = D_v * C_v^{eq}(P_b = 0, \kappa = 0) * f$
γ_b	Surface tension at the solid-cavity interface	$\gamma_b = 0.41 * (0.85 - 1.4 * 10^{-4}(T - 273))$ J/m ²
D_s	Surface diffusion coefficient [202]	$D_s = 50 \exp\left(\frac{-4.67\text{eV}}{kT}\right)$ m ² /s
q	Region without gas atoms in Mikhlin's suppression term [203]	1.5×10^{-27} m ³

TABLE 2.1: Physical parameters used in the model.

The diffusion coefficient of vacancies, D_v , is related to the uranium tracer coefficient, D_U , via the following expression:

$$D_U = D_v * C_v^{eq}(P_b = 0, \kappa = 0) * f \quad (2.4)$$

where f is the correlation factor that expresses that the U atoms do not exactly follow random-path theory because of the substitutional type of their diffusion. For the analyses in this thesis, we have taken the value of $f = 1$. $C_v^{eq}(P_b = 0, \kappa = 0)$ is the concentration of vacancy (vacancy/site) at equilibrium in a solid limited by a flat surface and no external pressure, defined earlier in Eq.2.3. This relation supposes that D_U was measured when the concentration of vacancy was at equilibrium.

The volume self-diffusion coefficient, D_U , can be calculated using Matzke's relation [201]:

$$D_U = 6.5 * 10^{-5} \exp\left(\frac{-5.6\text{eV}}{kT}\right) \text{m}^2/\text{s} \quad (2.5)$$

2.3 Methodology adopted in the model

The model simulates micro-structure evolution with time by taking into account the various aspects of interaction between defects and bubbles such as the diffusion of defects and the update of bubble characteristics. A general algorithm adopted in the model is depicted in Fig.2.2.

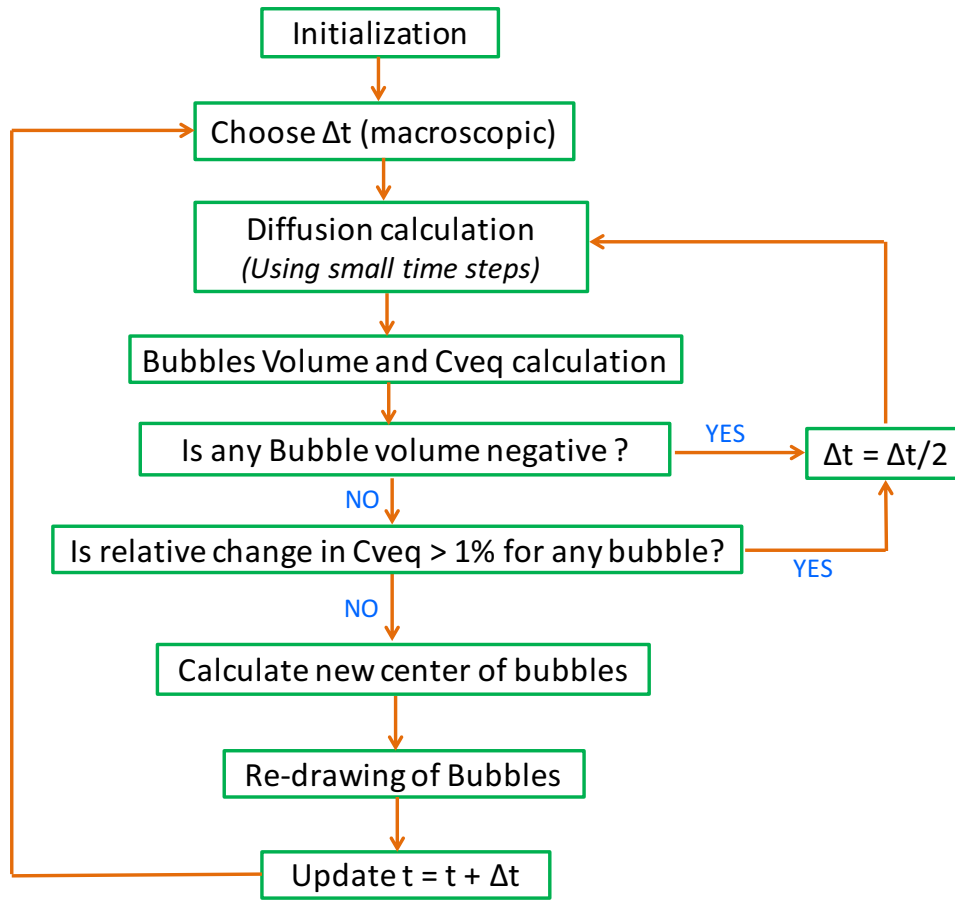


FIGURE 2.2: General algorithm adopted in the model

2.3.1 Initialization

The initial and boundary conditions as well as the physical properties are provided as input into the model. The initial representation can be viewed using the visualization application PARAVIEW [204]. In this manuscript, all the visualizations are represented in terms of RS , which is the solid ratio/fraction of a particular cell. $RS = 1$ (red region) means that the cell is completely solid and $RS = 0$ (black region) means the cell is completely void (cavity), with values of RS in between signifying an interface cell which is partly solid and partly cavity. Fig.2.3 illustrates a visualization in terms of RS . Here, the square domain is the solid bulk with two bubbles. The interface cells of the bubble-solid system can be seen distinctively.

2.3.2 Diffusion of point defects and crystal atoms

- For the 2-cells
The diffusion of defects is governed by the Fick's law. A defect balance equation is written for each 2-cell interacting with its neighbours. So the

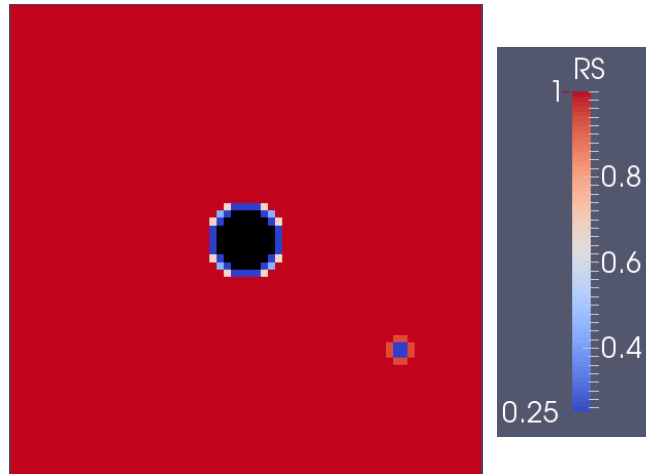


FIGURE 2.3: An example of a visualization in terms of RS using the PARAVIEW application.

defect balance equation is:

$$\frac{\partial C_v}{\partial t} = -\vec{\nabla} \cdot \vec{\phi}_v \quad (2.6)$$

Here $\vec{\phi}_v$ represents the flux of vacancies between 2-cells and is given as:

$$\vec{\phi}_v = -D_v \vec{\nabla} (C_v)$$

where D_v is the diffusion coefficient of vacancies.

- For the 1-cells, the atom balance equation is written as:

$$\frac{\partial C_a}{\partial t} = -\vec{\nabla} \cdot \vec{\phi}_a \quad (2.7)$$

The flux of atoms, $\vec{\phi}_a$, in theory, can occur through the flux of vacancies, gas in substitution or interstitials. However, in practice, since we consider only vacancies as diffusing species, exchanging with a 2-cell, the flux of atoms is a consequence of the flux of vacancies and can be determined as:

$$\vec{\phi}_a = -\vec{\phi}_v \quad (2.8)$$

The flux of atoms could also be along the interface (i.e. exchanging with another 1-cell) due to surface diffusion. In the model, the surface diffusion is not explicitly taken into account as a flux of atoms between two 1-cells. It has, however, been incorporated in the hypothesis about the shape of the bubbles being and remaining as spheres.

2.3.3 Space and Time Discretization

These diffusion equations are then discretized in space and time. There are several spatial schemes or stencils available for space discretization depending on the number or type of neighbours being used. For the present model, only the face neighbors have been taken into consideration using a 5-point stencil scheme in 2-D and 7-point stencil scheme in 3-D (Fig.2.4).

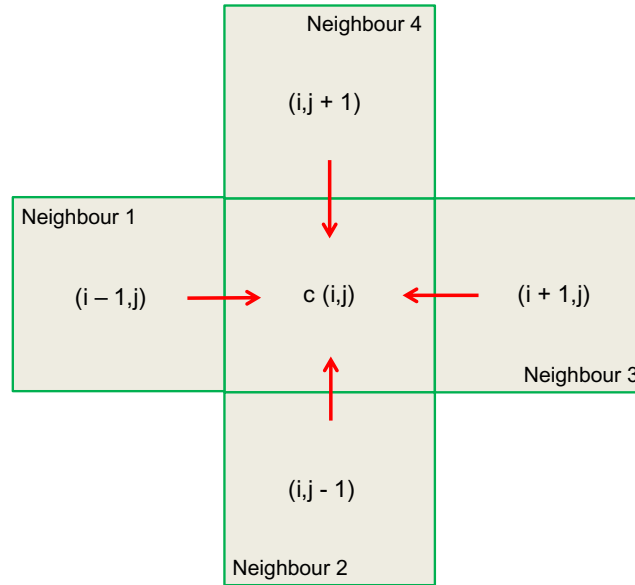


FIGURE 2.4: 5-point stencil scheme in 2-D for space discretization.

The evolution of vacancy concentration in the 2-cells can be evaluated using the expression:

$$\frac{\partial C_v(p)}{\partial t} = \sum_{\substack{n \in \text{face} \\ \text{neighbours}}} \frac{D_v}{h^2} [C_v(n) - C_v(p)] \quad (2.9)$$

here h is the grid size, p denotes the present cell and n denotes its neighbour cells. For a 1-cell, the evolution of the concentration of atoms is due to the fluxes of vacancies from its 2-cell neighbours. It can be represented as:

$$\frac{\partial C_a(p)}{\partial t} = - \sum_{\substack{n \in \text{2-cell} \\ \text{face neighbours}}} \frac{D_v}{h^2} [C_v(n) - C_v^{eq}(\kappa(p), P_b(p))] \quad (2.10)$$

where $\kappa(p)$ and $P_b(p)$ are the curvature and pressure of the bubble whose cell p is an interface cell.

Once the set of space-discretized equations is written, a set of ordinary differential equations is obtained. An Euler explicit scheme (forward difference in time) is then used for time discretization. For a solid cell p , the expression

for time discretization is:

$$C_v^{t+1}(p) = C_v^t(p) + \sum_{\substack{n \in \text{face} \\ \text{neighbours}}} \frac{\Delta t D_v}{h^2} [C_v^t(n) - C_v^t(p)] \quad (2.11)$$

where Δt is the time step for the calculation.

For an interface cell, the expression is analogous and is given as:

$$C_a^{t+1}(p) = C_a^t(p) - \sum_{\substack{n \in 2\text{-cell} \\ \text{face neighbours}}} \frac{\Delta t D_v}{h^2} [C_v^t(n) - C_v^{eq t}(\kappa(p), P_b(p))] \quad (2.12)$$

C_v^{eq} is considered constant with time during a time step. For this explicit scheme, Δt must not exceed the "von Neuman" limit (See Annex C). The advantage of this explicit scheme is its simplicity of implementation and the calculation of one time step. The drawback is that the maximum time step is very low. However, to overcome this limitation, an improvement can be incorporated to the method if the diffusion permanent state is expected to be reached before any large modification of the bubble takes place. Note that we use the term "large time step" or "macroscopic time step" for the time that includes an entire diffusion calculation and the update of the bubble. The diffusion calculation is done in several "small time steps", particularly in the case of Explicit method. As it is expected that within each large time step, the concentration of vacancies will eventually reach an equilibrium state for the diffusion problem, a check is kept on the inception of this permanent state. Once the relative change in the value of vacancy concentration is below a certain threshold for two small time steps, no further small time steps are taken and the next time step is taken as the jump to the prescribed large time step. This is possible and right because at this stage the vacancy fluxes are constant with time as well as the C_v in the 2-cell zones. Only the C_a in the 1-cell zones changes and they are just the integration of the negative of vacancy fluxes (see Eq.2.8) with time. A schematic explanation of the algorithm is depicted in Figure 2.5. Once the permanent state is reached at time t_c , the next time step is a leap to the prescribed delta time for that diffusion step. Incorporation of this algorithm allowed for faster calculation of the diffusion problem in the model.

2.3.4 Bubble volume calculation

After the vacancy diffusion process occurs and before the re-drawing of the bubble, the information that gives the total volume of the bubble lays in the preceding volume of the bubble and the change in the C_a (ΔC_a) of the 1-cells of the bubble. The new volume of the bubble can then be written as:

$$V_b^{new} = V_b^{old} - \sum_{\text{interface cells}} \Delta C_a * V_{cell} \quad (2.13)$$

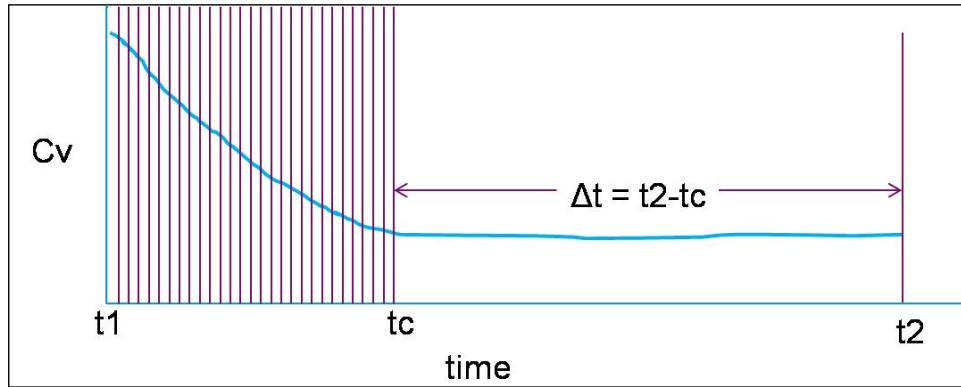


FIGURE 2.5: Schematic explanation of the algorithm adopted in Explicit Method

where $\sum_{interface\ cells} \Delta C_a * \frac{V_{cell}}{\Omega}$ is the total number of U atoms that filled the bubble because of the vacancy diffusion process during the macroscopic time step.

2.3.5 Determining the next center ("Target center") of bubble

If the flux of vacancies is not isotropic, the bubble is shifted from its position. In other words, the bubble moves. The direction of bubble movement depends on the direction of vacancy absorption or removal from the bubble surface. The new center of the bubble is calculated as the barycenter of voids (i.e., the 0-cells in the bubble and the void fraction $(1-RS=1-C_a)$ of the 1-cells). Since at each time step, the C_a values are modified during the diffusion process, the new (Target) centers of the bubbles are calculated accordingly. The variable "center of the bubble" is not directly over-written. Instead, a different variable "Target center" is updated and is used in the redrawing process of the bubble.

2.3.6 Re-drawing the bubble keeping the atom and volume balance

Once the new characteristics of the bubbles are updated, the list of interface cells of each bubble also has to be updated. This means that the spins of some cells may be changed and the $RS=C_a$ (solid ratio in the interface cells) are re-calculated as if the bubble was re-drawn geometrically. The value of RS for a particular 1-cell is calculated by recursively dividing the 1-cell into sub-grids. This is explained pictorially in Figure 2.6. When the minimum sub-grid size is attained, no more cell division can occur. At this point, the RS for the small sub-cell is calculated as the fraction of corners outside the bubble. In doing so, some error in the number of atoms is generated. This error adds up for every 1-cell each time the cell is updated and may grow with time. The yellow region in the figure is the solid region of the 1-cell as calculated by the algorithm. The dashed region shows the excess of atoms (lower region) and deficit of atoms (upper region) in the 1-cells during the re-drawing of the bubbles.

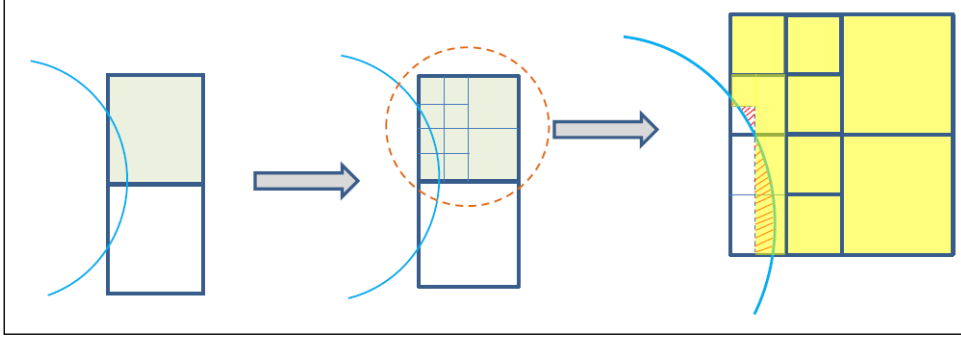


FIGURE 2.6: Description of cell division for calculating RS with the error generated in the atom balance

If the calculation of the new RS were exact for each 1-cell of the bubble, and if we kept track of the ΔRS ($\Delta RS = RS^{new} - RS^{old}$) that happened during the re-drawing process, the sum of those ΔRS for one bubble would be zero. No atom would be added or lost. In reality, however, the sum of ΔRS over all the interface cells of a bubble is not zero because of numerical errors. As C_a is reinitialized as $C_a = RS$ for each 1-cell, this is detrimental for the atom balance if the total number of atoms could only be known through the C_a field. To take this into consideration, we have introduced two new variables attached to each bubble: Δa and ΔV_{comp} .

During the redrawing process, when an interface cell is checked, 2 cases arise:

- If the change of spin is $1 \rightarrow 1$ or $0 \rightarrow 1$ or $1 \rightarrow 0$, C_a (new and old) identifies with RS (new and old).
- If the change of spin is $1 \rightarrow 2$ or $2 \rightarrow 1$, C_a (new or old) do not identify exactly with $RS = 1$ for the 2-cell (solid cell). Instead, $C_a^{new} = 1 - C_v^{eq}(bubble)$ if $RS^{new} = 1$ or $C_a^{old} = 1 - C_v$ if $RS^{old} = 1$.

Δa is defined as the excess of atoms numerically introduced in one bubble since the beginning of the calculation because of the successive re-drawings. Δa is updated at each changing of a 1-cell during the re-drawing process of the bubble and its value is updated as:

$$\Delta a = \Delta a + (C_a^{new} - C_a^{old}) \frac{V_{cell}}{\Omega} \quad (2.14)$$

ΔV_{comp} is updated when a 2-cell is involved in the changing. It is updated as:

$$\begin{aligned} \Delta V_{comp} &= \Delta V_{comp} - (1 - C_a^{old}) * V_{cell} && \text{for } 2 \rightarrow 1 \\ \Delta V_{comp} &= \Delta V_{comp} + (1 - C_a^{new}) * V_{cell} && \text{for } 1 \rightarrow 2 \end{aligned}$$

These definitions of Δa and ΔV_{comp} insure Eq.2.15 is always satisfied.

$$\sum_{interface\ cells} \Delta RS * V_{cell} = \Delta(\Delta a \Omega + \Delta V_{comp}) \quad (2.15)$$

Using Δa and ΔV_{comp} always verifies the following expression for the volume of a bubble:

$$V_b = V_b^{(0-cells)} + \sum_{interface\ cells} (1 - C_a) * V_{cell} + \Delta a \Omega + \Delta V_{comp} \quad (2.16)$$

here $V_b^{(0-cells)}$ is the volume in the 0-cells of the bubble, the second term is the volume added in the 1-cells of the bubble and Δa and ΔV_{comp} are as defined above.

In practice, Eq.2.16 is used for the calculation of the new bubble volume. During a macroscopic time step, just after the diffusion process, the C_a are changed whereas Δa and ΔV_{comp} are unchanged. So, using Eq.2.16 is strictly equivalent to using Eq.2.13. During the re-drawing process, both the C_a as well as the Δa and ΔV_{comp} are changed but compensate each other.

The total number of atoms in the domain can be calculated at any step of the algorithm by the following expression:

$$Total\ number\ of\ atoms = \sum_{cells} C_a \frac{V_{cell}}{\Omega} - \sum_{bubbles} \Delta a$$

This number should remain constant throughout the calculation. It was written to an output file and checked during the calculation and it was found that the variation in the total number of atoms was extremely low (of the order of 10^{-14}). This proves that the atom balance is respected in the code throughout and provides a verification of the proper functioning of the code.

Moreover, using Eq.2.13 or Eq.2.16 to calculate the new volume of the bubble ensures a good accuracy in the calculation of the volume even if a high accuracy for the RS calculation is not demanded, which spares computation time.

Another difficulty stems from the possible coalescence of bubbles. The algorithm that deals with the coalescence of 2 bubbles is valid when their surfaces just touch, exactly when two 1-cells belonging to 2 different bubbles become neighbours, not when 2 bubble surfaces cross. The re-drawing algorithm itself considers in turn every 1-cell of the former bubble, and checks the new spin of this cell using the new center of the bubble and its new radius. If the new center of the bubble is too far from the previous , all the 1-cells could be switched to 2-cells and the algorithm would just stop with an empty 1-cell list. In practice, a target center is calculated. If it is too far (distance > cell size) from the previous center, the re-drawing is done several times, each time with a new center on the path between the former center and the target center. Within this procedure, any coalescence event can be detected and processed successfully and no bubble loses its 1-cell from the 1-cell list.

Once the re-drawing process is done for each bubble, a new time step can begin with a new diffusion calculation.

2.3.7 Random movement of the bubbles

To incorporate the random movement of bubbles, the bubble diffusion coefficient is chosen depending on the mechanism adopted (volume or surface mechanism). For the volume diffusion mechanism, the bubble diffusion coefficient is expressed as:

$$D_b^{vol} = \frac{3\Omega}{4\pi r_b^3} D_U \exp \left[\frac{-\Omega}{kT} (P_b - \gamma_b \kappa) \right] \quad (2.17)$$

where the value of D_U , the volume self-diffusion coefficient is taken from Matzke [201] as defined in Eq.2.5. Similarly for the surface diffusion mechanism, the bubble diffusion coefficient is expressed as:

$$D_b^{surf} = \frac{3}{2\pi} \frac{\Omega^{4/3}}{r_b^4} D_s \left[1 - \frac{q}{V(r_b)} \right]^{N(r_b)} \quad (2.18)$$

where the value of D_s , is taken from Matzke [202]. The mechanisms of random movement of bubbles and their expressions along with further analyses based on them are discussed later in Chapter 4.

In 2-D, the most probable diffusion distance between the position of the bubble at time $t = 0$ and its position at Δt is given by the expression [205, 206]:

$$d = \sqrt{4D_b\Delta t} \quad (2.19)$$

where D_b is the bubble diffusion coefficient and Δt is the elapsed time. We then choose a direction of movement by randomly generating an angle, ϕ , such that $\phi \in [0, 2\pi[$. However, we want the diffusion distance for a single jump to not exceed the length of one cell (defined as 'h' in the model). So, in order to restrict our jump distance to h, we impose another limit on the time step that must not exceed:

$$\Delta t = \frac{h^2}{4D_b}$$

The random displacement (d, ϕ) of the bubble is added to the directed displacement calculated in section 2.3.5 to determine the target center of the bubble. The bubble is then re-drawn in the way described earlier.

2.4 Parallelizing the BEEP Model

The goal of parallelizing a model is to reduce the elapsed time, carry out larger computations and exploit the parallelism of modern processor architectures such as multi-core and multi-threading. However, the scalability can be reduced in some cases and the reason for this could be two-fold. Firstly, if there are enough elements used in the calculation, not all of these elements can be stored in the cache memory. The processor, thus, needs to access the RAM (main memory), which is slower and reduces the ability for parallelization. Secondly, within the cache memory, the elements are stored in cache

lines. Once a processor is accessing a particular cache line, this cache line is rendered unavailable for the other processors. If a cache line contains elements required by different processors, then the processor which accesses it first can use it for modification, whereas, the other processors have to wait until the cache line is available. This creates sort of a "data race" among the processors and affects the parallelization of the code, sometimes making it even slower than the serial code. So, in order to avoid the scalability issue some method needs to be adopted while implementing parallelization in the model.

2.4.1 Using OpenMP

At the beginning of introducing parallelization to the BEEP Model, OpenMP was used as the parallelization scheme. OpenMP is a multi-threaded model with shared memory. Threads communicate with each other by sharing variables. OpenMP is a library comprising a set of compiler guidelines and routines for parallel application development. The sharing of unwanted variables can, however, cause competitive situations (like data race mentioned earlier). It was observed that the scalability deteriorated if several processors were used. This was because, although several processors were used, since they were sharing memory, not all could access the shared variables simultaneously and lead to stagnation of the scalability irrespective of the large number of processors.

2.4.2 Implementing sub-domains

In order to minimize the access to the slower main memory and to avoid the data race among the processors, the large domain was divided into smaller sub-domains. The domain can be divided in several ways both in 2-D and 3-D. One way of subdividing the domain along the x-axis is represented in Figure 2.7. Here, the large domain can be divided into 2 sub-domains at the red line. Similarly, it can be divided into 4 sub-domains by dividing at the blue and red lines, and into 8 sub-domains by dividing at each of the green, blue and red lines. Dividing the domain into sub-domains allows more elements of the sub-domain to be accommodated in the cache memory, thus reducing the access to the slower main memory. Moreover, one processor is assigned per sub-domain in order to avoid the data race among the processors.

To test the scalability using the sub-domains, a large 3-D domain was considered with the size 752 x 128 x 128 cells. Firstly, the calculation was carried out in the entire domain with one, two, four and eight processors and then the sub-domains were incorporated into the test case. With the sub-domain concept, the test was carried out for one domain, two, four and eight sub-domains. OpenMP was used for the parallelization process. The test case carried out a simple diffusion calculation to calculate the new vacancy concentration of each cell with respect to its 6 neighbours in the domain. However, as the vacancy concentration was initialized as a constant (2×10^6) throughout

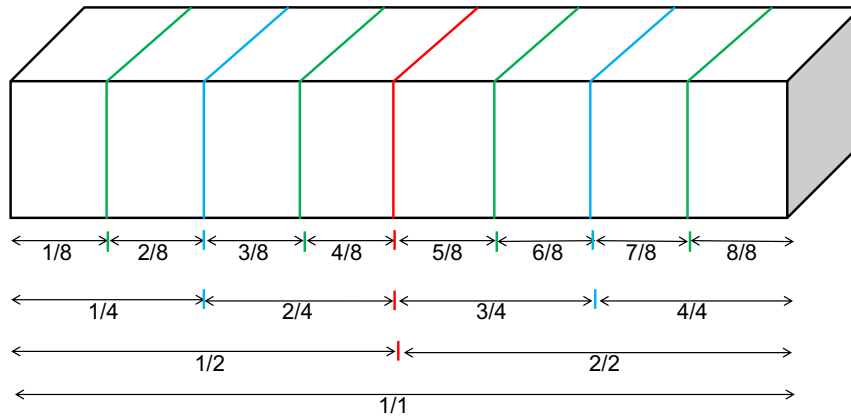


FIGURE 2.7: Division of a large domain into smaller sub-domains

the domain, there will be no change in the values of the vacancy concentration during the calculation. The same calculation was iterated 1000 times to allow longer calculation time to test the impact of sub-domains. The calculation was done on an Intel(R) Xeon(R) E5620 machine, having 4 cores and 8 processors operating at 2.4 Ghz. Fig.2.8 represents the scaling for the cases with and without the sub-domains. We designate the ratio of computation time for one domain with one processor to sub-domains with different number of processors as the "Time Ratio".

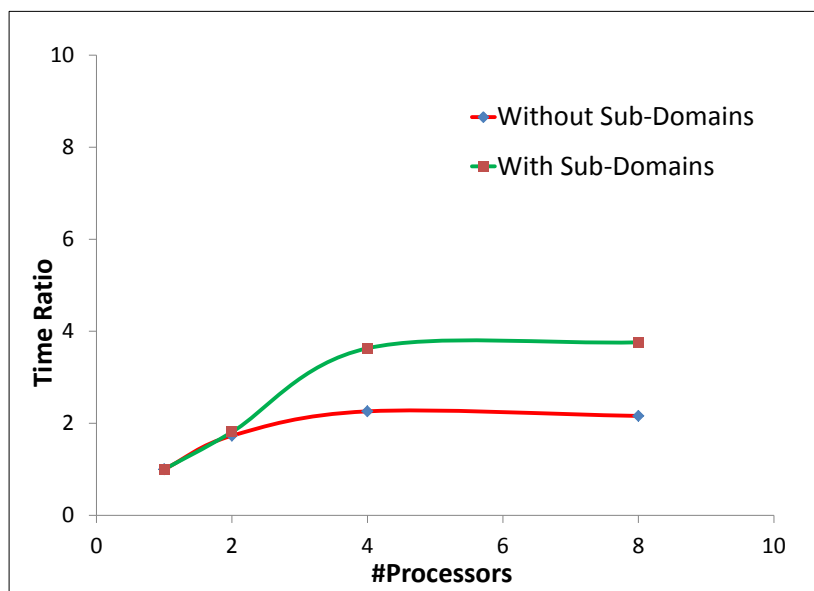


FIGURE 2.8: Speed-up (Time Ratio) using sub-domains.

An enhanced scalability was observed for the same case with the sub-domains as compared to without the sub-domains. However, the scaling still stagnated with more than four sub-domains. This test showed that using sub-domains can provide better scalability than before, but the shared memory

concept of OpenMP affects the usage of several processors. To counter this problem, we next tried the MPI scheme of parallelization. Moreover, in this test case, the sub-domains did not transfer data among each other. It did not affect the case here, as no value changed during the calculation, however, in a practical case, the changes in one sub-domain will impact the other sub-domains and thus data need to be transferred among the sub-domains. This issue was also overcome in the usage of MPI Parallelization which is discussed next.

2.4.3 Message Passing Interface (MPI)

For several processes to be done together, coordination is required. Message Passing Interface (MPI) is a library which allows process coordination by using the message-passing concept. MPI uses a distributed memory paradigm.

The BEEP Model was parallelized for obtaining better computation times using MPI. More precisely, we used MPI Parallelization to accelerate the computation of the diffusion process. To do so, the domain is divided into smaller sub-domains surrounded by ghost slices (dashed), as shown in Fig.2.9.

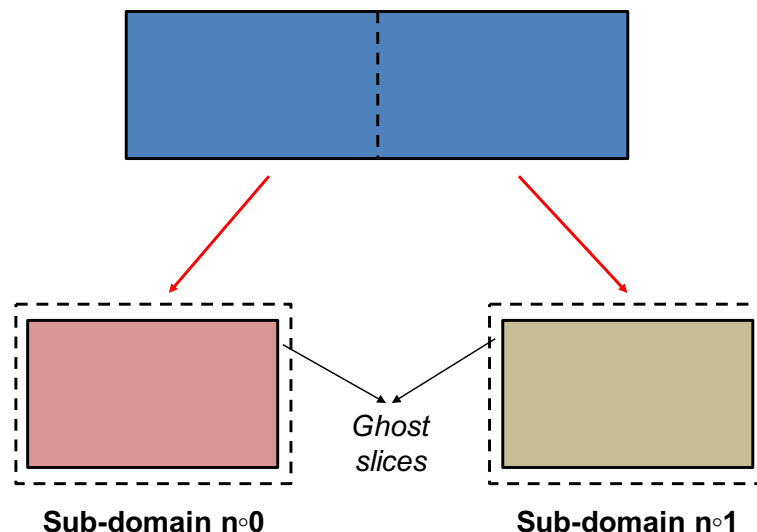


FIGURE 2.9: Sub-domains and ghost slices.

The same code is run on different processors, except for certain actions which are done or not depending on the processor. Processor $n^{\circ}0$ will process the diffusion calculation in subdomain 0 and the updating of the bubbles in the whole domain. Processor $n^{\circ}i$ will process the diffusion calculation on sub-domain $n^{\circ}i$. However, processor $n^{\circ}i$ needs information from processors $n^{\circ}i-1$ and $i+1$ for the diffusion calculation. Collection of this information is the role of the ghost slices.

So, during the calculation of the diffusion, before each diffusion sub-time step, data are passed among the sub-domains by using the MPI SEND and RECEIVE commands and placed in the ghost slices, as shown in Fig.2.10.

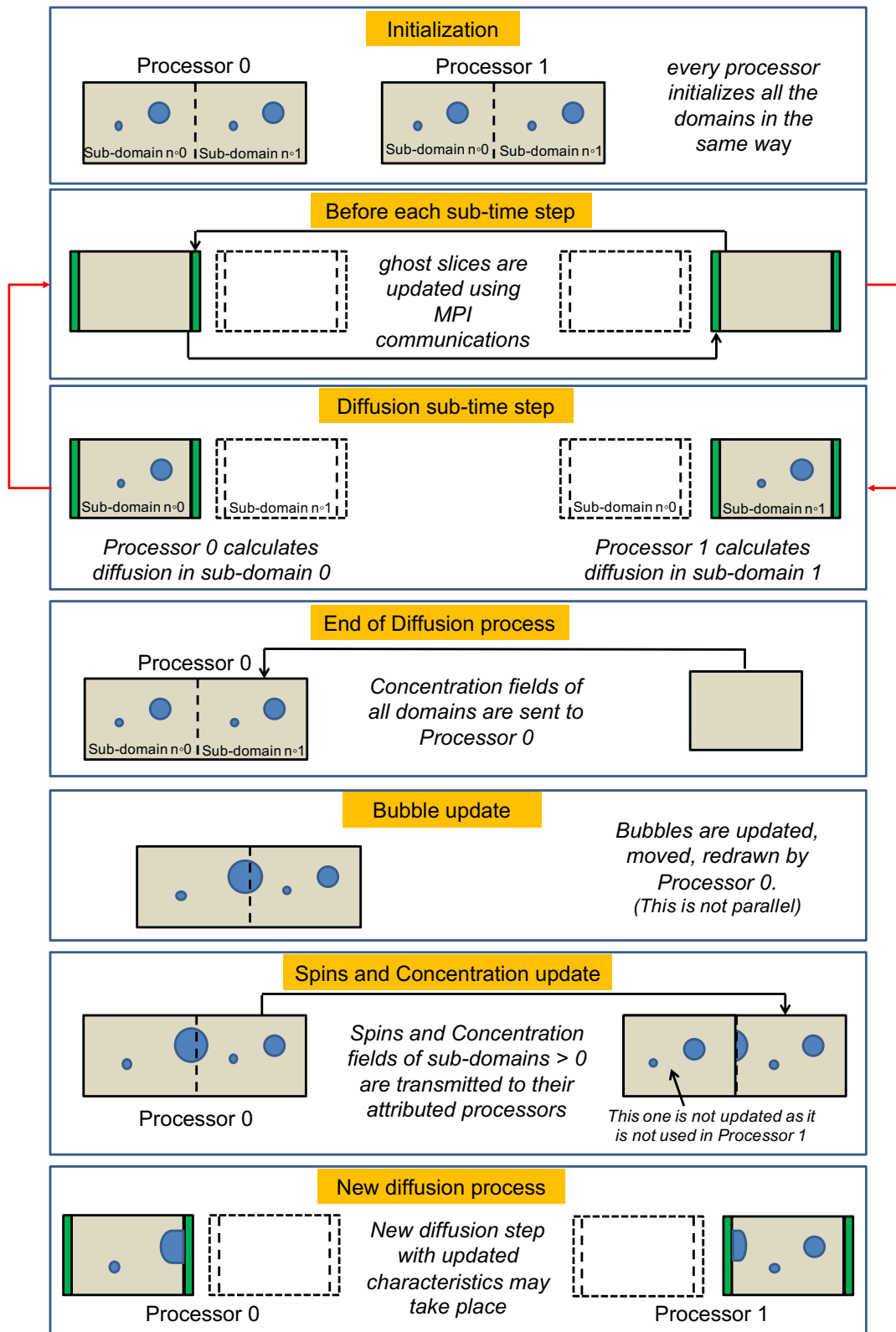


FIGURE 2.10: Algorithm for MPI Parallelization.

At the end of the diffusion calculation, all the processor i send the information about sub-domain i to the processor $n^{\circ}0$. Processor 0 updates the bubble and does the redrawing process, which affects every sub-domain. Then again, through SEND and RECEIVE commands, the information about sub-domain i is transmitted to processor $n^{\circ}i$ and a new diffusion calculation may be done.

To test the implementation of MPI along with the communications between the sub-domains, we considered a large 3-D domain of size $3000 \times 64 \times 32$ cells = $6144000 = 6.144 \times 10^6$ degrees of freedom (= variables to be calculated). So, it is a long box along the x-axis, and a concentration to be calculated in each cell, with periodic conditions on all box boundaries. The domain is divided into sub-domains $n^{\circ}0$ to $n^{\circ}n$ along the x-axis of the box. So the dimensions of the sub-domains along the y and z axis remained 64×32 . Each sub-domain had the same size as the others.

Similar to the test case for sub-domains, the diffusion calculation was carried out to determine the new vacancy concentration of each cell from its previous concentration and that of its 6 neighbours. However, here the calculation was iterated 10000 times. Moreover, the communications for the cells at the border of each sub-domain was done at each step. Also, at every 1000 steps, an update of the concentrations of sub-domains $n^{\circ}1$ to $n^{\circ}n$ was done at the processor 0 from each of the processor $n^{\circ}1$ to $n^{\circ}n$, where the concentration have been calculated. So every 1000 steps, the entire domain concentrations were available on processor 0. Indeed, in a real calculation with bubbles, the bubbles are updated by processor $n^{\circ}0$. So, at this stage of the algorithm, processor $n^{\circ}0$ needs to know the entire domain concentration field. That is why this communication was added (even though there were no bubbles here) to test the computation time. The machine used for the calculations was from a cluster of machines comprising Intel Xeon E5-2660 v3 with 20 processors operating at 2.6 Ghz. Up to 120 processors/ sub-domains were used to see the computation times and scalability using MPI. The results obtained are presented in Table 2.2.

Number of processors (and of sub-domains)	Elapsed time (s)	Total CPU time (s)	Speed-up
1	5840	5837	1
20	330	6479	17.7
40	181	7120	32.3
80	108	8321	54.1
120	80	9200	73.0

TABLE 2.2: Computation time and speed up for test case using MPI and communications between sub-domains.

Implementing MPI for parallelization allowed fast computation times for the case tested. Fig.2.11 shows the speed up with different number of processors used in the test case. It can be seen from the figure that unlike with OpenMP parallelization, and at least up to 120 processors, we do not reach a plateau for the speed up in function of the number of processors.

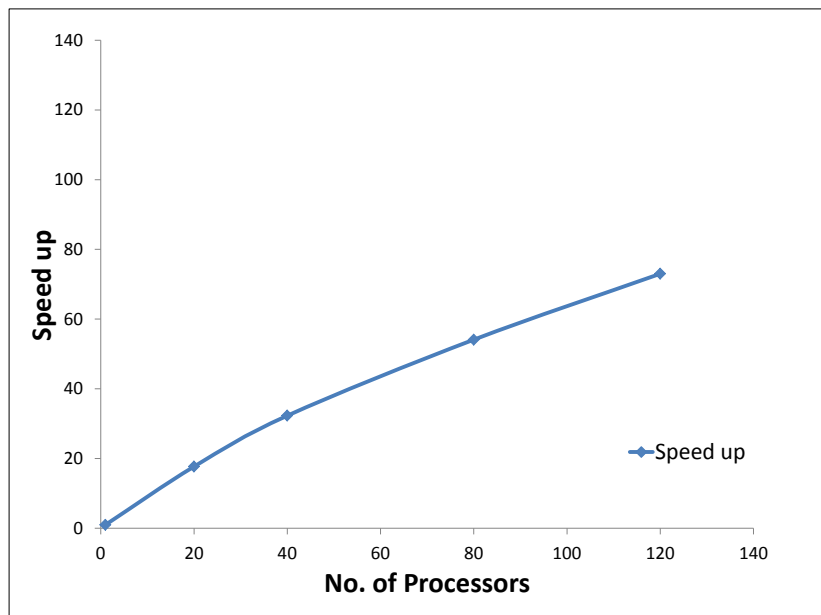


FIGURE 2.11: Speed up for different number of processors using MPI Parallelization.

The computation time reduced significantly and a better scalability was obtained during parallelization of the model. That is why we finally chose to use MPI parallelization and to use types of variables that were compatible with this approach.

2.5 Testing the Model

2.5.1 Crystal atom balance

The process of re-drawing of bubbles is done using a recursive procedure to identify the new interface cells and their new solid ratio ($RS = C_a$). This can be done more or less precisely, but a high precision costs computation time. As explained before, we used a procedure that keeps track of any error balance and avoid errors to cumulate with the time steps. Due to this procedure, the relative error in the crystal atom balance in the model is less than $4.5 \cdot 10^{-15}$ during the entire calculation.

2.5.2 Verification for calculation of solid ratio "RS"

The method to calculate the solid ratio, "RS", of a cell checks the particular cell for the number of its corners outside the bubble. For 2-D, if all 4 corners of a cell are outside the bubble, i.e., in the solid region, then $RS = 1$. If less than 4 corners are outside the bubble, the method divides the cell into 4 equal sub-cells (as shown in Fig.2.6) and checks each cell for the corners. This is done while the size of the sub-cells remains greater than a pre-defined fraction of

the grid size. This procedure works perfectly fine for bubbles which are large (usually larger than one grid). However, there can be scenarios where this procedure may fail. Such cases are usually with bubbles that are contained entirely within a cell. These cases are different since we cannot apply the procedure mentioned above to calculate RS . When a bubble is contained entirely within a cell, all the four corners of the cell would be outside the bubble and it would be considered a 2-cell (solid) in the model, which is not true as the cell should be a 1-cell (interface). So, special conditions were set for such scenarios in the model. To test if the model calculates correct values of RS for such scenarios, different bubble-1-cell configurations were checked and the analytical values were compared with the ones obtained from the model. Six different configurations were considered and for each case, RS of the 1-cell containing the center of the bubble was calculated. The details of calculating RS for the six configurations is presented in Annex D.

Table 2.3 shows the analytical and numerical values of RS for the different cases and the relative error in them¹. The numerical values of RS are in good agreement with the analytical values with the relative error never exceeding 10^{-7} .

CASE	RS (numerical)	RS (analytical)	Relative error
Case 1	0.214601926	0.214601836	$4.20 \cdot 10^{-7}$
Case 2	0.803650515	0.803650459	$7.00 \cdot 10^{-8}$
Case 3	0.07645846	0.076458468	$1.11 \cdot 10^{-7}$
Case 4	0.650324913	0.650324907	$9.23 \cdot 10^{-9}$
Case 5	0.889553392	0.889553383	$1.01 \cdot 10^{-8}$
Case 6	0.541226738 (0.326749616)*	0.541226713	$4.58 \cdot 10^{-8}$

TABLE 2.3: Analytical vs Numerical calculation of RS .

2.5.3 Verification for diffusion calculation

In order to verify the diffusion calculation in the model, a test was carried out in which the vacancies with an initial sinusoidal concentration profile were made to diffuse in the solid and the results obtained numerically were compared with the analytical results. The diffusion of vacancies in the solid follow the Fick's second law which is described by the equation:

$$\frac{\partial C_v(x, t)}{\partial t} = D_v \frac{\partial^2 C_v}{\partial x^2}$$

with

$$C_v(x, t = 0) = \sin\left(\frac{2\pi n}{a}x\right)$$

¹* This is the value of RS for the cell with the bubble center, calculated from the model.

An analytical solution of the above equation for a sinusoidal vacancy concentration profile can be obtained as:

$$C_v(x, t) = \exp\left(-\left(\frac{2\pi n}{a}\right)^2 D_v t\right) \sin\left(\frac{2\pi n}{a} x\right)$$

For the model, an initial concentration of vacancies was provided as a sinusoidal profile. A rectangular domain of size 128nm*64nm was taken with a grid size of 4 nm. Periodic boundary condition was imposed at all the boundaries. No bubbles were considered within the box for the test. One thing to note here is that this verification test is purely mathematical in the sense that $C_v(x, t)$ can take negative values (due to the sinusoidal profile).

The time evolution of vacancy concentration along the length of the domain was analyzed. For $n = 2$, the numerical and analytical solution of the vacancy concentration along the domain at various times is presented in Fig.2.12.

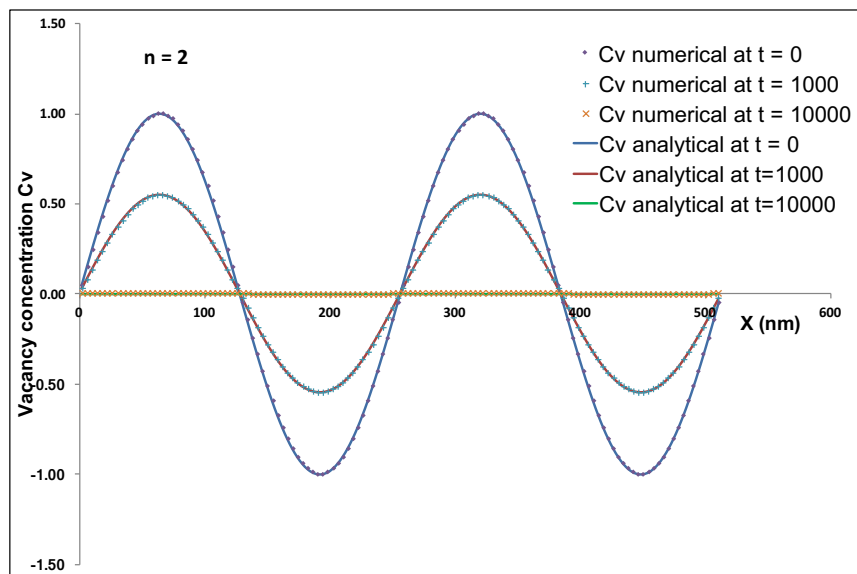


FIGURE 2.12: Numerical vs Analytical values for vacancy concentration.

As expected, with time the vacancies diffuse in the solid and the concentration profile becomes flatter and tends to zero with time. We defined the error as:

$$error = \sqrt{\frac{\sum_N \left(C_v^{analytic} - C_v^{num}\right)^2}{N}} \quad (2.20)$$

where N is the number of cells in the domain. This error never exceeds $4.06 \cdot 10^{-4}$ in the calculation. This verifies that the diffusion calculation in the model is carried out with good accuracy. Annex E shows that the order of convergence for the numerical method used (2 for space and 1 for time) is also checked.

2.5.4 Verification of particular functionalities of BEEP Model

In order to test the capability of the model to simulate the mechanisms related to fission gas bubble behaviour, some tests are carried out in 2-D. The simulation domain is a box of 64 x 64 cells. The grid size is taken as 4 nm, so the physical domain is a 256nm*256nm size box. The same domain has been adopted for all the cases discussed in this section. The bubble(s) are included in the domain box with size and number of bubbles depending on the requirements of the test case. The isothermal annealing temperature is taken as 1800°C. The physical properties used in the analysis are presented in Table 2.4. The following phenomena are modelled using the BEEP model.

Parameter	Description	Value
h	Grid size	4 nm
D_U	Matzke's self-diffusion coefficient	$1.62 \cdot 10^{-18} \text{ m}^2/\text{s}$
D_v	Vacancy diffusion coefficient	$1.62 \cdot 10^{-12} \text{ m}^2/\text{s}$
T	Isothermal annealing temperature	1800°C
kT	Energy term	$2.86 \cdot 10^{-20} \text{ J}$
γ_b	Surface tension at the solid-void interface	0.24518 J/m ²

TABLE 2.4: Quantities used in the model for the cases of coalescence and vanishing of bubbles at $T = 1800^\circ\text{C}$.

Coalescence of two bubbles

Due to bubble growth and migration, coalescence between two or more bubbles can occur in the grain. Coalescence leads to the overall coarsening of the bubbles but also decreases the number density of bubbles within the grain. In the presence of supersaturation of vacancies in the solid, the over-pressurized bubbles trap the vacancies in order to reduce their inner pressure. In doing so, the bubbles grow and the ones closer to each other may coalesce, forming bigger bubbles in the process. To test the phenomenon of coalescence of two bubbles, the bubbles are modeled with the properties mentioned in Table 2.5.

Bubble ID	Radius (nm)	Pressure (Pa)
1	12.1	28.53
2	5.9	$2.85 \cdot 10^7$

TABLE 2.5: Properties of bubbles for coalescence test.

The initial concentration of vacancies in the solid region is provided as high as $C_v^{ini} = 10^{-2}$ so that coalescence can occur quickly as the two bubbles will trap vacancies and grow. The criteria for coalescence of two bubbles is that a 1-cell of a bubble should be an immediate neighbour of a 1-cell of the other bubble. When this condition is satisfied, the two bubbles coalesce into one bigger bubble. During coalescence, the volume and gas content of the

resulting bubble is the sum of volume and gas content of the two bubbles. The center of the new bubble is the barycenter (weighted by the volume) of the centers of the two coalescing bubbles. The simulation is carried out for about 12 s of experiment time. The situation before and after annealing is seen using Paraview [204] and is represented in terms of RS , the solid fraction of a cell (Fig.2.13).

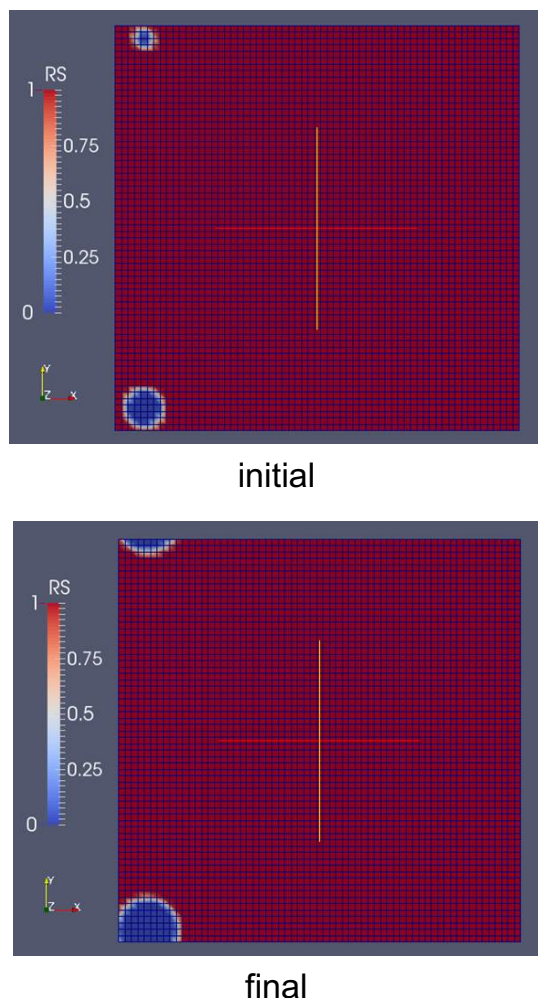


FIGURE 2.13: Coalescence of 2 bubbles, at time $t = 0$ and after annealing at $t = 12\text{s}$ of simulation time.

Coalescence occurred between the two bubbles forming a single bubble of radius 19.7 nm. The pressure within the new bubble is $2.50 \cdot 10^6$ Pa. The positions of the two bubbles were chosen as such to test the periodicity condition at the boundaries, which can be seen to be working as expected.

Vanishing of a bubble in the presence of a large bubble

In the case of empty bubbles with different sizes, the smaller bubble in the vicinity of a larger bubble decreases further in size and the larger bubble continues to grow further at the expense of the small bubble. This phenomenon is known as Ostwald Ripening. The small bubble may even vanish during the

process. To simulate the phenomenon of Ostwald Ripening in the model, two bubbles are modeled with different sizes and are provided with a very large volume per atom of gas (V_{at}) as 10^6 nm^3 , in order to have a very low pressure, almost to render the bubbles as empty. The bubble properties are mentioned in Table 2.6.

Bubble ID	Radius (nm)	Pressure (Pa)
1	20.0	28.53
2	5.0	28.53

TABLE 2.6: Properties of bubbles for vanishing test.

The initial vacancy concentration in the solid is taken as $C_v^{ini} = 1.04 \cdot 10^{-6}$, which is of the same order of magnitude as the two C_v^{eq} at the interfaces of the two bubbles. The algorithm adopted for vanishing of a bubble is that if the volume of a bubble gets less than a limit volume, the bubble is removed from the lattice and replaced by an equivalent number of vacancies. This limit volume is taken as 3% of the volume of a cell. The idea for this order of magnitude is that, in the model, each site represents a UO_2 atom. This site, which is a cuboid, has 26 neighbour sites. So, a vacancy needs 26 sites around it to be a vacancy and thus, the concentration of vacancies cannot exceed $\frac{1}{27} \approx 3.7\%$. The simulation is carried out for 10 minutes of experiment time. The situation before and after the diffusion is seen using Paraview and is represented in terms of RS , the solid fraction of a cell (Fig.2.14).

As expected, the small bubble vanishes and the big bubble grows to have a new radius of 20.6 nm. The evolution of the volumes of the big bubble and the small bubble with time are depicted in Figure 2.15.

It can be observed through the figure that the volume of the small bubble decreases down to the limit volume (1.92 nm^3) and then the bubble vanishes. The big bubble grows during this time at the expense of the small bubble. The saturation in the volume of the big bubble near the end indicates the vanishing of the small bubble at that time.

2.5.5 Verification for bubble movement

As discussed earlier, a pressurized bubble will move up in a vacancy concentration gradient by trapping vacancies emitted by a free surface at lower pressure or higher curvature. In order to verify that the bubble movement simulated by the model is accurate, we carry out a test for the bubble movement in a vacancy concentration gradient and compare the velocity of the bubble to the theoretical value obtained from literature (See Annex F). For the test, we consider a domain of $128\text{nm} \times 32\text{nm}$ with a grid size of 4 nm. We consider two exterior regions, Region 1 and Region 2, with width 1 nm and 255 nm, respectively, on both ends of the domain box and a bubble of radius 7.15 nm within the box. In the model, the interfaces solid-Region 1 and solid-Region 2 are dealt with exactly as the solid-bubble interface. This means that a concentration C_a of the crystal atoms is calculated at the interface cells and the surface can move accordingly. The only difference with the bubble surface is

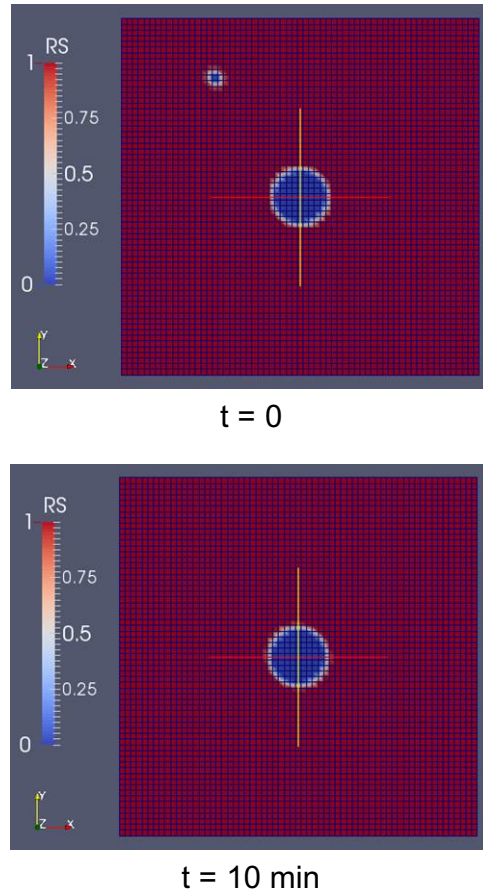


FIGURE 2.14: Vanishing of a bubble in the presence of a larger bubble, at time $t=0$ and after diffusion at $t=10$ min of experiment time

that this surface remains flat. We provide periodic boundary condition on the top and bottom and symmetric condition on the right and left boundaries.

We imposed constant pressures, P_1 and P_2 , in the two regions to maintain a constant vacancy gradient in the solid throughout the duration of the test.² The properties of the different regions and the bubble for the test are presented in Table 2.7. A linear profile for initial vacancy concentration is provided. The test is carried out for a simulated time of ~ 275 hours. The evolution of the bubble with time is depicted in Fig.2.16 in terms of RS which is the solid fraction/ratio in a cell. The figure shows that the bubble moves towards the Region 2 by trapping vacancies which are emitted by the surface of Region 2, and by emitting vacancies towards the Region 1 which traps the vacancies arriving at its surface. The bubble also grows by trapping the vacancies. In the meanwhile, Region 2 reduces in size due to the loss of vacancies from its surface and the contrary for Region 1.

²Note that here, the solid moves due to the vacancy flux (Nabarro-Herring creep) only. However, as P_1 and P_2 are different, they should induce a resulting effect that would shift the solid much more quickly towards the right, if the solid is not somehow held in another way. Here, we can imagine that the solid is a section of a very large and thin tube, with P_1 inside the tube and P_2 outside the tube.

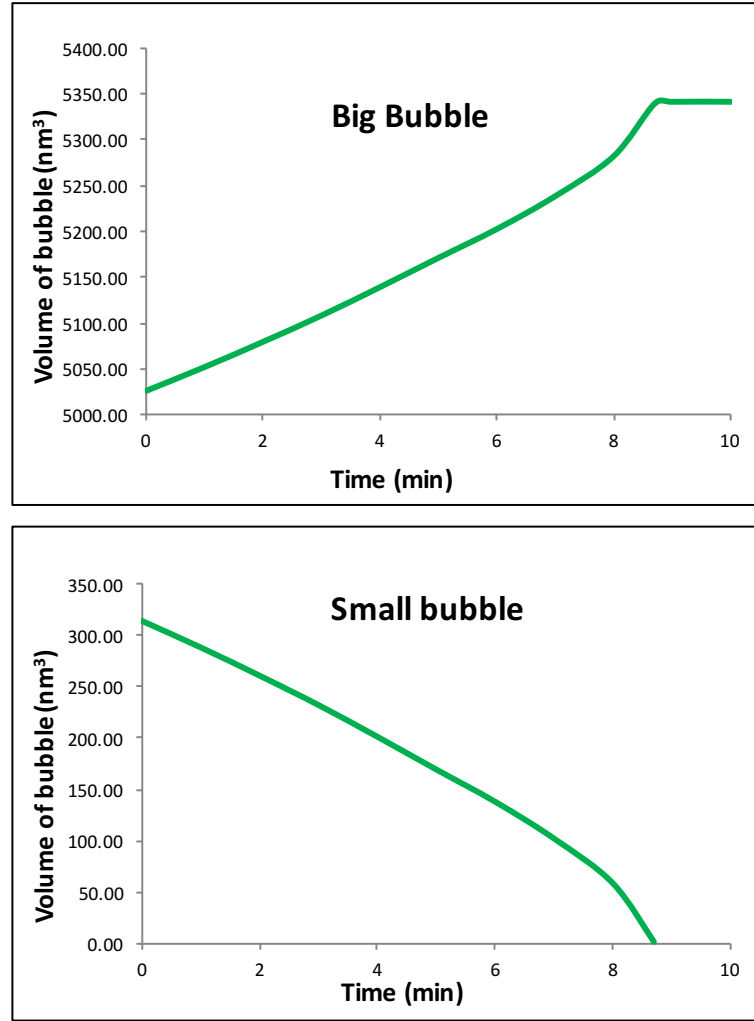


FIGURE 2.15: Evolution of volume of the small and big bubble with the experiment time.

The bubble can be seen to move up in the vacancy concentration gradient as expected. We compare the numerically calculated velocity of the bubble to the theoretical value. The velocity of a bubble moving in a vacancy concentration gradient in 2-D is given as:

$$\vec{v}_b = 2D_v \nabla \cdot C_v \quad (2.21)$$

where, D_v is the vacancy diffusion coefficient and $\nabla \cdot C_v$ is the vacancy concentration gradient (see Annex F).

Fig.2.17 shows the theoretical as well as the calculated (numerically) values of velocity as a function of time. The theoretical value of velocity is a constant since we assume/impose a constant gradient of vacancy concentration. It can be seen from the figure that the numerically calculated value of bubble velocity is in quite good agreement with the theoretical value considering that no adjustment was made to obtain the numerical value. Moreover, the numerical velocity tends to the theoretical one when the grid is refined (from $h = 4$ nm to $h = 2$ nm).

Type	Coordinate of center	Initial width/ Radius (nm)	Imposed pressure (Pa)
Region 1	(0,0)	1	$9.19 \cdot 10^9$ (P1)
Region 2	(512,0)	255	$9.04 \cdot 10^4$ (P2)
Bubble	(16,64)	7.15	-

TABLE 2.7: Conditions used in the model.

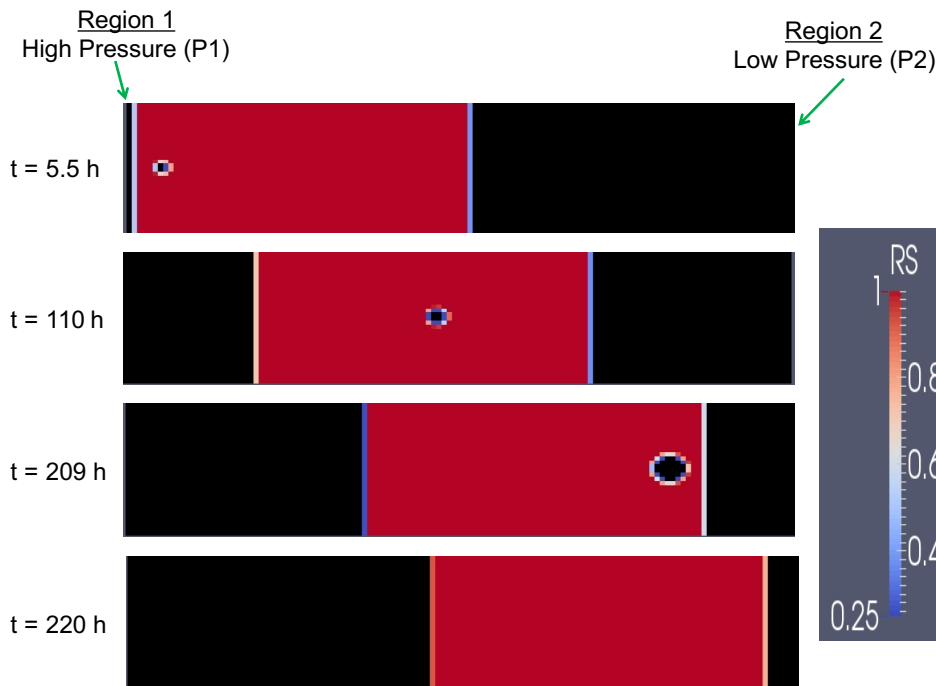


FIGURE 2.16: Bubble movement and growth in a vacancy concentration gradient.

2.6 Technical note on the exterior region ("Flat bubble")

In the section for the verification of the bubble movement, we talked about the two exterior regions. In the BEEP Model, the external regions are modelled just like the bubbles, only with the difference that the curvature of these bubbles is zero, i.e., they remain flat. The external regions in the model are, thus, also called as "Flat bubbles". They have all the characteristics of the intra-granular bubbles like the pressure, volume, gas content and the list of 1-cells. The center of the flat bubble lies at the external boundary of the domain with symmetry condition at the boundary. The surface of a flat bubble acts as an interface between the flat bubble and the solid and a concentration C_a of the crystal atoms is calculated at the interface cells and the surface can move accordingly.

The intra-granular bubbles reaching the vicinity of a flat bubble can simply coalesce with this flat bubble following the same condition for coalescence. The flat bubble can accommodate the gas content of the bubbles coalescing

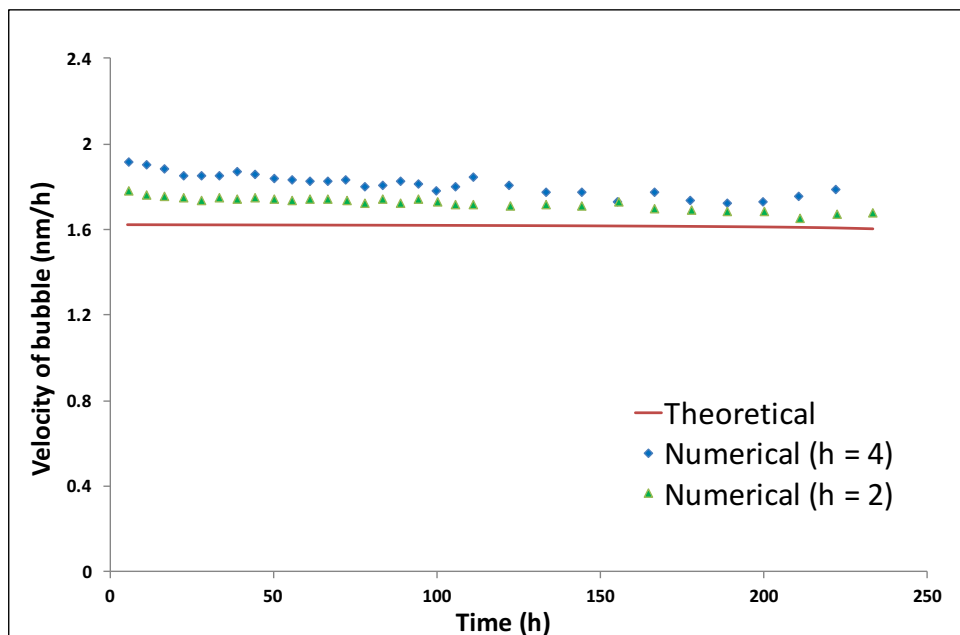


FIGURE 2.17: Theoretical vs Numerical value of bubble velocity.

with it and can, thus, be used to determine the FGR from the intra-granular bubbles. The pressure and gas content of the flat bubble can be initialized such that to provide a vacancy gradient between the flat bubble and the bubbles inside the domain. The pressure within the flat bubble can also be "fixed" (imposed) in order to have a continued gradient of vacancy concentration.

The concept of the flat bubble is utilized throughout the manuscript for the various analyses, such as the directed movement of bubbles in a vacancy gradient in the next chapter, and to determine the FGR from the intra-granular bubbles.

2.7 In Closing

In this chapter, we presented a new spatially resolved model to study the interactions between fission gas bubbles and point defects. This new model, BEEP Model, overcomes the limitation of the Cluster Dynamics models and the Phase-Field models. However, the model, in its present form, cannot simulate nucleation unlike the Cluster Dynamics models and it does not consider the various physical effects like elasticity which are present in the Phase-Field models.

The methodology adopted in the development of the model has been discussed in this chapter. Several verification tests carried out for the different phenomena in the model have been demonstrated and have proved the capability of the BEEP Model to simulate such phenomena. The model was further implemented to simulate the phenomena of coalescence of two bubbles and Ostwald ripening in the grain. These phenomena are very well simulated by the model and show good qualitative agreement with the associated physics.

The results obtained prove the ability of the model to simulate the phenomena associated with bubble growth and migration. This gives us the confidence to proceed further with the model to study, in detail, gas bubble migration within the grain and its impact to the overall fission gas release.

Chapter 3

FGR due to bubble migration in a vacancy gradient

As stated before, the transport of fission gas from within the fuel grains to the grain boundaries is a fundamental controlling mechanism of FGR in the nuclear fuel. At high temperature annealing conditions, the Xe gas atoms get trapped in the numerous intra-granular bubbles. Due to the absence of fission, no irradiation-induced resolution of gas atoms can occur and the most prominent mechanism for fission gas to be released out of the grain seems to be via the movement of gas containing intra-granular bubbles. In this chapter, we will discuss one of the mechanisms of intra-granular bubble movement which is the directed movement in a vacancy gradient and analyze its impact on the FGR during post-irradiation annealing conditions.

3.1 Directed movement of intra-granular bubbles in a vacancy gradient

Evans [100] proposed a mechanism for the transport of gas atoms by the movement of intra-granular bubbles containing the gas. According to him, during high temperature annealing, the influx of vacancies from the grain surface towards the grain would create a vacancy concentration gradient and this would impose a directed movement of intra-granular gas bubbles towards the boundary, eventually accelerating the gas release. He based this mechanism on the well-known mechanisms of movement of bubbles up vacancy gradients [99] and efficiency of grain boundaries and surfaces as high temperature vacancy sources, as recognized in the early works of Barnes et al. [207, 208] and later in [128, 209].

The mechanism of directed bubble migration can be understood better with a pictorial representation shown in Fig.3.1. From the figure, we see that the free surface - or grain boundary coated by large, already vented bubbles - generates vacancies which move towards the gas bubble due to the vacancy gradient and are trapped by the gas bubble. This gradient exists since the Bubble 1 is over-pressurized due to the presence of Xe gas atoms, which leads to a lower value of equilibrium vacancy concentration (see Eq.2.2) at

the bubble surface than at the free surface. Similarly, the vacancy flux may exist between the bubbles depending on the radius and pressure of each bubble and the gas bubbles may, in turn, emit vacancies towards other more pressurized bubbles. Indeed, for very high pressures, the effect of pressure on the equilibrium vacancy concentration dominates the radius effect.

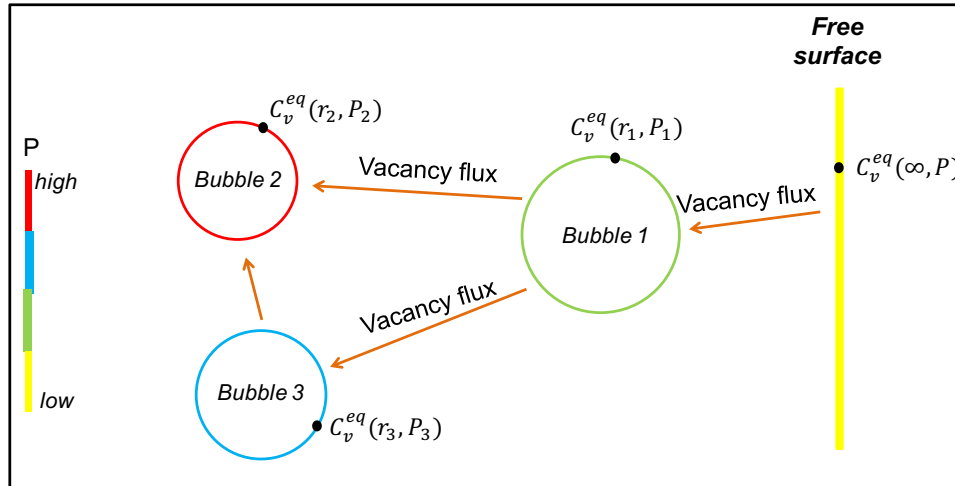


FIGURE 3.1: Vacancy concentration gradient existing between surfaces.

Due to the diffusion of vacancies, as a bubble traps vacancies at one surface (Fig.3.2), it shifts towards the free surface/grain boundary. So, the bubble moves up the vacancy gradient and may reach the grain boundary and eventually cause the gas within the bubble to be released.

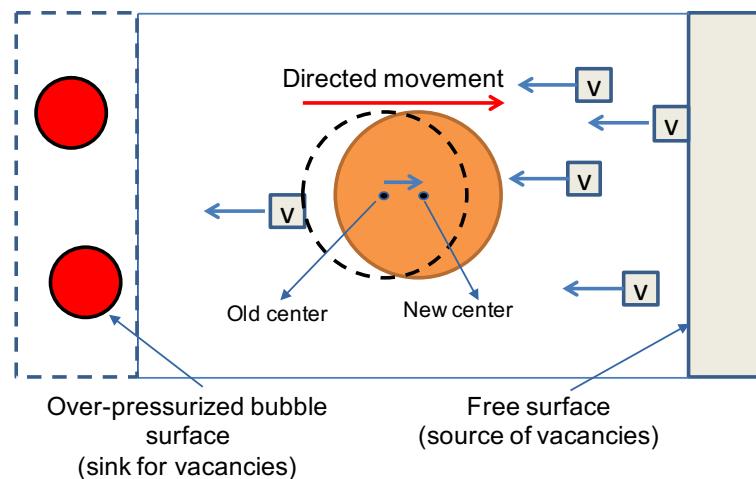


FIGURE 3.2: Directed movement of a bubble in a vacancy concentration gradient.

If the bubble does not emit the vacancies as it absorbs them, it grows, which releases its inner pressure and diminishes the vacancy gradient between the bubble and the free surface. A bubble may also undergo coalescence. In this case, the resulting bubble, with a larger radius, has a lower

equilibrium vacancy concentration (see Eq.2.2) than two identical bubbles at the same pressure, for example. This tends to maintain a high vacancy gradient with the free surface. These two phenomena - individual growth versus coalescence - have opposite effects. That is why the only way to access the kinetics of FGR through these phenomena is to model them. It is, however, sure that with the ingress of vacancies, a final equilibrium will be reached where the equilibrium vacancy concentration at the vicinity of the bubbles will be the same as the one at the free surface and the bubble movement in a vacancy gradient will stop. A particularly interesting question is to know if the FGR (out of the grain) can be important or not before the equilibrium is reached.

3.1.1 Evans' model for directed movement of bubbles

Evans also proposed a quantitative assessment [102] of the mechanism of directed movement of bubbles by using numerical calculations to simulate the phenomenon. He assumed a spherical grain with uniform distribution of over-pressurized gas bubbles. Annealing of the grain at high temperatures caused an influx of vacancies from the grain surface inwards the grain, causing the bubbles to grow. The model used by Evans postulates that there exists a front (defined by $C_v \approx 0$), where the bubbles undergo a local fractional swelling, ΔS , (a key parameter of his model) before the front progresses inwards the grain. Fig.3.3 shows the methodology of the Evans' Model considering a planar slice from the grain.

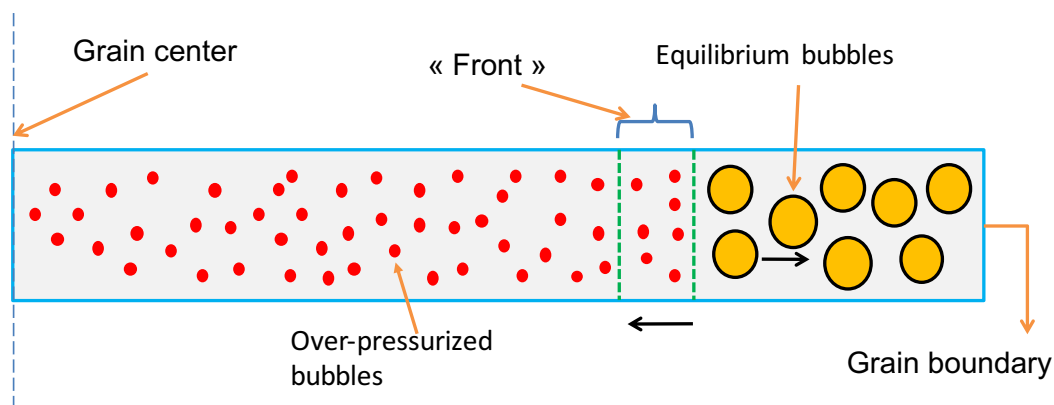


FIGURE 3.3: Evans model description.

In this model, the vacancies that arrive from the surface are supposed to be entirely trapped by the bubbles located on the front. This causes the vacancy gradient to last long enough to allow bubbles that are in the gradient to reach the grain boundary. However, the existence of this front has never been demonstrated. The FGR values are also found to be a function only of this fractional swelling in his model. Moreover, in this model, the bubbles which are further into the grain remain unaffected by the influx of vacancies while the bubbles at the front grow to equilibrium values. Though the bubbles closest to the grain boundary trap the vacancies first, it is not true that the

bubbles a little further from the grain boundary do not grow at all before the closest bubbles reach equilibrium values.

So, to overcome the limitations of this model, we require to develop more mechanistic models that would explicitly describe the bubbles and their migration in a vacancy gradient to access the impact of intra-granular bubble migration on the overall FGR. The BEEP Model serves this purpose with great detail and we will use it to analyze the FGR in the following sections.

3.1.2 Testing the movement and growth of bubbles in the BEEP Model

At the beginning of the development of the BEEP Model, the only condition at the frontiers of the domains were the periodic ones. So, to test the ability to move in a vacancy gradient, a vacancy gradient had to be created between the bubbles. This is why a 2-D case with a large empty bubble (low equilibrium concentration of vacancy) surrounded by small highly pressurized bubbles (high equilibrium concentration of vacancy) was chosen. The domain is a $256\text{nm} \times 256\text{nm}$ square with a grid size of 4 nm. One empty bubble with a radius of 30 nm is modeled at the center of the domain. The volume per atom of gas in the bubble is provided as 10^6 nm^3 . Randomly generated bubbles with a random size distribution (radius ϵ (0.4 nm, 1.0 nm)) are provided with volume per atom of gas approximately equal to the volume of one U site (0.04 nm^3). These highly pressurized bubbles are randomly distributed in the domain to surround the empty big bubble. A schematic representation of the domain is depicted in Fig.3.4.

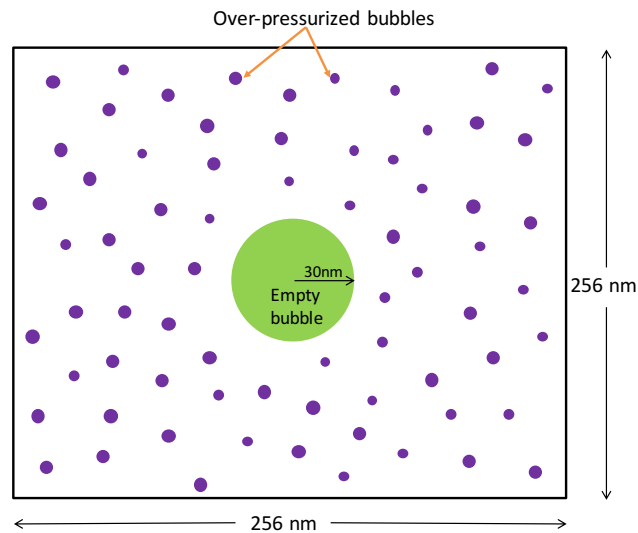


FIGURE 3.4: Schematic representation of domain for bubble movement and growth.

According to the mechanism proposed by Evans [100], due to the pressure difference between the small bubbles and the big bubble, a vacancy gradient will exist and there will be a flux of vacancies from the big bubble to the small

bubbles. This would lead to a directed movement of the small bubbles up the gradient towards the big bubble. At the same time, the smaller bubbles would also grow by trapping the vacancies from the big bubble and due to coalescence while migrating. The simulation is carried out for a time of 1 hour. The initial vacancy concentration in the solid is taken as $C_v^{ini} = 2 \cdot 10^6$, which is of the same order of magnitude as the C_v^{eq} at the interfaces of the big and small bubbles. The bubble distribution and migration in the domain is depicted in Fig.3.5 for time $t = 0$ to $t = 60$ min.

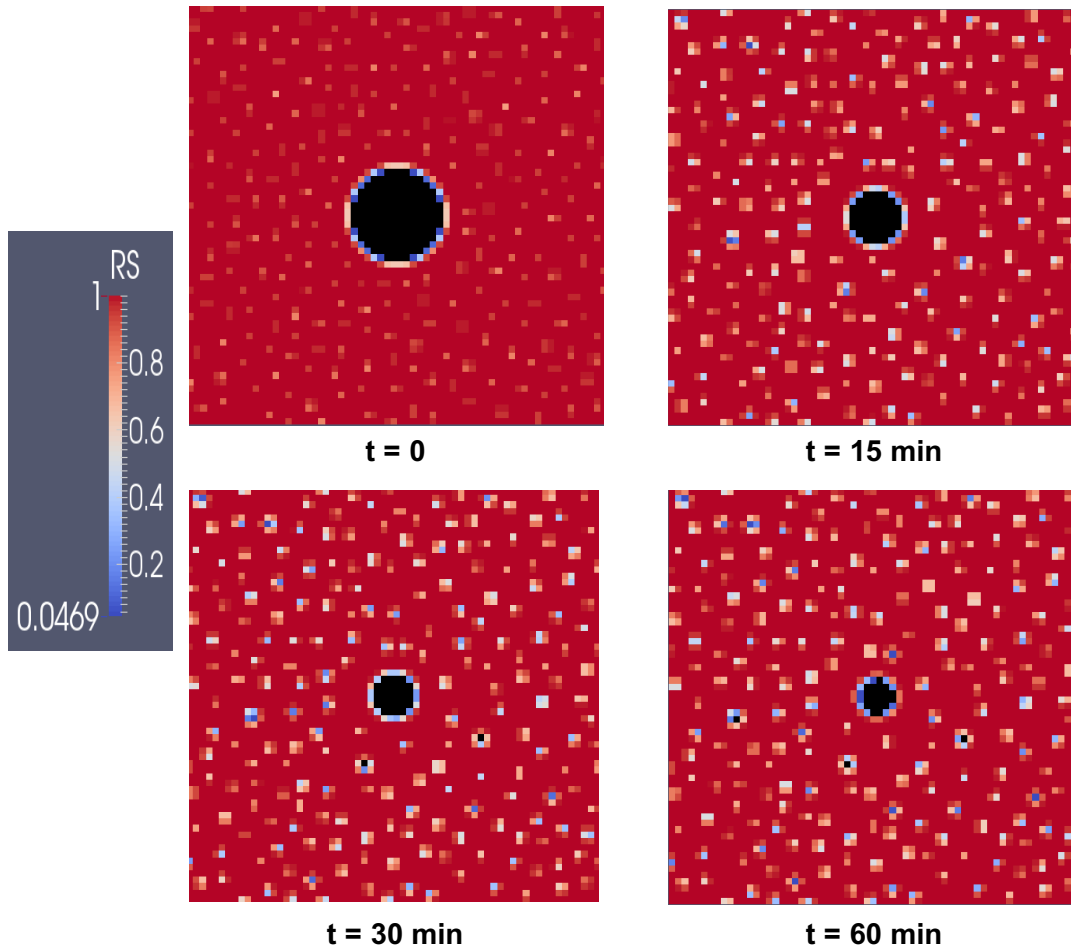


FIGURE 3.5: Movement and growth of bubbles in a vacancy gradient.

As can be observed in the Fig.3.5, as time progresses, the small, pressurized bubbles grow. The bigger bubble shrinks at the same time. This happens because each bubble is characterized by a value of C_v^{eq} at its vicinity. This value of C_v^{eq} depends on the bubble characteristics, pressure within the bubble and its radius (see Eq.2.1). Due to the difference in pressure within the bigger bubble and the smaller bubbles, there exists a vacancy flux from the bigger to the smaller bubbles. The smaller pressurized bubbles reduce their inner pressure by trapping the vacancies which are emitted by the bigger bubble. Since the vacancies are accumulated on the surface of the bubbles

facing the bigger bubble, the centers of these bubbles shift towards the bigger bubble. This leads to the movement of the smaller bubbles towards the bigger bubble. This bubble evolution continues while the gradient of vacancy concentration lasts between the bubbles. Once the vacancy concentration in the vicinity of the bubbles reach an equilibrium value, no further movement of the bubbles is observed. It can be seen from Fig.3.6, that the vacancy concentration values for the big bubble and one of the small bubbles has almost reached an equilibrium state in 1 hour of annealing time. When the case was continued up to 3 hours, it can be seen from Fig.3.7 that no bubble evolution occurred from $t = 1$ h to $t = 3$ h. Moreover, the mean radius of the bubbles can be seen to have saturated after the equilibrium was reached.

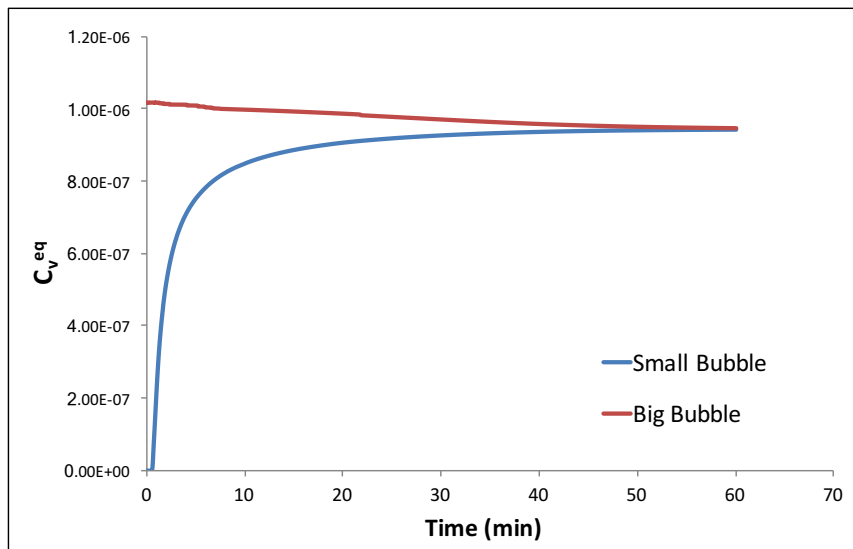


FIGURE 3.6: Equilibrium concentration of vacancies at the vicinity of bubbles as a function of time.

To further analyze the directed movement of bubbles up the vacancy gradient, the distance of a small bubble from the center of the initially big bubble is plotted against time (Fig.3.8). The radius of the big bubble is also plotted to act as a reference. We consider five different smaller bubbles at different distances from the big bubble and representing different behaviours. The properties of these bubbles before and after the simulation are given in Table 3.1. The distance between the centers of these bubbles and the big bubble are taken to calculate the distance moved by these bubbles.

It is observed from Fig.3.8 that the bubbles further away from the big bubble (Bubbles 1 and 2) move a very slight distance towards the bigger bubble. The bubbles near the big bubble, on the other hand, move much more distance towards it. For example, Bubble 5, which is the closest to the big bubble among the 5 bubbles considered, moves a distance of 24.8 nm towards the big bubble in 60 minutes. Some bubbles coalesce with each other while moving towards the big bubble and vanish, such as Bubbles 3 and 4. The kink in the curve for Bubble 5 at around 21 min is due to the coalescence of Bubble 4 with it, increasing the volume and shifting the center of Bubble 5 away from the center of the big bubble.

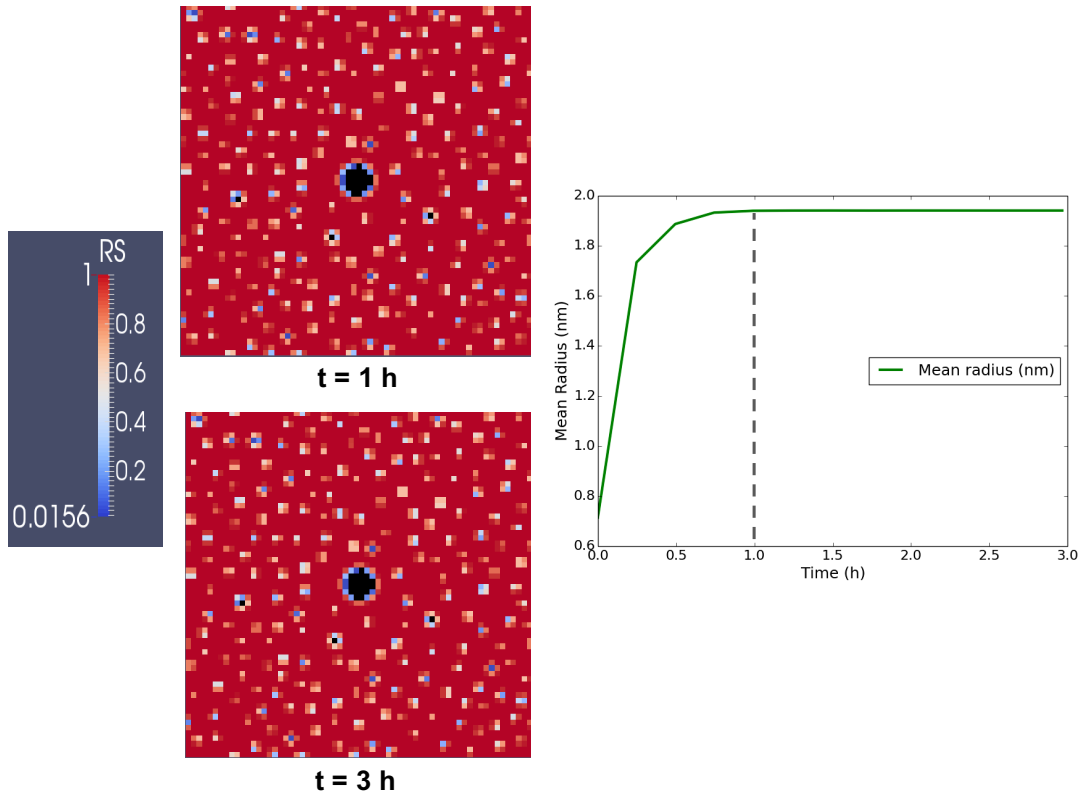


FIGURE 3.7: Distribution of bubbles in the domain after equilibrium concentration was reached and the mean radius of the bubbles.

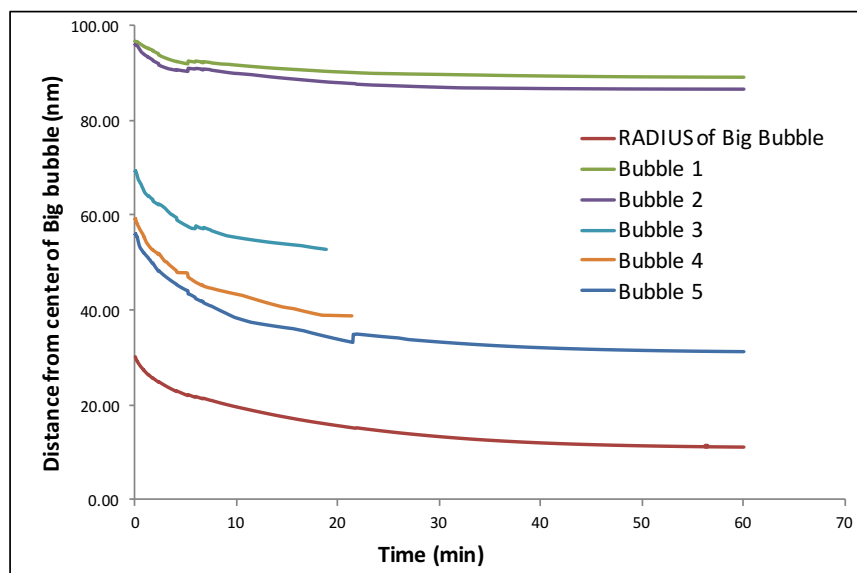


FIGURE 3.8: Directed motion of smaller bubbles towards the big bubble.

The evolution of quantities like the mean radius of small bubbles, their C_v^{eq} and mean pressure from time $t = 0$ to $t = 60 \text{ min}$ and the values for the big bubble are presented in Table 3.2. It is noted that the mean radius of small

Bubble	Initial distance from big bubble (nm)	Distance moved (nm)	Radius (nm)		Pressure (Pa)	
			Initial	Final	Initial	Final
Big Bubble	-	-	30	11.09	28.62	$6.15 \cdot 10^7$
Bubble 1	96.68	7.73	0.7	1.81	$1.06 \cdot 10^{10}$	$1.47 \cdot 10^8$
Bubble 2	95.68	9.22	0.6	1.47		$1.69 \cdot 10^8$
Bubble 3	69.22	16.37	0.5	1.13		$2.13 \cdot 10^8$
Bubble 4	59.23	20.54	0.5	1.16		$1.99 \cdot 10^8$
Bubble 5	55.90	24.86	0.6	2.11		$1.32 \cdot 10^8$

TABLE 3.1: Properties of the five bubbles with respect to the big bubble at $t = 0$ and $t = 60$ min.

bubbles increases with time and the pressure inside them is reduced. The radius of the big bubble reduces at the same time and the inside pressure increases significantly. The C_v^{eq} value in the vicinity of the big bubble reached almost the same values as the mean C_v^{eq} value in the vicinity of the small bubbles in 60 minutes. Some bubbles vanish due to coalescence reducing the number of bubbles from 245 to 213.

Quantity	At $t=0$	At $t=60$ min
Mean radius (small bubbles) (nm)	0.72	1.94
Mean C_v^{eq} (small bubbles)	$3.67 \cdot 10^{-13}$	$8.63 \cdot 10^{-7}$
Mean pressure (small bubbles) (Pa)	$1.06 \cdot 10^{10}$	$8.68 \cdot 10^8$
Number of small bubbles	245	213
Radius (big bubble) (nm)	30.	11.08
C_v^{eq} (big bubble)	$1.02 \cdot 10^{-6}$	$9.44 \cdot 10^{-7}$
Pressure (big bubble) (Pa)	28.62	$6.15 \cdot 10^7$

TABLE 3.2: Evolution of quantities from $t = 0$ to $t = 60$ min.

So, from this test case, it can be seen that the bubbles migrate towards the bigger bubble which has a larger value of equilibrium concentration of vacancies, thus, verifying the accurate simulation of the mechanism of directed movement of bubbles in a vacancy gradient. Next, we will carry out the simulation on a domain representing the actual size of the grain and analyze the FGR due to the directed movement of bubbles in a vacancy gradient during post-irradiation annealing.

3.1.3 Grid size and Coalescence

This first test also allowed to think of the question of the grid size. The grid size of 4 nm has not been chosen arbitrarily. It is the largest grid size compatible with the largest observed bubble densities ($1 - 2 \cdot 10^{24}$ bubbles of ~ 1 nm size, which gives a distance between surfaces of bubbles as 7 - 9 nm). This distance (~ 8 nm) may be considered as the physical distance of coalescence between two bubbles. Taking a grid size of 4 nm is consistent with this physical distance of coalescence.

However, in its present form, the model is not totally independent of the grid size because of this issue of the coalescence and that is not an ideal situation. Annex G shows a grid sensitivity analysis, where the influence of the grid size on the results is visible (as expected). However, it is shown from the analysis that the impact on the result remains quite low. In the annex, a perspective is also given to render the model independent from the grid size, also for the coalescence process.

3.2 Analysis of FGR via Directed Movement Mechanism

2-D analyses were carried out to determine the FGR due to intra-granular gas bubble movement to the grain boundary. The physical conditions used for the case and the target FGR value from experiments will be discussed in the following sections.

3.2.1 FGR values from experiments for comparison

The analyses carried out are presented in this section with the primary focus being on the fractional FGR due to intra-granular bubble migration. We compare the values of FGR obtained from our analyses to the results from the experiments of the thesis of Valin [8] as described in section 1.7.2. She had used a pellet of UO_2 fuel from a PWR which had been irradiated for one cycle. The fraction of FGR for 3 hours of isothermal annealing at 1600°C was found to be $\sim 65\%$.

The value of FGR obtained from the experiments of Valin is, however, the overall FGR, from the intra- as well as inter-granular bubbles. Earlier studies had been carried out using the MARGARET model [157] to discriminate the intra-granular and inter-granular retained gas. At the end of one cycle irradiation, we get approximately 10% of inter-granular gas. Supposing that the inter-granular gas has been completely released, then in Valin's experiment, 55% of the total created gas was coming from the grain in the FGR. This would mean that $\frac{0.55}{0.9} = 61\%$ of the intra-granular gas has been released during this annealing test.

Moreover, for our analyses, we use a planar geometry rather than the actual spherical geometry of the fuel. Going from spherical to planar geometry, we get an equivalent target value for the FGR as $\sim 27\%$ as compared to $\sim 61\%$ FGR from intra-granular bubbles (See Annex. H).

So, the reference value for FGR from intra-granular bubbles during post-irradiation annealing of UO_2 for 3 hours at 1600°C is 27% for comparison with the calculations.

3.2.2 Conditions for numerical analyses

For all the cases, in this chapter as well as the next one, we consider a planar domain of size $5120\text{nm} \times 128\text{nm}$ with a grid size of 4 nm (i.e., the mesh is 1280×32 cells). This domain size is representative of the actual grain size radius ($\sim 5\mu\text{m}$). We consider a free surface and an exterior region at a low pressure and a large number of over-pressurized bubbles within the grain. We try to respect a distance between the bubbles while generating the bubbles randomly in the grain that would be consistent with a bubble number density in the range $10^{23} - 10^{24}$ bubbles/ m^3 as observed in experiments [210, 211, 128]. The way it is done is that if we assume that a bubble is present at each corner of a cell (cuboid) of width 'd', then each cell has 8 bubbles contributing 1/8 to each cell. So, the volume per bubble would be d^3 and the number of bubbles per unit volume (number density), $N_b = d^{-3}$. So the distance between the bubbles in 3-D can be obtained from the known value of $N_b = 10^{23} - 10^{24}$. Using this value of distance in the planar domain, we get the relation $d = N_{b,2D}^{-1/2}$ and obtain the bubble number density in 2-D. Then the number of bubbles to be generated can be found from the relation, $N_{b,2D} \cdot \text{Area of domain}$.

However, obtaining a high number of bubbles is difficult if a coarse grid is used as the chance to generate a new bubble which is at a good distance to avoid coalescence with an already existing bubble is low. We reached an equivalent bubble density of $\sim 2.8 \cdot 10^{23}$ bubbles/ m^3 . The bubble size is distributed randomly with the radius, $r \in (0.4\text{ nm}, 1\text{ nm})$. We provide periodic boundary condition on the top and bottom boundaries and symmetric condition on the right and left boundaries. An isothermal annealing temperature of 1600°C is used for the analysis. A pictorial representation of the domain with the provided conditions is depicted in Fig.3.9 and the initial conditions used for the analyses are described in Table 3.3.

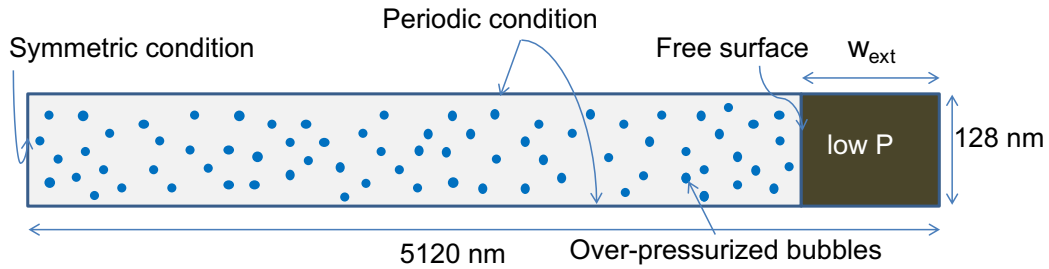


FIGURE 3.9: Domain used for the analyses with various conditions.

Since the domain used for the analyses is quite large as compared to the size of the bubbles, in order to have a better view of the evolution of the bubbles, we represent only an enlarged region of the domain (represented by dashed box in Fig.3.10) towards the vicinity of the exterior surface in all the cases. We calculate the fractional FGR due to intra-granular bubble migration by the increase in the net content of gas in the exterior region before and after annealing, divided by the total gas contained initially in the small bubbles.

Property	Description	Value
T	Annealing temperature	1600°C
N_b	Initial equivalent bubble number density	$2.8 \cdot 10^{23}$ bubbles/ m^3
w_{ext}	Exterior region width	255 nm
r_b	Small bubble Radius	(0.4 - 1) nm
Vol/at (ext)	Volume per atom of gas in the Exterior region	286 nm^3
Vol/at (bub)	Volume per atom of gas in the bubbles	$0.0409 (= \Omega) \text{ nm}^3$
t	Simulation time	3/110 h

TABLE 3.3: Initial conditions used for the analyses.

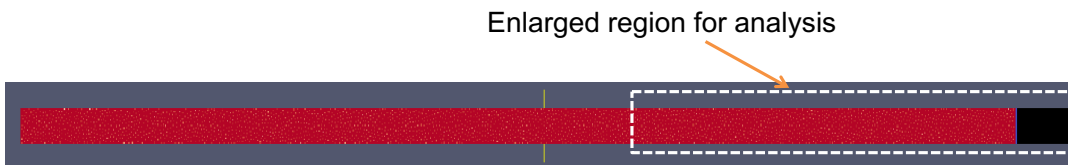


FIGURE 3.10: Dashed box representing the enlarged region of the actual domain presented in the results.

3.2.3 FGR analysis

In order to analyze the mechanism of bubble migration in a vacancy gradient and its impact on the fission gas release, we consider a constant initial vacancy concentration of $C_v^{ini} = 1.08 \cdot 10^{-12}$ in the solid, which is of the same order as the C_v^{eq} in the vicinity of the small bubbles. The simulation is carried out for a simulated time of 3 hours. We expect the bubbles in the vicinity of the exterior surface to grow by trapping the vacancies emitted from the surface and also to move towards the exterior surface in the vacancy gradient. The distribution of the bubbles near the exterior surface in 3 hours is depicted in Fig.3.11.

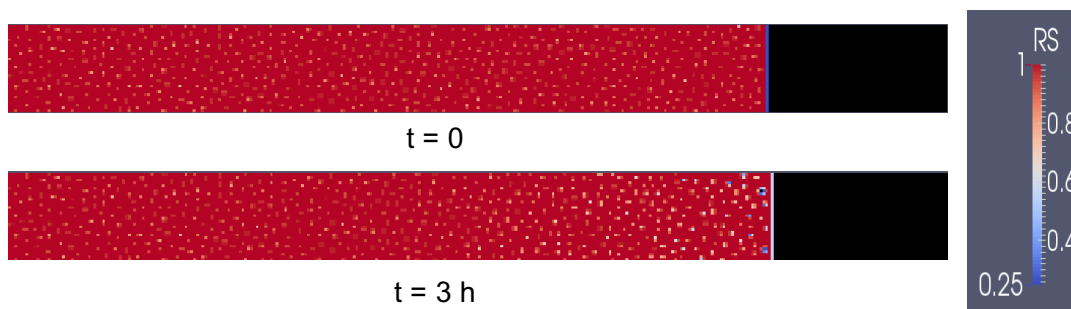


FIGURE 3.11: Bubble distribution in the domain during 3 hours of simulated time.

Fig.3.11 shows an enlarged view of the bubbles in the domain near the exterior surface at time $t = 0$ and at $t = 3$ h. It can be noticed that the bubbles grow by trapping the vacancies which are generated at the free surface. Some of the bubbles also move out of the grain into the exterior surface. The number of bubbles in the domain decreased from 2647 bubbles at time $t = 0$ to 2634 bubbles at $t = 3$ h. However, the fractional FGR after 3 hours of annealing was

found to be 0.112%, which is insignificant as compared to the values obtained from experiments, even if we compare it to our reference value (27%).

The analysis was continued for annealing up to 110 hours of simulated time in order to see any further evolution of the bubbles and the effect on the overall fission gas release. The bubbles grew further and up to a wider extent into the grain. The bubble evolution from time $t = 0$ to $t = 110$ h is depicted in Fig.3.12. The number of bubbles further reduced to 2266 at time $t = 110$ h. However, the fractional fission gas release went up to only 1.204%, which is still insignificant as compared to the values obtained from experiments. The values for various parameters at time $t = 0, 3$ and 110 h for the case are presented in Table 3.4.

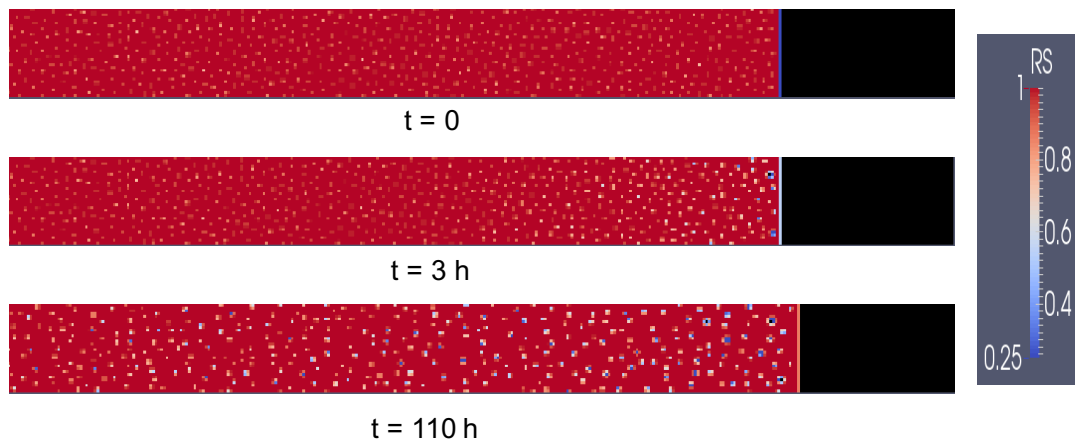


FIGURE 3.12: Bubble movement in a vacancy concentration gradient for 110 hours of simulated time.

time (h)	Number of bubbles	Mean radius (nm)	Mean gas content	FGR (%)
0	2647	0.719	167.664	-
3	2634	0.756	168.303	0.11 %
110	2266	0.966	193.496	1.20 %

TABLE 3.4: Evolution of various parameters with time for the directed movement case.

The mean radius of bubbles along the domain is depicted in Fig.3.13. It can be noticed that in 3 hours of annealing, the radii of the bubbles very close to the free surface increased, whereas, the bubble growth was up to a greater extent into the grain in 110 hours of annealing.

Even though the number of bubbles reduced from 2647 to 2266 in 110 hours of annealing, not a significant FGR could be observed. Although several bubbles moved out of the free surface due to directed movement, majority of the bubble number loss is due to the coalescence among the bubbles while migrating towards the free surface.

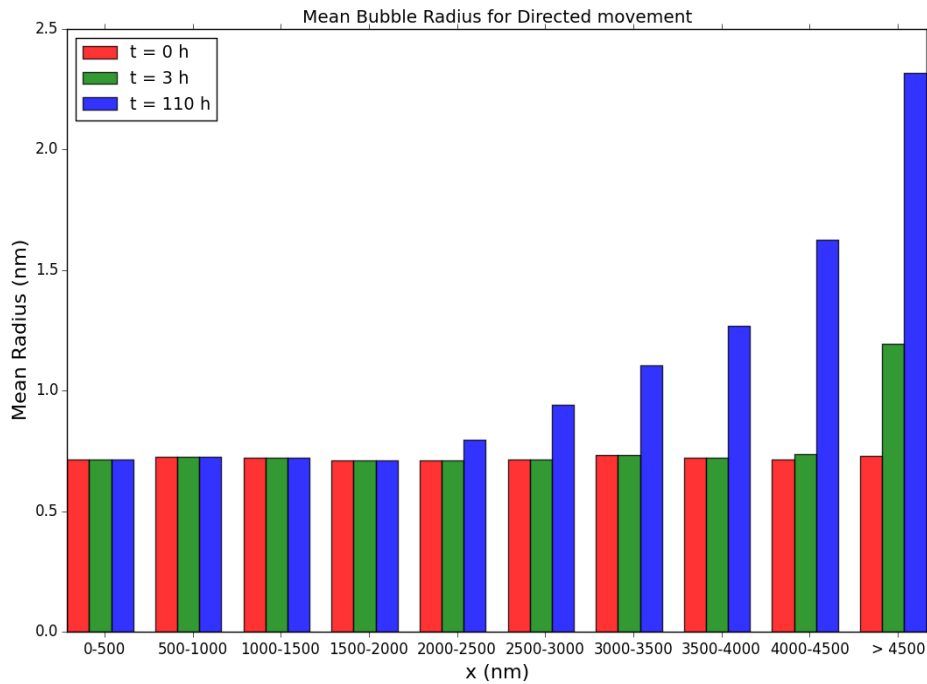


FIGURE 3.13: Mean bubble radius along the domain for directed movement case.

3.3 FGR analysis until vacancy gradient lasts

It seems evident that the target FGR can not be reached using the mechanism of directed movement of bubbles. However, we continued the calculation until the vacancy gradient existed between the free surface and the bubbles in the solid. The evolution of vacancy concentration in the domain length with time is plotted in Fig.3.14. It can be noted from the figure that the vacancy concentration values have not completely reached the equilibrium value. The value of equilibrium concentration of vacancies at the rightmost end, i.e., at the free surface is $2.31 \cdot 10^{-7}$. The simulation stopped after a simulation time of $t = 8569$ h because the external region that we considered had completely disappeared. This happened because of the swelling of the grain by exchanging crystal atoms with the vacancies generated at the free surface. At the end of the simulation, the value of equilibrium concentration of vacancies at the leftmost end had reached $2.08 \cdot 10^{-7}$ and the vacancy profile was nearly flat.

The bubble distribution in the grain with time is depicted in Fig.3.15. The swelling of the grain is very clearly evident as the simulation progresses, with the free surface progressing on the right. It can be seen that at $t = 8569$ h, the external region on the right has completely disappeared. The bubbles grew by trapping vacancies, not only near the vicinity of the free surface, but also further into the domain. The bubble distribution in the entire domain is presented in Fig.3.16. It can be seen that the bubbles have evolved in the entire domain at the end of the simulation at $t = 8569$ h. The bubbles at the vicinity of the free surface grow more, as expected, because of trapping the

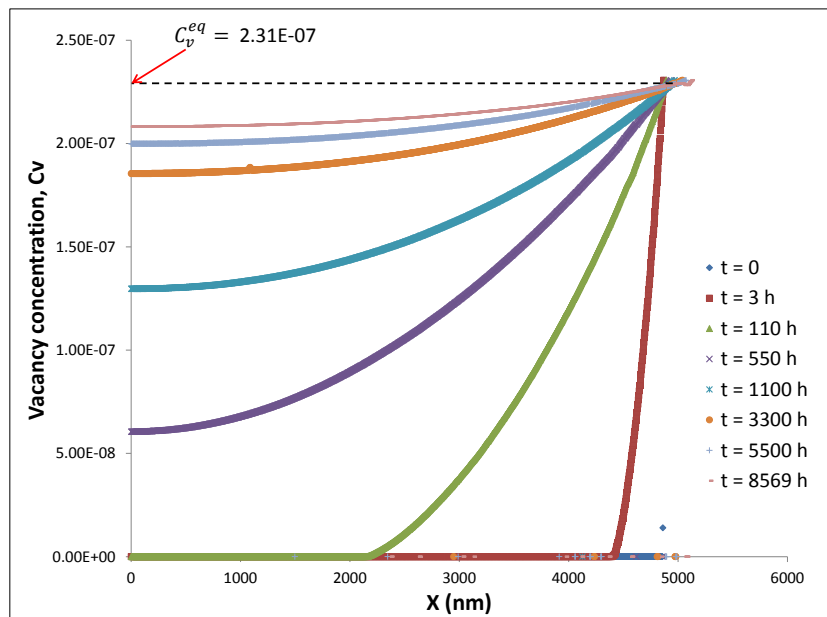


FIGURE 3.14: Vacancy concentration values along the grain at different times.

vacancies first and also because of coalescence among the bubbles as they move towards the free surface due to the vacancy gradient.

The mean radius of the bubbles at different distances from the free surface along the domain is shown in Fig.3.17. As compared to at $t = 110$ h, the bubbles can be seen to have grown more everywhere in the domain. Several bubbles have also moved out of the grain in this long duration. Out of the 2647 bubbles at the beginning, 2266 had remained after 110 hours of simulation time. The number of bubbles left within the grain at time $t = 8569$ h was found to be 860. The mean radius of these 860 bubbles was found to be 3.159 nm. Even with a large number of bubbles having moved out from within the grain, the FGR at time $t = 8569$ h was found to be 6.63%.

time	Number of bubbles	Mean radius (nm)	FGR (%)
0	2647	0.719	0.
3	2634	0.756	0.112
110	2266	0.966	1.204
550	1476	1.545	2.280
1100	1224	1.925	3.175
3300	1001	2.570	4.705
5500	936	2.850	6.048
8569	860	3.159	6.626

TABLE 3.5: Evolution of various parameters with time for the directed movement case continued until possible

The evolution of various parameters as the simulation time approached $t = 8569$ h is given in Table 3.5. The FGR and the mean radius of the bubbles

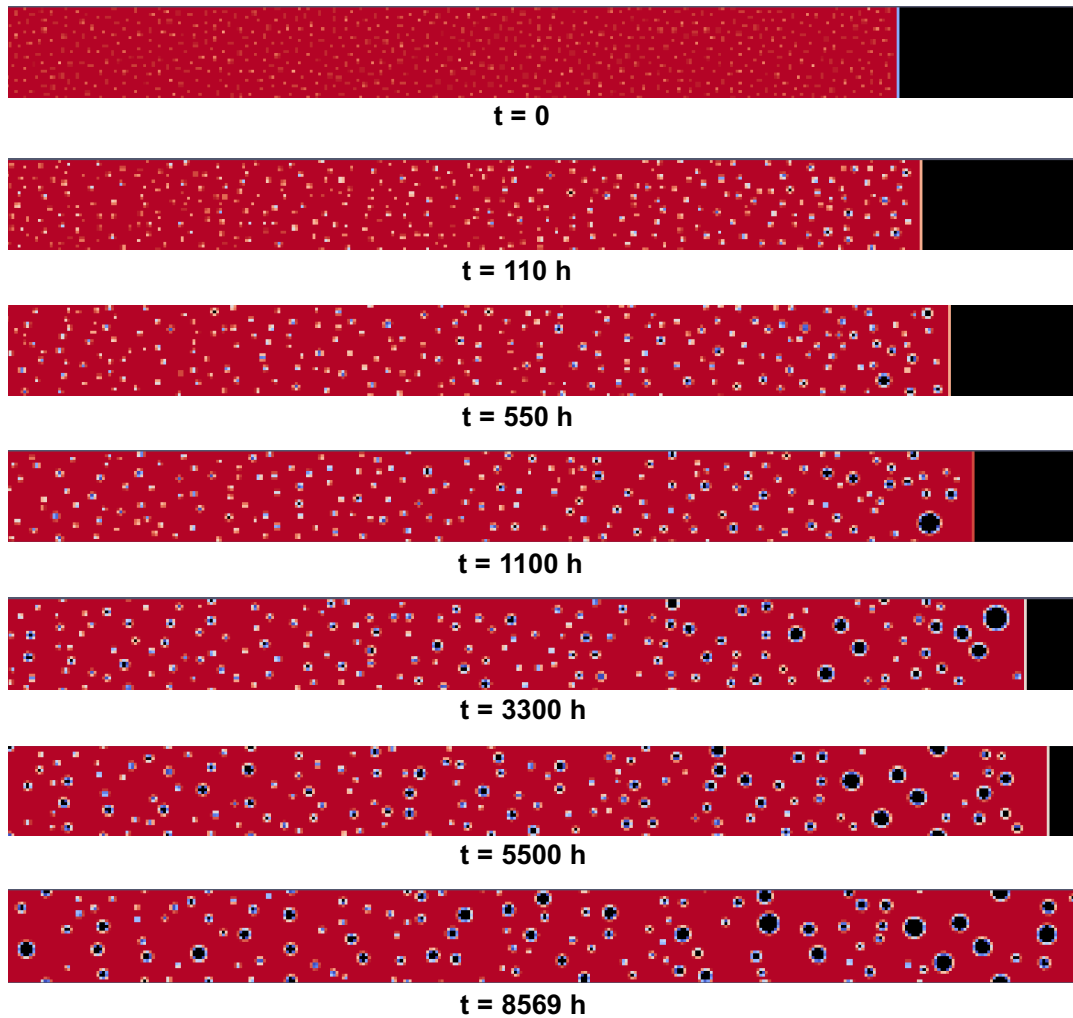


FIGURE 3.15: Bubble distribution in the domain until vacancy gradient lasts.

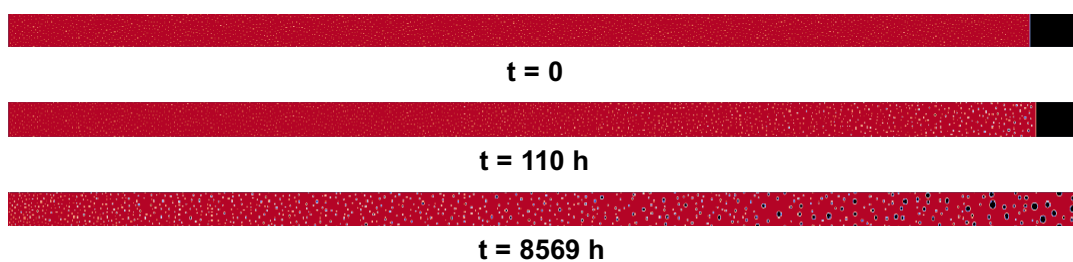


FIGURE 3.16: Bubble distribution in the entire domain at the end of the simulation.

in the grain is plotted with respect to time in Fig.3.18. It is to be noted that although only 1/3 of the bubbles remain within the grain as compared to the beginning, the FGR is still low as more bubbles have coalesced in comparison to being released out of the free surface to contribute to the FGR.

So, the analysis carried out for the FGR due to the directed movement of bubbles in a vacancy gradient shows that this mechanism alone cannot

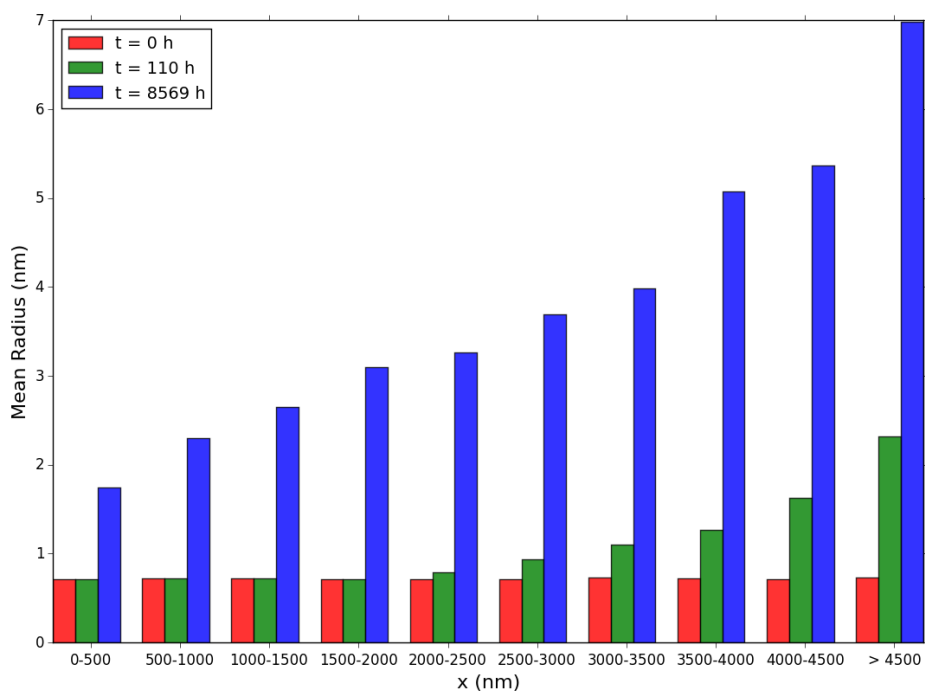


FIGURE 3.17: Mean bubble radius along the domain at the times $t = 110\text{h}$ and at the end of the simulation at $t = 8569\text{h}$.

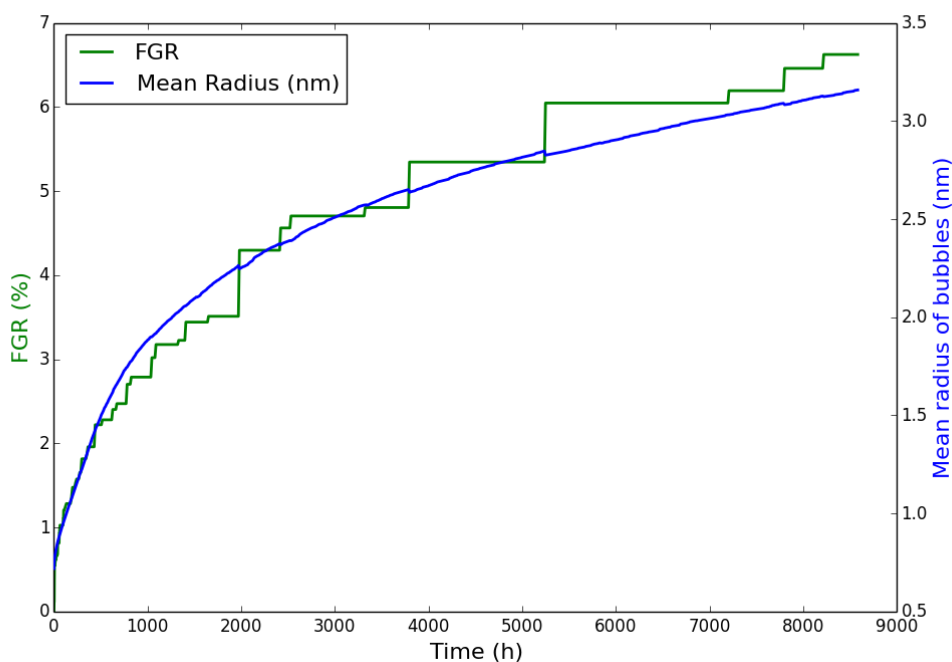


FIGURE 3.18: Evolution of FGR and mean radius of the bubbles during the simulation.

attribute to the FGR values observed in our reference experiment. Even allowing the simulation to be carried out up to 8569 hours could not achieve the high experimental values of FGR.

3.4 Uncertainty analysis of parameters

3.4.1 Uncertainty analysis of D_v

An interesting question is to evaluate the impact of D_v on this result. In practice, we solve the equations using a non-dimensional time constructed as

$$t^* = \frac{D_v}{l_{adim}^2} * t$$

with $l_{adim} = 1$ nm and the non-dimensional length as

$$l^* = \frac{l}{l_{adim}}$$

With this choice, the non-dimensional vacancy diffusion coefficient, $D_v^* = 1$. This was done in order to accelerate the calculation of the diffusion (by avoiding multiplication by D_v). The interest in the question is also that in this case of directed movement in a vacancy gradient, where the kinetics is solely governed by D_v , changing D_v means that the t^* is related differently to the real time. In this analysis, we showed that the vacancy gradient became almost flat before any significant gas release could take place. Taking another value for D_v only changes the axis of time by a multiplying factor, however, the conclusion remains the same.

So, having conducted the calculation up to a long duration is equivalent to having done a parametric study on D_v , for the case of directed bubble movement and there is no impact on the results whatsoever.

3.4.2 Uncertainty analysis of C_v^{eq}

The $C_v^{eq}(P_b=0, \kappa=0)$ is expressed as defined in Eq.2.3 and can be written as:

$$C_v^{eq}(P_b = 0, \kappa = 0) = \exp\left(\frac{s_v}{k}\right) \exp\left(-\frac{\epsilon_v}{kT}\right)$$

So, the C_v^{eq} depends on the value of the vacancy formation energy, ϵ_v , and the excess entropy of vacancy formation, s_v . In the analyses in this manuscript, we have used the value of $\epsilon_v = 2.47$ eV [11] and the value of $s_v = 0$. In order to test the uncertainty in $C_v^{eq}(P_b=0, \kappa=0)$, we carried out the analysis with the values of $C_v^{eq}(P_b=0, \kappa=0)$ 10 and 100 times higher than that used throughout the manuscript.

These values may correspond to lower values for ϵ_v (with s_v unchanged) or to higher values of s_v (with ϵ_v unchanged). These possibilities are indicated in Table 3.6 with factor = 1 being the case we use for the analyses in this manuscript.

The initialization of the vacancy field in between the bubbles at $t = 0$ was done consistently with these new values of $C_v^{eq}(P_b=0, \kappa=0)$, which means that they were also multiplied by 10 and 100, respectively.

Using higher values for $C_v^{eq}(P_b=0, \kappa=0)$ implies that a steeper vacancy gradient exists and a higher diffusion flux of vacancies into the bulk occurs. Using the two values obtained above to carry out simulation showed that the FGR for the case of 10 times larger $C_v^{eq}(P_b=0, \kappa=0)$ was 0.66% in 3 hours and 3.18% in 110 hours of annealing. For the case of 100 times larger $C_v^{eq}(P_b=0, \kappa=0)$, the FGR was 1.82% in 3 hours and 7.36% in 110 hours. The outcomes of the analysis are presented in Table 3.6.

factor	(ϵ_v, s_v) in (eV, *k)	FGR (%) in			intra-granular swelling (%)
		3 h	110 h	the end	
1	(2.47,0)	0.11	1.20	6.63	0.11
10	(2.098, 0) or (2.47, 2.3)	0.66	3.18	9.0	0.32
100	(1.726, 0) or (2.47, 4.6)	1.82	7.36	9.0	1.07

TABLE 3.6: FGR during uncertainty analysis of C_v^{eq} .

The gradient of vacancy concentration was almost flat at the time of terminating the simulation. The C_v^{eq} values at the rightmost end of the domain (in the vicinity of the free surface) and at the leftmost end at the different times of the simulation are presented in Table 3.7. It can be noticed that the gradient of vacancy concentration tends to be flat quicker with the higher C_v^{eq} as more vacancies would be diffused into the bulk of the domain, allowing equilibrium values to be attained more rapidly.

factor	$C_v^{eq}(P_b=0, \kappa=0)$ (rightmost)	$C_v^{eq}(P_b=0, \kappa=0)$ (leftmost)		
		in 3 h	in 110 h	at the end
1	$2.31 \cdot 10^{-7}$	$2.08 \cdot 10^{-13}$	$1.94 \cdot 10^{-13}$	$2.08 \cdot 10^{-7}$ (8569 h)
10	$2.31 \cdot 10^{-6}$	$2.00 \cdot 10^{-12}$	$1.29 \cdot 10^{-6}$	$2.20 \cdot 10^{-6}$ (2519 h)
100	$2.31 \cdot 10^{-5}$	$1.91 \cdot 10^{-11}$	$2.11 \cdot 10^{-5}$	$2.19 \cdot 10^{-5}$ (220 h)

TABLE 3.7: C_v^{eq} values at the rightmost and leftmost end of the domain.

From this analysis, we see that even using the values of C_v^{eq} 10 times and 100 times larger, we do not achieve a significant increase in the FGR in 3 hours and even 110 hours of annealing simulation. Even with the vacancy gradient profile becoming almost flat at the end of the simulations, the FGR was not significant. So, even using larger values of C_v^{eq} , we do not reach anywhere near the target FGR values.

3.5 In Closing

In this chapter we discussed the movement of intra-granular bubbles via the mechanism of directed movement of bubbles in a vacancy concentration gradient. The analysis for FGR was carried out using the BEEP Model. It could be concluded from the analysis that the FGR from the grain cannot solely be due to the transport of gas via intra-granular bubble movement in a vacancy concentration gradient. Other mechanisms of gas release have to play a significant role in the overall fission gas release during post-irradiation annealing of UO_2 .

In the next chapter, we will discuss another mechanism of bubble movement, which is the Brownian (random) movement of bubbles and see how it impacts the FGR during post-irradiation annealing.

Chapter 4

Brownian motion of bubbles and impact on FGR

In the previous chapter, we saw that the directed movement of intra-granular bubbles in a vacancy gradient could not account for the high value of FGR observed in our reference experiment during post-irradiation annealing. The flux of vacancies from the free surface to the pressurized bubbles was the driving force for the bubble movement in the direction of the free surface. However, the bubbles can also migrate within the grain, even in the absence of any driving force, due to the Brownian (random) motion. The mechanisms leading to this random movement of the bubbles and their impact on the FGR will be discussed in this chapter. Classical rate theory failed in predicting FGR in annealing condition considering the random movement of bubbles (see Annex I). However, classical rate theory incorporates simplifications that have been avoided in the BEEP Model. So, it is worth studying this random movement with this new tool.

4.1 Random (Brownian) movement of bubbles

A bubble can move in a solid without any driving force - in particular no temperature gradient - by the transfer of atoms around it. This transfer of atoms can be governed via volume or surface diffusion mechanisms. Another mechanism of random bubble movement is via vapour transport (evaporation - condensation), however, it takes place only at high temperatures and is more relevant to fast reactors rather than LWRs. These mechanisms are random by nature. We will discuss the equations governing the diffusion of bubbles via the volume and surface diffusion mechanisms of random motion in the following sections.

4.1.1 Bubble diffusion by volume diffusion mechanism

The volume diffusion mechanism is the transfer of crystal atoms via vacancies in the bulk solid near the bubble and in the absence of any driving forces. The

diffusion of bubbles is characterized by the diffusion coefficient, D_b^{vol} , which is defined according to the expression given by Olander [10] as:

$$D_b^{vol} = \frac{3}{4\pi} \frac{\Omega}{r_b^3} D_v C_v^{eq}(bubble) \quad (4.1)$$

where Ω is the atomic volume, r_b is the radius of the bubble, D_v is the vacancy diffusion coefficient and $C_v^{eq}(bubble)$ is the concentration of vacancy (at the vicinity of a bubble) in equilibrium with the bubble.

The relation that we use between D_v and the uranium tracer coefficient, D_U , is the one expressed in Eq.2.4 as:

$$D_U = D_v * C_v^{eq}(P_b = 0, \kappa = 0) * f \quad (4.2)$$

where f is the correlation factor. The value of f for FCC lattice is 0.7815 [212], however, we took it as $f = 1$ in all the analyses in this thesis. $C_v^{eq}(P_b = 0, \kappa = 0)$ is the equilibrium vacancy concentration (vacancy/site) defined in Eq.2.3.

The volume self-diffusion coefficient, D_U , can be calculated using Matzke's relation [201]

$$D_U = 6.5 * 10^{-5} \exp\left(\frac{-5.6eV}{kT}\right) m^2/s \quad (4.3)$$

From Eq.2.2 in Section.2.2.1, we have the expression for $C_v^{eq}(bubble)$ as:

$$C_v^{eq}(bubble) = C_v^{eq}(P_b = 0, \kappa = 0) \exp\left(\frac{-\Omega}{kT}(P_b - \gamma_b \kappa)\right) \quad (4.4)$$

where P_b is the pressure in the bubble in Pa, γ_b is the surface tension in J/m^2 and κ is the curvature of the bubble surface in m^{-1} . So, using Eq.2.4 and Eq.4.4 in Eq.4.1, we get the expression for D_b^{vol} as:

$$D_b^{vol} = \frac{3\Omega}{4\pi r_b^3} D_U \exp\left[\frac{-\Omega}{kT}(P_b - \gamma_b \kappa)\right] \quad (4.5)$$

So, the random movement of bubbles via volume diffusion mechanism is governed by the diffusion coefficient as given in Eq.4.5.

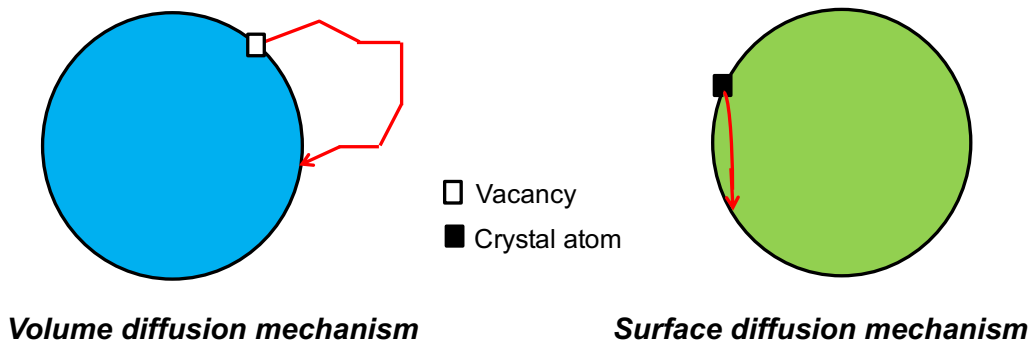


FIGURE 4.1: Random movement of bubbles by volume and surface diffusion mechanism.

4.1.2 Bubble diffusion by surface diffusion mechanism

The surface diffusion mechanism is the transfer of crystal atoms on the surface of the bubbles. The coefficient of bubble diffusion via surface diffusion mechanism can be expressed from [10] as:

$$D_b^{surf} = \frac{3}{2\pi} \frac{\Omega^{4/3}}{r_b^4} D_s \quad (4.6)$$

where again, Ω is the atomic volume, r_b is the radius of the bubble and D_s is the surface diffusion coefficient.

Different values for the surface diffusion coefficient, D_s , have been used by different authors in the past. The main experimental difficulties with measuring D_s in UO_2 are its high vapour pressure and the anisotropy of its surface energy [202]. The value for D_s is usually obtained by either mass transport methods [213, 214, 215] such as grain boundary grooving or scratch decay or by means of tracers [216, 217, 218, 219]. The expressions for D_s used by different authors are listed in Table 4.1. Using results obtained from 9 different experiments with mass transport method, Matzke [202] presented the following expression for D_s :

$$D_s = 50 \exp\left(\frac{-4.67\text{eV}}{kT}\right) m^2/s \quad (4.7)$$

The most accepted expression for D_s recently [10, 220, 221, 222] is the one given by Maiya[215] or by Matzke[202] in the temperature range of 1200-1800°C as:

$$D_s = 50 \exp\left(\frac{-4.5\text{eV}}{kT}\right) m^2/s \quad (4.8)$$

Author(s)	Year	Method	Expression for D_s (m^2/s)
Henny and Jones [214]	1968	grain boundary grooving	$D_s = 1.3 * 10^4 \exp(\frac{-4.7 \pm 0.65\text{eV}}{kT})$
Marlow and Kaznoff [216]	1968	Tracer	$D_s = 5.64 * 10^3 \exp(\frac{-5.24\text{eV}}{kT})$
P.S. Maiya [215]	1971	grain boundary grooving	$D_s = 34 \exp(\frac{-4.68\text{eV}}{kT})$
Matthews and Wood [223]	1979	-	$D_s = 50 \exp(\frac{-3.90\text{eV}}{kT})$
Zhou and Olander [219]	1984	Tracer	$D_s = 5 * 10^2 \exp(\frac{-3.12 \pm 0.65\text{eV}}{kT})$
Matzke [202]	1989	mass transport method	$D_s = 50 \exp(\frac{-4.67\text{eV}}{kT})$

TABLE 4.1: Values of surface diffusion coefficient, D_s from literature.

The results from Baker's data [126] showed an increase in the bubble diffusivity with increasing radius in the small radius regime which is in contradiction with both the expressions of D_b^{vol} and D_b^{surf} . Mikhlin [203] suggested a mechanism for the observed suppression of these small gas bubble diffusion mobility in solids. According to him, the interaction of ad-atoms with gas atoms, which are present in high density in small bubbles, causes a decrease of the ad-atom jump frequency on the bubble surface leading to the observed suppression of small gas bubble mobility. The expression for the bubble diffusion coefficient can be modified by incorporating a suppression factor, W_b , which is equal to the probability that a region near an ad-atom is free of gas atoms and is expressed as:

$$W_b = \left[1 - \frac{q}{V_b} \right]^{N_b} \quad (4.9)$$

where q is the volume of the region with no gas atoms so that a jump can occur, N_b is the number of gas atoms in the bubble of volume V_b .

In order to incorporate Mikhlin's suppression factor in the diffusion coefficient of bubbles via surface diffusion, we multiply the Mikhlin's suppression factor, W_b , with the expression for D_b^{surf} . The expression for the bubble diffusion coefficient including Mikhlin's suppression factor becomes:

$$D_b^{surf} = \frac{3}{2\pi} \frac{\Omega^{4/3}}{r_b^4} D_s \left[1 - \frac{q}{V_b} \right]^{N_b} \quad (4.10)$$

So, the bubble diffusion by surface diffusion mechanism use Eq.4.10 for the diffusion coefficient with Eq.4.8 for the value of D_s .

4.2 Influence of random bubble movement without vacancy diffusion

The influence of random movement of bubbles within the grain on the evolution of bubbles was tested. We present the analysis of random bubble movement via volume and surface diffusion mechanisms in the following section. In order to emphasize on the random movement only, we do not consider any driving force (diffusion of vacancies) in the solid. The simulation is carried out for a simulated time of 3 hours. To account for the variability due to randomness, all calculations are carried out 10 times and the mean of these values is used as the results. We consider the same initial conditions as for the directed movement analysis in the previous chapter. Fig.4.2 depicts the enlarged section of the domain near the vicinity of the free surface at time $t = 0$, i.e., before the annealing has started.

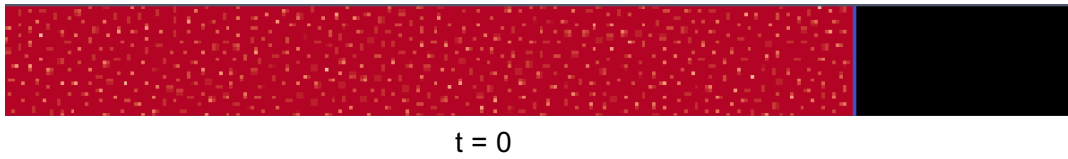


FIGURE 4.2: Random bubble distribution at time $t = 0$.

4.2.1 Random movement of bubbles due to volume diffusion mechanism

The random movement of the bubbles by volume diffusion mechanism is governed by the bubble diffusion coefficient, D_b^{vol} , which is defined by the Eq.4.5. It was observed from the analysis that there was negligible movement of bubbles via volume diffusion mechanism. After 3 hours of annealing, the number of bubbles remained the same, 2647, as before. The mean value for the diffusion coefficient of bubbles, D_b^{vol} also remained unaltered at a very low value of $2.10 \cdot 10^{-27} \text{ m}^2/\text{s}$. The bubble distribution via volume diffusion mechanism at time $t = 3 \text{ h}$ is depicted in Fig.4.3.

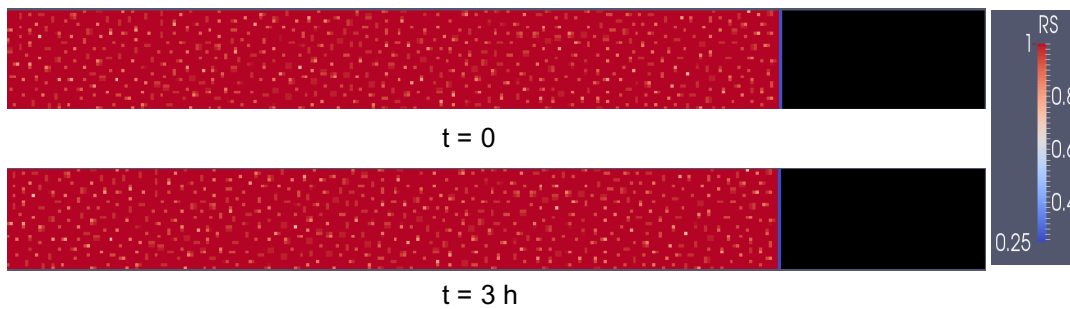


FIGURE 4.3: Random movement of bubbles at time = 3 hours by volume diffusion mechanism.

So, it could be noted from this analysis that there is no significant contribution of volume mechanism to the random movement of the bubbles and, thus, no additional impact on the fractional FGR.

4.2.2 Random movement of bubbles due to surface diffusion mechanism

The random movement of the bubbles by surface diffusion mechanism is governed by the bubble diffusion coefficient, D_b^{surf} , which is defined by the Eq.4.10. Using the value of q as $1.5 \cdot 10^{-27} \text{ m}^3$, as proposed by Mikhlin for UO_2 , to evaluate the value of W_b and multiplying the expression for D_b^{surf} with W_b , we obtain the values for the diffusion coefficient of bubbles. The values of diffusion coefficient with the suppression factor are found to be very low and the mean value of D_b^{surf} at $t = 0$ is $3.79 \cdot 10^{-31} \text{ m}^2/\text{s}$. There is no movement of bubbles because of such low values of the diffusion coefficients. After

3 hours of annealing, the number of bubbles remained the same, 2647, as before. The mean value for the diffusion coefficient of bubbles, D_b^{surf} also remained unaltered at a very low value of $3.79 \cdot 10^{-31} \text{ m}^2/\text{s}$. The bubble distribution via surface diffusion mechanism including Mikhlin's suppression term at time $t = 3 \text{ h}$ is depicted in Fig.4.4.

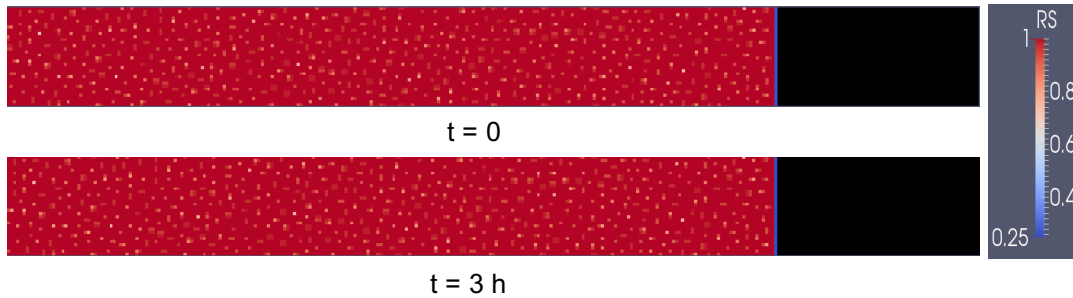


FIGURE 4.4: Random movement of bubbles at time = 3 hours by surface diffusion mechanism with Mikhlin's suppression term.

So, from this analysis of the random movement of bubbles, we can conclude that neither the volume diffusion mechanism nor the surface diffusion mechanism can solely explain the observed FGR. However, since the Mikhlin's suppression term in the bubble diffusion coefficient suppresses the diffusion of small bubbles, an interesting scenario can further be considered if we provide the diffusion of vacancies into the grain and allow random motion of bubbles via surface diffusion including the Mikhlin suppression term. As the bubbles trap vacancies and grow, the suppression of diffusion of small bubbles would reduce. This would eventually enhance the diffusion of such bubbles and account for a higher fractional gas release.

4.3 FGR due to combined random and directed bubble movement in a vacancy concentration gradient

We now try to analyze the overall fractional FGR via intra-granular gas bubble movement, taking into consideration the directed movement in the vacancy concentration gradient as well as the random movement of the bubbles due to surface diffusion mechanism including Mikhlin's suppression factor. The simulation time for the analysis is 3 h and 110 h, similar to the directed movement analysis.

For incorporating the diffusion of bubbles due to surface mechanism, we determine the diffusion coefficient of bubbles by Eq.4.10. The existence of a vacancy gradient between the exterior surface (at low pressure) and the over-pressurized bubbles within the grain allows for the directed movement of the bubbles. The bubble evolution for this case at time $t = 0, 3$ and 110 h is depicted in Fig.4.5.

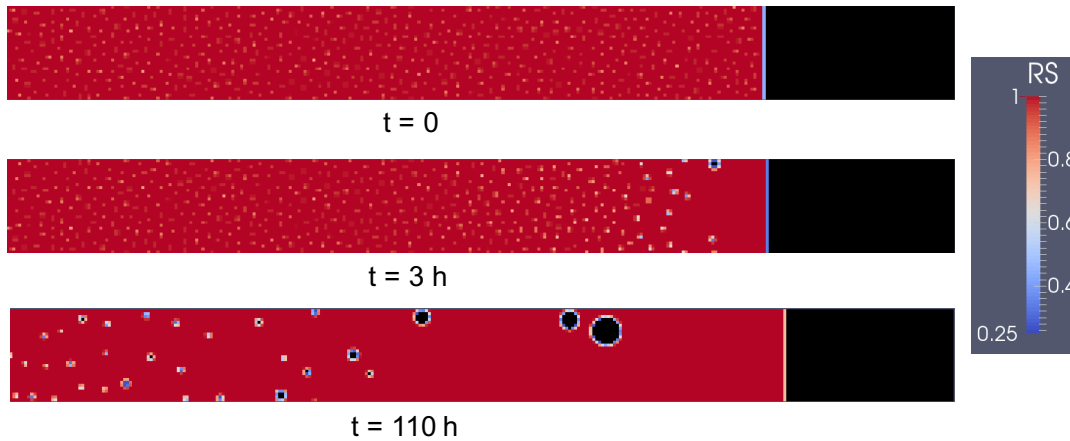


FIGURE 4.5: Bubble movement in a vacancy concentration gradient with random movement of bubble by surface diffusion for 110 hours of simulated time.

As can be observed from Fig.4.5, at time $t = 3$ h, the bubbles at the vicinity of the exterior surface have moved significantly as compared to time $t = 0$. The number of bubbles in the domain decreased from 2647 bubbles at time $t = 0$ to 2560 bubbles at $t = 3$ h. The decrease in the number of bubbles could be attributed to both, movement of bubbles outside the grain, as well as their coalescence. The mean diffusion coefficient of bubbles increased from its initial value of $3.76 \cdot 10^{-31} \text{ m}^2/\text{s}$ at $t = 0$ to $6.69 \cdot 10^{-23} \text{ m}^2/\text{s}$ at 3 hours, as can be seen from Fig.4.6. As the bubbles begin to trap vacancies coming from the free surface, they grow, which lowers the suppression of surface diffusion allowing the diffusion coefficient to increase. However, after a certain time, the dependency of the diffusion coefficient on the radius of the bubble start balancing out the increase due to reduction in the suppression and the growth of diffusion coefficient saturates to some extent. The dependence of D_b^{surf} on the radius of the bubble is explored further in the next section. The fractional FGR for the combined movement via directed and random surface diffusion of bubbles was found to be merely 0.84% after 3 hours of annealing simulation.

At time $t = 110$ h, the bubble movement is extended further into the solid (Fig.4.5). The number of bubbles in the domain reduced to 1879 bubbles at the end of 110 hours. It can be seen that the bubbles at the vicinity of the free surface have either moved out of the grain or have coalesced among themselves to form larger (and scarcer) bubbles. The radius of the largest bubble, which was also closest to the free surface, was found to be 20.72 nm. The mean diffusion coefficient of bubbles was found to be $3.91 \cdot 10^{-23} \text{ m}^2/\text{s}$ and the fractional FGR increased merely to 2.32% at the end of 110 hours of annealing.

We notice that the bubble diffusion due to surface diffusion was enhanced as the vacancies were trapped by the bubbles and caused significant bubble movement. The reduction in number of bubbles was, however, attributed majorly to the coalescence of bubbles rather than the transfer of bubbles outside the grain and, thus, the FGR is still too low. The values of various quantities at

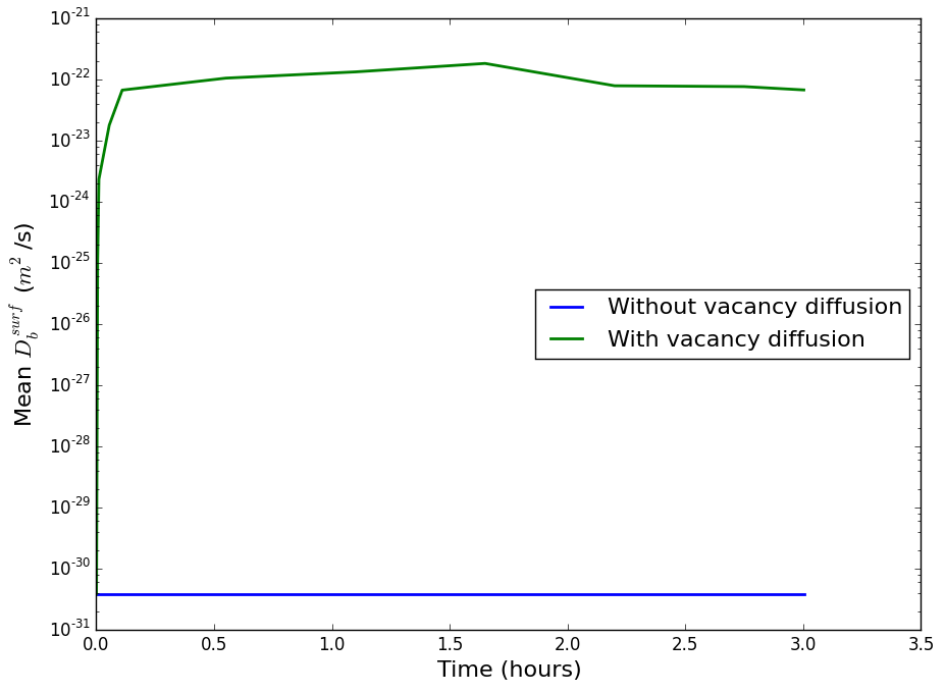


FIGURE 4.6: Bubble diffusion coefficient via surface mechanism with and without the diffusion of vacancies in 3 hours of simulated time.

time $t = 0, 3$ and 110 h for the case are presented in Table 4.2 and the mean radius of bubbles along the domain is depicted in Fig.4.7.

time (hr)	Mean D_b (m^2/s)	Number of bubbles	Mean radius (nm)	Mean gas content (at)	FGR (%)
0	$3.76 \cdot 10^{-31}$	2647	0.719	167.66	-
3	$6.69 \cdot 10^{-23}$	2560	0.743	171.65	0.84
110	$3.91 \cdot 10^{-23}$	1879	0.899	231.09	2.32

TABLE 4.2: Evolution of various quantities with time for the combined directed and random movement case.

4.4 Dependence of bubble diffusion coefficient via surface diffusion mechanism on the bubble radius

As stated earlier, D_b^{surf} depends on the radius of the bubble. The bubble diffusion coefficient by surface diffusion using Mikhlin's suppression term depends

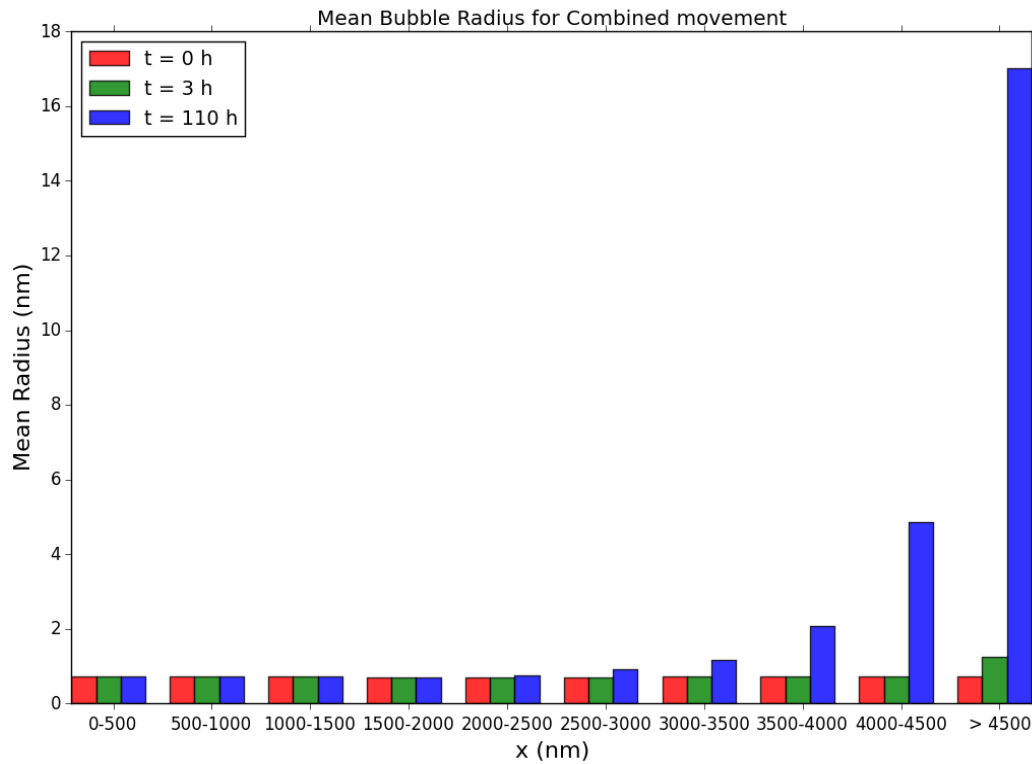


FIGURE 4.7: Mean Bubble radius along the domain for combined movement case.

on two opposing factors depending on the radius of bubbles:

$$D_b^{surf} = \underbrace{\frac{3}{2\pi} \frac{\Omega^{4/3}}{r_b^4}}_{(I)} D_s \underbrace{\left[1 - \frac{q}{V_b}\right]}_{(II)}^{N_b}$$

The first term (I) of Eq.4.10, reduces the bubble diffusion coefficient as the radius of the bubble increases. The mean of the first term for bubbles at different regions in the domain is depicted at time $t = 0, 3$ and 110 h in Fig.4.8.

It can be observed from the figure that in 3 hours, the first term decreases slightly for the bubbles near the vicinity of the free surface. In the first 3 hours, only the bubbles at the proximity of the free surface had started to grow (as can be noted from Fig.4.7) implying the slight decrease in the first term.

However, in 110 hours, the bubbles further into the domain had started to grow by trapping vacancies and the impact on the first term is evident from the figure. The first term decreased not only for bubbles at the vicinity of the free surface, but also for those further into the domain.

At the same time, the dependence of the second term (the suppression factor) on the bubble radius has an opposite effect. Increasing the radius of the bubble - leading to an increase in the volume of the bubble - increases

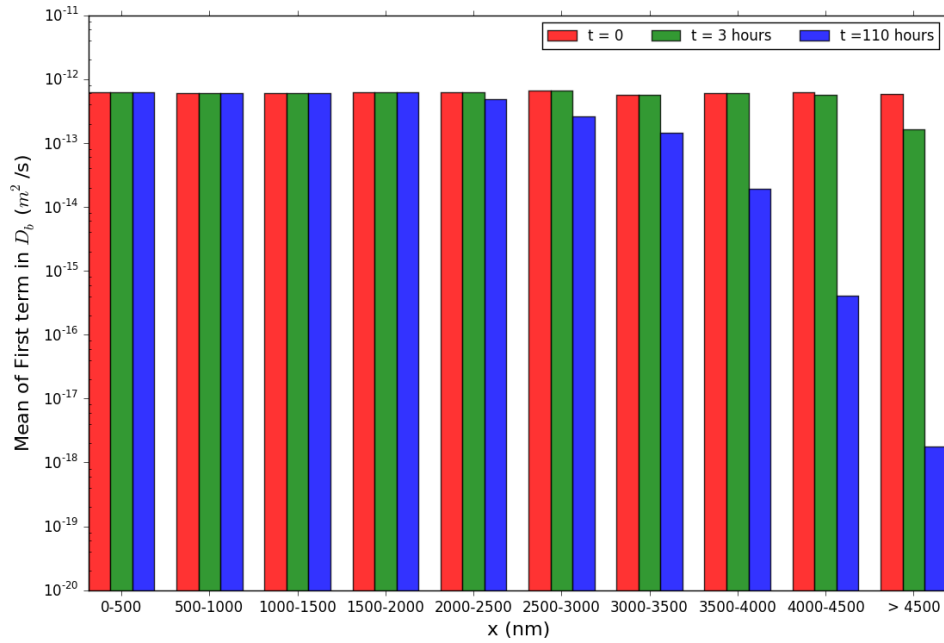


FIGURE 4.8: Mean of first term in D_b^{surf} along the domain up to time $t = 110$ h.

the suppression factor term (II), making the bubble diffusion coefficient to increase. The mean of the suppression factor term for bubbles at different regions in the domain is depicted at time $t = 0, 3$ and 110 h in Fig.4.9.

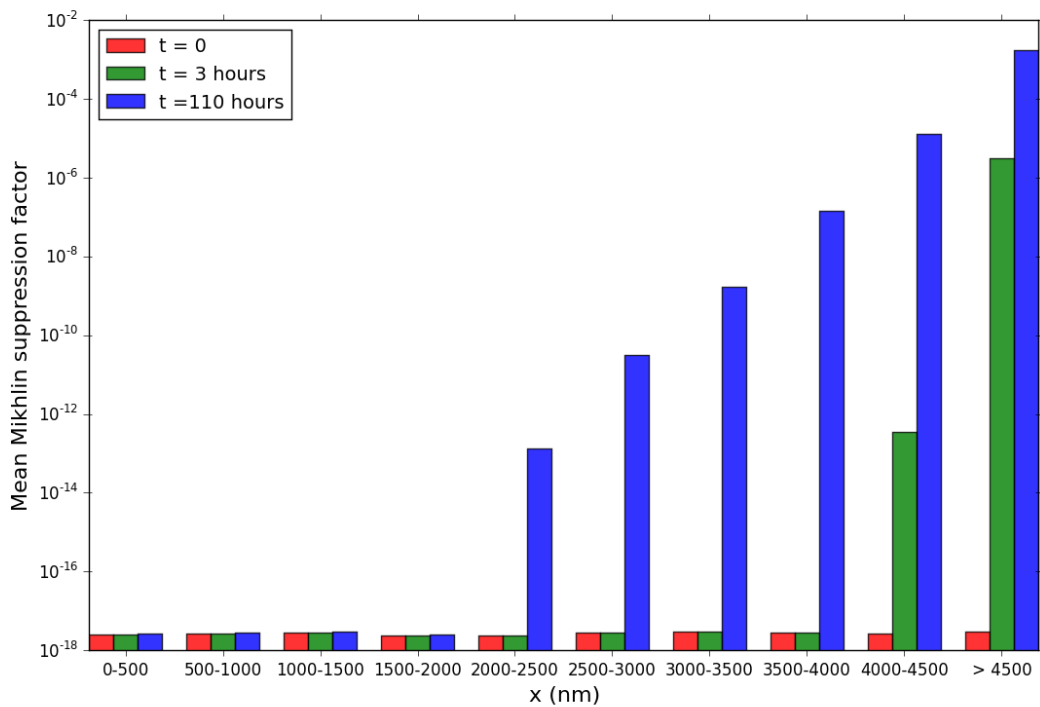


FIGURE 4.9: Mean Mikhlin Suppression Factor for bubbles along the domain up to time $t = 110$ h.

It is evident from the figure that the suppression factor term increases for

bubbles as they grow. It is also noted that this term increases faster than the decrease in the first term. The overall evolution of the bubble diffusion coefficient is then a competition between both the terms.

Fig.4.10 depicts the overall mean diffusion coefficient of bubbles at different distances within the domain. It can be observed that for time $t = 3$ h, the mean diffusion coefficient of bubbles in the vicinity of the exterior surface increases. This implies that the suppression factor term dominates the first term in the bubble diffusion coefficient expression. The extent of enhanced bubble diffusion coefficient is even further into the grain as time goes to $t = 110$ h. We note that the bubble diffusion coefficient enhancement due to increasing radius continues even at 110 hours of annealing time, however, the decreasing impact of the first term is evident as the increase in D_b^{surf} is not significant as compared to at time $t = 3$ h. This means that the contribution of the suppression factor term in aiding the bubble diffusion continues even at 110 hours of annealing, however, the fission gas release observed in 110 hours is merely 2.32%, which is not enough compared to the value from experiments.

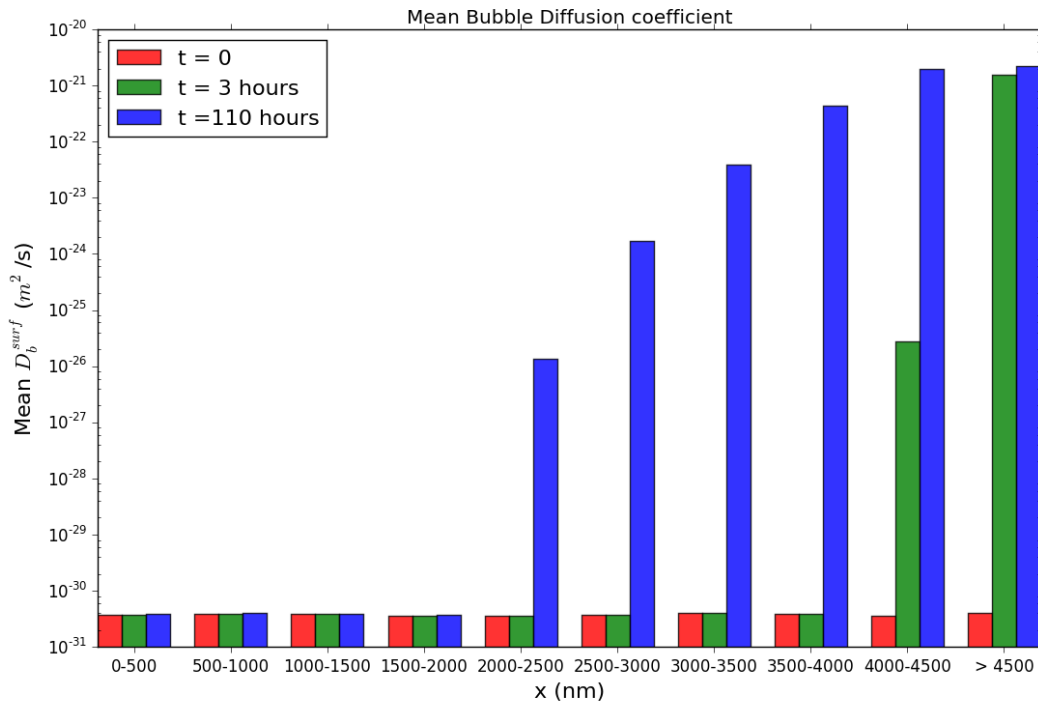


FIGURE 4.10: Mean Bubble diffusion coefficient for bubbles along the domain.

4.5 FGR due to combined movement until vacancy gradient lasts

Finally, we tried to continue the calculation until the concentration of vacancies in the solid reaches equilibrium value. This was done to check the extent

to which the FGR values reach as long as the vacancy concentration gradient lasts. The evolution of vacancy concentration in the domain length with time is plotted in Fig.4.11. It can be noted from the figure that the vacancy concentration values have not completely reached the equilibrium value. The simulation was discontinued after a simulation time of $t = 3080$ h because immediately after $t = 3080$ h, the two largest bubbles closest to the exterior surface coalesced with each other and formed a bubble with diameter larger than the width of the domain (see Fig.4.12). The model did not consider any condition for such a scenario and, thus, the simulation could not be continued further. As is evident from Fig.4.12, on continuing the simulation after 110

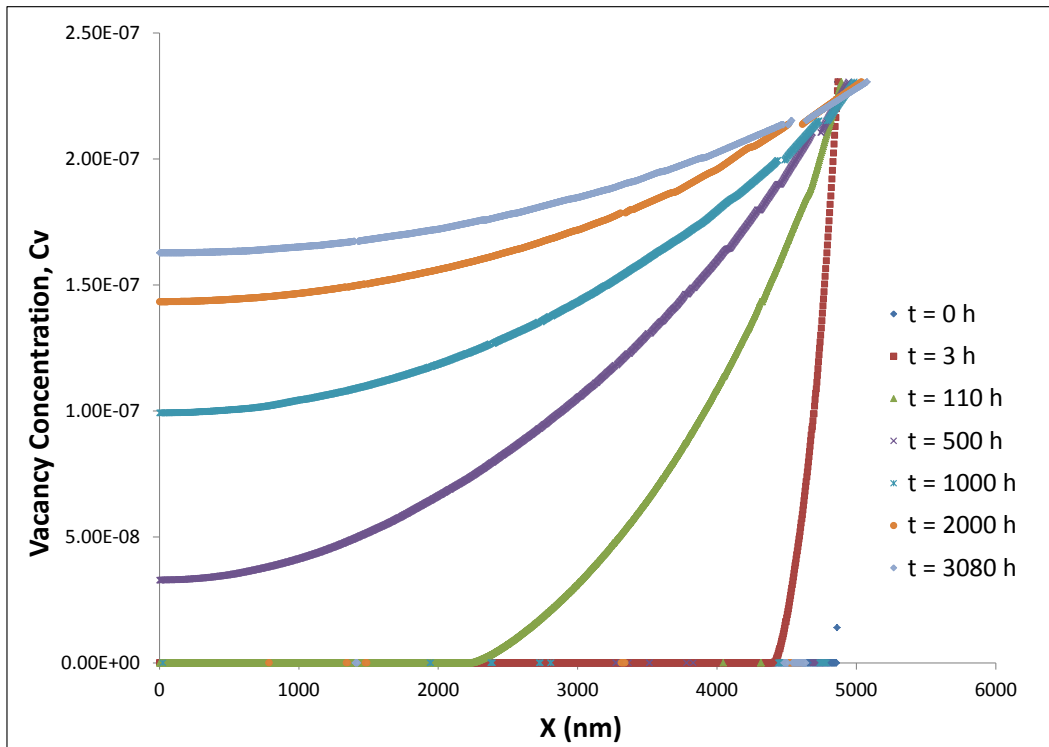


FIGURE 4.11: Vacancy concentration values along the grain at different times.

hours, the bubbles grew further and further into the domain. In the meantime, the grain also underwent swelling due to exchanging crystal atoms with vacancies generated at the free surface. The fractional swelling in the grain can be determined by the net change in the volume of the grain. At the time when the simulation ended ($t = 3080$ h), the fractional swelling in the grain was calculated to be 4.37%. The vacancy concentration at the rightmost end of the domain was $2.31 \cdot 10^{-7}$ and at the leftmost end was $1.63 \cdot 10^{-7}$ at $t = 3080$ h. The two largest bubbles, before their coalescence and eventually before the end of simulation, had radii of 53.83 nm and 31.68 nm, respectively.

At $t = 3080$ h, only 20 bubbles remained in the domain with a mean bubble diffusion coefficient of $1.39 \cdot 10^{-21} \text{ m}^2/\text{s}$ and a mean radius of 20.4 nm. The bubble distribution in the entire domain is depicted in Fig.4.13. The FGR from

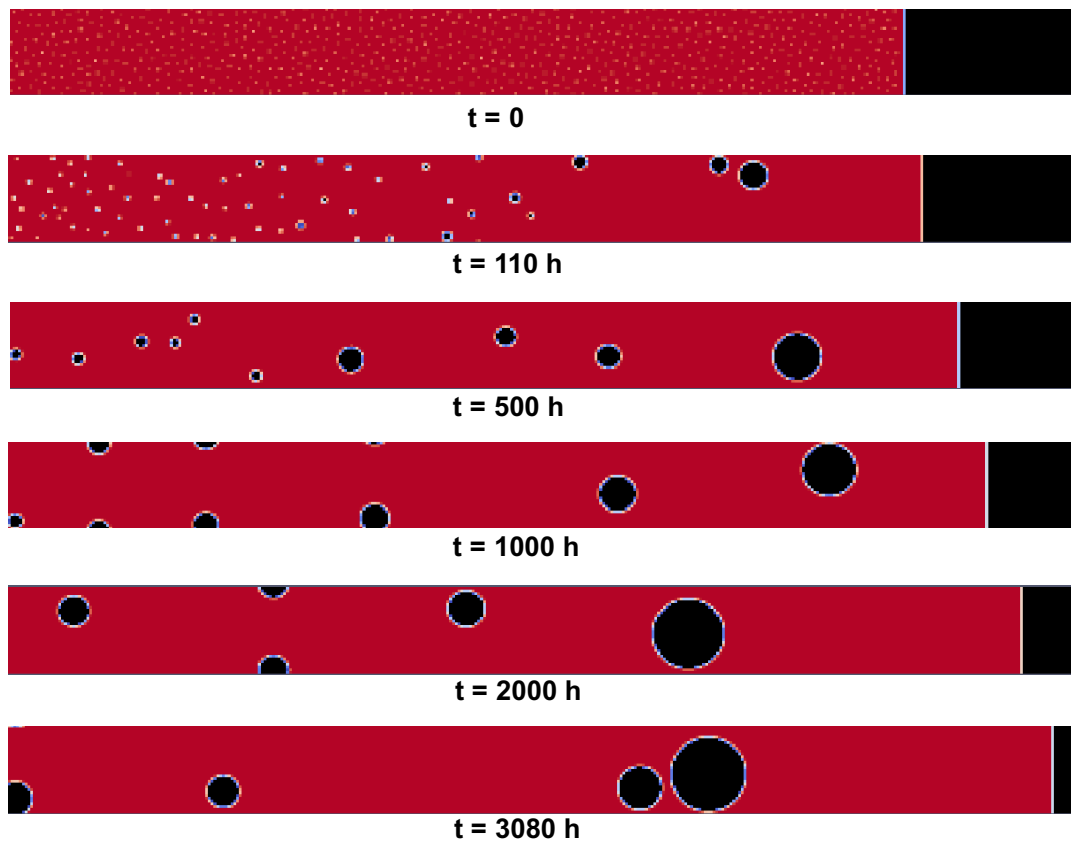


FIGURE 4.12: Bubble distribution in the domain until vacancy gradient lasts.

the grain in 3080 hours was still found to be 2.158%, same as that at 110 hours. Note that this value is lower than the one presented at $t = 110$ h (2.32%) as the calculations up to $t = 110$ h were done 10 times to account for the variability due to randomness and the mean of these calculations was used as the FGR value, whereas, only one of these calculations was continued for the longer duration and it had a FGR of 2.158% at $t = 110$ h.

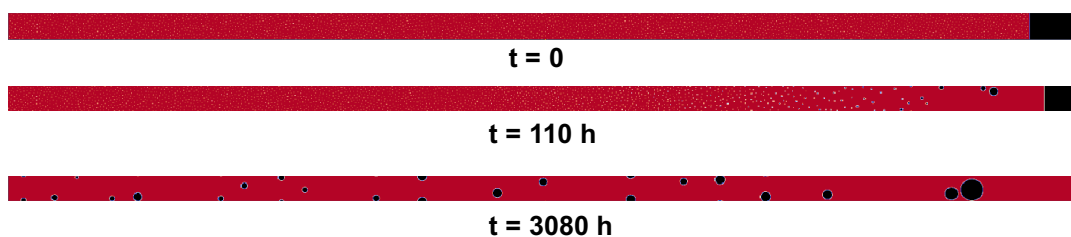


FIGURE 4.13: Bubble distribution in the entire domain at the end of the simulation.

The bubbles grew by trapping the vacancies and coalesced among themselves but did not move out of the grain, thus, not contributing to the FGR. Even if we assume that the large bubble (nearest to the free surface) formed after coalescence moves out of the grain at some point, the FGR would reach

18.5%. So, even though the simulation could not be carried out till the equilibrium value for vacancy concentration was reached, it is still conclusive that the extent of FGR would still be less than the equivalent target value of $\sim 27\%$ from experiments.

After $t = 3080$ h, the diffusion coefficient of bubbles will be reduced due to its dependence on the bubble radius (quite large by $t = 3080$ h) because the increase of Mikhlin's term is already finished everywhere in the domain. The mean D_b^{surf} values of the bubbles along the domain up to $t = 3080$ h is depicted in Fig.4.14. Only D_b^{surf} are talked about because the volume diffusion is negligible compared to the surface diffusion as the bubbles grow.

So, as the equilibrium value of vacancy concentration would be attained, there will neither be a driving force for the bubbles to move via directed movement, nor via random surface diffusion.

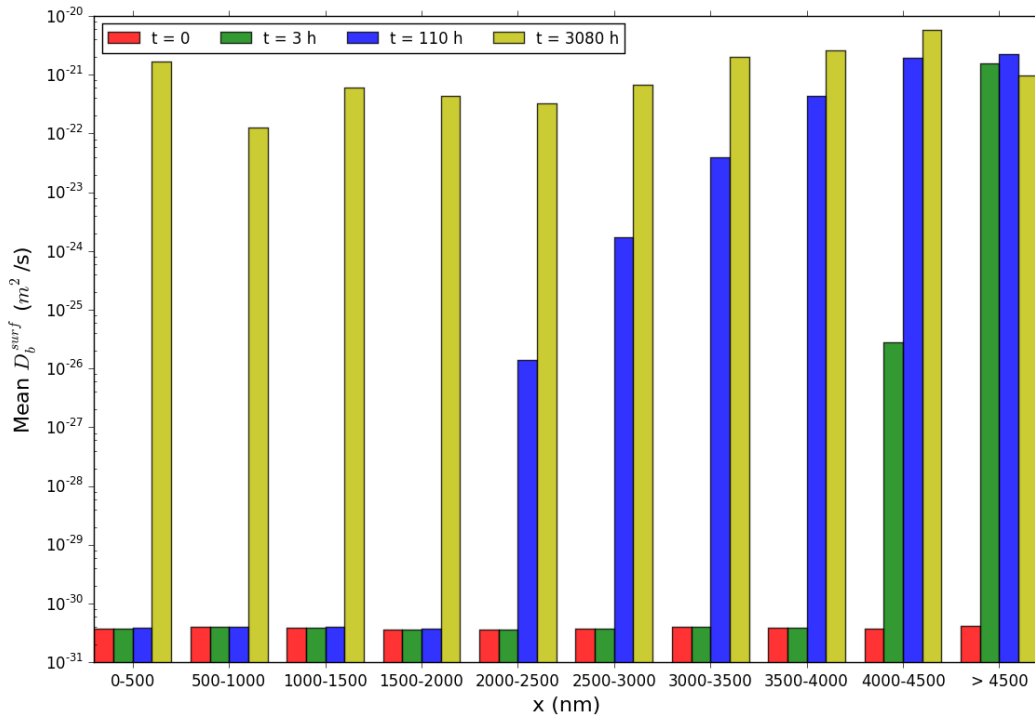


FIGURE 4.14: Mean Bubble diffusion coefficient for bubbles along the domain until simulation lasts.

4.6 Parametric investigation of Mikhlin's suppression term

From the analyses carried out in this chapter, it has been noted that the Mikhlin's suppression term affects the bubble migration and is an important parameter. We observed that the diffusion of bubbles via surface diffusion mechanism was negligible due to the suppression of small pressurized bubbles. However, as the bubbles trapped vacancies and grew, the suppression

of surface diffusion of bubbles reduced drastically and the bubbles could migrate. We now try to evaluate the influence of the suppression term on the bubble migration. In order to do so, the Mikhlin's suppression term was excluded from the expression of bubble diffusion coefficient. This was done by using the value of q in Eq.4.9 as 0, making $W_b=1$. $W_b=1$ implies that there is no hindrance in the transfer of ad-atoms on the surface of the bubble. The resulting expression which is given by Eq.4.6 is used to calculate the diffusion coefficient of bubbles.

Here again, we do not consider the driving force of vacancy diffusion and consider only random movement by surface diffusion mechanism. The simulation was carried out for 3 hours of annealing. The bubble distribution in the enlarged domain near the free surface from time $t = 0$ to $t = 3$ h is shown in Fig.4.15(a). It was observed that the mean value of D_b^{surf} was very large. At time $t = 0$, the mean value of D_b^{surf} was found to be $6.04 \times 10^{-13} \text{ m}^2/\text{s}$. Due to the high diffusion coefficient, the bubbles were observed to move quickly and coalesce with each other and the number of bubbles reduced from 2647 to just 5 bubbles at time $t = 3$ h. The bubble distribution via surface diffusion mechanism at time $t = 3$ h in the entire domain is depicted in Fig.4.15(b). The

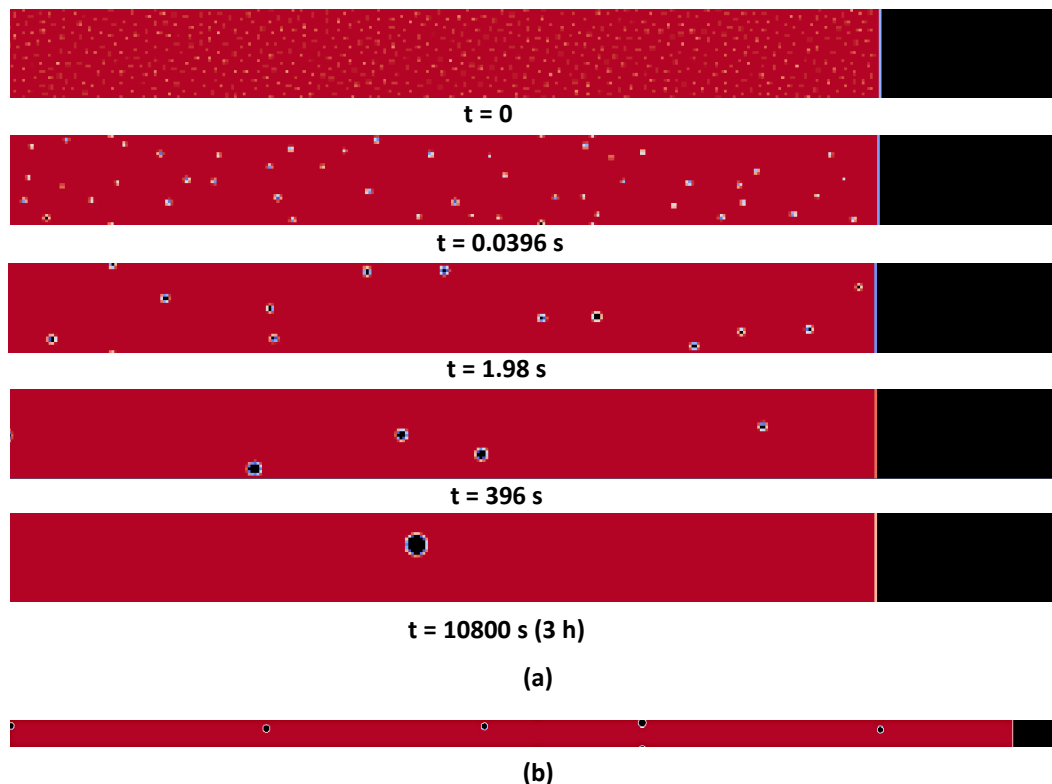


FIGURE 4.15: Bubble distribution due to random movement by surface diffusion mechanism at time = 3 hr.

D_b^{surf} values reduced gradually as the bubbles grew by coalescence and the mean D_b^{surf} at time $t = 3$ h was found to be $1.46 \times 10^{-18} \text{ m}^2/\text{s}$. The mean radius of the remaining 5 bubbles was found to be 16.33 nm. The fractional FGR in

this time was calculated to be 6.64%. This suggests that the majority of the bubbles coalesced with each other due to their high diffusion coefficient and still contain the larger part of the gas content within them.

Since the FGR values were comparatively higher for this case in 3 hours of annealing, this case was continued further for a longer duration. The simulation was carried out up to the time $t = 5500$ h. It was, however, realized that the remaining 5 bubbles also coalesced with each other leaving a single large bubble to move within the grain. This bubble can no longer coalesce with any other bubble, however, in principle, due to the periodicity conditions along the top and bottom boundaries, there exist bubbles similar to the one large bubble which it can interact with. So, in order to encounter the problem in a more realistic manner, we consider a domain 10 times larger in the vertical direction. For the new case, we consider the initial conditions to be the same as at time $t = 3$ h. The new domain is a $5120\text{nm} \times 1280\text{nm}$ box with grid size of 4 nm (i.e., a mesh of 1280×320 cells). Using the periodic conditions, the initial number of bubbles for the new case are 50. The mean radius of the 50 bubbles is 16.3 nm and the mean bubble diffusion coefficient is $1.46 \times 10^{-18} \text{ m}^2/\text{s}$. The initial conditions of the domain with the bubbles (at $t = 0$, after the first 3 hours) are depicted in Fig.4.16.

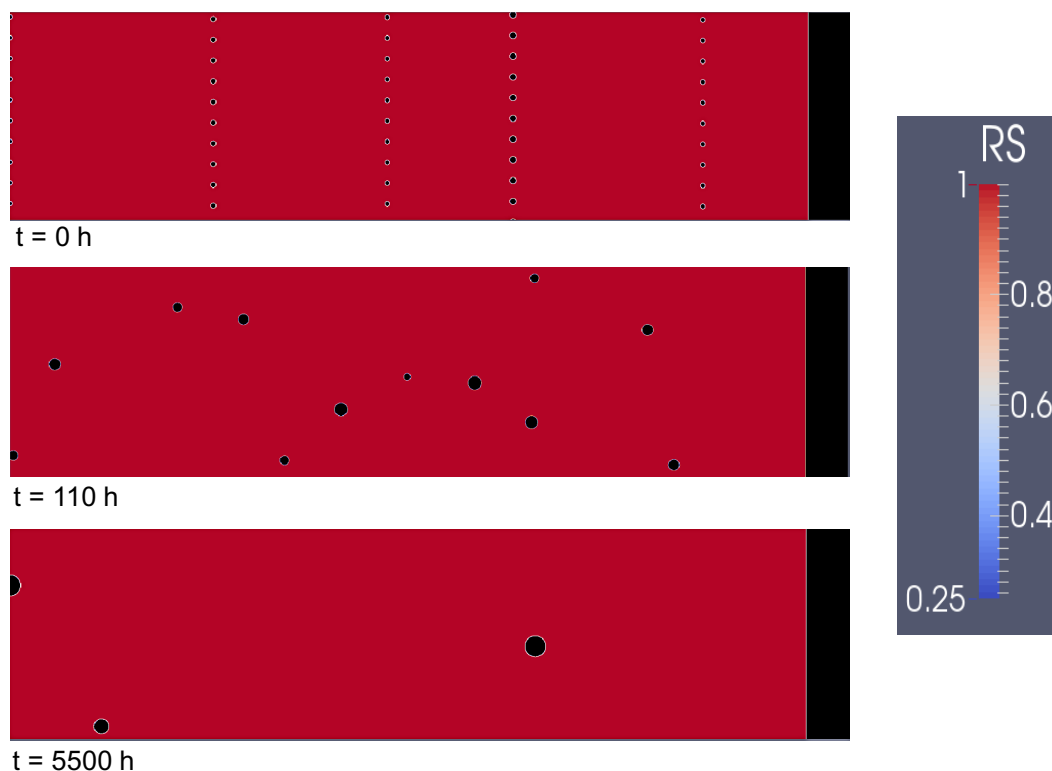


FIGURE 4.16: Random movement of bubbles via surface diffusion in the new domain at time $t = 0$, $t = 110$ h and $t = 5500$ h, after the first 3 hours.

The simulation was carried out and we observed that the bubbles moved randomly within the grain. The bubbles majorly coalesced with each other

and at time $t = 110$ h, only 12 bubbles remained in the grain (Fig.4.16). However, no bubbles moved out of the grain and, thus, did not contribute to any further FGR. As the simulation continued, further coalescence occurred and some bubbles also moved out of the grain. By the end of the simulation time of 5500 hours, only 3 bubbles remained within the grain. The mean radius of these bubble was 57.96 nm and the mean bubble diffusion coefficient was $1.085 \cdot 10^{-20} \text{ m}^2/\text{s}$. The overall FGR at $t = 5500$ h after the first 3 hours was calculated to be 28.67%. This FGR had been achieved at ~ 3366 h and then the bubbles continued to move randomly within the grain but did not contribute to further FGR. The bubble distribution at time $t = 5500$ h is depicted in Fig.4.16.

This investigation shows that even after neglecting the Mikhlin's suppression term, the random movement of bubbles do not explain the observed FGR obtained after 3 hours of annealing. The target values for FGR are reached in 3366 hours, which implies that in order to attain the target FGR in 3 hours, the value of D_s required would have to be $\sim 10^3$ times larger with no Mikhlin's suppression of surface diffusion. However, in our opinion, doing so would lead us too far from the literature recommendations.

4.7 In Closing

The random movement of bubbles via volume and surface diffusion mechanisms was discussed in this chapter. It was noted that neither of these mechanisms caused significant bubble migration if no other driving force (vacancy flux) was added to the simulation. However, with the diffusion of vacancies into the domain, the suppression of surface diffusion was reduced and some bubble migration could take place. The FGR from this combined movement by directed and random surface diffusion was found to be 0.84% in 3 hours and 2.32% in 110 hours. Further continuing the simulation even up to 3080 hours did not lead to any further FGR. The obtained values of FGR are very insignificant as compared to our reference experiment (with 27% FGR in 3 hours of annealing).

The Mikhlin's suppression factor was noted to be a key parameter in bubble diffusivity via surface diffusion mechanism and was studied to see its impact on bubble migration and FGR. Not accounting for the suppression of surface diffusion allowed us to achieve high bubble mobility and 6.64% FGR in 3 hours. The simulation was further extended and a FGR of 28.67% could be obtained in ~ 3366 hours. However, such FGR is observed in 3 hours of annealing in our reference experiment.

So from the analyses carried out in this chapter, it can be concluded that, as far as crystal atoms diffusion at the surface and the Mikhlin's suppression term are reliable, the gas bubble migration in a vacancy gradient and its random movement cannot solely be responsible for the high value of FGR observed during post-irradiation annealing tests. This result does not depend on the diffusion coefficient of vacancies since we showed that even if the calculation is performed until vacancy equilibrium is reached, the FGR is too low as compared to the experiment.

Chapter 5

Bubble movement via Dislocations

It has been widely accepted that the intra-granular bubbles have an important role to play in the FGR during post-irradiation annealing (PIA) tests. However, it was analyzed in the previous chapters that the mechanisms of directed movement of bubbles in a vacancy gradient, as well as their random movement, could not account for the high values of FGR observed during PIA tests. In this chapter, we discuss a scenario of FGR via the mechanism of dislocation climb and bubble movement along with it. In order to carry out the analyses, dislocations have been incorporated into the BEEP Model. The methodology adopted in the model is discussed along with simple 3-D analyses to understand the behaviour of dislocations and bubble movement.

5.1 Introduction to Dislocations

As introduced in Chapter 1, dislocations are linear defects, around which the atoms of the crystal lattice are misaligned. The two types of dislocations are the "edge" dislocation, caused by the termination of a plane of atoms in the middle of a crystal, and the "screw" dislocation, resulting from shear distortion such that the atoms over the cut surface are shifted in a direction parallel to the dislocation line. For the case of the edge dislocations, the adjacent planes are bend around the edge of the terminating plane so that the crystal structure is perfectly ordered on either side. The screw dislocation is rather difficult to visualise, but basically comprises a structure in which a helical path is traced around the dislocation line by the atomic planes of atoms in the crystal lattice. The direction and magnitude of the distortion resulting from the presence of a dislocation is expressed in terms of a Burgers vector (b), which is perpendicular to the dislocation line for an edge type, whereas parallel to the dislocation line in the cases of the screw type dislocations. Dislocations can be observed using transmission electron microscopy, field ion microscopy and atom probe techniques.

In the nuclear fuels, dislocation networks are likely to be formed due to the slowing down of fission fragments in high temperature conditions during in-reactor operations. Point defect clusters and dislocation loops produced in bulk uranium dioxide by fission damage were observed and studied by TEM

by Whapham and Sheldon [224]. Onofri et al. [225] recently carried out a full characterization of dislocations in ion-irradiated polycrystalline UO_2 . Studies from the thesis of Michel [226] showed large bubbles (tens nanometers in size) on the dislocation network whereas nanometer-sized bubbles between the dislocation lines suggesting that dislocations are preferential sites for the growth of fission gas bubbles.

5.1.1 Mechanisms of Dislocation movement

Dislocations can move if the atoms from one of the surrounding planes break their bonds and re-bond with the atoms at the terminating edge. The movement of dislocations can occur due to either of the two mechanisms discussed below.

Dislocation glide

At low temperatures, the movement of dislocations occurs by the mechanism of gliding. For a dislocation to glide, the atomic rows in the vicinity of the core of the dislocation must make a small displacement (see Fig. 5.1). In order to glide, the dislocation must, therefore, overcome an intrinsic friction to the atomic stack. It is a conservative movement of dislocations without the assistance of point defects. The glide movement takes place only in the plane that contains the dislocation line and the Burgers vector.

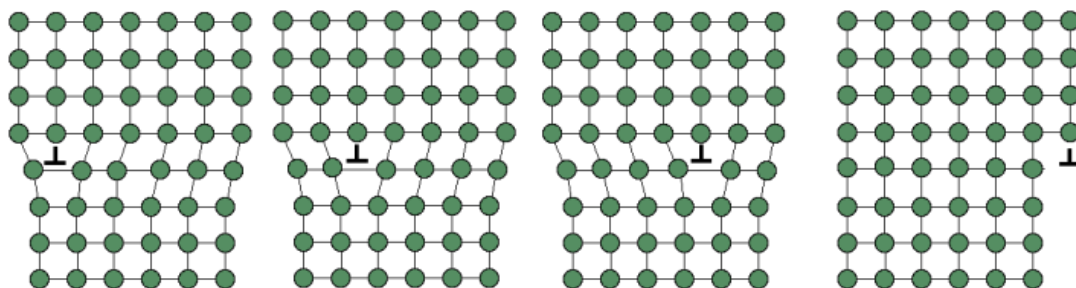


FIGURE 5.1: Dislocation movement via glide mechanism.

Dislocation climb

Edge dislocations can also move by a different mechanism. This particular process of dislocation movement is called climb of dislocations. Unlike the glide mechanism, the movement does not take place in the glide plane of the dislocation but perpendicular to it. Moreover, this mechanism is a non-conservative displacement, assisted by the atomic diffusion phenomena (Fig. 5.2). The migration of point defects occur more easily at high temperatures than at low temperatures, and thus, the dislocation climb can be activated thermally.

A dislocation climbs as a result of vacancies diffusing either from or to the dislocation core. The climb is called a positive climb if a vacancy replaces an

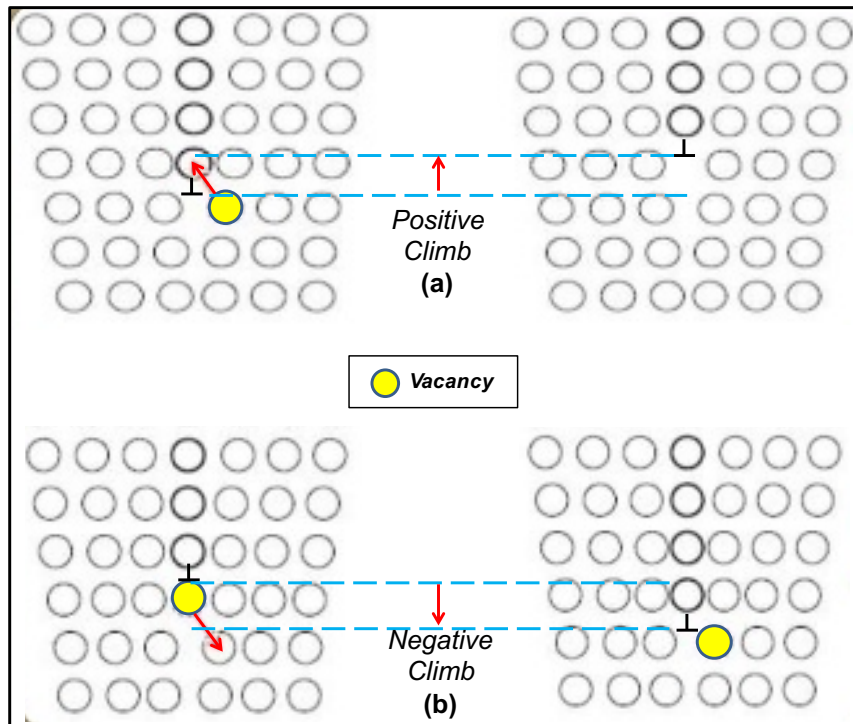


FIGURE 5.2: Dislocation movement via climb mechanism: (a) Positive climb by vacancy annihilation, (b) Negative climb by vacancy generation.

atom from the half plane, whereas it is called a negative climb if the vacancy is removed from the half plane of atoms.

5.2 Scenario of bubble movement with dislocation climb

As stated in the previous chapters, due to the low solubility of fission gases in the UO_2 fuel matrix, the gas atoms precipitate into bubbles. These bubbles can be intra-granular, formed within the grain, or inter-granular, forming at the grain boundaries. With the presence of dislocations in the matrix, the gas atoms can also segregate towards the dislocations. Sonoda et al. [227] studied the formation of the rim structure in irradiated UO_2 through high resolution SEM and TEM and observed the dislocations and grain boundaries to be heavily decorated with fission gas bubbles. Studies have shown that there is a strong thermodynamic driving force for the segregation of fission products to dislocations. Segregation of xenon to dislocations and grain boundaries in uranium dioxide was studied using pair potential calculations by Nerikar et al. [49]. They found segregation of Xe to tensile regions around the dislocations in UO_2 . They further stated that the Xe segregation to the screw dislocation was stronger as compared to the edge dislocation. Segregation of ruthenium

to edge dislocations in uranium dioxide was analyzed using atomic level simulations by Goyal et al. [228]. They found that the small Ru^{4+} tends to segregate in the compression region of the strain field for the edge dislocations in UO_2 and supported the conclusions of the study by Nerikar et al. [49] for Xe segregation. It has been proposed that the fission gases may diffuse faster through the fuel grains (along dislocations) due to the relatively lower density of material present in the core of a dislocation [229]. Earlier simulations have shown a significant diffusivity enhancement of the intrinsic O^{2-} and U^{4+} species in the tensile region of edge dislocations' strain fields in UO_2 [230]. Murphy et al. [50] studied the influence of dislocations on the diffusivity of Xe atoms in UO_2 using molecular dynamics (MD) simulations employing empirical potentials. Their simulations suggest that the activation energy for Xe diffusion in the tensile region of the dislocation strain field is reduced dramatically so long as the Xe atoms are isolated. They concluded that Xe atoms in the vicinity of dislocations are swept-up and channelled along the dislocation where they become trapped in the form of small bubbles.

The fission gas bubble distribution in post-irradiation annealed UO_2 was examined by TEM by Whapham [52]. At dose rates of 1.6×10^{20} fission/ cm^3 , he observed that the bubbles were coarser than that expected by the homogeneous nucleation of the bubbles, and it was believed that the bubbles coalesced. Large areas of the matrix were found to be clear of bubbles, and this was attributed to sweeping of the bubbles by the dislocation loops and network.

Fission gas release from irradiated UO_2 fuel under high-temperature annealing conditions was modelled by Veshchunov and Shestak [231]. As the dislocations and grain boundaries can act as sources of vacancies, they incorporated the model for dislocation climb as a mechanism of bubble movement and FGR along with the mechanism of bubble movement in a vacancy gradient. According to [231], the bubble sweeping via dislocation climb mechanism offers an additional mechanism of bubbles transport to grain boundaries to explain the burst release observed in experiments ([128, 96, 131]). However, after some time, a strong pinning of dislocations by swept bubbles can saturate this source (dislocations) of point defects and grain boundaries become the dominant source of vacancies during the subsequent period of the annealing tests. The bubbles movement can then be attributed to their biased movement in a vacancy gradient field arising from the flux of vacancies from the grain boundary in their model. However, as we see from our previous analyses (Chapter 3 and 4), the movement of the bubbles in a vacancy gradient is not sufficient to address the question of high FGR during PIA tests. Consequently, the influence of dislocations on bubble movement need to be re-examined.

In this chapter, we implement the dislocations in the BEEP Model to analyse the dislocation climb mechanism and its ability to cause bubble movement and eventually lead to enhanced FGR. We consider a scenario in which the bubbles pinned on the dislocation can move along with it when it moves via dislocation climb mechanism. Figure 5.3 depicts the scenario of bubble movement with dislocation climb.

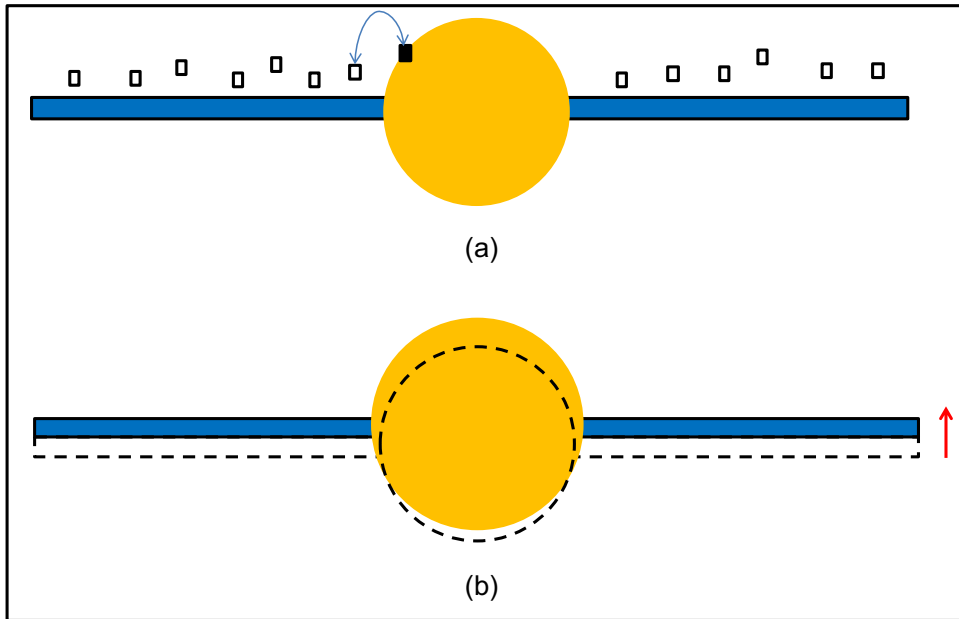


FIGURE 5.3: Scenario of bubble movement via dislocation climb mechanism.

Fig.5.3(a) shows a dislocation and a bubble pinned on it. The vacancies generated along the dislocation can replace the crystal atoms present at the surface of the bubble. After several such exchanges between the vacancies and the crystal atoms, a new layer of atoms can form along the dislocation, causing it to climb (Fig.5.3(b)). The bubble pinned to the dislocation grows (and relax its pressure), and is supposed to move along with the dislocation. This bubble can eventually move out of the grain, enhancing FGR.

So, in this scenario, over-pressurized bubbles that are pinned on edge dislocations are a driving force for the dislocation climb mechanism and move with the dislocation as it climbs.

5.3 Implementation of Dislocations in BEEP Model

The goal of this development in the BEEP Model is to perform the same kind of calculation as in Chapter 4, namely an elongated domain along the x-axis, containing a free surface on the right and a symmetry plane for $x = 0$, but also taking into account dislocations. Note that a 3-D approach is mandatory if the dislocation lines are explicitly represented and evolve in the model.

5.3.1 Assumptions

In order to implement dislocations into the BEEP Model, several assumptions and simplifications were done. Some of these are stated below:

- The orientation of the dislocations is set such that it is compatible with the periodic condition in the y and z directions. The considered dislocations are parallel to the y and z axes. They are edge dislocations.

- The diffusion of vacancies towards the bubble pinned on the dislocation, along the dislocation, is considered to be dominant as compared to the diffusion of vacancies from the dislocation towards unpinned bubbles.
- Bubbles are considered to be able to move along with the dislocation when it climbs.
- The coefficient of vacancy diffusion along the dislocations is considered as a parameter.
- No interaction between dislocations is considered. The interaction between two dislocations is modelled only as the interaction between their pinned bubbles.
- The bubbles pinned on the same dislocations equilibrate instantaneously with one another in terms of the Xe atoms and vacancies. Otherwise, a straight dislocation would not remain straight and that was beyond the scope of this thesis.

5.3.2 Formulation

The idea for the formulation of the growth of a bubble pinned on a dislocation was adopted from the approach of Speight and Beere [232] for the vacancy potential and void growth on grain boundaries. They demonstrate how cavity growth (and shrinkage) proceeds by absorption of vacancies generated on the grain boundaries. They relate the total load applied on the solid with the chemical potential of vacancies. Chemical potential of vacancies along the dislocation can be expressed in terms of the free energy (F) and the number of vacancies on the dislocation (N_{v_d}) as:

$$\mu = \left(\frac{dF}{dN_{v_d}} \right)$$

This can also be represented in terms of the formation energy of vacancy (E_{v_d}) as (See Annex J):

$$\mu = E_{v_d} + kT \ln(x_{v_d}) \quad (5.1)$$

if we define the vacancy concentration at equilibrium as:

$$x_{v_d}^{eq} = \exp\left(-\frac{E_{v_d}}{kT}\right)$$

then we get,

$$E_{v_d} = -kT \ln(x_{v_d}^{eq})$$

and the chemical potential can be represented as:

$$\begin{aligned} \mu &= -kT \ln(x_{v_d}^{eq}) + kT \ln(x_{v_d}) \\ \mu &= kT \ln\left(\frac{x_{v_d}}{x_{v_d}^{eq}}\right) \end{aligned}$$

For the case, where we consider that x_{v_d} is in general close to $x_{v_d}^{eq}$,

$$\mu = kT \ln \left(\frac{x_{v_d}^{eq} + \delta x_{v_d}}{x_{v_d}^{eq}} \right) \approx kT \left(\frac{\delta x_{v_d}}{x_{v_d}^{eq}} \right)$$

(because $\ln(1+x) \approx x$, when $x \ll 1$)

So, the Laplacian of μ is:

$$\nabla^2 \mu = \frac{kT}{x_{v_d}^{eq}} \nabla^2 x_{v_d} \quad (5.2)$$

because $\nabla^2 x_{v_d} = \nabla^2 \delta x_{v_d}$, since $x_{v_d}^{eq}$ is constant.

From the Fick's law, we have the diffusion equation as:

$$\frac{D_{v_d}}{\Omega} \nabla^2 x_{v_d} + \beta = 0$$

here $\frac{x_{v_d}}{\Omega}$ is a concentration in vac/m³, β is a source term in vac/m³/s, and D_{v_d} is the coefficient of vacancy diffusion along the dislocation in m²/s.

Using eq. 5.2, the above diffusion equation can be transformed into:

$$\nabla^2 \mu + \frac{\beta \Omega kT}{D_{v_d} x_{v_d}^{eq}} = 0$$

which can be written as:

$$\nabla^2 \mu + \frac{\beta \Omega kT}{D^*} = 0 \quad (5.3)$$

where $D^* = D_{v_d} \cdot x_{v_d}^{eq}$

Now, we can get the average vacancy chemical potential of the segment L_i (See Fig.5.4).

Integrating eq. 5.3 twice, with $\mu(x = L_i/2) = \mu(x = -L_i/2) = 0$, gives us:

$$\mu = -\frac{\beta \Omega kT}{2D^*} \left[x^2 - \left(\frac{L_i}{2} \right)^2 \right]$$

Integrating the above in the limits of $-L_i/2$ to $L_i/2$:

$$\int_{-L_i/2}^{L_i/2} \mu dx = -\frac{\beta \Omega kT}{2D^*} \int_{-L_i/2}^{L_i/2} \left[x^2 - \left(\frac{L_i}{2} \right)^2 \right] dx$$

and then dividing by L_i , we get the average vacancy chemical potential for i , as:

$$\bar{\mu}_i = \frac{\beta \Omega kT}{12D^*} L_i^2 \quad (5.4)$$

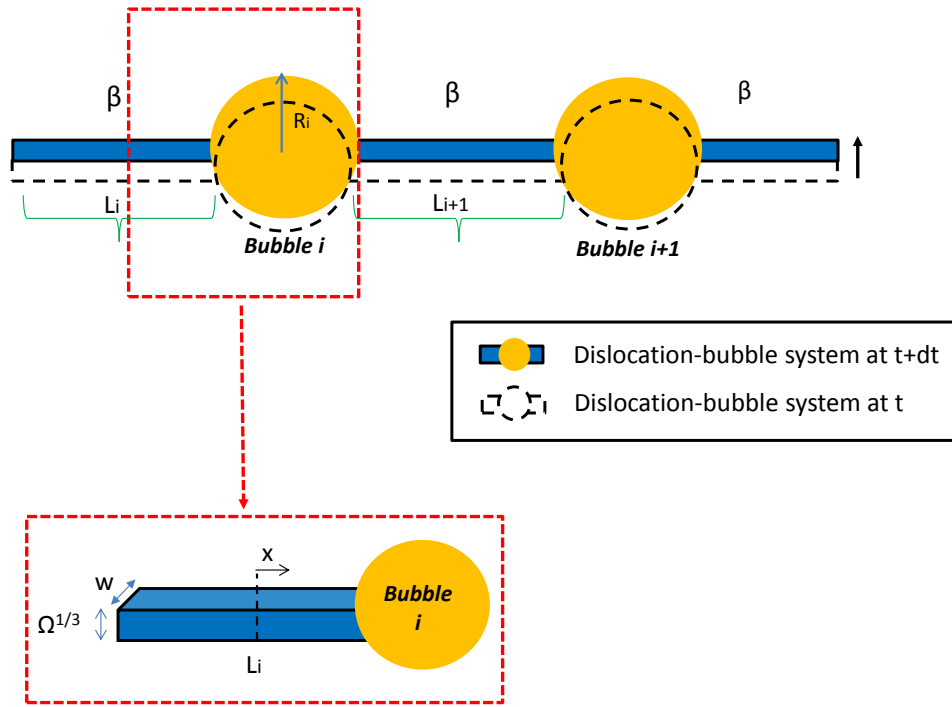


FIGURE 5.4: Pinned bubbles on dislocation.

In time Δt , in order to allow the dislocation to climb one layer ($\Omega^{1/3}$), vacancies are created in the dislocation region (of volume $\Omega^{1/3} * w * \sum_i L_i$) at a rate of β and are replaced by the atoms coming from the bubble surface.

At the same time, an additional volume is provided to the bubble because the crystal goes apart around the bubble when the dislocation climbs. This volume is $\Omega^{1/3} w \sum_i d_i$, where d_i is the diameter of the bubble 'i'.

The flux of vacancies arriving at the bubble 'i' per second is:

$$\left(\beta \Omega^{1/3} w \frac{L_i}{2} + \beta \Omega^{1/3} w \frac{L_{i+1}}{2} \right)$$

The net work done on the solid is (Fig.5.5):

$$\sum_{\text{bubble } i} \left[\underbrace{\beta dt \Omega^{1/3} w \frac{L_i + L_{i+1}}{2} \Omega}_{\text{(I)}} + \underbrace{\Omega^{1/3} w \sum_i d_i}_{\text{(II)}} \left(P_i - \frac{2\gamma}{R_i} \right) - \underbrace{P_{\text{ext}} \Omega^{1/3} w \left(\sum L_i + \sum d_i \right)}_{\text{(III)}} \right] \quad (5.5)$$

The term (I) represents the volume change of the bubble due to the flux of vacancies and term (II) represents the additional volume change. The term

(III) is the resistant work done on the system by the external pressure.

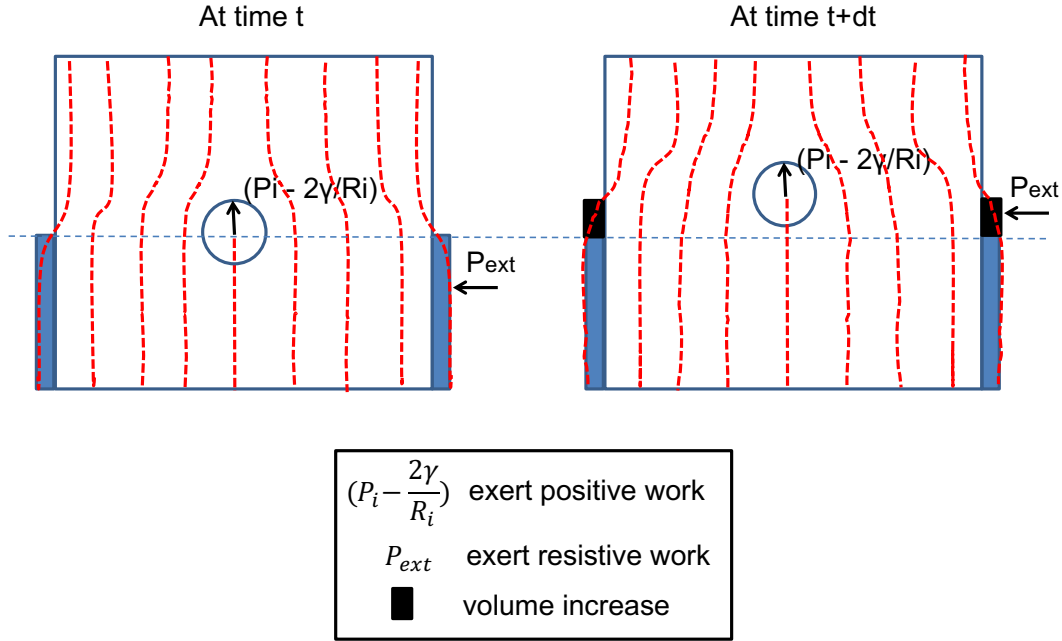


FIGURE 5.5: Net work done on the solid.

In time Δt , we add a volume of $\Omega^{1/3}w (\sum L_i + \sum d_i)$. In order to do so, we need to create $\frac{\Omega^{1/3}w \sum L_i}{\Omega}$ vacancies in volume $\Omega^{1/3}w \sum L_i$. This means:

$$\beta \Delta t * \Omega^{1/3}w \sum L_i = \frac{\Omega^{1/3}w \sum L_i}{\Omega}$$

which gives us

$$\beta \Delta t = \frac{1}{\Omega} \quad (5.6)$$

Using the expression for $\beta \Delta t$ from Eq. 5.6 in term (I) in Eq. 5.5, defining the sum of dislocation segment lengths and bubble diameter as L_{tot} , and considering that all the bubbles on the same dislocation are equilibrated (i.e., same P_i and R_i), we get the net work done in Eq. 5.5 as:

$$\Omega^{1/3}w \sum_{bubble\ i} \left(P_i - \frac{2\gamma}{R_i} - P_{ext} \right) L_{tot} \quad (5.7)$$

The net work done can be related to the vacancy chemical potential (average) as:

$$Net\ work\ done\ on\ the\ system = \sum_i \bar{\mu}_i \frac{\Omega^{1/3}w L_i}{\Omega}$$

Using the expression for $\bar{\mu}_i$ from Eq.5.4 and the net work done from Eq.5.7 and rearranging for β , we get:

$$\beta = \frac{12D^*}{kT} \frac{\left(P_i - \frac{2\gamma}{R_i} - P_{ext}\right) L_{tot}}{\sum_i L_i^3} \text{ in vacancy}/m^3/s \quad (5.8)$$

Moreover, for the dislocation velocity, we have $velocity = \frac{distance\ climbed}{time}$, so:

$$v_d = \frac{\Omega^{1/3}}{\Delta t}$$

and from Eq. 5.6, we can get $1/\Delta t$. So the dislocation velocity is defined in terms of β as:

$$v_d = \beta \Omega^{4/3}$$

The width of the dislocation, w , is not mandatory taken as $\Omega^{1/3}$ because the edge dislocation may not be the result of the addition of one crystallographic plan, but several. Indeed, due to the stacking fault energy, several added plans may be more favourable than just one. Following the analysis from the thesis of Le Prioux [233], we took the width $w = 3\Omega^{1/3}$.

With these formulations, dislocation climb continues as long as the bubbles on the dislocations are over-pressurized. A situation where the dislocation is highly decorated with bubbles (small $\sum_i L_i^3$) is also favourable for the dislocation climb as well as for an easy diffusion of vacancies along the dislocation (pipe diffusion) and a low formation energy of vacancies (E_{v_d}) in the vicinity of dislocations. The question to be asked is whether this dislocation climb mechanism is sufficient to explain the FGR in annealing condition?

5.3.3 Methodology

Several methods were added to the existing BEEP Model to account for the dislocations and their interactions with the existing modelled microstructure. Fig. 5.6 depicts the addition to the algorithm followed in the BEEP Model.

The general algorithm of the BEEP Model remains the same with new methods for the dislocations. At initialization, the dislocations are initialized through a set of characteristics defining the dislocation. While calculating the volume of the bubbles, the pinned bubbles also consider the effect of vacancy creation on the dislocation and vacancy flux through the dislocation. All the bubbles on a particular dislocation are equilibrated in terms of their volumes and gas content for simplicity. The centers of the pinned bubbles at the end of the time step are calculated taking into account the dislocation velocity. During the re-drawing of the bubbles, it is checked whether any new bubbles are pinned on any dislocation or whether coalescence occurred between bubbles during re-shaping. If two bubbles that are pinned on distinct dislocations coalesce, the resulting bubble is pinned on the dislocation of the bigger bubble. So, the other dislocation loses a bubble. Once all the bubbles are re-drawn, the time step is updated for the next calculation.

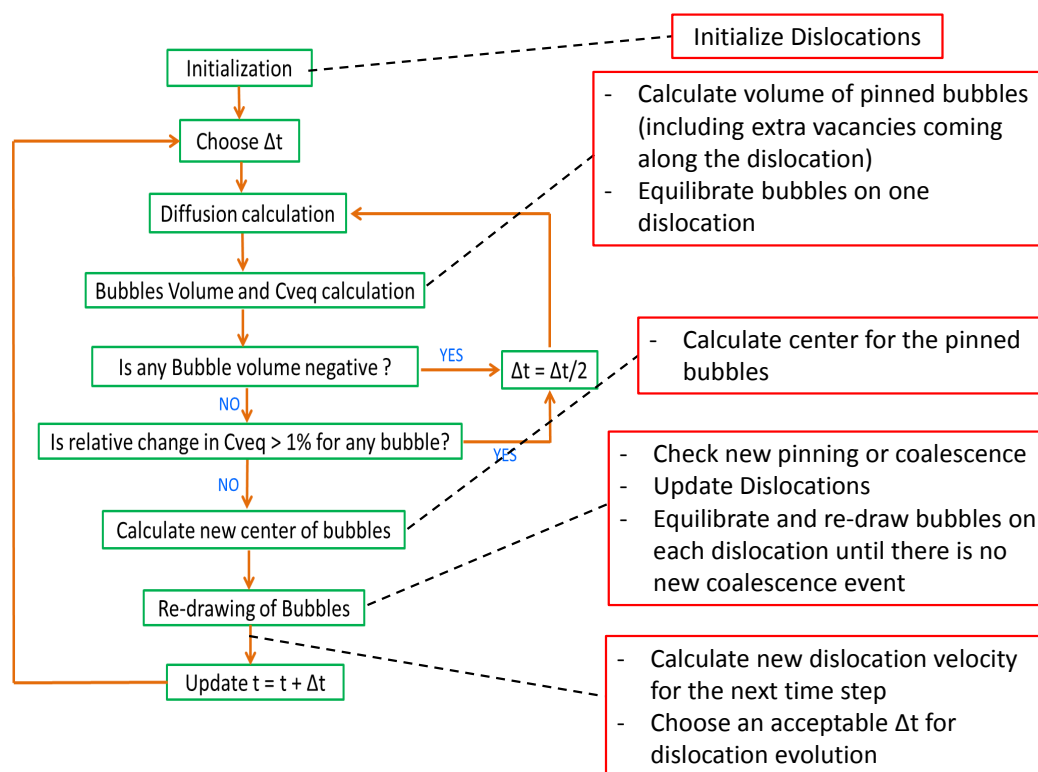


FIGURE 5.6: Incorporation of dislocations into BEEP Model.

Initialization

The dislocations are initialized through input files, which provide the values for different characteristics of the dislocations. The width of the dislocations, the coordinates of one point on the dislocation, a vector indicating the direction of the dislocations (which are straight lines), the dislocation ID (identification number), the coefficient of vacancy diffusion along the dislocation and the external pressure are provided as input.

Visualization

The visualization of the 3-D cases carried out for the analyses with dislocations was done using the PARAVIEW Application. Same as all the cases in the previous chapters, the domain was visualized in terms of the solid fraction, RS with $RS = 1$ (red) for solid cells, $RS = 0$ (black) for empty cells and RS in between 0 and 1 for the interface cells. For the 2-D cases, up to now, the domain could be visualized as a slice with bubbles visible on it. However, for the 3-D cases, the visualization of bubbles within the 3-D volume was difficult as the solid region (red) in the entire domain was overshadowing the bubbles (with interface cells of shade lighter than the red of the solid cells). The visualization of the 3-D domain can be seen in Fig. 5.7(a).

In order to avoid this, a filter was added to the visuals which only included the values of spin strictly less than 2. This caused the solid region (red) with

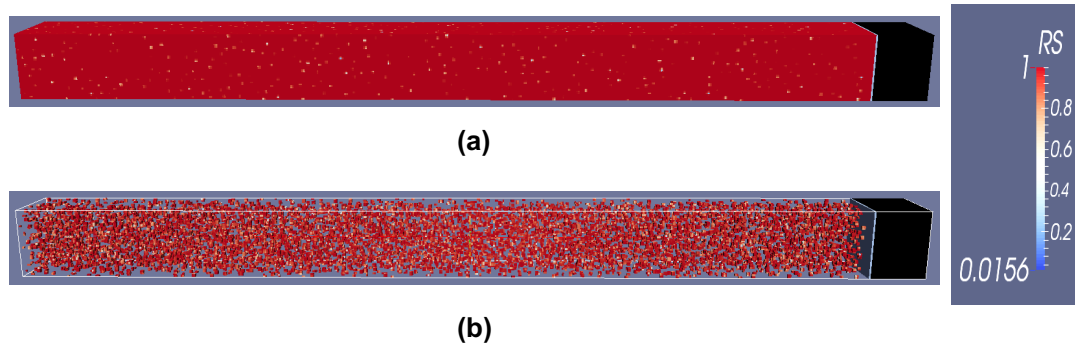


FIGURE 5.7: Visualization of 3D cases in the BEEP Model.

spin = 2 to be avoided from the visual and the interface cells and the empty cells of the bubbles could be visualized clearly (Fig.5.7(b)).

Calculating the volume of pinned bubbles

In general, the volume of the bubbles is calculated as presented in Section 2.3.4. However, for the bubbles pinned on a dislocation, the volume will also have the influence of the contribution from the vacancy flux into the bubbles from the dislocations. Fig.5.8 represents a system of dislocation and pinned bubble.

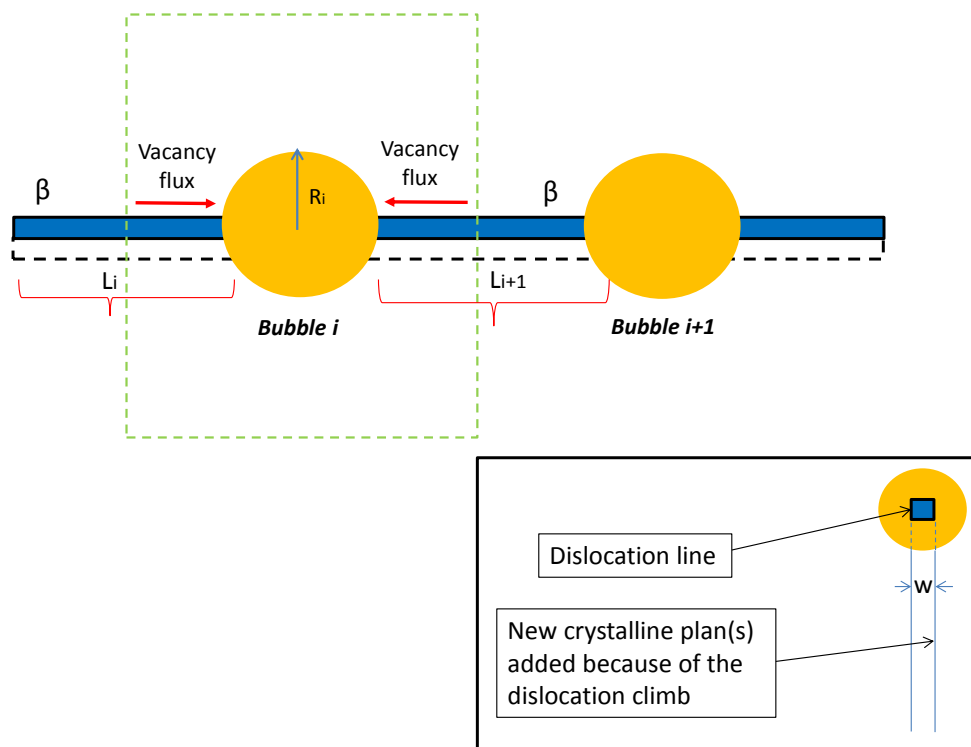


FIGURE 5.8: Calculating the volume of bubble pinned on a dislocation.

The total flux of vacancies (vac/s) into the bubble from the two regions of the dislocation around the bubble 'i' is given as:

$$\beta\Omega^{1/3}w\frac{L_i}{2} + \beta\Omega^{1/3}w\frac{L_{i+1}}{2}$$

and the volume added due to this flux of vacancies becomes

$$V_{flux_disloc} = \left(\beta\Omega^{1/3}w\frac{L_i}{2} + \beta\Omega^{1/3}w\frac{L_{i+1}}{2} \right) \Omega * dt$$

Apart from the vacancy flux, the volume of the pinned bubble is also increased due to the climb of the dislocation. This bubble volume increase can be compared to the increase in grain-boundary cavities due to vacancy formation which forces apart the adjacent crystals in [232]. This additional volume increase can be written as:

$$V_{add.} = \left(\beta\Omega^{1/3}w * 2R_i \right) \Omega * dt$$

So, apart from the volume increase calculated as usual, the pinned bubbles have an additional volume increase due to the V_{flux_disloc} and $V_{add.}$ as described above.

Equilibrating bubbles on a dislocation

If more than one bubble is pinned on a dislocation, then the bubbles are equilibrated in order to have the same effective pressure (bubble pressure minus the Laplace pressure) within the bubbles. This is done by taking the mean of the volumes and gas content of all the bubbles and providing this mean value to all the bubbles on that particular dislocation. Doing so allows us to focus on the dislocation climb mechanism for dislocation and bubble movement and ignore the flux of vacancies between the bubbles on a dislocation due to the difference in the effective pressures among them.

Center targets for bubbles pinned on dislocations

For the bubbles pinned on a dislocation, as well as for the new bubbles that have to be pinned to a dislocation, the center of the bubble needs to be on the dislocation at the end of the time step and so the center target is adjusted to lie on the dislocation. More precisely, $\overrightarrow{CC_T}$ is first calculated as usual (see Fig.5.9), but then C_T is corrected so that the bubble lie on the dislocation at time t+dt. So, random movement of bubbles are still allowed along the dislocation direction.

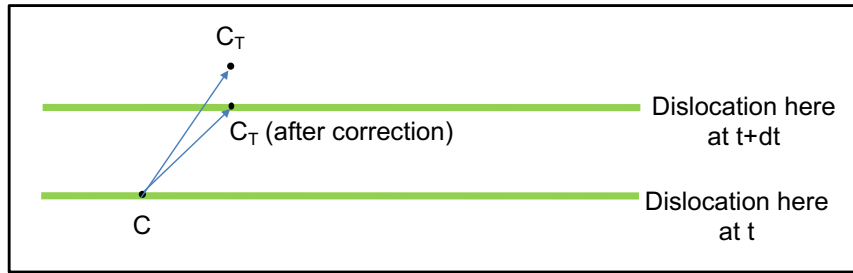


FIGURE 5.9: Correction of target center for pinned bubble.

Updating dislocations

During the re-shaping of the bubbles, it is checked if any new bubbles have been pinned on any dislocation or if coalescence of pinned or unpinned bubbles with any pinned bubble has occurred. If there is any new pinning or coalescence, then the affected dislocation characteristics, such as the bubble effective pressures and the segment numbers and lengths are updated. All the bubbles on a particular dislocation are then equilibrated to the same effective pressure, and re-drawn. The process of updating the dislocation characteristics, equilibrating the bubbles and re-drawing the bubbles is repeated until no new coalescence event is detected. Then the position of the point characterizing the dislocation is changed. The direction of the dislocation remains unchanged.

Calculating the new dislocation velocities

Once the dislocations and bubbles are updated, a new vacancy source term, β , and the new velocities of dislocations are calculated. The velocity of each dislocation depends on the characteristics of the bubbles pinned on it.

Choosing an acceptable Δt for dislocation evolution

The Δt is checked so that it respects the following conditions for all the dislocations:

- $v_d \Delta t \leq h$,
- Relative change in C_v^{eq} due to the vacancy flux along the dislocation during Δt is less than a threshold.

5.4 First 3D Test Case for Dislocation and bubble movement

A first 3D case was carried out with dislocations incorporated into the BEEP Model. We considered a domain with a size of $128\text{nm} \times 64\text{nm} \times 64\text{nm}$ and a grid size of $h = 4\text{nm}$. Like the previous cases, we consider an exterior region with a free surface. The length of the exterior region is 10nm . The domain contains

5 bubbles of radius 5 nm each, with the first bubble (designated as Bubble 1) pinned to a dislocation. Only one dislocation is assumed in the domain. The volume per atom of gas is taken equal to Ω , the atomic volume, in each bubble. The pictorial representation of the initial condition of the domain is shown in Fig.5.10.

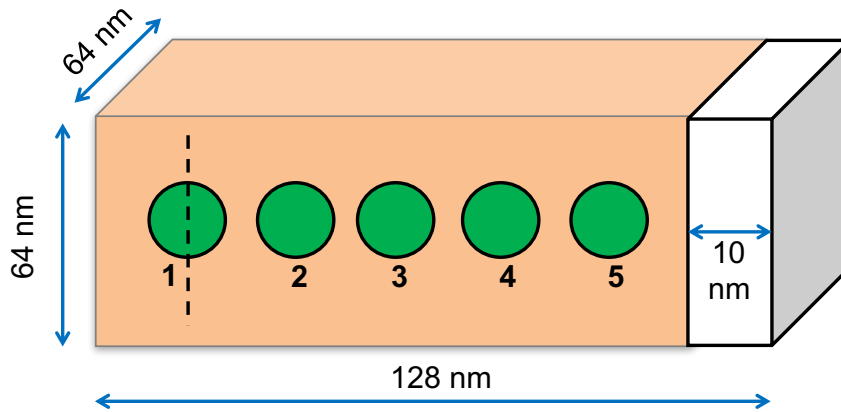


FIGURE 5.10: Schematic representation of the initial condition of the domain.

Since the diffusion of vacancies on the dislocation is not known, we consider it as a parameter and take the value for $D^* = 3.93 \cdot 10^{-18} \text{ m}^2/\text{s}$ in order to have a velocity of dislocation so that it can eventually move out of the surface on the right. The simulation was carried out for a time of 2178 s at the isothermal annealing temperature of 1600°C . The simulation was started and the evolution of the bubbles in the domain is shown in Fig.5.11 from (a) to (i).

The case (a) shows the initial state of the simulation, with the five bubbles numbered from 1 to 5. As the simulation starts, the dislocation, along with the Bubble 1 pinned to it, begin moving towards the right, in the direction of the exterior region. The velocity of the dislocation is found to be $9.49 \cdot 10^{-2} \text{ nm/s}$. After 26.9 s, (as can be seen in case (b)), the Bubble 1 moves towards the exterior region and encounters Bubble 2 and coalesces with it. Due to coalescence, the Bubble 2, as such, disappears from the domain and forms a larger Bubble 1. At this point, the Bubble 1 has grown to have a radius equal to 6.51 nm and the dislocation moves with a velocity of $7.34 \cdot 10^{-2} \text{ nm/s}$. Case (c) shows that the dislocation along with the pinned Bubble 1 continues to move towards the other bubbles and coalesces with Bubble 3. The coalescence occurs at 470.7 s since the start of simulation. At this point the Bubble 3 disappears from the domain and the radius of the Bubble 1, after coalescence, is 8.37 nm and it moves along with the dislocation with a velocity of $2.83 \cdot 10^{-2} \text{ nm/s}$. In case (d), the Bubble 1 can be seen to continue moving closer to the remaining bubbles. The coalescence of Bubble 1 with Bubble 4 occurs at time 897.4 s, as seen in case (e). At this point, Bubble 4 disappears and the radius of Bubble 1 is 9.45 nm and it moves along with the dislocation with a velocity of $2.64 \cdot 10^{-2} \text{ nm/s}$. The Bubble 1 continues to move towards the exterior region and the remaining bubble (Bubble 5) in case (f) and coalesces with Bubble 5 at time 1306.8 s, as seen in case (g). At this point, the radius of

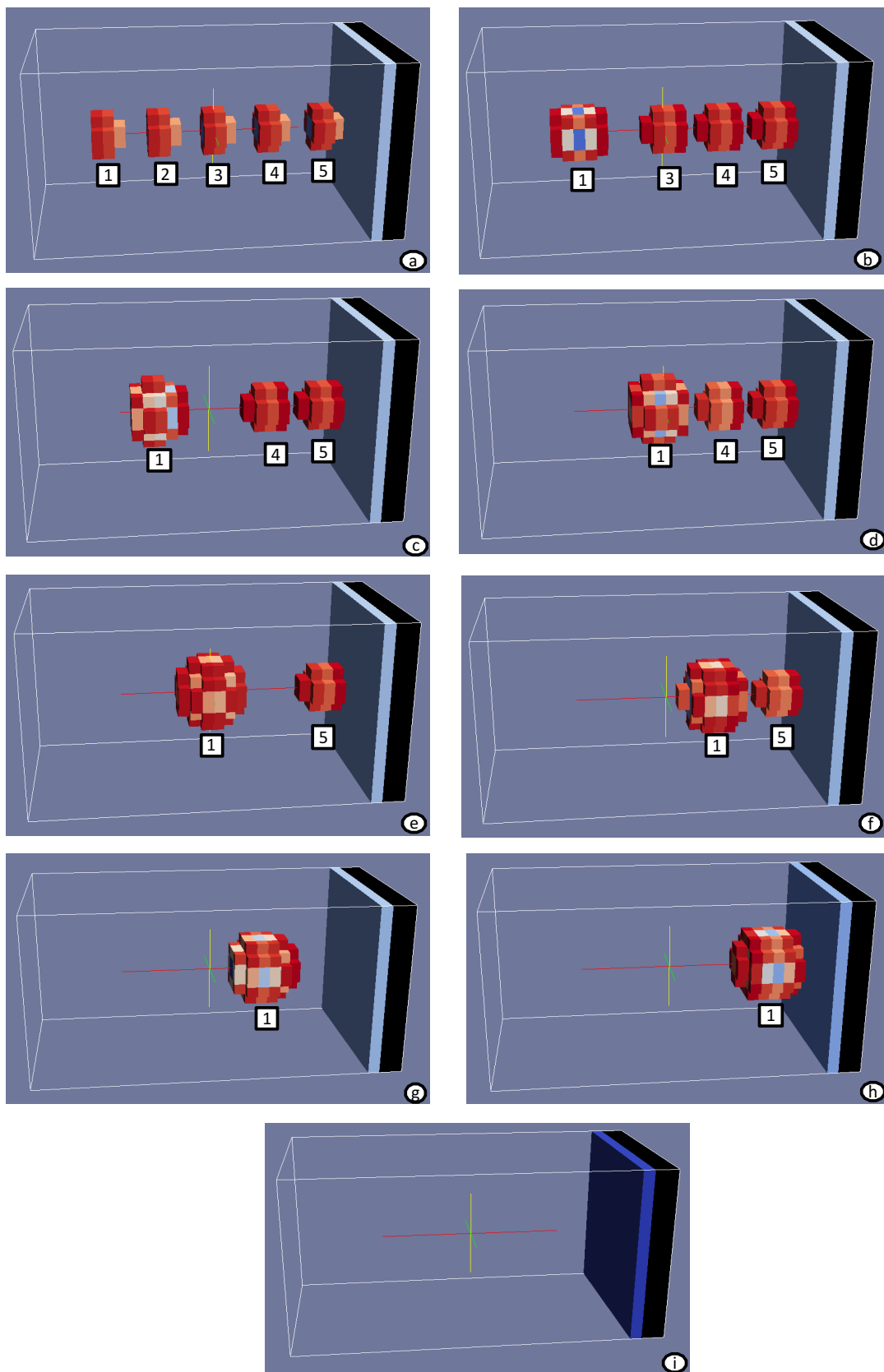


FIGURE 5.11: Bubble movement via Dislocation climb mechanism.

Bubble 1 is 10.28 nm and it moves along with the dislocation with a velocity of $2.76 \cdot 10^{-2}$ nm/s. In case (h), the Bubble 1 pinned to the dislocation continues to move towards the exterior region and it contains the entire gas content of all initial five bubbles. At time 1980 s, Bubble 1 coalesces with the exterior region and the entire gas is released along with it (as shown in case (i)). The radius of the Bubble 1 just before coalescence with the exterior region is found to be 10.51 nm.

The velocity of the dislocation and the gas content of the Bubble 1 pinned to the dislocation are plotted against simulation time in Fig.5.12. Each kink

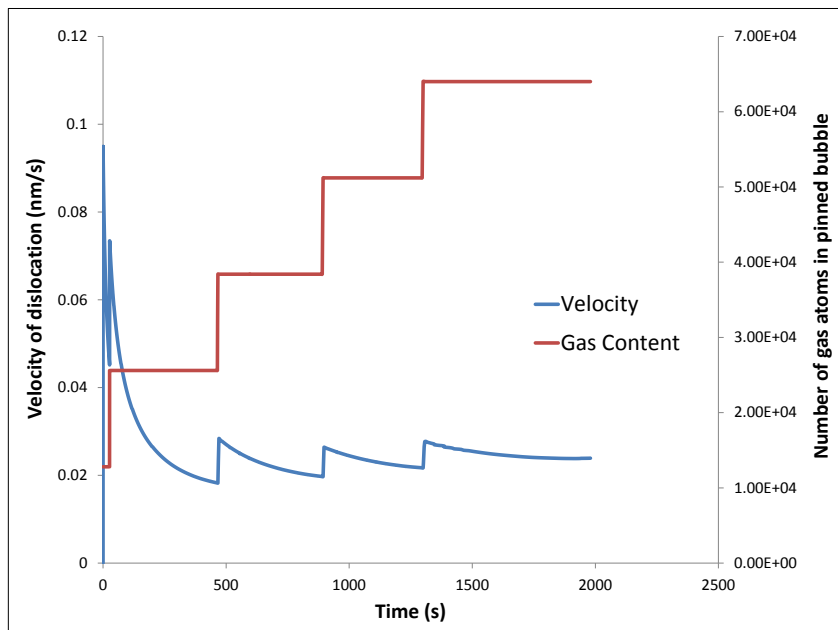


FIGURE 5.12: Evolution of the velocity of the dislocation and pinned bubble gas content with time.

or step corresponds to the coalescence of Bubble 1 with another bubble in the domain. The gas content of Bubble 1 increases each time it coalesces with another bubble as the resulting Bubble 1 acquires the gas atoms from the bubble disappearing due to coalescence. The dislocation velocity, on the other hand, depends on the effective pressure (defined as $P_i - \frac{2\gamma}{R_i}$) exerted by the bubble and on the free dislocation segment lengths, i.e., the lengths of dislocation where vacancies are generated and replaced by atoms.

From the figure (Fig.5.12), we note that the velocity of the dislocation decreases as the simulation progresses. This decrease can be attributed to the fact that the effective pressure reduces and becomes closer to the external pressure, causing the driving force to seize. There is a sudden increase in the dislocation velocity every time that coalescence occurs as the Bubble 1, pinned to the dislocation, acquires the gas atoms and the volume of the coalesced bubble. Indeed, the coalescence of Bubble 1 and Bubble 2, for instance, increases the internal pressure of the resulting Bubble 1 because Bubble 1 had already begun to relax its inner pressure with the vacancies

coming from the dislocation, while Bubble 2 had its high inner pressure unchanged. There is also the effect of the new radius of the resulting Bubble 1, which causes the Laplace pressure ($\frac{2\gamma}{R_i}$) to decrease. Both the effects make the effective pressure ($P_i - \frac{2\gamma}{R_i}$) and the over-pressurization of Bubble 1 to increase just after coalescence. So, the dislocation velocity increases instantly and continues on the downward curve thereafter.

The volume of the Bubble 1 pinned to the dislocation is plotted against time in Fig.5.13. As described earlier, the bubble grows by exchanging crystal atoms from its surface with the vacancies generated at the dislocation. The volume increases sharply each time coalescence occurs between the Bubble 1 and any other bubble as the other bubble disappears and the resulting Bubble 1 has the total volume of itself and the coalesced bubble.

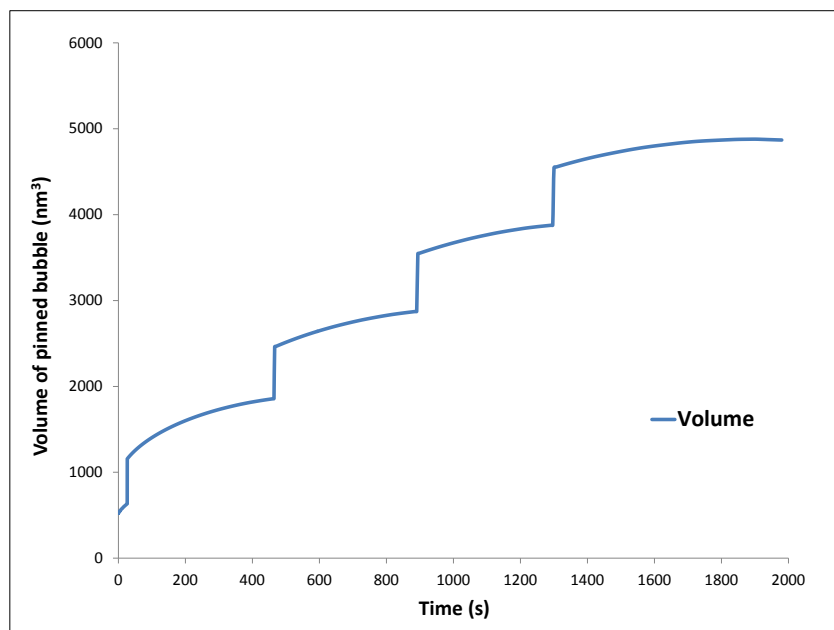


FIGURE 5.13: Volume of the pinned bubble on dislocation.

5.5 Scenario of FGR via bubble movement with Dislocations

Now that we are able to carry out simulations in 3-D with the incorporation of dislocations in the BEEP Model, next we try to simulate a more practical case.

5.5.1 Conditions for analysis

Due to the high computational costs incurred during 3-D calculations, we consider a smaller domain (rather than the $5 \mu\text{m}$ large domain representing the radius of a grain). The domain we use for the analysis has the physical dimensions of $1608\text{nm} \times 120\text{nm} \times 120\text{nm}$ including an external region of length 98

nm. Since we are carrying out 3-D calculations, we can actually get the concentration of gas in mol/m^3 created for base irradiation. We have the relation between burn up and fission rate as:

$$BU(\text{GWd}/t_U) = 3.7384 * 10^{-26} \int \dot{F} dt (\text{fissions}/\text{m}^3)$$

So, for base irradiation ($\sim 10 \text{ GWd}/t_U$), we get $\int \dot{F} dt = 2.76 * 10^{26}$ and, thus, the creation of gas atoms (Xe + Kr) with yield of 0.3 as:

$$0.3 * \int \dot{F} dt = 8.02 * 10^{25} \text{ atoms}/\text{m}^3$$

$$\approx 133.3 \text{ mol}/\text{m}^3$$

We generated bubbles randomly in the domain with bubble radius, $R_b \sim 1$ nm and the volume per atom of gas in the bubbles equal to Ω , the atomic volume of a site. We tried to reach the desired macroscopic concentration for the gas atoms. A new bubble was accepted at the condition that it does not coalesce with any of the other existing bubbles. After a few trials, we could achieve a concentration of gas equal to $139 \text{ mol}/\text{m}^3$ at the beginning of the simulation. This could be achieved by taking the grid size as 3 nm. The number of bubbles generated containing this $139 \text{ mol}/\text{m}^3$ was found to be 6136. The boundary conditions provided are the periodic boundary condition in the top, bottom, front and back faces and the symmetric boundary condition on the right and left sides of the domain. A schematic representation of the domain including the bubbles, and boundary conditions is depicted in Fig.5.14.

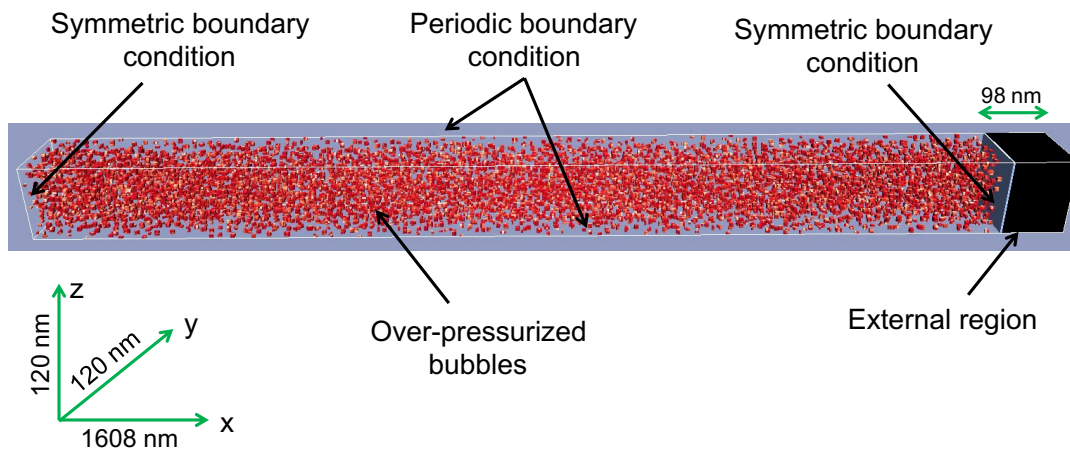


FIGURE 5.14: Schematic representation of domain with boundary and initial conditions.

We initialize the domain with 20 dislocations parallel to the y or the z axis and these dislocations are randomly distributed within the domain. The width of each dislocation is taken as $3 * \Omega^{1/3}$. The value for the vacancy diffusion coefficient along the dislocation is not known and is taken as a parameter such that the value of D^* is equal to $6.9 * 10^{-16} \text{ m}^2/\text{s}$. The values of physical conditions used in the analysis are summarized in Table 5.1.

Parameter	Symbol	Value
Physical domain	-	1608nm*120nm*120nm
Length of external region	-	98 nm
Grid size	h	3 nm
Number of bubbles	-	6136
Number of dislocations	-	20
Width of dislocations	w	1.03 nm ($3*\Omega^{1/3}$)
Vacancy diffusion coefficient $\times x_{v_d}^{eq}$	D^*	$6.9*10^{-16} m^2/s$
External Pressure	P_{ext}	$10^5 Pa$
Annealing Temperature	T	1600°C

TABLE 5.1: Physical parameters used for the analysis.

5.5.2 FGR analysis without any diffusion of vacancies from free surface

A scenario for the FGR including all the phenomena presented in this work is described here. The domain contains a high density of over-pressurized nano-bubbles. Their mobility is more or less suppressed due to their high inner pressure. However, the bubbles in the vicinity of the free surface, or in the vicinity of dislocations, or pinned on the dislocation, can trap vacancies emitted from these sources and become more mobile.

In the vicinity of the free surface, a few bubbles are released out of the domain due to the combined random and directed movement of the bubbles in the vacancy gradient. In the bulk, some of the mobile bubbles get pinned on the dislocations, giving the dislocations a driving force to climb. Bubbles on the dislocations can, on one hand, relax their pressure by the vacancies arriving along the dislocations, or on the other hand, can also emit vacancies towards other more pressurized bubbles nearby. So, the driving force that moves the dislocations may not diminish very quickly. Moreover, the moving dislocations may sweep new over-pressurized bubbles, which would aid the dislocation to continue moving. Since the movement of the dislocations is always in the same direction, it would turn to be more efficient than the random movement to push the bubbles pinned on it out of the grain.

The BEEP Model is designed to model this scenario. However, we lacked the time to carry out a full simulation in 3-D. We chose a less demanding situation to test if, at least, the model with dislocations could lead to large FGR or not. We have assumed that:

- At least one bubble is pinned on each dislocation at the start of the simulation.
- The random Brownian movement of bubbles by surface and volume diffusion mechanism takes place freely (without the suppression of surface diffusion due to the Mikhlin's suppression term) except for the pinned bubbles, which can move randomly only along the dislocation. The Mikhlin's suppression of surface diffusion of small, high gas density bubbles is neglected as the bubbles in the vicinity of the dislocations

would actively trap the vacancies generated along the dislocations and get pinned on the dislocations.

- The direction of climb is always in the +x direction.
- The diffusion of vacancies was not considered (which exclude the movement of bubbles in the vacancy gradient).

As mentioned before, the domain used for the analysis is 1608 nm in length with an external region of length 98 nm. It can be seen as a part of the original domain (5 μm) of Chapter 4 representing the region closer to the vicinity of the external region, and treated in 3-D. Using all the conditions stated in Table 5.1, we carry out the simulation for 3 hours of isothermal annealing. The bubble distribution and evolution in the 3 hours of annealing is shown in Fig. 5.15.

It can be seen that at time $t = 0$, the bubbles are distributed randomly in the domain. The bubbles undergo quick coalescence as soon as the simulation starts and are reduced to just 100 bubbles in a matter of 5 s into the simulation. The mean radius of these bubbles is 6.7 nm. Several bubbles get pinned on the dislocations. At the start of the simulation each dislocation had one bubble pinned to it. At time $t = 5$ s, 59 bubbles are pinned on the different dislocations with mean radius of 7.1 nm. The bubbles pinned on the dislocations can be better visualized in Fig. 5.16. The three screenshots are taken in succession and the dislocations with bubbles pinned on them can be seen to move in the direction of the external region. At least three dislocations have been marked as A, B and C at different regions of the domain to show their movement and also of the bubbles pinned on them, towards the external region. At time $t = 5$ s, the mean velocity of the 20 dislocations is found to be 2.98 nm/s.

At time $t = 1122$ s, most of the bubbles have coalesced into larger bubbles or moved out with the moving dislocations and only 6 bubbles remain with each of them pinned to one dislocation. At this time the mean velocity of the 6 dislocations is found to be 5.87×10^{-2} nm/s. The mean radius of these bubbles is 19.77 nm. At $t = 2490$ s, one of the bubbles on a dislocation coalesce with another bubble in a different dislocation. Only 5 bubbles remain in the domain with a mean radius of 21.76 nm. The mean velocity of the 5 dislocations is found to be 5.27×10^{-2} nm/s. At $t = 3717$ s, one of the dislocations with a pinned bubble moves out of the domain. At this time only 4 bubbles remain in the domain with a mean radius of 19.82 nm. The 4 dislocations pinned with the 4 bubbles move with a mean velocity of 3.10×10^{-2} nm/s. These dislocations continue to move slowly towards the external region up to $t = 7830$ s at which point another dislocation with a pinned bubble moves out of the external region. At this point only 3 dislocations with 3 pinned bubbles remain in the domain. The mean radius of these bubbles is 18.49 nm. After $t = 7830$ s, the remaining 3 dislocations with pinned bubbles, which are quite further away from the external region, continue to move slowly with a mean velocity of 1.03×10^{-2} nm/s. At the end of the simulation ($t = 10800$ s = 3 h), these three dislocations and bubbles remain in the domain. The mean radius of these bubbles at the end of 3 hours of simulation is found to be 19.10 nm and their mean velocity is 7.69×10^{-3} nm/s.

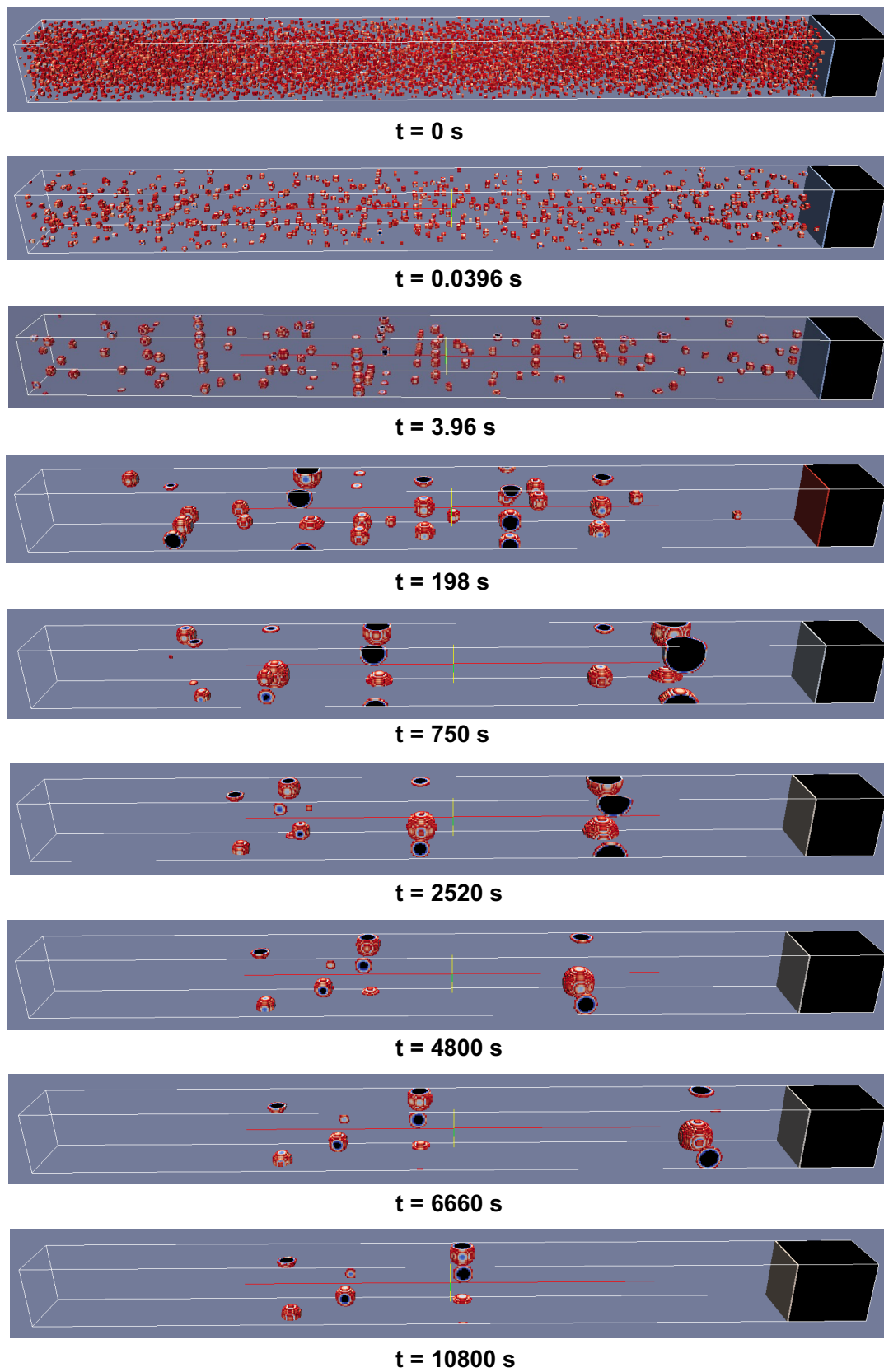


FIGURE 5.15: Bubble movement via Dislocation climb mechanism for 3 hours of annealing simulation.

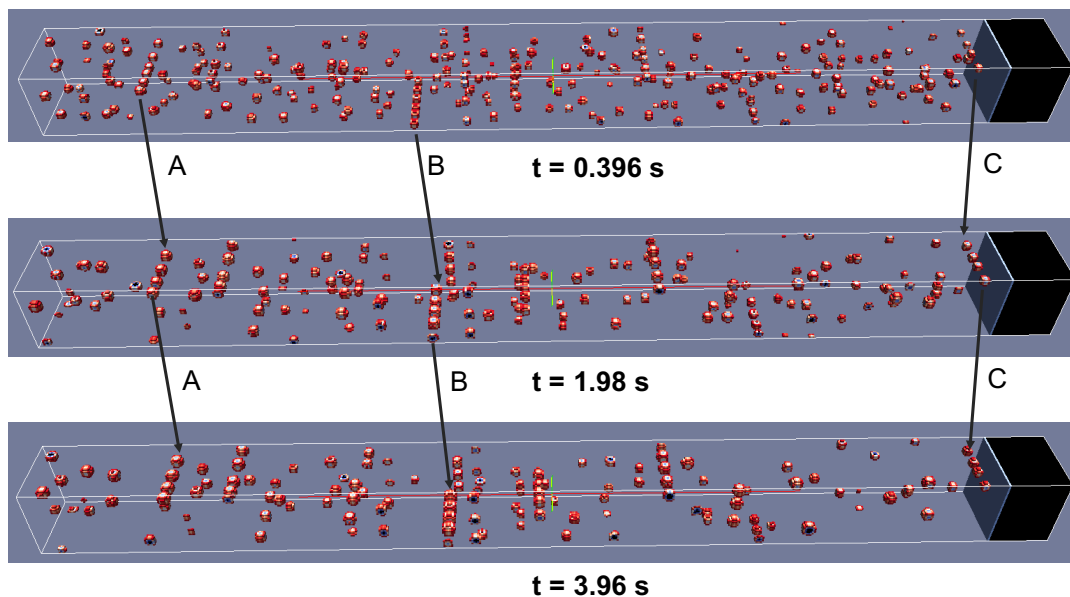


FIGURE 5.16: Bubbles pinned on dislocation move via dislocation climb mechanism.

The fractional FGR in the 3 hours of annealing simulation is plotted with time in Fig.5.17. The dislocations moving towards the exterior region and eventually moving out with their pinned bubbles cause the FGR. At $t = 386$ s, the fractional FGR is already 45.3%. At $t = 1122$ s, when only six dislocations and six pinned bubbles remain, it becomes 69.3%. At $t = 3717$ s, the FGR is 84.85%. It becomes 93.76% in time $t = 7830$ s and remains the same up to 3 hours of annealing ($t = 10800$ s).

Even up to 386 s, the FGR reaches 45.3% by the coalescence of bubbles and their pinning on the dislocations and eventual movement of the dislocations causing the bubbles to move out of the domain. Fig.5.18 shows the FGR up to $t = 386$ s. At $t = 1.4$ s of the simulation, the FGR is 1.51%. At this time all the dislocations have bubbles pinned on them and this release is due to the bubbles at the vicinity of the free surface randomly moving out of the domain. The total bubbles in the domain at time $t = 1.4$ s is 157, out of which 65 are pinned on the dislocations. At time $t = 18$ s, one dislocation having 4 bubbles pinned to it reaches close to the free surface and its bubbles coalesce with the free surface and move out. This causes the FGR to reach 2.26%. At this point, there are 66 bubbles in the domain out of which 43 are pinned on the dislocations.

At time $t = 85$ s, another dislocation having 2 large bubbles (having large gas content) pinned on it reaches the vicinity of the free surface and the bubbles move out, causing the FGR to be 33.65%. One of the dislocations near the free surface, after its initial bubbles had moved out, had another bubble pinned to it and at time $t = 246$ s, this bubble pinned to it also moves out, causing the FGR to be 35.19%. After this several bubbles coalesce with each other and many dislocations lose the bubbles pinned on them due to the coalescence of their bubbles with larger bubbles on other dislocations.

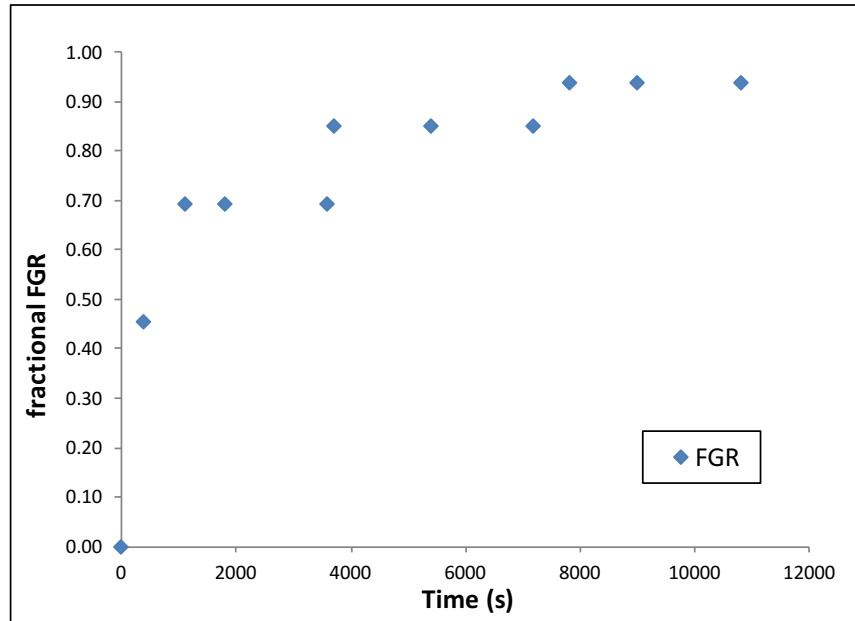


FIGURE 5.17: FGR in 3h hours via dislocation climb mechanism.

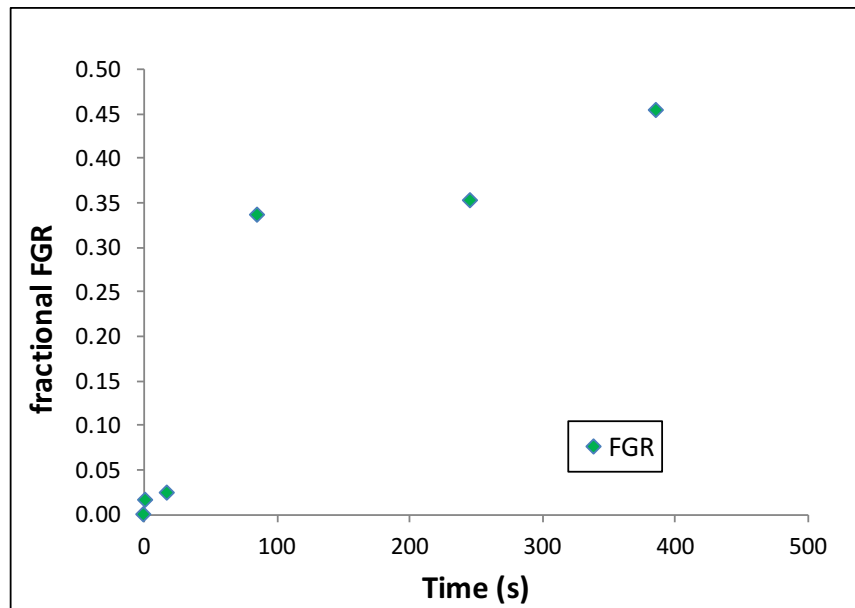


FIGURE 5.18: FGR in the first 386 s via dislocation climb mechanism.

Just before $t = 386$ s, there are 9 dislocations with bubbles pinned on them with total of 12 bubbles in the domain, all pinned on these dislocations. At $t = 386$ s, one of the dislocations having two bubbles pinned on it reaches the vicinity of the free surface and the bubbles move out, causing the FGR to reach 45.3%. After 386 s, other bubbles on dislocations also coalesce and at $t = 1122$ s, one dislocation having one bubble pinned to it moves out and the FGR reaches 69.3%. At this point there remain the six dislocations with one bubble pinned to each which are discussed in detail already. So, we see that

except the first 1.51%, the entire FGR even up to $t = 386$ s occurred only by the bubbles which moved out of the domain with the dislocations.

From the analysis, it is seen that the dislocation climb mechanism can prove to be an important mechanism for causing the bubble movement and the eventual FGR. Almost complete FGR could be achieved in the case tested above. The domain considered here is 32% ($\frac{1.608\mu m}{5\mu m}$) of the domain considered in Chapter 4. Considering 93.76% of FGR from this region, it gives at least 30% of FGR for the original domain of Chapter 4. The target FGR was 27% in the cases discussed in Chapter 4. So, here, with the dislocations, the obtained FGR is in the range of what was expected. However, several conditions were assumed to enhance the scenario of FGR using the dislocation climb mechanism. It can be studied in detail to provide a more accurate outcome.

5.5.3 Factors influencing the velocity of dislocations

The velocity of the dislocations depends on the vacancy source term, β , which in itself is influenced by two opposing factors. From Eq.5.8, it is evident that the driving force for β depends on the effective pressure of the bubble (P_i - Laplace pressure) and the segment length, L_i . The effective pressure is given by the expression:

$$P_{eff} = P_i - \frac{2\gamma}{R_i}$$

β would increase if the effective pressure of the pinned bubble increases and the vacancies can be generated as long as the effective pressure remains larger than the external pressure, P_{ext} . On the other hand, β would decrease if the segment length, L_i increases. For instance, consider a dislocation having an over-pressurized bubble pinned to it. In order to release its pressure, the bubble will trap the vacancies generated along the dislocation and grow. This will cause the internal pressure of the bubble, P_i to decrease, but the Laplace pressure ($\frac{2\gamma}{R_i}$) to increase. Only the effective pressure ($P_i - \frac{2\gamma}{R_i}$) will determine how the dislocation velocity will be affected. Moreover, as the pinned bubble would grow, it will occupy more length on the dislocation and the segment length between the bubbles, L_i , would decrease. This would cause β to increase, causing the velocity to increase. The net effect of the effective pressure and the segment length will govern the dislocation velocity.

To see the effect of these factors on the dislocation velocity, let us consider the six dislocations which remained in the domain after 1122 s. At this time each dislocation had one bubble pinned on it. We examine the evolution of these dislocations to understand the velocity evolution with time during the simulation. The characteristics of the dislocations and the pinned bubbles at time $t = 1122$ s are presented in Table 5.2.

The radius of the six pinned bubbles on the six dislocations are plotted against time after 1122 s in Fig.5.19. The radius of the bubbles increases gradually for all the bubbles. The dislocations with ID 1, 12 and 13 are the ones that remained in the domain at the end of the simulation. At the end

Dislocation ID	Pinned Bubble Radius (nm)	Effective Pressure (Pa)	Velocity of dislocation (nm/s)
1	13.26	$3.55 \cdot 10^7$	$2.35 \cdot 10^{-2}$
5	27.11	$7.00 \cdot 10^7$	$1.33 \cdot 10^{-1}$
12	13.41	$3.94 \cdot 10^7$	$2.64 \cdot 10^{-2}$
13	17.03	$7.88 \cdot 10^7$	$6.71 \cdot 10^{-2}$
15	22.13	$1.21 \cdot 10^7$	$1.50 \cdot 10^{-2}$
20	25.68	$5.21 \cdot 10^7$	$8.71 \cdot 10^{-2}$

TABLE 5.2: Characteristics of the dislocations and the pinned bubbles at time $t = 1122$ s.

of the simulation, the radius of bubbles pinned on the Dislocation ID 1, 12 and 13 are found to be 16.57 nm, 17.01 nm and 23.72 nm, respectively. The

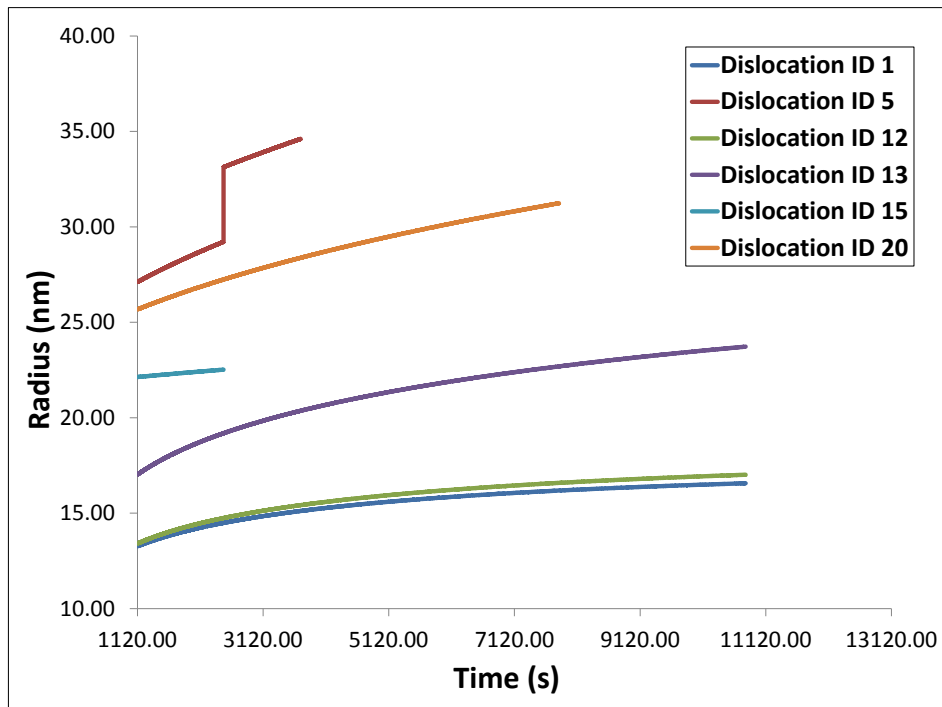


FIGURE 5.19: Radius evolution of the 6 pinned bubbles on the remaining dislocations after 1122 s.

bubble pinned to the dislocation with ID 20 moves out of the domain at time $t = 7830$ s. Its radius just before its escape is found to be 31.24 nm. The bubbles on dislocations with ID 5 and 15 are the ones that coalesced with each other at time $t = 2490$ s. The bubble on dislocation ID 15, with a radius of 22.52 nm coalesced with the bubble on dislocation ID 5 having a radius of 29.22 nm, to form a resulting bubble of radius 33.13 nm pinned on the dislocation with ID 5. A sudden rise in the radius of bubble on dislocation ID 5 can be seen exactly where bubble on dislocation ID 15 disappears in Fig. 5.19. The bubble on dislocation with ID 5 continues to move towards the exterior

region and eventually goes out at time $t = 3717$ s. Its radius just before its escape is found to be 34.61 nm.

The effective pressure exerted by the pinned bubbles is plotted against time in Fig. 5.20. The effective pressure decreases gradually for all the bubbles.

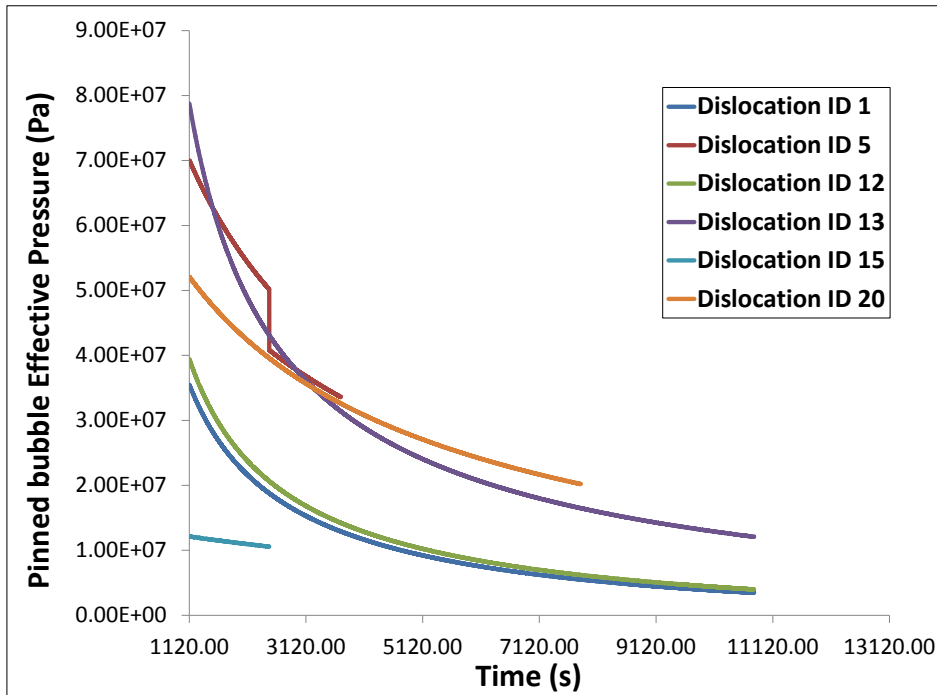


FIGURE 5.20: Effective pressure of the 6 pinned bubbles on the remaining dislocations after 1122 s.

The effective pressure of the bubbles pinned on dislocations with ID 1, 12 and 13 decreases and by the end of the simulation, reaches values of 3.36×10^6 Pa, 3.98×10^6 Pa, and 1.21×10^7 Pa, respectively. The decrease in effective pressure for these bubbles is steeper at the beginning when the radius of these bubbles is growing sharply. As the bubble growth starts to slow down, the decrease in effective pressure also starts to slow down. The bubble pinned on the dislocation with ID 20 shows similar trend and had an effective pressure of 2.02×10^7 Pa before it escaped from the domain. The effective pressure of the bubble on dislocation with ID 5 can be seen to decrease sharply and plummet to 4.08×10^7 Pa from 5.01×10^7 Pa at time $t = 2490$ s when the bubble pinned to the dislocation with ID 15 coalesces with it. The effective pressure of the bubble on dislocation with ID 5 further fall to 3.36×10^7 Pa before it moves out of the domain. The effective pressure of the bubble on dislocation with ID 15 just before its coalescence is found to be 1.06×10^7 Pa.

It appears from the trends for the radius of the pinned bubbles that the velocity should increase since as the bubbles grow larger that occupy more space on the dislocations and the segment length of the dislocations decrease. The effective pressures of the pinned bubbles, on the other hand, indicate that the velocity of the dislocations should decrease. The velocities

of the six dislocations are plotted against time in Fig.5.21. It can be seen that the overall effect of the bubble radius and effective pressure causes the velocity of the dislocations to gradually decrease with time.

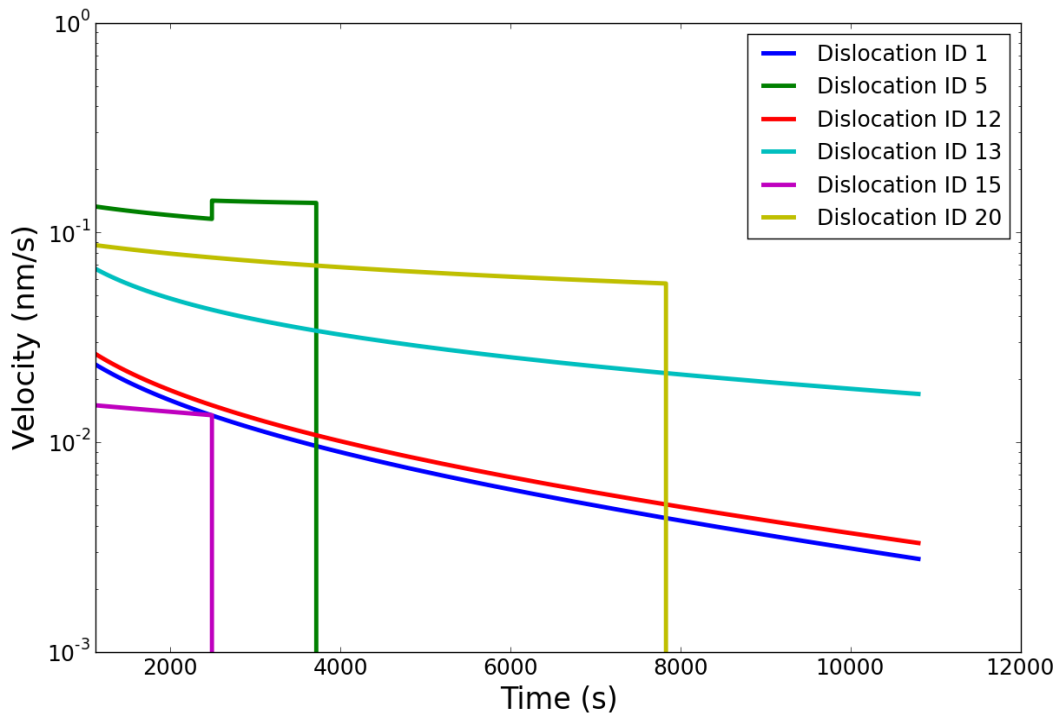


FIGURE 5.21: Velocity of the six dislocations remaining after 1122 s.

The impact of the decreasing effective pressure appears to be the dominant driving force for the dislocations to move. The three dislocations with ID 1, 12 and 13, that remain in the domain at the end of the simulation, have velocities of 2.78×10^{-3} nm/s, 3.31×10^{-3} nm/s and 1.69×10^{-2} nm/s, respectively. The velocity of the dislocation with ID 20 is found to be 5.72×10^{-2} nm/s at time $t = 7830$ s before it moves out from the domain. The dislocation with ID 15 has a velocity of 1.34×10^{-2} nm/s just before the bubble pinned to it coalesces with the bubble on dislocation with ID 5 at time $t = 3717$ s. The velocity of dislocation with ID 5 increases from 0.116 nm/s to 0.142 nm/s as soon as the bubbles coalesce and remains almost the same at 0.138 nm/s before it moves out from the domain.

So, the velocity of the dislocations is governed by the pinned bubble radius, which, on one hand, reduces the segment length as the bubble grows but, on the other hand, may also reduce the effective pressure. The net effect causes the dislocations to move with the bubbles pinned on them, with a predominant impact of the effective pressure.

5.6 In Closing

Having analyzed the FGR by intra-granular bubble movement via the mechanisms of directed movement in a vacancy gradient and the random movement in the previous chapters, this chapter focused on bubble movement via the dislocation climb mechanism. The scenario of FGR by the bubble movement along with the dislocation via the climb mechanism was discussed. The implementation of dislocations into the BEEP Model was also presented. The model was tested in a first 3-D simulation and was found to simulate the dislocation and pinned bubble movement as expected. The scenario for FGR seems consistent. The analysis showed that the dislocation climb mechanism could lead to the majority of the gas to be released from the region that was represented (32% of the domain of Chapter 4) and can provide an alternate mechanism of gas bubble movement during post-irradiation annealing tests and an explanation for the observed FGR.

Several assumptions and parameters have been adopted for the present analysis, however, a more complete analysis remains in the scope of the BEEP model, whilst it is out of the scope of this thesis due to time restraints. An interesting perspective would be to evaluate the coefficient of vacancy diffusion in the vicinity of a dislocation using Molecular Dynamics and then using this value in a scenario where the entire domain ($\sim 5\mu\text{m}$) would be considered with the dislocation climb in both the +x and -x directions.

General Conclusion

Fission gases (Xe, Kr) produced during irradiation in a nuclear fuel play a significant role in the thermo-mechanical behaviour of fuel rods and cause the swelling of the fuel and the fission gas release from it. Understanding the fission gas behaviour has led to several in-pile and out of pile tests and modelling to simulate and predict the phenomena associated with it. One aspect of fission gas behaviour which has piqued researchers' interest has been the transport of intra-granular gas to the grain boundary. It has been found that during post-irradiation annealing of nuclear fuels, the transport of intra-granular gas to the grain surface is very rapid as compared to results predicted from the effective diffusion theory. Several mechanisms have been proposed for such a behaviour and it has been noted that the movement of intra-granular bubbles containing the gas atoms plays a major role in the FGR.

In the framework of this thesis, the intra-granular gas bubble movement was analyzed for its impact on the overall gas release during post-irradiation annealing tests. A new spatialized model called the BEEP Model, was developed for fission gas bubble and vacancy interactions at the meso-scale. This kind of mechanistic evaluation had been lacking, to our knowledge. The BEEP Model was verified for various aspects like grid sensitivity, diffusion calculation and bubble movement and was found to simulate the various aspects with good precision. Intra-granular gas bubble migration and fission gas release was analyzed in 2-D via the mechanism of directed movement in a vacancy concentration gradient as well as for the random movement without any driving force. A combined effect of directed and random movement due to surface mechanism was also analyzed. The target FGR value from the reference experiment, for comparison with the planar geometry in the 2-D analysis was determined as 27%. The conclusions for the different cases using these two mechanisms of intra-granular bubble movement and their combination are as follows:

- The fission gas release due to directed movement in a vacancy concentration gradient was found to be 0.11% in 3 hours and 1.2% in 110 hours of annealing at 1600°C. This is far less than the values of fission gas release observed during our post-irradiation annealing reference experiment.
- The random movement of bubbles without the diffusion of vacancies was tested for volume and surface diffusion mechanisms. The bubble movement was negligible due to both, the volume diffusion mechanism and

the surface diffusion mechanism with the Mikhlin's suppression term.

- The fission gas release due to combined directed movement and random movement by surface diffusion mechanism including Mikhlin's suppression term was found to be 0.84% in 3 hours and 2.32% in 110 hours of annealing time. Even the combined movement mechanism could not account for the observed high values of fission gas release during the post-irradiation annealing test. Even if the calculation was continued till the vacancy concentration gradient lasted, the value of FGR did not increase beyond 2.32%.
- Parametric study of the Mikhlin's suppression term to test its influence on the overall FGR was done. It was found that the FGR is sensitive to the Mikhlin's suppression term. However, even after neglecting the Mikhlin's suppression term completely, the random movement of bubbles did not explain the observed FGR obtained after 3 hours of annealing.

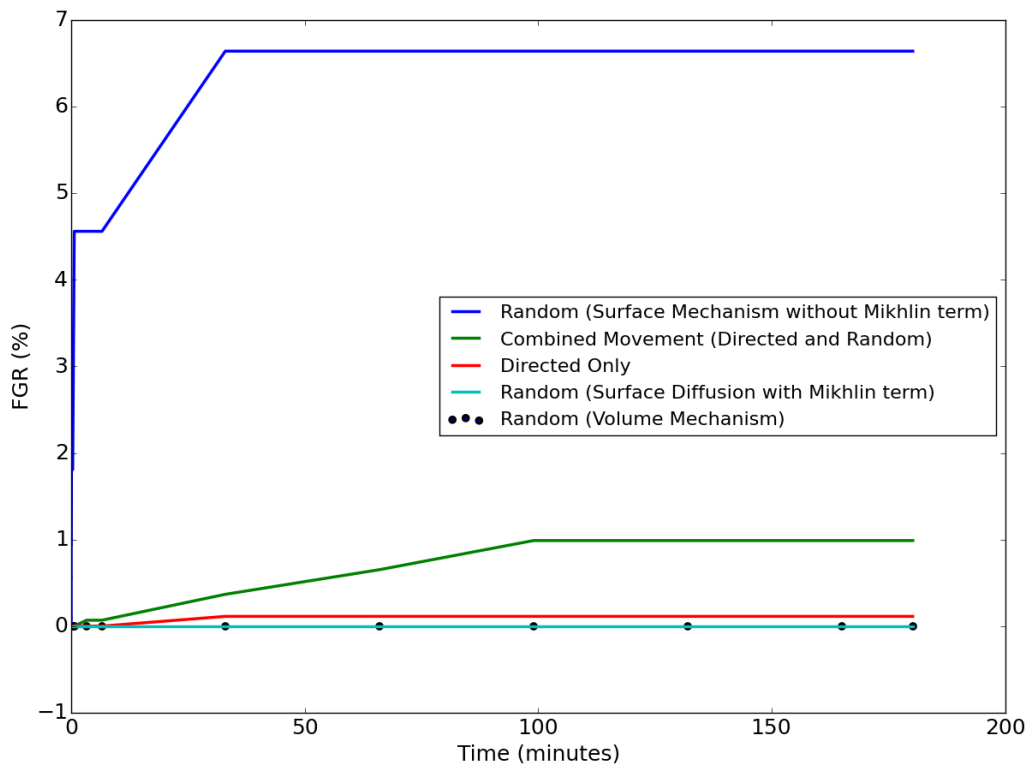


FIGURE 5.22: FGR in 3 hours with the different mechanisms of bubble movement adopted in the 2-D analysis.

The analyses showed that based on bulk diffusion coefficient of vacancies and the surface diffusion of crystal atoms, and on the Mikhlin's suppression term, the directed movement of bubbles in a vacancy concentration gradient cannot account for the large FGR which is observed during the post-irradiation annealing test of UO_2 sample that we took as a reference, even if the directed movement is assisted by random movement of bubbles due to surface diffusion.

Another scenario for the FGR via intra-granular bubble movement was analyzed. This scenario took into account the dislocations and their movement via the mechanism of dislocation climb. The climbing dislocations can move out of the grain along with the gas bubble(s) pinned to them, providing an alternate mechanism of FGR during post-irradiation annealing tests.

In order to analyze this scenario, dislocations were incorporated into the BEEP Model and their movement was tested in a smaller 3-D domain. The movement of dislocations and the pinned bubbles was demonstrated to be simulated consistently by the model. The 3-D analysis of FGR using this scenario was done using the BEEP Model and it was demonstrated that this scenario could lead to a FGR that is compatible with the target FGR (27%) induced from experiments. However, several assumptions were used in the analysis and the value, for example, for the coefficient of vacancy diffusion (multiplied by $x_{v_d}^{eq}$) along the dislocation was taken as a parameter due to lack of information. This analysis emphasized the need for studies at the lower scale to obtain values which can then be used in meso-scale models, such as BEEP, to carry out further analysis on the FGR during post-irradiation annealing tests.

In perspective, Molecular Dynamic calculations are planned to access the influence of inner pressure on the bubble mobility (equivalent to the Mikhlin's term). Moreover, a complete calculation, including dislocation climb and vacancy diffusion should also be done. The BEEP Model should also be accelerated in terms of computation time by utilizing both the MPI parallelization (for diffusion calculation) and OpenMP to parallelize the independent loops on the bubbles.

Appendix A

Fuel Performance Codes

Most of the fuel performance codes consider a cylindrical geometry and adopt axi-symmetry for the modelling. A majority of the codes represent the cylindrical fuel rod using a 1.5D geometrical approach. Such codes include FRAPCON [234, 143, 235], ENIGMA [66, 236] and TRANSURANUS [151]. In these 1.5D approach codes, all transport processes are solved in one (radial) dimension, and the axial segments are coupled via balance equations. Some exceptions to the traditional 1.5D codes include FALCON [237], which is 2D and ALCYONE [147] and BISON [150, 238], which can be either 2D or 3D. FGR is also modelled in other fuel performance codes such as GRASS-SST [144, 118], FASTGRASS [239, 240], SFPR [154], among others. Some of the fuel performance codes are discussed below:

- ALCYONE

ALCYONE [147] is a multi-dimensional PWR fuel code. It has been developed in the framework of the PLEIADES environment [241] in order to benefit simultaneously of the chemo-physical models available in the METEOR application [242] and of the detailed thermo-mechanical description of the fuel pellet proposed in the TOUTATIS code [243]. The fission gas models of the METEOR 1D code have been introduced in ALCYONE and a specific iterative loop has been developed to couple fission gas swelling to the thermo-mechanical solution of the 2D and 3D problem. The fission gas models account for intra-granular bubbles growth, coalescence and migration, for inter-granular bubbles growth and migration, for gas transport in the porosity and for gas release in the plenum. The usefulness of 1D fuel codes relies on their ability to model correctly the experimental data available. The different schemes available in the ALCYONE code use the same Finite Element code CAST3M [244] to solve the thermo-mechanical problem and share the same physical material models at each node or integration points of the mesh. This makes the comparison of simulated results from one scheme to another possible with no dependency on the constitutive models. MARGARET [148] is a mechanistic model integrated in the ALCYONE to describe the behavior of the inert gases, xenon and krypton generated by fission of uranium or plutonium in the fuel during in-reactor irradiations or power ramps. MARGARET is not a macroscopic model in the sense that there are no connections between the calculations performed at different nodes. It is a local model that describes the behavior of inert fission gas at the grain scale.

- SFPR
A new mechanistic code, Single Fuel Rod ↔ Performance (SFPR), was developed for modeling of single fuel rod performance under various regimes of LWR operation by Veshchunov et al. [154]. The code was designed by coupling two stand-alone mechanistic codes MFPR [155, 156] and SVECHA/QUENCH, or S/Q [245, 246]. Both these codes were initially designed for accident conditions and later extended to various normal operation conditions. Coupling of the two codes allowed mechanistic modeling of LWR fuel element behavior in steady, transient and abnormal modes under conditions of high fuel burnup, which implied self-consistent description of several processes such as the diffusion and release of gaseous fission products from UO₂ fuel, fuel pellet densification at the initial stages of irradiation and subsequent swelling, thermo-mechanical behavior of the fuel rod and physico-chemical interactions at high temperatures, thermal conductivity of the "fuel – gas gap – cladding" system, and radial diffusion of oxygen in temperature gradient in a fuel pellet. The SFPR code has a modular structure that makes suitable implementation of new models or replacement of simplified models by more advanced ones.
- TRANSURANUS
TRANSURANUS [151] is a computer program for the thermal and mechanical analysis of fuel rods in nuclear reactors and was developed at the European Institute for Transuranium Elements (ITU). It is an improved version of the URANUS code [247, 248]. The TRANSURANUS code consists of a clearly defined mechanical-mathematical framework into which physical models can easily be incorporated. It is a quasi two-dimensional (1.5D) code designed for the treatment of a whole fuel rod for any type of reactor and any situation. Besides its flexibility for different fuel rod designs, the TRANSURANUS code can deal with very different situations, as given for instance in an experiment, under normal, off-normal and accident conditions. The time scale of the problems to be treated may range from milliseconds to years. Different models are optional for densification, gas release and swelling, relocation, for predicting the fuel structure, cladding failure, the radial power density, the formation and closure of the central void (FBR), the waterside corrosion, etc.

For the fission gas release model in TRANSURANUS, an investigation of the efficient numerical techniques used to solve the diffusion equation for fission gas in a spherical fuel grain was reported by Elton and Lassmann [139]. It was found that the AERE algorithm [135] provided the most accurate solution over the greatest range of applicability. For low gas releases (less than 10%), the URGAS algorithm (introduced in that paper [139]) was the most acceptable of those examined. In a latter investigation by Lassmann and Beck [141], numerical algorithms for intragranular fission gas release, including the improved URGAS algorithm

and the new FORMAS algorithm [138, 152], were analyzed. The UR-GAS algorithm was superior in the range of fission gas release, $f < 0.05$, whereas the new FORMAS algorithm could be considered as an almost exact solution above $f = 0.1$. Taking all arguments together, both these algorithms were incorporated into the TRANSURANUS code.

- FRAPCON-3

The FRAPCON-3 [234, 249, 143, 235], the USNRC's steady state fuel performance code, was developed at Pacific Northwest National Laboratory (PNNL), US. FRAPCON-3 is a Fortran 90 computer code that calculates the steady-state response of LWR fuel rods during long-term burnup. The code calculates the temperature, pressure, and deformation of a fuel rod as functions of time-dependent fuel rod power and coolant boundary conditions. The phenomena modeled by the code include heat conduction through the fuel and cladding to the coolant; cladding elastic and plastic deformation; fuel-cladding mechanical interaction; fission gas release from the fuel and rod internal pressure; and cladding oxidation. The code contains necessary material properties, water properties, and heat-transfer correlations. For the fission gas release analysis, FRAPCON-3 includes three model options: ANS-5.4 [250]; the modified Forsberg and Massih model [138], modified at PNNL; and the FRAPFGR model developed at PNNL. The Massih model is recommended by PNNL and is the default model. The ANS-5.4 model is useful for calculating the release of short-lived radioactive gas nuclides and has been shown to provide very conservative release values. The FRAPFGR model is useful for initializing the transient gas release model for RIA events in FRAPTRAN code [251]. All three of these release models are based on earlier formulations for diffusion from a sphere by Booth [134]. However, neither the ANS-5.4 model nor the FRAPFGR model predicts stable fission gas release as well as the Massih model does. For this reason, PNNL recommends the Massih model for best-estimate calculation of stable fission gas release.

- ENIGMA

The ENIGMA fuel performance code [66, 236, 252] has been under development in the UK since the mid-1980s. In recent years it has become the principal code for UO₂ fuel licensing for both PWR and AGR reactor systems in the UK. The code attempts to model the fuel and clad properties and in-reactor processes which determine fuel behaviour. The ENIGMA code embodies a sophisticated mechanistic fission gas release and swelling model [20]. The model was formulated solely on the basis of UO₂ fuel measurements and has been validated against a broad range of experimental and commercial irradiations.

- BISON

The multi-physics object oriented simulation environment (MOOSE) is a

high performance computational framework developed at the Idaho National Laboratory (INL) for rapidly deploying multi-physics simulation applications that solve engineering problems with multiple interacting physical phenomena [253]. BISON [150, 238] is an INL fuel performance code developed within the MOOSE framework and utilizes fuel material and physical models from MATPRO, FALCON, and TRANSURANUS. BISON is a finite element-based nuclear fuel performance code applicable to a variety of fuel forms including light water reactor fuel rods, TRISO particle fuel, and metallic rod and plate fuel. The code can be applied to steady-state and transient fuel simulations and solves the fully-coupled equations of thermomechanics and species diffusion, for either 2D axi-symmetric or 3D geometries. Fuel models are included to describe temperature and burnup dependent thermal properties, fission product swelling, densification, thermal and irradiation creep, fracture, and fission gas production and release. Plasticity, irradiation growth, and thermal and irradiation creep models are implemented for clad materials. Models are also available to simulate gap heat transfer, mechanical contact, and the evolution of the gap/plenum pressure with plenum volume, gas temperature, and fission gas addition. A physics-based model [153, 64] is used for analysing the coupled phenomena of fission gas swelling and release in UO_2 fuel during irradiation. The model incorporates a direct description of the fundamental physical processes of gas generation, diffusion and precipitation in grains, growth and coalescence of gas bubbles at grain faces, and thermal gas release.

Appendix B

Multi-scale modelling

The phenomena occurring in the nuclear fuels lead to very diverse physical and chemical transformations and evolution at various scales including transformations such as cracking, fission gas bubble precipitation, restructuring, fission product migration and interaction. Semi-empirical macroscopic modelling has been used for the last 5 decades to gain significant experience on the modelling and simulation of fuel rods behaviour at long length and time scales. However, due to the complex character of the nuclear fuel behaviour, a detailed and clear understanding of the underlying phenomena of the nuclear fuel and fission products behaviour from the atomic scale to the continuum scale, via the meso-scale is necessary. The necessity to develop models at various scales arises for (1) atomic scale processes, such as diffusion of chemical species and defects, cascades of atomic displacements; (2) nano- and micro-scale processes, such as the creation of fission gas bubbles or aggregates, development and movement of nanostructural features such as dislocations that govern plastic deformation, changes in grain boundary behaviour; and (3) macroscale processes, such as continuum thermomechanical calculations of stress and strain field, fission gas release, pellet-clad interaction. In order to improve the fuel performance codes, it becomes necessary that the calculations at a particular scale provide information to the higher scales, in order to derive improved modelling of material properties in the models at the higher level. Using models in one scale and using the results obtained to another scale models has come to be known as **multi-scale modelling**. Several examples using multi-scale modelling have been published by various important international organizations through dedicated initiatives focused on the construction of consistent multi-scale / multi-physics modelling approaches. Some of these initiatives are the F-BRIDGE project [254] in Europe; the Nuclear Energy Advanced Modelling and Simulation (NEAMS) Program [255], the Consortium for Advanced Simulation of Light Water Reactors (CASL) [256], and the Center for Material Science of Nuclear Fuels (CMSNF) [257] in the US; and the PLEAIDES platform specifically in France (CEA) [241].

The objective of the F-BRIDGE European project [254] was to develop a consistent multi-scale approach enabling the description of the transport properties in UO_2 under irradiation at the meso-scopic level. Various methods from the atomic to the meso-scopic scale were used. The investigations performed during the F-BRIDGE European project at the atomic scale along with the transfer of results from the atomic scale to meso-scale models were

synthesised in [258].

Several studies have been done taking advantage of the multi-scale modelling approach. The thermal expansion and thermal conductivity of unirradiated UO_2 fuel were extracted using Molecular dynamics computations and the correlation was implemented in the FRAPCON code [259]. The interaction of a He or Xe filled bubble with a fission fragment was simulated using MD analysis [260]. Empirical potential simulations were applied to predict swelling due to soluble solid fission in a fuel performance code [261]. The consequences of fission gas production and evolution, such as swelling, a reduction in the thermal conductivity and fission gas release, have been treated separately and uncoupled in typical empirical models of fuel properties. Efforts have been made to couple these phenomena and to incorporate them in fuel performance codes. A physics-based model was developed for analysing the coupled phenomena of fission gas swelling and release in UO_2 fuel during irradiation by Pastore et al. [153]. This new model was verified through implementation and testing in the TRANSURANUS fuel rod analysis code. Further, a fission gas release model was coupled to a model of the impact of the fission gas on the fuel thermal conductivity [262]. The coupled fission gas release and thermal conductivity model was implemented in INL's BISON fuel performance code [150]. A formulation was proposed by Van Uffelen et al. [263] for modelling the process of intra-granular diffusion of fission gas during irradiation of UO_2 under both normal operating conditions and power transients. The development of the new model relies on results obtained by means of molecular dynamics (MD) simulations as well as finite element computations. The formulation is incorporated in the TRANSURANUS fuel performance code.

The greatest challenge for multi-scale modelling of fuels is the integration of the properties and behaviour across a broad range of time and length scales. Atomistic models need to inform the meso-scale models, in order to deal with issues such as grain growth and species migration. Moreover, these phenomena should provide properties and relations to the macroscale, thus, allowing simulation of phenomena such as cracking and fission product release.

Appendix C

Von Neuman stability condition for Explicit scheme

Consider any parabolic equation of the form:

$$\frac{\partial U}{\partial t} - \lambda \frac{\partial^2 U}{\partial x^2} = 0 \quad (\text{C.1})$$

Using the finite difference method with the Explicit scheme, with forward difference in time and central difference in space in 2-D, we get:

$$\frac{\partial U_{j_1, j_2}^n}{\partial t} \approx \frac{U_{j_1, j_2}^{n+1} - U_{j_1, j_2}^n}{dt}$$

and

$$\frac{\partial^2 U_{j_1, j_2}^n}{\partial x^2} \approx \frac{U_{j_1+1, j_2}^n + U_{j_1-1, j_2}^n + U_{j_1, j_2+1}^n + U_{j_1, j_2-1}^n - Dim * 2U_{j_1, j_2}^n}{dx^2} + o(dx^2)$$

where (j_1, j_2) are the coordinates of the point in 2-D and Dim is the dimension, which here in the demonstration is 2 but can be generalized to 3-D as well.

Replacing the terms in Eq.C.1 with the expressions above, we get:

$$\frac{U_{j_1, j_2}^{n+1} - U_{j_1, j_2}^n}{dt} = \lambda \frac{U_{j_1+1, j_2}^n + U_{j_1-1, j_2}^n + U_{j_1, j_2+1}^n + U_{j_1, j_2-1}^n - Dim * 2U_{j_1, j_2}^n}{dx^2}$$

In terms of U_{j_1, j_2}^{n+1} , which gives:

$$U_{j_1, j_2}^{n+1} = \frac{\lambda dt}{dx^2} \left[U_{j_1+1, j_2}^n + U_{j_1-1, j_2}^n + U_{j_1, j_2+1}^n + U_{j_1, j_2-1}^n - Dim * 2U_{j_1, j_2}^n \right] + U_{j_1, j_2}^n$$

Taking $\frac{\lambda dt}{dx^2} = \sigma$ and rearranging, we get,

$$U_{j_1, j_2}^{n+1} = (1 - Dim * 2\sigma)U_{j_1, j_2}^n + \sigma \left[U_{j_1+1, j_2}^n + U_{j_1-1, j_2}^n + U_{j_1, j_2+1}^n + U_{j_1, j_2-1}^n \right] \quad (\text{C.2})$$

Now, we use Fourier transform to decompose a function $U^n(x)$ in terms of the sin and cosine as:

$$U_{j_1, j_2}^n(x) = \sum_{k, l} f_{k, l}^n e^{ik j_1 dx} \cdot e^{il j_2 dx}$$

Using the expression for the Fourier transform in Eq.C.2, we get:

$$\begin{aligned} \sum_{k,l} f_{k,l}^{n+1} e^{ik j_1 dx} . e^{il j_2 dx} &= (1 - Dim * 2\sigma) \sum_{k,l} f_{k,l}^n e^{ik j_1 dx} . e^{il j_2 dx} \\ &+ \sigma \left(e^{ik dx} + e^{-ik dx} + e^{il dx} + e^{-il dx} \right) \sum_{k,l} f_{k,l}^n e^{ik j_1 dx} . e^{il j_2 dx} \end{aligned}$$

Now, in the above equation, we can use:

$$\begin{aligned} e^{ik dx} + e^{-ik dx} &= 2 \cos(k dx) \\ e^{il dx} + e^{-il dx} &= 2 \cos(l dx) \end{aligned}$$

So, after rearranging, the equation becomes:

$$\sum_{k,l} f_{k,l}^{n+1} e^{ik j_1 dx} . e^{il j_2 dx} = [1 - 2\sigma(Dim - \cos(k dx) - \cos(l dx))] \sum_{k,l} f_{k,l}^n e^{ik j_1 dx} . e^{il j_2 dx} \quad (C.3)$$

We consider the evolution of $f_{k,l}^n$, which is the coefficient of each mode (k,l) and find the amplification factor of mode (k,l) as:

$$f_{k,l}^{n+1} = g(k,l) f_{k,l}^n$$

From Eq.C.3, we have:

$$f_{k,l}^{n+1} = \underbrace{[1 - 2\sigma(Dim - \cos(k dx) - \cos(l dx))]}_{g(k,l)} f_{k,l}^n$$

So, we find $g(k,l)$ as:

$$g(k,l) = 1 - 2\sigma[Dim - \cos(k dx) - \cos(l dx)]$$

Here, for 2-D, $Dim = 2$ and the cos terms can be written as:

$$\begin{aligned} \cos(k dx) &= 1 - 2 \sin^2\left(\frac{k dx}{2}\right) \\ \cos(l dx) &= 1 - 2 \sin^2\left(\frac{l dx}{2}\right) \end{aligned}$$

and we get the term $g(k,l)$ as:

$$g(k,l) = 1 - 4\sigma \left[\sin^2\left(\frac{k dx}{2}\right) + \sin^2\left(\frac{l dx}{2}\right) \right] \quad (C.4)$$

Now the condition for stability for all the (k,l) is:

$$\|g(k,l)\| < 1$$

which implies

$$\begin{aligned} & \|1 - 4\sigma[\sin^2(\frac{kdx}{2}) + \sin^2(\frac{ldx}{2})]\| < 1 \\ \Rightarrow & -1 < 1 - 4\sigma[\sin^2(\frac{kdx}{2}) + \sin^2(\frac{ldx}{2})] < 1 \end{aligned}$$

Now, the \sin^2 terms are always positive and their values lies between 0 and 1, so the sum of the two \sin^2 terms, denoted by X , will be between 0 and 2. The stability condition thus, becomes:

$$\begin{aligned} & -1 < 1 - 4\sigma X < 1 \\ \Rightarrow & -2 < -4\sigma X < 0 \\ \Rightarrow & 2 > 4\sigma X > 0 \\ \Rightarrow & \frac{1}{2\sigma} > X \end{aligned}$$

Since the maximum value of X is 2, this can be written as:

$$\begin{aligned} & \frac{1}{2\sigma} > 2 \\ \Rightarrow & \frac{1}{2 * 2} > \sigma \\ \Rightarrow & \frac{1}{2 * Dim} > \sigma \end{aligned}$$

Using the expression for σ , we have:

$$\begin{aligned} & \frac{1}{2 * Dim} > \frac{\lambda dt}{dx^2} \\ \Rightarrow & dt < \frac{dx^2}{2\lambda * Dim} \end{aligned} \tag{C.5}$$

For 3-D, the same calculation can be done, but instead of two indices k, l in the Fourier transform, we would have 3 indices k, l, m and 3 cosines in Eq.C.3. At the end, the same condition (Eq.C.5) would be obtained. So, the Von Neuman stability condition for the Explicit scheme for finite difference method is given by Eq.C.5.

For the work done in this thesis, the parabolic equation is the diffusion equation with λ being D , the diffusion coefficient, and dx being the grid size, h . So the limit on the time step, dt , in the analyses in this thesis is given as:

$$dt < \frac{h^2}{2D * Dim} \quad Dim = 2 \text{ or } 3$$

This condition is also called the Courant-Friedrichs-Lewy (CFL) condition.

Appendix D

RS Calculation for six different cases

The RS is calculated analytically for the six configurations presented in Fig.D.1. The width of each cell is fixed as $h = 4$ nm. The solid ratio of the cell is calculated analytically as the area of the cell (square) not covered by the bubble (circle).

- **Case 1**

For the first case, we consider a bubble of radius, $r = 2$ nm with its centre coinciding with the center of the cell. So, the bubble is ‘just’ contained within a cell. However, all 4 corners of the cell are outside the bubble. Here, the area of the cell is h^2 and the area of the circle is πr^2 . So, RS can be calculated analytically as:

$$RS = \frac{Area(cell) - Area(Bubble)}{Area(cell)}$$

- **Case 2**

In this case, we have a similar configuration as Case 1 but the radius of the bubble is $r = 1$ nm. This case accounts for a bubble completely contained within one cell. We can calculate the RS analytically by the same relation as in Case 1.

- **Case 3**

This case considers another unique scenario where all 4 corners of the cell are outside the bubble but the cell is not a solid but rather an interface cell. The radius of the bubble is $r = 2.3$ nm. To get the RS for of this cell, we need to first calculate the area of the region of the bubble outside the cell. This area can be calculated as follows:

Consider the Fig.D.2. The area of the shaded region of the circle can be expressed as:

$$Area(shaded) = \frac{1}{2}R^2(\alpha - \sin \alpha)$$

with

$$\alpha = 2\theta = 2 * \cos^{-1} \left(1 - \frac{l}{R} \right)$$

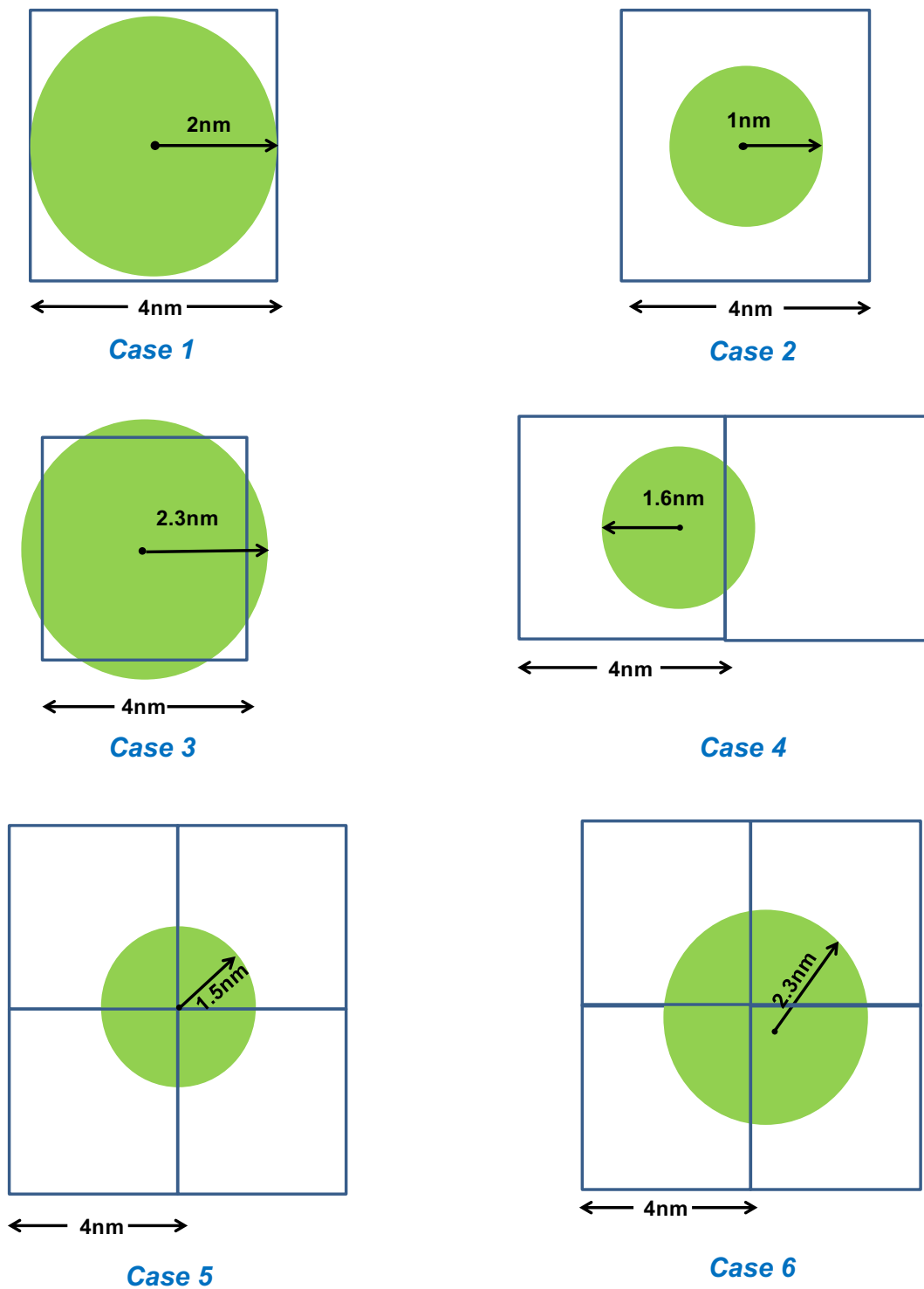


FIGURE D.1: Different bubble configurations in the 1-cells to verify numerical calculation of RS with the theoretical.

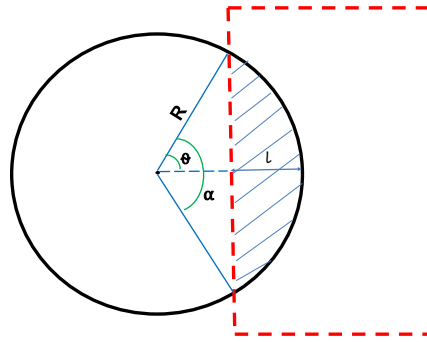


FIGURE D.2: Calculating the area of bubble outside the cell.

where α is the angle made by the arc and l is the length of the sagitta with R being the radius of the arc (here of the bubble). We have four such shaded regions in the four neighbour cells. So, the RS for the cell with the center of the bubble can be calculated analytically as:

$$RS = \frac{Area(cell) - [Area(Bubble) - 4 * Area(shaded)]}{Area(cell)}$$

- **Case 4**

In this case, we have a bubble shared by two adjacent cells with all four corners of the cell with the bubble center outside the bubble. The radius of the bubble is $r = 1.6$ nm. Like Case 3, we need to calculate the area of the region of the bubble outside the cell with the bubble center. Then the RS can be calculated as in the previous case, but without the factor 4 in the Area of the shaded region as there is just one such region in this case.

- **Case 5**

This case explores a scenario in which a bubble is shared among four cells with the center of the bubble being at the point of intersection of the four cells. The radius of the bubble is $r = 1.5$ nm. For this case, no cell has the centre of the bubble in it, however, the RS would be the same for each cell. We calculate the RS for the top-right cell. The area of the sector in the prescribed cell will be given as:

$$Area(sector) = \frac{1}{2}R^2\theta(rad)$$

where θ is the angle subtended by the sector, which here is $(\pi/2)$. So, RS can be calculated analytically as:

$$RS = \frac{Area(cell) - Area(sector)}{Area(cell)}$$

- **Case 6**

This case is similar to Case 3, however, the bubble is shared by four cells with the center of the bubble not overlapping the center of any cell.

The radius of the bubble is $r = 2.3$ nm. Using the formula for the shaded region we can calculate the regions $(B1 + B2)$, $(B1 + B3)$, $(B3 + B4)$ and $(B4 + B2)$. (See Fig.D.3).

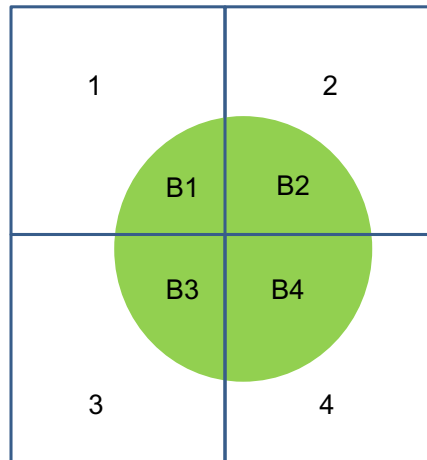


FIGURE D.3: Calculating the RS of cells.

This gives us four equations with four unknowns that can be solved.

Appendix E

Checking the order of convergence for space and time discretization

We perform an analysis of the order of convergence in space and time for the numerical method adopted in the model.

To determine the order of convergence in space, we choose a small Δt and perform several calculations by varying 'h'. Each time the error defined in Eq.2.20 is calculated at the same time of C_v evolution. Then we plot $\log(\text{error})$ as a function of $\log(h)$. As expected for our numerical scheme, we obtain a straight line with a slope close to 2.0 (Fig.E.1). The dependence of error in function of h is found to be $10^{-4.6864} * h^{2.0176}$.

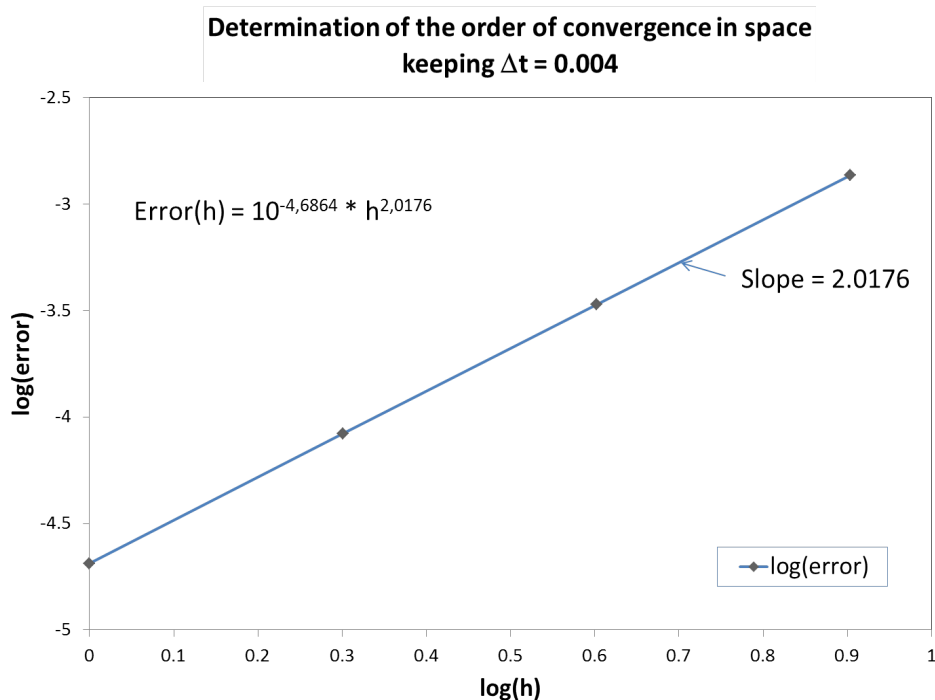


FIGURE E.1: Determining the order of convergence in space.

To determine the order of convergence in time, we perform several calculations with different Δt and a fixed h. We plot $\log(\text{error} - 10^{-4.6864} * h^{2.0176})$ in function of $\log(\text{frac}_{\Delta t_{CFL}})$, with $\text{frac}_{\Delta t_{CFL}} = \Delta t / \Delta t_{CFL}$ ¹. Fig.E.2 shows the plot and as expected, we obtain aligned points with a slope close to 1.

¹ Δt_{CFL} is equal to $\frac{h^2}{D_v * 2 * 2}$ (the domain is 2-D)

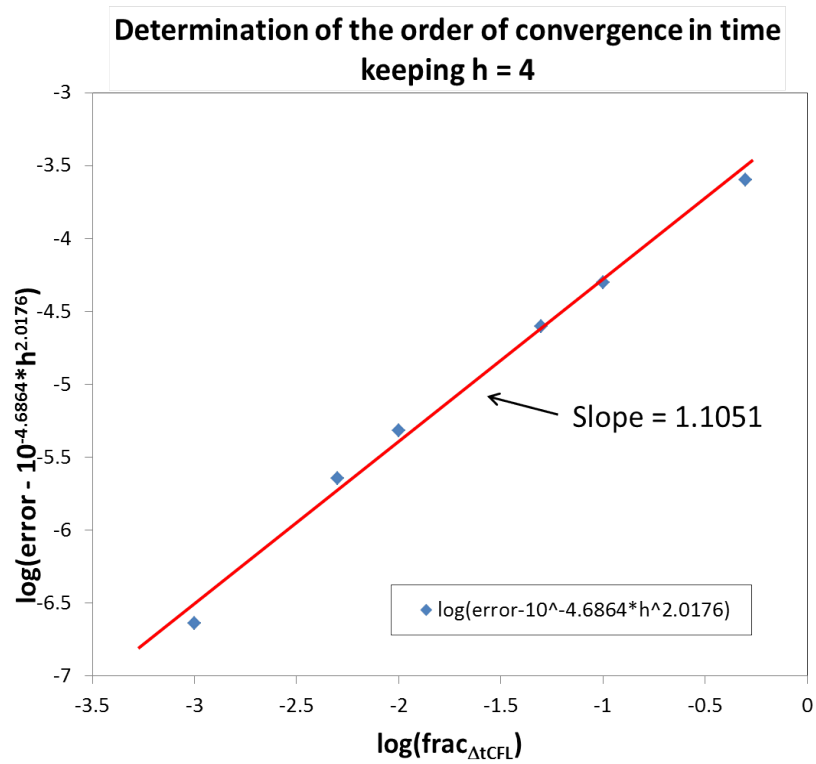


FIGURE E.2: Determining the order of convergence in time.

The tests of order of convergence in space and time are found to behave as expected for the numerical scheme we adopt in this model.

Appendix F

Demonstration for the bubble velocity in a vacancy gradient

Following Geguzin et al.[264], the vacancy field in the permanent state around a bubble placed in a vacancy gradient is the following :

$$C_v(\vec{r}) = C_{v0} + \vec{r}_B \cdot \vec{\nabla} C_{v\infty} + (C_v^{eq}(bubble) - C_{v0} - \vec{r}_B \cdot \vec{\nabla} C_{v\infty}) \frac{R}{r'} + (1 - \frac{R^3}{r'^3}) \vec{r}' \cdot \vec{\nabla} C_{v\infty}$$

where

- $C_v(\vec{r})$ is the vacancy concentration (fraction of sites) at a particular position \vec{r}
- C_{v0} is the vacancy concentration (fraction of sites) at the origin of the position vectors
- $\vec{\nabla} C_{v\infty}$ is the vacancy gradient far from the bubble
- $C_v^{eq}(bubble)$ is the equilibrium vacancy concentration at the vicinity of the bubble. It is the limit condition of the vacancy concentration field at the bubble surface.
- \vec{r}_B is the position of the bubble center
- R is the bubble radius
- $\vec{r}' = \vec{r} - \vec{r}_B$

We can re-write the above equation by adopting C_{v0} for $C_{v0} + \vec{r}_B \cdot \vec{\nabla} C_{v\infty}$, and taking the center of the bubble as the origin. This gives:

$$C_v(\vec{r}) = C_{v0} + (C_v^{eq}(bubble) - C_{v0}) \frac{R}{r} + (1 - \frac{R^3}{r^3}) \vec{r} \cdot \vec{\nabla} C_{v\infty}$$

where the definitions that have changed are below :

- \vec{r} is the position of a point, the center of the bubble being the origin
- C_{v0} is the vacancy concentration (fraction of sites) that would be at the origin (center of the bubble) if the bubble was not there

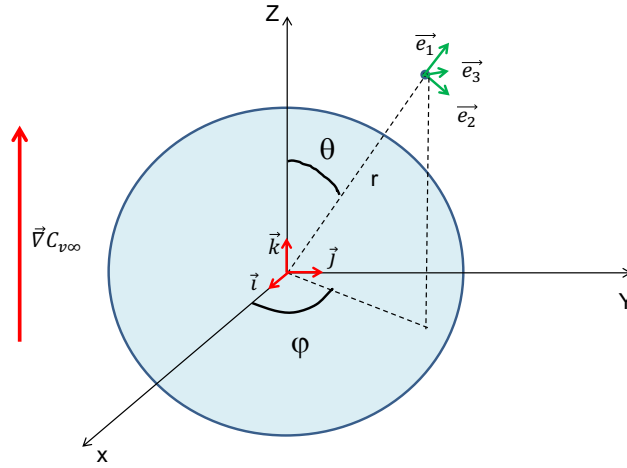


FIGURE F.1: Spherical coordinates in 3D.

Now, if we consider the spherical coordinates (r, θ, φ) , and the z-axis placed in the direction of $\vec{\nabla}C_{v\infty}$, as in Fig.F.1.

$$C_v(\vec{r}) = C_{v0} + \underbrace{(C_v^{eq}(bubble) - C_{v0})\frac{R}{r}}_{T1(r)} + \underbrace{(1 - \frac{R^3}{r^3})rcos\theta\|\vec{\nabla}C_{v\infty}\|}_{T2(r,\theta)}$$

Considering that the vacancy field does not depend on φ , it can be easily verified that :

$$\Delta(C_v(\vec{r})) = \frac{1}{r^2} \frac{\partial}{\partial r} (r^2 \frac{\partial C_v(\vec{r})}{\partial r}) + \frac{1}{r^2 \sin\theta} \frac{\partial}{\partial \theta} (\sin\theta \frac{\partial C_v(\vec{r})}{\partial \theta}) = 0$$

The gradient of the vacancy concentration field is the sum of the gradients of the T1 and T2 fields which can be described as:

$$\vec{\nabla}(T1) = -(C_v^{eq}(bubble) - C_{v0})\frac{R}{r^2} \vec{e}_1$$

and

$$\vec{\nabla}(T2) = \frac{\partial T2}{\partial r} \vec{e}_1 + \frac{1}{r} \frac{\partial T2}{\partial \theta} \vec{e}_2 = \|\vec{\nabla}C_{v\infty}\| (1 + 2\frac{R^3}{r^3}) \cos\theta \vec{e}_1 - \|\vec{\nabla}C_{v\infty}\| (1 - \frac{R^3}{r^3}) \sin\theta \vec{e}_2$$

The growth rate of the bubble is defined by :

$$\frac{\partial V}{\partial t} = -\Omega \int_S \vec{\varphi}_v \cdot \vec{dS} = D_v \int_S \vec{\nabla}(T1 + T2) \cdot \vec{dS}$$

where V is the volume of the bubble, t is the time, Ω is the vacancy volume, $\vec{\varphi}_v = -\frac{1}{\Omega} D_v \vec{\nabla}(C_v(\vec{r}))$ is the vacancy flux (m^{-2}), \vec{dS} is the elementary surface vector oriented towards the exterior of the bubble, and D_v is the vacancy

diffusion coefficient.

$$d\vec{S} = R^2 \sin\theta d\theta d\varphi \vec{e}_1$$

It appears that the contribution to the growth rate of the bubble is only due to the T1 field, and this gives :

$$\frac{\partial V}{\partial t} = 4\pi R D_v (C_{v0} - C_v^{eq}(\text{bubble}))$$

Now, to calculate the bubble velocity, let us define the center of the bubble at t as C , the center of the bubble at $t + dt$ as C' , a current point on the bubble surface as M . C' may be defined as the center of voids of the bubble at t and the different new voids added to the bubble in each point M of the surface. With an arbitrary fixed origin point O , this gives :

$$\vec{OC}' = \frac{1}{V(t+dt)} \left(V(t)\vec{OC} + dt \int_S \vec{OM} \times -\Omega \vec{\varphi}_v \cdot d\vec{S} \right) \quad (\text{F.1})$$

This may be transformed, using $\vec{OM} = \vec{OC} + \vec{CM} = \vec{OC} + \vec{r}$, into :

$$\vec{OC}' = \frac{1}{V(t+dt)} \left(V(t+dt)\vec{OC} + dt \int_S \vec{r} \times -\Omega \vec{\varphi}_v \cdot d\vec{S} \right)$$

$$\vec{OC}' = \vec{OC} + \frac{dt}{V(t+dt)} \int_S \vec{r} \times -\Omega \vec{\varphi}_v \cdot d\vec{S}$$

The bubble velocity \vec{v} is obtained by :

$$\vec{v} = \lim_{dt \rightarrow 0} \frac{\vec{CC}'}{dt} = \frac{D_v}{V} \int_S \vec{r} \times \left(\vec{\nabla}(T1 + T2) \cdot d\vec{S} \right)$$

Because of the spherical symmetry of the field $T1$, it does not contribute to the bubble velocity. The contribution from $T2$ can be calculated using the expressions of $\vec{\nabla}(T2)$ and $d\vec{S}$ to calculate $\vec{\nabla}(T2) \cdot d\vec{S}$ in function of r and θ first, and then using the expression of \vec{r} :

$$\vec{r} = R \cos\varphi \sin\theta \vec{i} + R \sin\varphi \sin\theta \vec{j} + R \cos\theta \vec{k}$$

to integrate the limits on φ from 0 to 2π , and on θ from 0 to π . The contributions along \vec{i} and \vec{j} are nil because of the cylindrical symmetry of the problem.

Finally, the expression for the bubble velocity is:

$$\vec{v} = 3D_v \|\vec{\nabla}C_{v\infty}\| \vec{k}$$

Note that this velocity has been calculated in the fixed referential. In the model, we calculate the new center of the bubble using the numerical equivalent of the relation F.1, and the numerical bubble velocity has been calculated by $\vec{v} = \frac{\vec{CC}'}{dt}$ based on the output file that gives the bubble center position for each

time of the simulation. So the numerical bubble velocity is also calculated in the fixed referential.

In several articles, the bubble velocity is said to be equal to $2D_v \|\vec{\nabla} C_{v\infty}\|$. As Geguzin explains, this is the velocity of the bubble in a system of coordinates linked to the matter far from the bubble, in the case where the solid moves like in the test case, because of the vacancy flux that goes through it.

For a numerical simulation in 3D, the numerical velocity should be compared with $3D_v \|\vec{\nabla} C_{v\infty}\|$. However, the simulations presented in this paper are 2D. That is why we need to find a theoretical expression in 2D.

In 2D, if we consider a bubble that has reached equilibrium with the vacancy field at the position where its center stands ($C_v^{eq}(bubble) = C_{v0}$), the solution for the vacancy field in 2D would be:

$$C_v(\vec{r}) = C_{v0} + \underbrace{\left(1 - \frac{R^2}{r^2}\right)rcos\theta}_{T2(r,\theta)} \|\vec{\nabla} C_{v\infty}\|$$

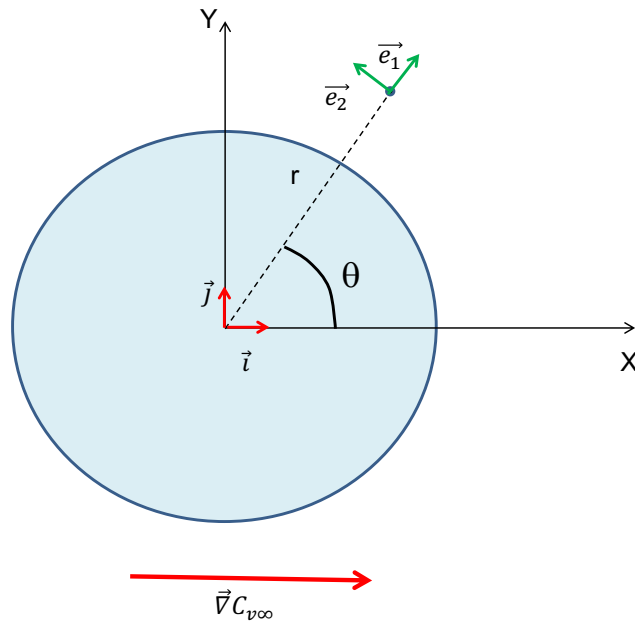


FIGURE F.2: Polar coordinates in 2D.

In 2D, we verify that :

$$\Delta(C_v(\vec{r})) = \frac{1}{r} \frac{\partial}{\partial r} \left(r \frac{\partial T2}{\partial r} \right) + \frac{1}{r^2} \frac{\partial^2}{\partial \theta^2} (T2) = 0$$

We also have

$$\vec{\nabla}(T2) = \frac{\partial T2}{\partial r} \vec{e}_1 + \frac{1}{r} \frac{\partial T2}{\partial \theta} \vec{e}_2 = \|\vec{\nabla} C_{v\infty}\| \left(1 + \frac{R^2}{r^2}\right) \cos\theta \vec{e}_1 - \|\vec{\nabla} C_{v\infty}\| \left(1 - \frac{R^2}{r^2}\right) \sin\theta \vec{e}_2$$

and

$$d\vec{S} = R d\theta \vec{e}_1$$

The growth rate of the bubble is nil, which is consistent with the fact that the bubble is already at equilibrium.

The velocity of the bubble is calculated exactly as above

$$\vec{v} = \frac{D_v}{V} \int_S \vec{r} \times (\vec{\nabla}(T_2) \cdot d\vec{S})$$

with $\vec{r} = R \cos\theta \vec{i} + R \sin\theta \vec{j}$ and $V = \pi R^2$.

Finally, the expression of the bubble velocity **in 2D and in a fixed referential** is :

$$\vec{v} = 2D_v \|\vec{\nabla} C_{v\infty}\| \vec{i}$$

This latter expression is the suitable one for comparison with our numerical velocity in the analysis.

Appendix G

Grid Sensitivity and impact on the coalescence process

G.1 Grid sensitivity analysis

Before moving on to a domain representing the actual size of the grain, we carried out a grid sensitivity study to analyze the dependence of the model on the grid size. We consider the same case presented for the testing of bubble movement and growth in Chapter 3. We take three different grids for the analysis. Grid 1 has 64 x 64 cells with a grid size of 4 nm. Similarly, Grid 2 has 128 x 128 cells with grid size 2 nm and Grid 3 has 256 x 256 cells with grid size 1 nm. The analysis is carried out for a simulated time of 1 hour with isothermal annealing temperature of 1800°C. All the box boundaries are provided with periodic boundary conditions.

We observe the mean radius of small bubbles with time using the three grids and the same has been plotted in Fig.G.1. We expect the mean small bubble radius to increase initially as they trap more and more vacancies emitted from the larger empty bubble and to saturate with time as the vacancy concentration gradient is reduced and reach an equilibrium value. We see that the mean small bubble radius follows the expected trend with all the three different grids and the results are in close agreement with each other.

The grid, however, does impact the rate of coalescence of bubbles in the model, as the condition for coalescence depends on the interface cells (1-cells) of the bubbles. The coalescence of two bubbles occurs if 1-cells of two different bubbles are adjacent to each other. This means that a finer grid results in lesser or delayed occurrence of coalescence between bubbles. When two highly pressurized bubbles coalesce, the resulting bubble has a higher tendency to trap vacancies due to its smaller curvature. So less coalescence induces a reduced bubble growth for the small highly pressurized bubbles. This will cause the mean small bubble radius to be smaller with finer mesh and this is evident from Grid 1 and Grid 2 in the Fig.G.1. Following the same concept, the mean small bubble radius should reduce further with an even finer mesh in Grid 3. However, we notice that the Grid 3 gives mean bubble radius values in between the Grid 1 and Grid 2 values. The reason for this apparent anomaly can be understood from the bubble distribution images at the end of the simulation at time $t = 1$ h in Fig.G.2.

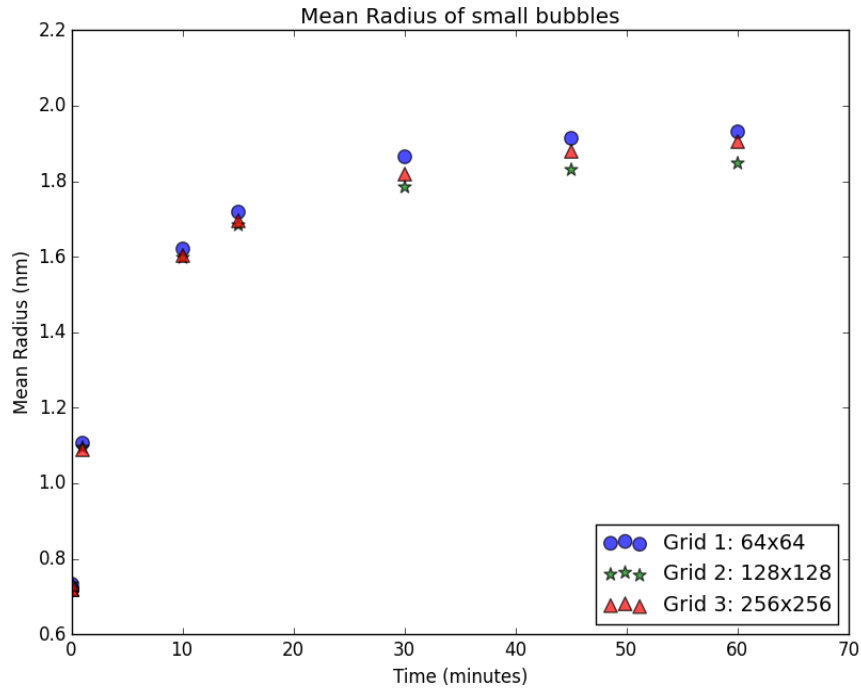


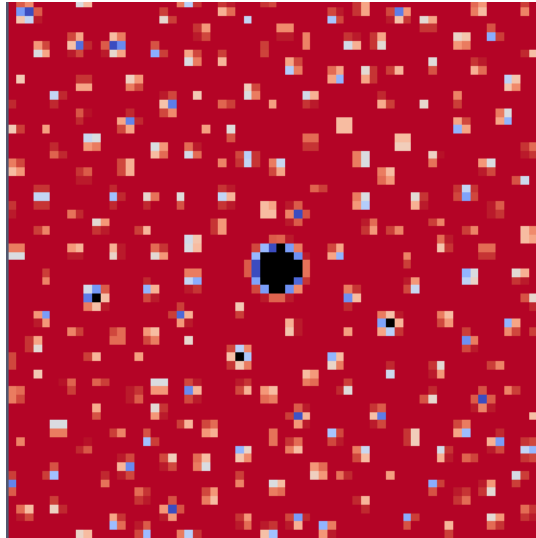
FIGURE G.1: Grid sensitivity analysis: Plot for mean bubble radius with time for 3 different grids.

It can be noticed that in the case of Grid 3, the bubbles at the vicinity of the larger bubble did not coalesce with it, whereas in the Grid 2, the coalescence occurred. These additional bubbles in the Grid 3 case, which are quite large as compared to the other small bubbles, cause the mean radius of the small bubbles to increase as compared to the Grid 2 case. The other bubbles in all the cases can be seen to have evolved similarly. This study shows that even if the rate of coalescence depends on the grid size in our model, the general trends are captured even with the coarse grid. The mean relative difference between values for mean small bubble radius using Grid 1 and Grid 2 is $\sim 1.5\%$ and the values lie in between Grid 1 and 2 using the Grid 3. The following section develops a perspective to make the coalescence phenomena independent of the grid in the model.

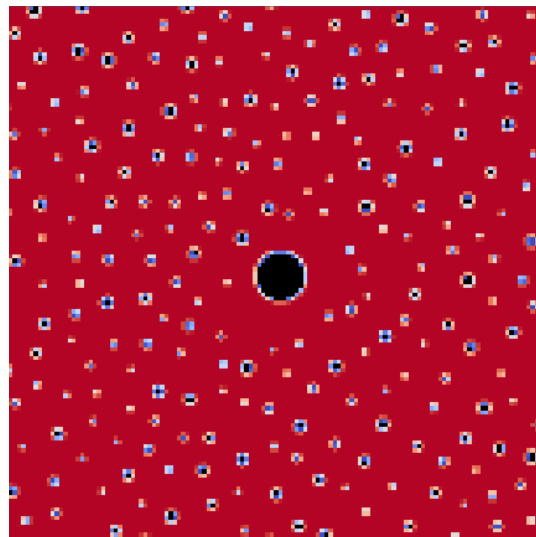
G.2 Perspective for coalescence and space discretization in the model

In the present formulation of the model, the problem of the coalescence of bubbles is not completely independent of the spatial discretization as the coalescence condition is "If two interface cells are neighbours and they belong to two different bubbles, then the two bubbles have to coalesce". Another approach that could be adopted to deal with the coalescence is to define a physical distance of coalescence, d_{coal} (minimum acceptable distance between the bubble surfaces), and write the condition for coalescence differently. For instance, if $d_{coal} > 2h$, then at least the second shell around each interface cell

Grid 1
64x64



Grid 2
128x128



Grid 3
256x256

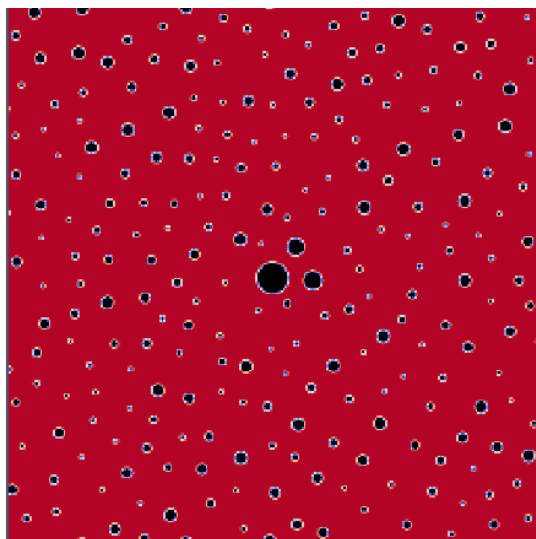


FIGURE G.2: Grid sensitivity analysis: bubble distribution after 1 hour for large (Grid 1), medium (Grid 2) and small (Grid 3) grids.

should be analyzed to check for coalescence. With such an algorithm, the solution, including the coalescence, should remain stable even if h is diminished. The development and tests of such an algorithm is beyond the scope of this work, but is feasible.

Our calculations, with $h = 4$ nm and the present algorithm, correspond to a $d_{coal} \sim 8$ nm which is reasonable since $d_{coal}^{-3} = 1.95 * 10^{24} m^{-3}$ is of the order of magnitude of the maximum bubble densities observed.

Appendix H

Target value of FGR (From spherical to planar geometry)

Following the idea of Evans[102], if the spherical grain is divided into shells and the FGR comes from the outermost shell of the grain, then a sphere of radius R_{ext} would be depleted of gas bubbles up to the radius R_1 (Fig.H.1).

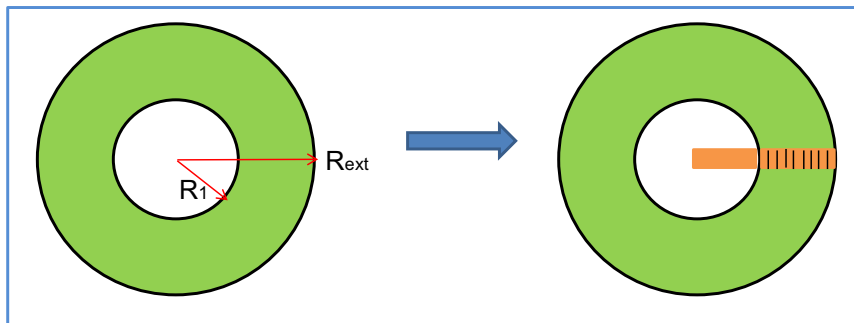


FIGURE H.1: Target value of FGR from spherical to Planar geometry.

The volume of FGR from the sphere can be represented as:

$$\frac{4}{3}\pi(R_{ext}^3 - R_1^3)$$

This volume represents 61% of total gas release, so

$$\frac{4}{3}\pi(R_{ext}^3 - R_1^3) = 0.61 * \frac{4}{3}\pi R_{ext}^3$$

which gives us the fraction of gas retained in the sphere as:

$$\frac{R_1}{R_{ext}} = 0.7306$$

Now, if we consider the same R_1 and R_{ext} in a planar geometry, then the fraction of gas released would be given by $1 - \frac{R_1}{R_{ext}}$ and this value is 0.2694.

So, for a 61% FGR in a spherical geometry, we can roughly have an equivalent FGR of $\sim 27\%$ in the planar geometry.

Appendix I

Problems with classical rate theory in predicting FGR in annealing condition with the random movement of bubbles

To illustrate the problems that are encountered with classical rate theory in the annealing situation, we performed a simple calculation with MARGARET [148].

We modelled the irradiation of a fuel with $10\mu\text{m}$ grain size until a burnup of approximately $10\text{GWd}/t_M$. The fission rate is 10^{19} fissions/ m^3/s , and the temperature of irradiation is 900°C .

Then this fuel is placed in the conditions of the annealing, namely no fission rate, a temperature of 1600°C . Moreover, to facilitate the analysis, we opened the grain boundaries (like if a generalized fracturing occurred) instantly at the beginning of the annealing. The diffusion coefficient D_U and D_s are the same as in BEEP. D_b^{vol} and D_b^{surf} are calculated the same way as in BEEP, except that the term $\exp(-\Omega * (P_{int} - 2\gamma/r)/kT)$ is not present in D_b^{vol} (we had taken directly the expression from Olander [10], and did not correct it, in MARGARET). The Mikhlin's term is not considered.

Note that all these differences tend to make the bubbles more mobile than in BEEP and than the best modelling that can be done taking into account the theory and literature. In spite of this, the fission gas release from the grain remains quite low. It is due, in the modelling, to the random movement of bubbles.

The figures I.1 and I.2 show the FGR from the grain and the evolution of the bubble characteristics during the annealing.

This small calculation shows how rate theory model that only consider the usual gas trapping and the random movement of bubbles fail to predict large FGR in annealing conditions.

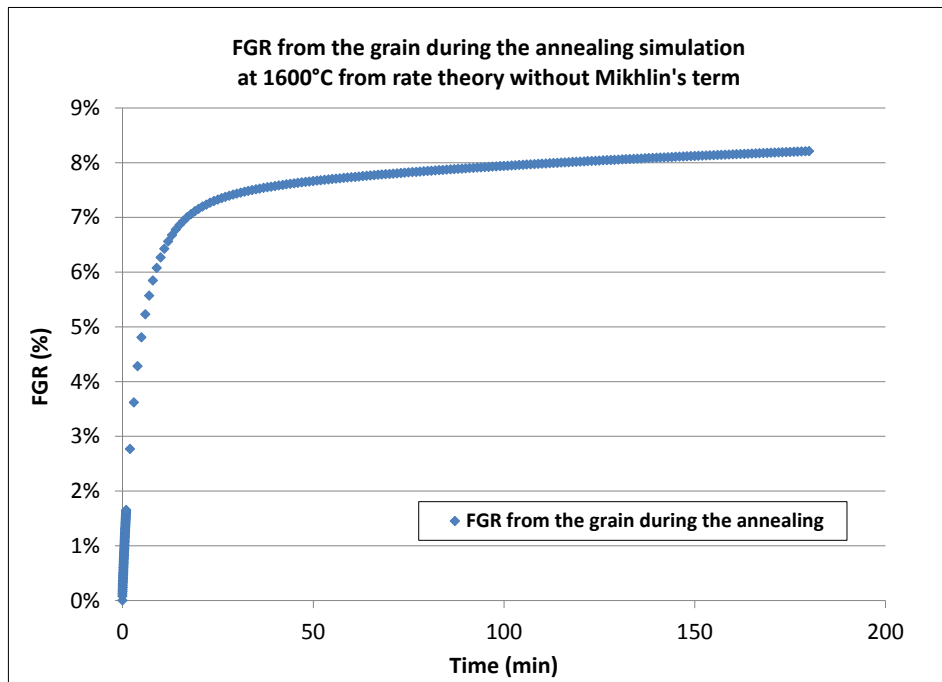


FIGURE I.1: FGR from the grain during the annealing simulation at 1600°C from rate theory without Mikhlin's suppression term.

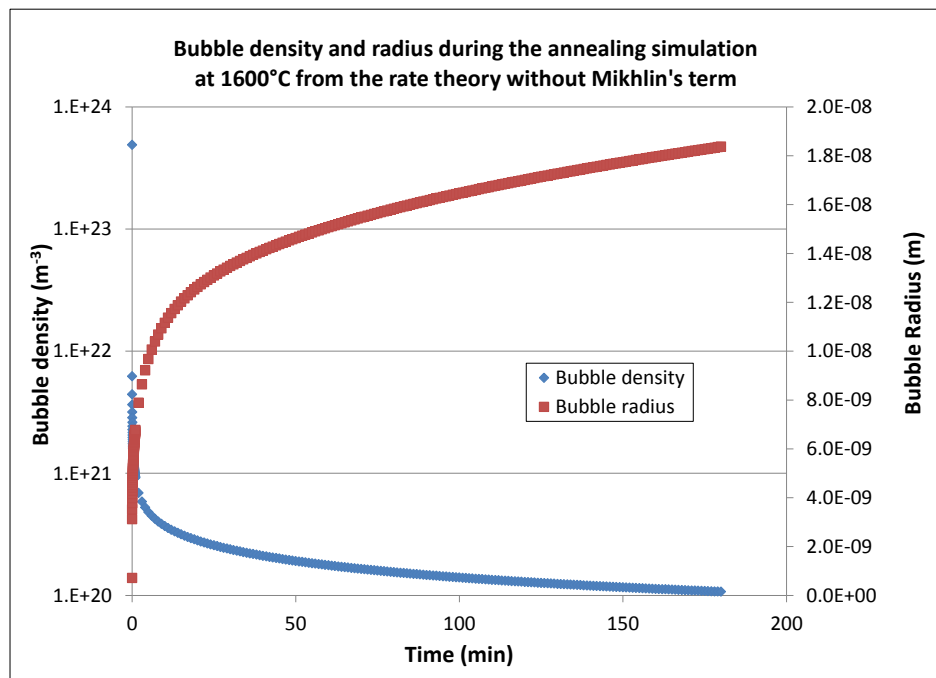


FIGURE I.2: Bubble density and radius during the annealing simulation at 1600°C from the rate theory without Mikhlin's suppression term.

Appendix J

Chemical potential in terms of vacancy formation energy

The chemical potential can be expressed in terms of the free energy (F) and the number of vacancies (N_v) as:

$$\mu = \left(\frac{dF}{dN_v} \right) \quad (\text{J.1})$$

Now, consider a system with just the vacancy sites (N_v) and the normal sites (N_s) of a domain that represents the dislocation region (Fig.J.1).

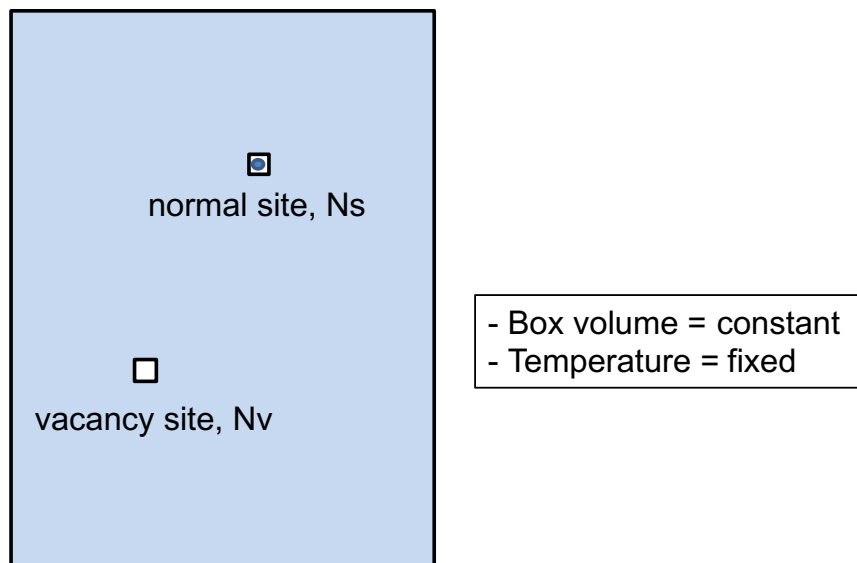


FIGURE J.1: Box containing vacancies and normal (crystal atom) sites.

The total number of sites = $N_v + N_s = \text{constant}$, which gives:

$$dN_s = -dN_v \quad (\text{J.2})$$

From Olander [10, Eq.1.25 , pg5], we get the expression for the free energy as:

$$F = -kT \ln(Z)$$

where k is the Boltzmann constant, T is the temperature (K) and Z is the partition function of the defected lattice. The partition function Z can be expressed as a product of the three terms, Z_1 , Z_2 and Z_3 which are:

- Z_1 : involves the energies of the defects at zero Kelvin. So for the system presented above

$$Z_1 = \exp\left(-N_s \frac{E_0}{kT} - N_v \frac{E_v}{kT}\right)$$

where E_0 and E_v are the energies of the crystal atom and the vacancy site in the lattice at 0 K.

- Z_2 : represents the number of ways to distribute a particular site among all the sites available. For the system here

$$Z_2 = \frac{(N_s + N_v)!}{N_v! N_s!}$$

- Z_3 : accounts for the vibration modes of all the atoms. The changes in Z_3 are neglected in the following.

From the above expressions, we can derive:

$$\ln(Z_1) = -N_s \frac{E_0}{kT} - N_v \frac{E_v}{kT}$$

and using the Stirling formula, $\ln(N!) = N \ln(N) - N$, we derive:

$$\ln(Z_2) = (N_s + N_v) \ln(N_s + N_v) - N_s \ln(N_s) - N_v \ln(N_v)$$

For the derivation, we use the relation between the total and partial derivatives. From Eq.J.2:

$$\frac{d}{N_v} = \frac{\partial}{\partial N_v} * \frac{\partial N_v}{\partial N_v} + \frac{\partial}{\partial N_s} * \frac{\partial N_s}{\partial N_s} = \frac{\partial}{\partial N_v} * 1 + \frac{\partial}{\partial N_s} * (-1) = \frac{\partial}{\partial N_v} - \frac{\partial}{\partial N_s}$$

Now, the chemical potential, from Eq.J.1

$$\begin{aligned} \mu &= \left(\frac{dF}{dN_v} \right) = -kT \left[\frac{d}{dN_v} \ln(Z) \right] \\ &= -kT \left[\frac{d}{dN_v} \ln(Z_1) + \frac{d}{dN_v} \ln(Z_2) \right] \\ &= -kT \left[-\frac{(E_v - E_0)}{kT} + \ln(N_s + N_v) - \ln(N_v) - \ln(N_s + N_v) + \ln(N_s) \right] \\ &= -kT \left[-\frac{(E_v - E_0)}{kT} - \ln \frac{N_v}{(N_s + N_v)} + \underbrace{\ln \frac{N_s}{(N_s + N_v)}}_{\approx 0} \right] \end{aligned}$$

So, we get

$$\mu = (E_v - E_0) + kT \ln \frac{N_v}{(N_s + N_v)}$$

If we define

$$x_{v_d} = \frac{N_v}{N_s + N_v}$$

as the local concentration of vacancies in the dislocation region (in fraction/site), we get the relation for chemical potential as:

$$\mu = (E_v - E_0) + kT \ln(x_{v_d})$$

$(E_v - E_0)$ is the formation of a vacancy in the dislocation region, denoted as E_{v_d} in Eq.5.1 in Chapter 5. It may be obtained by DFT or MD calculations comparing the energies of two boxes. The first one contains a dislocation with a vacancy at its vicinity (dislocation region). The other one contains the same dislocation without the vacancy, such that:

$$E_{v_d} = (E_v - E_0) = E_{Box1} - E_{Box2}$$

Bibliography

- [1] PRIS Database, IAEA. <https://pris.iaea.org/PRIS/WorldStatistics/OperationalReactorsByType.aspx>.
- [2] Nuclear Power Reactors - World Nuclear Association. <http://www.world-nuclear.org/information-library/nuclear-fuel-cycle/nuclear-power-reactors/nuclear-power-reactors.aspx>.
- [3] Nuclear Fuel Fabrication - World Nuclear Association. <http://www.world-nuclear.org/information-library/nuclear-fuel-cycle/conversion-enrichment-and-fabrication/fuel-fabrication.aspx>.
- [4] P.A. Scholle and D.S Ulmer-Scholle. Environmental Science 5: Energy efficiency, renewable and non-renewable energy resources. SEPM Photo CD-14, p.637, 1997.
- [5] G. Leinders, T. Cardinaels, K. Binnemans, and M. Verwerft. Accurate lattice parameter measurements of stoichiometric uranium dioxide. *J. Nucl. Mater.*, 459:135 – 142, 2015.
- [6] G. Delette and M. Charles. Thermal conductivity of fully dense unirradiated UO_2 : a new formulation from experimental results between 100°C and 2500°C , and associated fundamental properties. In *Technical Committee Meeting on 'Water Reactor Fuel Element Modelling at High Burnup and Experimental Support*, IAEA-TECDOC-957, pages 203–216, 1994.
- [7] H. Kleykamp. The chemical state of the fission products in oxide fuels. *J. Nucl. Mater.*, 131(2):221–246, 1985.
- [8] Sylvie Valin. *Etude des mécanismes microstructuraux liés au relâchement des gaz de fission du dioxyde d'uranium irradié*. PhD thesis, Institut National Polytechnique de Grenoble, 1999.
- [9] J.C. Rousseau, G. Houdayer, and M. Réocreux. The CATHARE code development. In *5th International Meeting on Thermal Nuclear Reactor Safety*, 1984.
- [10] D. R. Olander. *Fundamental Aspects of Nuclear Reactor Fuel Elements, TID-26711-P1*. Technical Information Center, Office of Public Affairs Energy Research and Development Administration, University of California, Berkeley, 1976.

-
- [11] E. Vathonne, J. Wiktor, M. Freyss, G. Jomard, and M. Bertolus. DFT+U investigation of charged point defects and clusters in UO_2 . *J. Phys. Condens. Matter*, 26(32):325501, 2014.
- [12] P. Li and Z.F. Zhang. Standing wave effect and fractal structure in dislocation evolution. *Scientific Reports*, 7:4062, 2017.
- [13] A. Michel, C. Sabathier, G. Carlot, M. Cabié, S. Bouffard, and P. Garcia. A TEM study of bubbles growth with temperature in Xenon and Krypton implanted Uranium Dioxide. volume 323 of *Defect and Diffusion Forum*, pages 191–196, 2012.
- [14] G. Brillant, F. Gupta, and A. Pasturel. Fission products stability in uranium dioxide. *J. Nucl. Mater.*, 412(1):170 – 176, 2011.
- [15] D. Olander. Nuclear fuels - Present and future. *J. Nucl. Mater.*, 389(1):1–22, 2009.
- [16] G. Nilsson. Ejection of uranium atoms from sintered UO_2 by fission fragments in different gases and at different gas pressures. *J. Nucl. Mater.*, 20(2):215–230, 1966.
- [17] C. Wise. Recoil release of fission products from nuclear fuel. *J. Nucl. Mater.*, 136(1):30–47, 1985.
- [18] B.J. Lewis. Fission product release from nuclear fuel by recoil and knockout. *J. Nucl. Mater.*, 148(1):28 – 42, 1987.
- [19] I.J. Hastings, C.E.L. Hunt, and J.J. Lipsett. Release of short-lived fission products from UO_2 fuel: Effects of operating conditions. *J. Nucl. Mater.*, 130:407–417, 1985.
- [20] R.J. White and M.O. Tucker. A new fission-gas release model. *J. Nucl. Mater.*, 118(1):1–38, 1983.
- [21] R.J. White. The development of grain-face porosity in irradiated oxide fuel. *J. Nucl. Mater.*, 325(1):61–77, 2004.
- [22] M. Freyss, N. Vergnet, and T. Petit. Ab initio modeling of the behavior of helium and xenon in actinide dioxide nuclear fuels. *J. Nucl. Mater.*, 352(1):144–150, 2006.
- [23] Y. Yun, H. Kim, H. Kim, and K. Park. Atomic diffusion mechanism of Xe in UO_2 . *J. Nucl. Mater.*, 378(1):40–44, 2008.
- [24] D. A. Andersson, B. P. Uberuaga, P. V. Nerikar, C. Unal, and C. R. Stanek. U and Xe transport in $\text{UO}_{2\pm x}$: Density functional theory calculations. *Phys. Rev. B*, 84(5):054105, 2011.
- [25] X. Y. Liu, B. P. Uberuaga, D. A. Andersson, C. R. Stanek, and K. E. Sickafus. Mechanism for transient migration of xenon in UO_2 . *App. Phys. Lett.*, 98(15):151902, 2011.

-
- [26] A. E. Thompson and C. Wolverton. Pathway and energetics of xenon migration in uranium dioxide. *Phys. Rev. B*, 87(10):104105, 2013.
- [27] D.A. Andersson, P. Garcia, X.-Y. Liu, G. Pastore, M. Tonks, P. Millett, B. Dorado, D.R. Gaston, D. Andrs, R.L. Williamson, R.C. Martineau, B.P. Uberuaga, and C.R. Stanek. Atomistic modeling of intrinsic and radiation-enhanced fission gas (Xe) diffusion in $\text{UO}_{2\pm x}$: Implications for nuclear fuel performance modeling. *J. Nucl. Mater.*, 451(1):225–242, 2014.
- [28] C. R. A. Catlow and W. C. Marshall. Fission gas diffusion in uranium dioxide. *Proc. Royal Society of London. A. Mathematical and Physical Sciences*, 364(1719):473–497, 1978.
- [29] R. G. J. Ball and R. W. Grimes. Diffusion of Xe in UO_2 . *J. Chem. Soc., Faraday Trans.*, 86(8):1257–1261, 1990.
- [30] K. Govers, S.E. Lemehov, and M. Verwerft. On the solution and migration of single Xe atoms in uranium dioxide – an interatomic potentials study. *J. Nucl. Mater.*, 405(3):252–260, 2010.
- [31] S. T. Murphy, A. Chartier, L. Van Brutzel, and J. P. Crocombette. Free energy of Xe incorporation at point defects and in nanovoids and bubbles in UO_2 . *Phys. Rev. B*, 85(14):144102, 2012.
- [32] M.W.D. Cooper, C.R. Stanek, J.A. Turnbull, B.P. Uberuaga, and D.A. Andersson. Simulation of radiation driven fission gas diffusion in UO_2 , ThO_2 and PuO_2 . *J. Nucl. Mater.*, 481:125–133, 2016.
- [33] M. Tonks, D. Andersson, R. Devanathan, R. Dubourg, A. El-Azab, M. Freyss, F. Iglesias, K. Kulacsy, G. Pastore, S. R. Phillpot, and M. Welland. Unit mechanisms of fission gas release: Current understanding and future needs. *J. Nucl. Mater.*, 504:300 – 317, 2018.
- [34] S. Nicoll, H.J. Matzke, and C.R.A. Catlow. A computational study of the effect of Xe concentration on the behaviour of single xe atoms in UO_2 . *J. Nucl. Mater.*, 226(1):51–57, 1995.
- [35] H.J. Matzke. *Diffusion in ceramic oxide systems*. Hastings, I.J, American Ceramic Society, Columbus, OH (USA), 1986.
- [36] H. J. Matzke. Gas release mechanisms in UO_2 - a critical review. *Radiation Effects*, 53(3-4):219–242, 1980.
- [37] W Miekeley and F.W Felix. Effect of stoichiometry on diffusion of xenon in UO_2 . *J. Nucl. Mater.*, 42(3):297–306, 1972.
- [38] M.A. Mansouri and D.R. Olander. Fission product release from trace irradiated UO_{2+x} . *J. Nucl. Mater.*, 254(1):22–33, 1998.

- [39] M. Hirai, J.H. Davies, and R. Williamson. Diffusivities of fission gas species in UO_2 and $(\text{U,Gd})\text{O}_2$ nuclear fuels during irradiation. *J. Nucl. Mater.*, 226(1):238–251, 1995.
- [40] P.T. Sawbridge, C. Baker, R.M. Cornell, K.W. Jones, D. Reed, and J.B. Ainscough. The irradiation performance of magnesia-doped UO_2 fuel. *J. Nucl. Mater.*, 95(1):119–128, 1980.
- [41] Y. Harada. Sintering behaviour of niobia-doped large grain UO_2 pellet. *J. Nucl. Mater.*, 238(2):237–243, 1996.
- [42] J.C. Killeen. Fission gas release and swelling in UO_2 doped with Cr_2O_3 . *J. Nucl. Mater.*, 88(2):177–184, 1980.
- [43] N. Djourellov, B. Marchand, H. Marinov, N. Moncoffre, Y. Pison, N. Bérerd, P. Nédélec, L. Raimbault, and T. Epicier. Study of temperature and radiation induced microstructural changes in Xe-implanted UO_2 by TEM, STEM, SIMS and positron spectroscopy. *J. Nucl. Mater.*, 443(1):562 – 569, 2013.
- [44] R. Bès, P. Martin, E. Vathonne, R. Delorme, C. Sabathier, M. Freyss, M. Bertolus, and P. Glatzel. Experimental evidence of Xe incorporation in Schottky defects in UO_2 . *Appl. Phys. Lett.*, 106(11):114102, 2015.
- [45] J. H. Evans. *Recent Experimental Studies on Thermal and Irradiation-Induced Resolution of Gas Atoms from Bubbles in Solids*, pages 307–319. Springer US, Boston, MA, 1991.
- [46] J.R. MacEwan and W.H. Stevens. Xenon diffusion in UO_2 : some complicating factors. *J. Nucl. Mater.*, 11(1):77–93, 1964.
- [47] J. H. Evans, A. Van Veen, and K. T. Westerduin. A TEM and TDS study of gas release from bubbles in krypton-implanted uranium dioxide. *J. Nucl. Mater.*, 195:250–259, 1992.
- [48] C. Matzke, H.J. and Ronchi and C. Baker. Precipitation of Xe and Cs into bubbles, kinetics of bubble migration and alternative release processes. *Eur. App. Res. Rept.*, 5(6):1105–1157, 1984.
- [49] P. V. Nerikar, D. C. Parfitt, L. A. Casillas Trujillo, D. A. Andersson, C. Unal, S. B. Sinnott, R. W. Grimes, B. P. Uberuaga, and C. R. Stanek. Segregation of xenon to dislocations and grain boundaries in uranium dioxide. *Phys. Rev. B*, 84(17):174105, 2011.
- [50] S. T. Murphy, P. Fossati, and R. W. Grimes. Xe diffusion and bubble nucleation around edge dislocations in UO_2 . *J. Nucl. Mater.*, 466:634–637, 2015.
- [51] M. V. Speight. A calculation on the migration of fission gas in material exhibiting precipitation and re-resolution of gas atoms under irradiation. *Nucl. Sci. Eng.*, 37(2):180–185, 1969.

-
- [52] A. D. Whapham. Electron microscope observation of the fission-gas bubble distribution in UO_2 . *Nucl. Appl.*, 2(2):123–130, 1966.
- [53] A.J. Manley. Transmission electron microscopy of irradiated UO_2 fuel pellets. *J. Nucl. Mater.*, 27(2):216–224, 1968.
- [54] R.S. Nelson. The stability of gas bubbles in an irradiation environment. *J. Nucl. Mater.*, 31(2):153 – 161, 1969.
- [55] J.A. Turnbull. The distribution of intra-granular fission gas bubbles in UO_2 during irradiation. *J. Nucl. Mater.*, 38(2):203–212, 1971.
- [56] R.M. Cornell. An electron microscope examination of matrix fission-gas bubbles in irradiated uranium dioxide. *J. Nucl. Mater.*, 38(3):319–328, 1971.
- [57] J. A. Turnbull. A review of irradiation induced re-resolution in oxide fuels. *Rad. Effects*, 53(3-4):243–249, 1980.
- [58] G.T. Lawrence. A review of the diffusion coefficient of fission-product rare gases in uranium dioxide. *J. Nucl. Mater.*, 71(2):195–218, 1978.
- [59] D.R. Olander and D. Wongsawaeng. Re-resolution of fission gas - A review: Part I. Intragranular bubbles. *J. Nucl. Mater.*, 354(1):94–109, 2006.
- [60] M. Toulemonde, E. Paumier, and C. Dufour. Thermal spike model in the electronic stopping power regime. *Rad. Effects Defects Solids*, 126(1-4):201–206, 1993.
- [61] D. Schwen, M. Huang, P. Bellon, and R.S. Averback. Molecular dynamics simulation of intra-granular Xe bubble re-resolution in UO_2 . *J. Nucl. Mater.*, 392(1):35–39, 2009.
- [62] M. Huang, D. Schwen, and R.S. Averback. Molecular dynamic simulation of fission fragment induced thermal spikes in UO_2 : Sputtering and bubble re-resolution. *J. Nucl. Mater.*, 399(2):175–180, 2010.
- [63] K. Govers, C.L. Bishop, D.C. Parfitt, S.E. Lemehov, M. Verwerft, and R.W. Grimes. Molecular dynamics study of Xe bubble re-resolution in UO_2 . *J. Nucl. Mater.*, 420(1):282–290, 2012.
- [64] G. Pastore, L.P. Swiler, J.D. Hales, S.R. Novascone, D.M. Perez, B.W. Spencer, L. Luzzi, P. Van Uffelen, and R.L. Williamson. Uncertainty and sensitivity analysis of fission gas behavior in engineering-scale fuel modeling. *J. Nucl. Mater.*, 456:398–408, 2015.
- [65] L. Noirot. A method to calculate equilibrium concentrations of gas and defects in the vicinity of an over-pressured bubble in UO_2 . *J. Nucl. Mater.*, 447:166–178, 2014.

- [66] R.A. Jackson and C.R.A. Catlow. Trapping and solution of fission Xe in UO_2 : Part 1. Single gas atoms and solution from underpressurized bubbles. *J. Nucl. Mater.*, 127(2):161 – 166, 1985.
- [67] R.A. Jackson and C.R.A. Catlow. Trapping and solution of fission Xe in UO_2 : Part 2. Solution from small overpressurized bubbles. *J. Nucl. Mater.*, 127(2):167–169, 1985.
- [68] J. R. MacEwan and P. A. Morel. Migration of Xenon through a UO_2 matrix containing trapping sites. *Nucl. Appl.*, 2:158, 1968.
- [69] D.A. MacInnes and I.R. Brearley. A model for the release of fission gas from reactor fuel undergoing transient heating. *J. Nucl. Mater.*, 107(2):123–132, 1982.
- [70] I. R. Brearley and D. A. MacInnes. Modelling of fission-gas release from fuel undergoing isothermal heating. *J. Nucl. Mater.*, 118:68–72, 1983.
- [71] C. Ronchi. On diffusion and precipitation of gas-in-solid. *J. Nucl. Mater.*, 148(3):316–323, 1987.
- [72] R.J. White. The growth of intra-granular bubbles in post-irradiation annealed UO_2 fuel. In *IAEA, Technical committee on nuclear fuel behaviour modeling at high burn-up and its experimental support*, Windermere, UK, 2000.
- [73] I.M. Lifshitz and V.V. Slyozov. The kinetics of precipitation from supersaturated solid solutions. *J. Phys. Chem. Solids*, 19(1):35 – 50, 1961.
- [74] M.S. Veshchunov. On the theory of fission gas bubble evolution in irradiated UO_2 fuel. *J. Nucl. Mater.*, 277(1):67–81, 2000.
- [75] H.J. Matzke. Diffusion in doped UO_2 . *Nucl. App.*, 2(2):131–137, 1966.
- [76] B. Dorado. *Etude des propriétés de transport atomique dans le dioxyde d'uranium par le calcul de structure électronique : influence des fortes corrélations*. PhD thesis, Aix-Marseille University, 2010.
- [77] H.J. Matzke. *Fundamental aspects of inert gas behaviour in nuclear fuels: oxides, carbides and nitrides*, pages 401–414. Springer US, Boston, MA, 1991.
- [78] J. Janek and H. Timm. Thermal diffusion and Soret effect in $(\text{U,Me})\text{O}_{2+\delta}$: the heat of transport of oxygen. *J. Nucl. Mater.*, 255(2):116 – 127, 1998.
- [79] J.A. Turnbull, C.A. Friskney, J.R. Findlay, F.A. Johnson, and A.J. Walter. The diffusion coefficients of gaseous and volatile species during the irradiation of uranium dioxide. *J. Nucl. Mater.*, 107(2):168–184, 1982.
- [80] P. Shewmon. *Diffusion in Solids*. Springer International Publishing, 2nd edition, 2016.

-
- [81] I. Kaur, Y. Mishin, and W. Gust. *Fundamentals of grain and interphase boundary diffusion*. John Wiley, New York, 3rd edition, 1995.
- [82] A. Atkinson. Diffusion along grain boundaries and dislocations in oxides, alkali halides and carbides. *Solid State Ionics*, 12:309–320, 1984.
- [83] M.V. Speight and J.A. Turnbull. Enhanced fission-product release by grain-boundary diffusion. *J. Nucl. Mater.*, 68(2):244–249, 1977.
- [84] J.A. Turnbull and C.A. Friskney. The release of fission products from nuclear fuel during irradiation by both lattice and grain boundary diffusion. *J. Nucl. Mater.*, 58(1):31–38, 1975.
- [85] J.A. Turnbull, C.A. Friskney, F.A. Johnson, A.J. Walter, and J.R. Findlay. The release of radioactive gases from uranium dioxide during irradiation. *J. Nucl. Mater.*, 67(3):301–306, 1977.
- [86] D.R. Olander. *Combined grain-boundary and lattice diffusion in fine-grained ceramics*. Hastings, I.J, American Ceramic Society; Columbus, OH (USA), 1986.
- [87] U. M. El-Saied and D.R. Olander. Fission gas release during grain growth in a microstructure with a distribution of grain sizes. *J. Nucl. Mater.*, 207:313–326, 1993.
- [88] N.L. Peterson. *Diffusion mechanisms in grain boundaries in solids*. CONF-820547-16. American Ceramic Society; Cincinnati, OH (USA), 1982.
- [89] E. Bourasseau, M. Bertolus, M. Freyss, G. Jomard, I.C. Njifon, M S. Talla. Noutack, C.T. Takoundjou, and A. Germain. Atomic scale calculations of nuclear fuel properties to sustain multiscale modeling of fuel behavior. MMM2018, Osaka, Japan, 2018.
- [90] A. Denis and R. Piotrkowski. Simulation of isothermal fission gas release. *J. Nucl. Mater.*, 229:149–154, 1996.
- [91] L.C Bernard and E. Bonnaud. Finite volume method for fission gas release modeling. *J. Nucl. Mater.*, 244(1):75–84, 1997.
- [92] Koo Yang-Hyun, Sohn Dong-Seong, and Yoon Young-Ku. An analysis method for the fuel rod gap inventory of unstable fission products during steady-state operation. *J. Nucl. Mater.*, 209(1):62–78, 1994.
- [93] C.T. Walker and M. Mogensen. On the rate determining step in fission gas release from high burn-up water reactor fuel during power transients. *J. Nucl. Mater.*, 149(2):121–131, 1987.
- [94] C.T. Walker, P. Knappik, and M. Mogensen. Concerning the development of grain face bubbles and fission gas release in UO₂ fuel. *J. Nucl. Mater.*, 160(1):10–23, 1988.

-
- [95] M. O. Tucker. Grain boundary porosity and gas release in irradiated UO_2 . *Rad. Effects*, 53(3-4):251–255, 1980.
- [96] K. Une and S. Kashibe. Fission gas release during post irradiation annealing of BWR fuels. *J. Nucl. Sci. Technol.*, 27(11):1002–1016, 1990.
- [97] M. E. Gulden. Migration of gas bubbles in irradiated uranium dioxide. *J. Nucl. Mater.*, 23(1):30–36, 1967.
- [98] F.A. Nichols. Pore migration in ceramic fuel elements. *J. Nucl. Mater.*, 27(2):137–146, 1968.
- [99] F.A. Nichols. Kinetics of diffusional motion of pores in solids: A review. *J. Nucl. Mater.*, 30(1):143–165, 1969.
- [100] J. H. Evans. Bubble diffusion to grain boundaries in UO_2 and metals during annealing: A new approach. *J. Nucl. Mater.*, 210:21–29, 1994.
- [101] F.A. Nichols. Transport phenomena in nuclear fuels under severe temperature gradients. *J. Nucl. Mater.*, 84(1):1–25, 1979.
- [102] J.H. Evans. The role of directed bubble diffusion to grain boundaries in post-irradiation fission gas release from UO_2 : A quantitative assessment. *J. Nucl. Mater.*, 238(2):175 – 182, 1996.
- [103] J.H. Evans. Post-irradiation fission gas release from high burn-up UO_2 fuel annealed under oxidising conditions. *J. Nucl. Mater.*, 246(2):121–125, 1997.
- [104] D. R. Olander. Interaction of stresses with inclusions in solids - A review. *J. Nucl. Mater.*, 92(2):163–183, 1980.
- [105] H.V. Atkinson. Overview no. 65: Theories of normal grain growth in pure single phase systems. *Acta Metall.*, 36(3):469–491, 1988.
- [106] R. Hargreaves and D.A. Collins. A quantitative model for fission gas release and swelling in irradiated uranium dioxide. *J. Br. Nucl. Energy Soc.*, 15(4):311–318, 1976.
- [107] M. V. Speight and G. W. Greenwood. Grain boundary mobility and its effects in materials containing inert gases. *Philos. Mag.*, 9(100):683–689, 1964.
- [108] M. Mogensen, C. Bagger, and C.T. Walker. An experimental study of the distribution of retained xenon in transient-tested UO_2 fuel. *J. Nucl. Mater.*, 199(2):85–101, 1993.
- [109] J.A. Turnbull. The effect of grain size on the swelling and gas release properties of UO_2 during irradiation. *J. Nucl. Mater.*, 50(1):62–68, 1974.
- [110] M.O. Tucker and R.J. White. The release of unstable fission products from UO_2 during irradiation. *J. Nucl. Mater.*, 87(1):1–10, 1979.

-
- [111] M. Mogensen, C.T. Walker, I.L.F. Ray, and M. Coquerelle. Local fission gas release and swelling in water reactor fuel during slow power transients. *J. Nucl. Mater.*, 131(2):162 – 171, 1985.
- [112] J. Noirot, I. Zacharie-Aubrun, and T. Blay. Focused ion beam–scanning electron microscope examination of high burn-up UO_2 in the center of a pellet. *Nucl. Eng. Technol.*, 50:259–267, 2018.
- [113] R.G. Bellamy and J.B. Rich. Grain-boundary gas release and swelling in high burn-up uranium dioxide. *J. Nucl. Mater.*, 33(1):64–76, 1969.
- [114] M. J. F. Notley and J. R. MacEwan. Stepwise release of fission gas from UO_2 fuel. *Nucl. Technol.*, 2(6):477–480, 1966.
- [115] I.J. Hastings, A.D. Smith, P.J. Fehrenbach, and T.J. Carter. Fission gas release from power-ramped UO_2 fuel. *J. Nucl. Mater.*, 139(2):106–112, 1986.
- [116] K. Une and S. Kashibe. Fission gas release during postirradiation annealing of UO_2 -2 wt% Gd_2O_3 fuels. *J. Nucl. Mater.*, 189(2):210–216, 1992.
- [117] R. M. Carroll, J. G. Morgan, R. B. Perez, and O. Sisman. Fission density, burnup, and temperature effects on fission-gas release from UO_2 . *Nucl. Sci. Eng.*, 38(2):143–155, 1969.
- [118] J. Rest and S.M. Gehl. The mechanistic prediction of transient fission-gas release from LWR fuel. *Nucl. Eng. Des.*, 56(1):233–256, 1980.
- [119] W. Hering. The KWU fission gas release model for LWR fuel rods. *J. Nucl. Mater.*, 114(1):41–49, 1983.
- [120] Y. H. Koo, B. H. Lee, and D. S. Sohn. Cosmos: A computer code to analyze LWR UO_2 and MOX fuel up to high burnup. *Ann. Nucl. Energy*, 26(1):47–67, 1999.
- [121] P. Van Uffelen, A. Schubert, J. Van De Laar, and C. Győri. Development of a transient fission gas release model for TRANSURANUS. In *Water Reactor Fuel Performance Meeting*, 2008.
- [122] L.C. Bernard, J.L. Jacoud, and P. Vesco. An efficient model for the analysis of fission gas release. *J. Nucl. Mater.*, 302(2):125–134, 2002.
- [123] G. Pastore, D. Pizzocri, J.D. Hales, S.R. Novascone, D.M. Perez, B.W. Spencer, R.L. Williamson, P. Van Uffelen, and L. Luzzi. Modelling of transient fission gas behaviour in oxide fuel and application to the BISON code. 2014.
- [124] P. Chakraborty, M. R. Tonks, and G. Pastore. Modeling the influence of bubble pressure on grain boundary separation and fission gas release. *J. Nucl. Mater.*, 452(1):95–101, 2014.

- [125] E. Ya. Mikhlin and V. F. Chkuaseli. Gas release and swelling in oxide fuel; modeling of the kinetics of gas porosity development. *J. Nucl. Mater.*, 105:223–230, 1982.
- [126] C. Baker and J.C. Killeen. Materials for nuclear reactor core applications. In *Int. Conf. on Materials for Nuclear Reactor Core Applications*, page 153, Bristol, UK, 1987. BNES.
- [127] G.J. Small. Fission gas release and bubble development in UO_2 during high temperature transients. In *Proc. IAEA Specialists' Meeting on Water Reactor Fuel Element Computer Modelling in Steady State, Transient and Accident Conditions*, IAEA-TC-659/4.3, pages 209–220. IAEA, Vienna, 1988.
- [128] S. Kashibe, K. Une, and K. Nogita. Formation and growth of intragranular fission gas bubbles in UO_2 fuels with burnup of 6–83 GWd/t. *J. Nucl. Mater.*, 206(1):22 – 34, 1993.
- [129] J. Noiro, Y. Pontillon, S. Yagnik, and J.A. Turnbull. Post-irradiation examinations and high-temperature tests on undoped large-grain UO_2 discs. *J. Nucl. Mater.*, 462:77 – 84, 2015.
- [130] H. Zimmermann. *Eur. App. Res. Rept.-Nucl. Sci. Technol.*, 5:1349, 1984.
- [131] I. Zacharie, S. Lansart, P. Combette, M. Troabas, M. Coster, and M. Groos. Thermal treatment of uranium oxide irradiated in pressurized water reactor: Swelling and release of fission gases. *J. Nucl. Mater.*, 255(2):85 – 91, 1998.
- [132] Isabelle Zacharie. *Traitements thermiques de l'oxyde d'uranium irradié dans un réacteur à eau pressurisée (R.E.P.) : gonflement et relâchement des gaz de fission*. PhD thesis, Ecole centrale de Paris, 1997.
- [133] P.S. Copeland. Onset of gas release and grain face vesting rates in large grain fuel. AEAT-0254, AEA Technology, 1996.
- [134] A. H. Booth. *A method of calculating fission gas diffusion from UO_2 fuel and its application to the X-2-f loop test*. AECL-496, Chalk River, Ontario, 1957.
- [135] J.R. Matthews and M.H. Wood. An efficient method for calculating diffusive flow to a spherical boundary. *Nucl. Eng. Des.*, 56(2):439–443, 1980.
- [136] K. Ito, R. Iwasaki, and Y. Iwano. Finite element model for analysis of fission gas release from UO_2 fuel. *J. Nucl. Sci. Technol.*, 22(2):129–138, 1985.
- [137] T. Nakajima. FEMAXI-IV: A computer code for the analysis of fuel rod behavior under transient conditions. *Nucl. Eng. Des.*, 88(1):69–84, 1985.

-
- [138] K. Forsberg and A.R. Massih. Fission gas release under time-varying conditions. *J. Nucl. Mater.*, 127:141–145, 1985.
- [139] P.T. Elton and K. Lassmann. Calculational methods for diffusional gas release. *J. Nucl. Mater.*, 101:259–265, 1987.
- [140] P. Lösönen. Methods for calculating diffusional gas release from spherical grains. *Nucl. Eng. Des.*, 196(2):161–173, 2000.
- [141] K. Lassmann and H. Benk. Numerical algorithms for intragranular fission gas release. *J. Nucl. Mater.*, 280:127–135, 2000.
- [142] K. Forsberg, F. Lindström, and A.R. Massih. Modelling of some high burnup phenomena in nuclear fuel. In *Proc. Technical Committee Meeting on Water reactor fuel element modelling at high burnup and its experimental support*, IAEA-TECDOC-957, pages 251–275, Windermere, UK, 1994.
- [143] G.A. Berna, G.A. Beyer, K.L. Davis, and D.D. Lanning. FRAPCON-3: A computer code for the calculation of steady-state, thermal-mechanical behavior of oxide fuel rods for high burnup. 1997. Technical Report NUREG/CR-6534-Vol.2.
- [144] J. Rest. GRASS-SST: A comprehensive, mechanistic model for the prediction of fission-gas behavior in UO_2 -base fuels during steady-state and transient conditions. NUREG/CR-0202; ANL-78-53, Argonne National Laboratory, 1978.
- [145] D.M. Dowling, R.J. White, and M.O. Tucker. The effect of irradiation-induced re-solution on fission gas release. *J. Nucl. Mater.*, 110(1):37–46, 1982.
- [146] P. Van Uffelen, J. Hales, W. Li, G. Rossiter, and R. Williamson. A review of fuel performance modelling. *J. Nucl. Mater.*, 516:373 – 412, 2019.
- [147] G. Thouvenin, J.M. Ricaud, B. Michel, D. Plancq, and P. Thevenin. ALCYONE: the PLEIADES fuel performance code dedicated to multidimensional PWR studies. Proceedings of Top Fuel, 2006.
- [148] L. Noirot. MARGARET: A comprehensive code for the description of fission gas behavior. *Nucl. Eng. Des.*, 241:2099–2118, 2011.
- [149] G. Jomard, C. Struzik, A. Bouloure, P. Mailhé, V. Auret, and R. Largenton. CARACAS: An industrial model for description of fission gas behavior in LWR-UO₂ fuel. Proceedings of Top Fuel Conference, Sendai, Japan, 2014.
- [150] R.L. Williamson, J.D. Hales, S.R. Novascone, M.R. Tonks, D.R. Gaston, C.J. Permann, D. Andrs, and R.C. Martineau. Multidimensional multiphysics simulation of nuclear fuel behavior. *J. Nucl. Mater.*, 423(1):149–163, 2012.

- [151] K. Lassmann. TRANSURANUS: a fuel rod analysis code ready for use. *J. Nucl. Mater.*, 188:295–302, 1992.
- [152] K. Forsberg and A.R. Massih. Diffusion theory of fission gas migration in irradiated nuclear fuel UO₂. *J. Nucl. Mater.*, 135(2):140–148, 1985.
- [153] G. Pastore, L. Luzzi, V. Di Marcello, and P. V. Uffelen. Physics-based modelling of fission gas swelling and release in UO₂ applied to integral fuel rod analysis. *Nucl. Eng. Des.*, 256:75–86, 2013.
- [154] M.S. Veshchunov, A.V. Boldyrev, V.D. Ozrin, V.E. Shestak, and V.I. Tarasov. A new mechanistic code SFPR for modeling of single fuel rod performance under various regimes of LWR operation. *Nucl. Eng. Des.*, 241(8):2822–2830, 2011.
- [155] M.S. Veshchunov, V.D. Ozrin, V.E. Shestak, V.I. Tarasov, R. Dubourg, and G. Nicaise. Development of the mechanistic code MFPR for modelling fission-product release from irradiated UO₂ fuel. *Nucl. Eng. Des.*, 236(2):179–200, 2006.
- [156] M.S. Veshchunov, R. Dubourg, V.D. Ozrin, V.E. Shestak, and V.I. Tarasov. Mechanistic modelling of uranium fuel evolution and fission product migration during irradiation and heating. *J. Nucl. Mater.*, 362(2):327–335, 2007.
- [157] L. Noirot. MARGARET: An advanced mechanistic model of fission gas behavior in nuclear fuel. *J. Nucl. Sci. Technol.*, 43(9):1149–1160, 2006.
- [158] M. S. Daw, S. M. Foiles, and M. I. Baskes. The embedded-atom method: a review of theory and applications. *Mater. Sci. Rep.*, 9(7):251–310, 1993.
- [159] D.J. Bacon, A.F. Calder, and F. Gao. Defect production due to displacement cascades in metals as revealed by computer simulation. *J. Nucl. Mater.*, 251:1–12, 1997.
- [160] B.D. Wirth, G.R. Odette, D. Maroudas, and G.E. Lucas. Dislocation loop structure, energy and mobility of self-interstitial atom clusters in bcc iron. *J. Nucl. Mater.*, 276(1):33–40, 2000.
- [161] N.D. Morelon, D. Ghaleb, J.M. Delaye, and L. Van Brutzel. A new empirical potential for simulating the formation of defects and their mobility in uranium dioxide. *Philos. Mag.*, 83(13):1533–1555, 2003.
- [162] C.B. Basak, A.K. Sengupta, and H.S. Kamath. Classical molecular dynamics simulation of UO₂ to predict thermophysical properties. *J. Alloys Compd.*, 360(1):210–216, 2003.
- [163] E. Yakub, C. Ronchi, and D. Staicu. Molecular dynamics simulation of premelting and melting phase transitions in stoichiometric uranium dioxide. *J. Chem. Phys.*, 127(9):094508, 2007.

-
- [164] V. Tikare, M. Braginsky, and E.A. Olevsky. Numerical simulation of solid-state sintering: I, Sintering of three particles. *J. Am. Ceram. Soc.*, 86(1):49–53, 2003.
- [165] A. Barbu and E. Clouet. Cluster dynamics modeling of materials: Advantages and limitations. *Solid State Phenom.*, 129:51–58, 2007.
- [166] R. Skorek, S. Maillard, A. Michel, G. Carlot, E. Gilabert, and T. Jourdan. Modelling fission gas bubble distribution in UO_2 . In *Diffusion in Materials - DIMAT 2011*, volume 323 of *Defect and Diffusion Forum*, pages 209–214. Trans Tech Publications, 2012.
- [167] T. Jourdan, G. Bencteux, and G. Adjanor. Efficient simulation of kinetics of radiation induced defects: A cluster dynamics approach. *J. Nucl. Mater.*, 444(1):298 – 313, 2014.
- [168] A. Karma and W.J. Rappel. Quantitative phase-field modeling of dendritic growth in two and three dimensions. *Phys. Rev. E*, 57(4):4323–4349, 1998.
- [169] L.Q. Chen. Phase-Field models for microstructure evolution. *Ann. Rev. Mater. Res.*, 32(1):113–140, 2002.
- [170] I. Steinbach, B. Böttger, J. Eiken, N. Warnken, and S. G. Fries. CALPHAD and Phase-Field modeling: A successful liaison. *J. Phase Equilib. Diff.*, 28(1):101–106, 2007.
- [171] I. Steinbach. Phase-field models in materials science. *Model. Simul. Mater. Sci. Eng.*, 17(7):073001, 2009.
- [172] M. Kuroda, K. Yoshioka, S. Yamanaka, H. Anada, F. Nagase, and H. Uetsuka. Influence of precipitated hydride on the fracture behavior of zircaloy fuel cladding tube. *J. Nucl. Sci. Tech.*, 37(8):670–675, 2000.
- [173] C. Bailey and M. Cross. A finite volume procedure to solve elastic solid mechanics problems in three dimensions on an unstructured mesh. *Int. J. Numer. Meth. Eng.*, 38(10):1757–1776, 1995.
- [174] G. A. Taylor, C. Bailey, and M. Cross. A vertex-based finite volume method applied to non-linear material problems in computational solid mechanics. *Int. J. Numer. Meth. Eng.*, 56(4):507–529, 2003.
- [175] M. Stan. Discovery and design of nuclear fuels. *Materials Today*, 12(11):20–28, 2009.
- [176] Y. Li, S. Hu, R. Montgomery, F. Gao, X. Sun, M. Tonks, B. Biner, P. Millett, V. Tikare, B. Radhakrishnan, and D. Andersson. Mesoscale simulations of intra-granular fission gas bubbles in UO_2 under post-irradiation thermal annealing. In *Mesoscale Benchmark Demonstration*, FCR&D-MDSM-2012-000098, PNNL-21295, 2012.

- [177] Y. Li, S. Hu, X. Sun, and M. Stan. A review: applications of the phase field method in predicting microstructure and property evolution of irradiated nuclear materials. *npj Computational Materials*, 3(1):16, 2017.
- [178] S Maillard, R Skorek, K Hoang, and M Bertolus. Application of mesoscale approaches to the diffusion processes in UO₂. *F-BRIDGE Deliverable D-225*, 2012.
- [179] A.F. Voter. Introduction to the Kinetic Monte Carlo Method. In K.E. Sickafus, E.A. Kotomin, and B.P. Uberuaga, editors, *Radiation Effects in Solids*, pages 1–23, Dordrecht, 2007. Springer Netherlands.
- [180] G. Martin. Atomic mobility in Cahn’s diffusion model. *Phys. Rev. B*, 41:2279–2283, 1990.
- [181] G. Martin and F. Soisson. *Kinetic Monte Carlo Method to model diffusion controlled phase transformations in the solid state*, pages 2223–2248. Springer Netherlands, Dordrecht, 2005.
- [182] C.S. Deo, D.J. Srolovitz, W. Cai, and V.V. Bulatov. Stochastic simulation of dislocation glide in tantalum and Ta-based alloys. *J. Mech. Phys. Solids*, 53(6):1223–1247, 2005.
- [183] L. Malerba, C.S. Becquart, and C. Domain. Object kinetic Monte Carlo study of sink strengths. *J. Nucl. Mater.*, 360(2):159–169, 2007.
- [184] M. Wen, A. Takahashi, and N.M. Ghoniem. Kinetics of self-interstitial cluster aggregation near dislocations and their influence on hardening. *J. Nucl. Mater.*, 392(3):386–395, 2009.
- [185] J. Dalla Torre, J.-L. Bocquet, N.V. Doan, E. Adam, and A. Barbu. JERK, an event-based Kinetic Monte Carlo model to predict microstructure evolution of materials under irradiation. *Philos. Mag.*, 85(4-7):549–558, 2005.
- [186] V. Tikare, M. Braginsky, D. Bouvard, and A. Vagnon. Numerical simulation of microstructural evolution during sintering at the mesoscale in a 3d powder compact. *Comput. Mater. Sci.*, 48(2):317 – 325, 2010.
- [187] N. Moelans, B. Blanpain, and P. Wollants. An introduction to phase-field modeling of microstructure evolution. *Calphad*, 32(2):268–294, 2008.
- [188] S. Rokkam, A. El-Azab, P. Millett, and D. Wolf. Phase field modeling of void nucleation and growth in irradiated metals. *Model. Simul. Mater. Sci. Eng.*, 17(6):064002, 2009.
- [189] C. Ronchi. Extrapolated equation of state for rare gases at high temperatures and densities. *J. Nucl. Mater.*, 96(3):314–328, 1981.
- [190] L.Q. Chen and Jie Shen. Applications of semi-implicit fourier-spectral method to phase field equations. *Comput. Phys. Commun.*, 108(2):147–158, 1998.

-
- [191] Y. Li, S. Hu, R. Montgomery, and X. Gao, F. Sun. Phase-field simulations of intragranular fission gas bubble evolution in UO_2 under post-irradiation thermal annealing. *Nucl. Instrum. Meth. Phys. Res. Sect. B (Beam Interactions with Materials and Atoms)*, 303:62–67, 2013.
- [192] M. R. Tonks, D. Gaston, P. C. Millett, D. Andrs, and P. Talbot. An object-oriented finite element framework for multiphysics phase field simulations. *Comput. Mater. Sci.*, 51:20–29, 2012.
- [193] E. Hernandez-Rivera. *Development of Hybrid Deterministic-Statistical Models for Irradiation Influenced Microstructural Evolution*. PhD thesis, University of Michigan, 2015.
- [194] Z.H. Xiao, A.A. Semenov, C.H. Woo, and S.Q. Shi. Single void dynamics in phase field modeling. *J. Nucl. Mater.*, 439(1):25 – 32, 2013.
- [195] T. Hochrainer and A. El-Azab. A sharp interface model for void growth in irradiated materials. *Philos. Mag.*, 95(9):948–972, 2015.
- [196] Linyun Liang, Zhi-Gang Mei, Yeon Soo Kim, Mihai Anitescu, and Abdellatif M. Yacout. Three-dimensional phase-field simulations of intragranular gas bubble evolution in irradiated U-Mo fuel. *Comput. Mater. Sci.*, 145:86 – 95, 2018.
- [197] M. J. Welland, E. Tenuta, and A. A. Prudil. Linearization-based method for solving a multicomponent diffusion phase-field model with arbitrary solution thermodynamics. *Phys. Rev. E*, 95:063312, 2017.
- [198] R.O.A. Hall, M.J. Mortimer, and D.A. Mortimer. Surface energy measurements on UO_2 — A critical review. *J. Nucl. Mater.*, 148(3):237–256, 1987.
- [199] N.F. Carnahan and K.E. Starling. Equation of state for nonattracting rigid spheres. *J. Chem. Phys.*, 51(2):635–636, 1969.
- [200] I.R. Brearley and D.A. MacInnes. An improved equation of state for inert gases at high pressures. *J. Nucl. Mater.*, 95(3):239 – 252, 1980.
- [201] HJ. Matzke. Atomic transport properties in UO_2 and mixed oxides (U,Pu) O_2 . *J. Chem. Soc., Faraday Trans. 2*, 83(7):1121–1142, 1987.
- [202] HJ. Matzke. Surface diffusion and surface energies of ceramics with application to the behavior of volatile fission products in ceramic nuclear fuels. In L-C. Dufour et al., editor, *Surfaces and Interfaces of Ceramic Materials*, pages 241–272. Springer Netherlands, Dordrecht, 1989.
- [203] E.Ya. Mikhlin. The mobility of intragranular gas bubbles in uranium dioxide. *J. Nucl. Mater.*, 87(2):405 – 408, 1979.
- [204] Utkarsh Ayachit. *The ParaView Guide: A Parallel Visualization Application*. Kitware, 2015. ISBN 978-1930934306.

- [205] R.S. Barnes and R.S. Nelson. *UKAEA (Harwell) Report AERE-R4952*, 1965.
- [206] J.A. Turnbull. The mobility of intra-granular bubbles in uranium dioxide during irradiation. *J. Nucl. Mater.*, 62(2):325 – 328, 1976.
- [207] R. S. Barnes, G. B. Redding, and A. H. Cottrell. The observation of vacancy sources in metals. *Phil. Mag.*, 3(25):97–99, 1958.
- [208] R. S. Barnes. The generation of vacancies in metals. *Phil. Mag.*, 5(54):635–646, 1960.
- [209] V.F. Chkuaseli. Modelling of fission gas spatial distribution in single grains of UO₂ fuel. *J. Nucl. Mater.*, 204:81 – 84, 1993.
- [210] R. M. Cornell. The growth of fission gas bubbles in irradiated uranium dioxide. *Phil. Mag.*, 19(159):539–554, 1969.
- [211] C. Baker. The fission gas bubble distribution in uranium dioxide from high temperature irradiated SGHWR fuel pins. *J. Nucl. Mater.*, 66(3):283 – 291, 1977.
- [212] G. L. Montet. Integral methods in the calculation of correlation factors in diffusion. *Phys. Rev. B*, 7:650–662, 1973.
- [213] G. L. Reynolds. The surface self-diffusion of uranium dioxide. *J. Nucl. Mater.*, 24:69–73, 1967.
- [214] J. Henney and J. W. S. Jones. Surface-diffusion studies on UO₂ and MgO. *J. Nucl. Mater.*, 3:158–164, 1968.
- [215] P. S. Maiya. Surface diffusion, surface free energy, and grain-boundary free energy of uranium dioxide. *J. Nucl. Mater.*, 40:57–65, 1971.
- [216] M.O. Marlowe and A.I. Kaznoff. Tracer study of the surface diffusivity of UO₂. *J. Nucl. Mater.*, 25:328 – 333, 1968.
- [217] W.M. Robertson. Surface diffusion of oxides (A review). *J. Nucl. Mater.*, 30:36 – 49, 1969.
- [218] D.R. Olander. Interpretation of tracer surface diffusion experiments on UO₂—roles of gas and solid transport processes. *J. Nucl. Mater.*, 96:243 – 254, 1981.
- [219] S.Y. Zhou and D.R. Olander. Tracer surface diffusion on uranium dioxide. *Surface Science*, 136(1):82–102, 1984.
- [220] L Bourgeois, Ph Dehaut, C Lemaignan, and J.P Fredric. Pore migration in UO₂ and grain growth kinetics. *J. Nucl. Mater.*, 295(1):73 – 82, 2001.

-
- [221] M.S. Veshchunov and V.E. Shestak. An advanced model for intragranular bubble diffusivity in irradiated UO₂ fuel. *J. Nucl. Mater.*, 376(2):174 – 180, 2008.
- [222] Karim Ahmed, Janne Pakarinen, Todd Allen, and Anter El-Azab. Phase field simulation of grain growth in porous uranium dioxide. *J. Nucl. Mater.*, 446(1):90 – 99, 2014.
- [223] J.R. Matthews and M.H. Wood. Modelling the transient behaviour of fission gas. *J. Nucl. Mater.*, 84(1):125 – 136, 1979.
- [224] A. D. Whapham and B. E. Sheldon. Radiation damage in uranium dioxide. *Philos. Mag.*, 12(120):1179–1192, 1965.
- [225] C. Onofri, M. Legros, J. L  chelle, H. Palancher, C. Baumier, C. Bachelet, and C. Sabathier. Full characterization of dislocations in ion-irradiated polycrystalline UO₂. *J. Nucl. Mater.*, 494:252 – 259, 2017.
- [226] A. Michel. *Etude du comportement des gaz de fission dans le dioxyde d'uranium: m  canismes de diffusion, nucl  ation et grossissement de bulles*. PhD thesis, University of Caen Basse-Normandie, 2011.
- [227] T. Sonoda, M. Kinoshita, I.L.F. Ray, T. Wiss, H. Thiele, D. Pellottiero, V.V. Rondinella, and H.J. Matzke. Transmission electron microscopy observation on irradiation-induced microstructural evolution in high burn-up UO₂ disk fuel. *Nucl. Instr. and Meth. B*, 191(1):622 – 628, 2002.
- [228] A. Goyal, T. Rudzik, B. Deng, M. Hong, A. Chernatynskiy, S. B. Sinnott, and S. R. Phillpot. Segregation of ruthenium to edge dislocations in uranium dioxide. *J. Nucl. Mater.*, 441(1):96 – 102, 2013.
- [229] J. Shea. An extension to fission gas release modelling at high temperatures. *EHPG Storefjell*, 2013.
- [230] S. T. Murphy, E. E. Jay, and R. W. Grimes. Pipe diffusion at dislocations in UO₂. *J. Nucl. Mater.*, 447(1):143 – 149, 2014.
- [231] M.S. Veshchunov and V.E. Shestak. Modelling of fission gas release from irradiated UO₂ fuel under high-temperature annealing conditions. *Journal of Nuclear Materials*, 430(1):82–89, 2012.
- [232] M. V. Speight and W. Beere. Vacancy potential and void growth on grain boundaries. *Metal Sci.*, 9(4):190–191, 1975.
- [233] Arno Le Prioux Halna du Fretay. *Mod  lisation par th  orie   lastique et potentiels empiriques des boucles de dislocation interstitielles dans l'UO₂ pour la dynamique d'amas*. PhD thesis, Aix-Marseille University, 2017.
- [234] D.D. Lanning, C.E. Beyer, and C.L. Painter. New high burnup fuel models for NRC's licensing audit code, FRAPCON. page 141, 1996.

- [235] K.J. Geelhood and W.G. Luscher. FRAPCON-3.5: A computer code for the calculation of steady-state, thermal-mechanical behavior of oxide fuel rods for high burnup. NUREG/CR-7022, PNNL-19418, Pacific Northwest National Laboratory (PNNL), 2014.
- [236] P.A. Jackson, J.A. Turnbull, and R.J. White. Enigma fuel performance code. *Nucl. Energy*, 29(2):107–114, 1990.
- [237] Y Rashid, R Dunham, and R Montgomery. Fuel analysis and licensing code: FALCON MOD01. *EPRI Report*, 1011308, 2004.
- [238] J. D. Hales, R. L. Williamson, S. R. Novascone, G. Pastore, B. W. Spencer, D. S. Stafford, K. A. Gamble, D. M. Perez, and W. Liu. BISON theory manual the equations behind nuclear fuel analysis. INL/EXT-13-29930, Idaho National Lab. (INL), 2016.
- [239] J. Rest. An improved model for fission product behavior in nuclear fuel under normal and accident conditions. *J. Nucl. Mater.*, 120(2):195 – 212, 1984.
- [240] J. Rest and S.A. Zawadzki. FASTGRASS: A mechanistic model for the prediction of Xe, I, Cs, Te, Ba, and Sr release from nuclear fuel under normal and severe-accident conditions. NUREG/CR-5840, ANL-92/3, Argonne National Laboratory, 1992.
- [241] D. PLANCQ. Pleiades : A unified environment for multidimensional fuel performance modeling. Proc. Int. Meeting on LWR Fuel Performance, Orlando, Florida USA, 2004.
- [242] C. Struzik, M. Moyne, and J.P. Piron. High burn-up modelling of UO₂ and MOX fuel with METEOR/TRANSURANUS version 1.5. ANS International Topical Meeting on Light Water Reactor Fuel Performances, Portland, 1997.
- [243] F. Bentejac and N. Hourdequin. TOUTATIS: An application of the CAST3M finite element code for PCI three-dimensional modeling. Proc. Pellet-clad Interaction in Water Reactor Fuels, 2005.
- [244] Cast3m. <http://www-cast3m.cea.fr/>.
- [245] M.S. Veshchunov, A.V. Palagin, A.M. Volchek, N.V. Yamshchikov, A.V. Boldyrev, R.R. Galimov, and S.Y. Kurchatov. Code package SVECHA: Modelling of core degradation phenomena at severe accidents. *Transactions of SMiRT-13 Conference*, 1:159–163, 1995.
- [246] A.V. Berdyshev, A.V. Boldyrev, A.V. Palagin, V.E. Shestak, and M.S. Veshchunov. Proceedings of the ninth international topical meeting on nuclear reactor thermal hydraulics (nureth-9), paper log 19. San Francisco, CA, USA, 1999.
- [247] K. Lassmann and A. Moreno. The light-water-reactor version of the URANUS integral fuel-rod code. *Atomkernenergie*, 30:207–215, 1977.

-
- [248] K. Lassmann. URANUS — A computer programme for the thermal and mechanical analysis of the fuel rods in a nuclear reactor. *Nucl. Eng. Des.*, 45(2):325–342, 1978.
- [249] D.D. Lanning, C.E. Beyer, and C.L. Painter. FRAPCON-3: Modifications to fuel rod material properties and performance models for high-burnup application. NUREG/CR-6534-Vol.1; PNNL-11513-Vol.1, Pacific Northwest Laboratory, 1997.
- [250] W.N. Rausch and F. E. Panisko. ANS54: A computer subroutine for predicting fission gas release. NUREG/CR-1213, PNL-3077, Pacific Northwest Laboratory, 1979.
- [251] K.J. Geelhood, W.G. Luscher, J.M. Cuta, and I.A. Porter. FRAPTRAN-2.0: a computer code for the transient analysis of oxide fuel rods. Rev2, PNNL-19400, Pacific Northwest National Laboratory (PNNL), 2016.
- [252] I. Palmer, G. Rossiter, and R.J. White. Development and validation of the ENIGMA code for MOX fuel performance modelling, IAEA-CSP-3/P. Proc. International symposium on MOX fuel cycle technologies for medium and long term deployment, 1999.
- [253] D. Gaston, C. Newman, G. Hansen, and D. Lebrun-Grandié. MOOSE: A parallel computational framework for coupled systems of nonlinear equations. *Nucl. Eng. Des.*, 239(10):1768 – 1778, 2009.
- [254] C. Valot, M. Bertolus, R. Konings, J. Somers, and S. de Groot. Basic research in support of innovative fuels design for the GEN IV systems: The F-BRIDGE project. *Nucl. Eng. Des.*, 241(9):3521–3529, 2011.
- [255] K. Bradley. NEAMS: The nuclear energy advanced modeling and simulation program. ANL/NEAMS-13/5, Argonne National Laboratory, 2013.
- [256] Consortium for Advanced Simulation of Light Water Reactors. <https://www.cas1.gov/>.
- [257] T.R. Allen. Energy Frontier Research Center, Center for Materials Science of Nuclear Fuels. INL/EXT-11-21924, Idaho National Laboratory, 2011.
- [258] M. Bertolus, M. Freyss, B. Dorado, G. Martin, K. Hoang, S. Maillard, R. Skorek, P. Garcia, C. Valot, A. Chartier, L. Van Brutzel, P. Fossati, R. W. Grimes, D. C. Parfitt, C. L. Bishop, S. T. Murphy, M. J.D. Rushton, D. Staicu, E. Yakub, S. Nichenko, M. Krack, F. Devynck, R. Ngayam-Happy, K. Govers, C. S. Deo, and R. K. Behera. Linking atomic and mesoscopic scales for the modelling of the transport properties of uranium dioxide under irradiation. *J. Nucl. Mater.*, 462:475 – 495, 2015.
- [259] T. Watanabe, S. G. Srivilliputhur, P. K. Schelling, J. S. Tulenko, S. B. Sinnott, and S. R. Phillpot. Thermal transport in off-stoichiometric uranium dioxide by atomic level simulation. *J. Am. Ceram. Soc.*, 92(4):850–856, 2009.

- [260] D. C. Parfitt and R. W. Grimes. Predicting the probability for fission gas resolution into uranium dioxide. *J. Nucl. Mater.*, 392(1):28–34, 2009.
- [261] S. C. Middleburgh, R. W. Grimes, K. H. Desai, P. R. Blair, L. Hallstadius, K. Backman, and P. Van Uffelen. Swelling due to fission products and additives dissolved within the uranium dioxide lattice. *J. Nucl. Mater.*, 427(1):359–363, 2012.
- [262] M. R. Tonks, P. C. Millett, P. Nerikar, S. Du, D. Andersson, C. R. Stanek, D. Gaston, D. Andrs, and R. Williamson. Multiscale development of a fission gas thermal conductivity model: Coupling atomic, meso and continuum level simulations. *J. Nucl. Mater.*, 440(1):193–200, 2013.
- [263] P. Van Uffelen, G. Pastore, V. Di Marcello, and L. Luzzi. Multiscale modelling for the fission gas behaviour in the TRANSURANUS code. *Nucl. Eng. Technol.*, 43(6):477–488, 2011.
- [264] Ya. E. Geguzin and M. A. Krivoglas. *Migration of Macroscopic Inclusions in Solids*. Consultants Bureau, New York and London, 1973.

Résumé en français

Etude spécialisée du couplage entre défauts étendus et espèces mobiles dans le combustible nucléaire

Introduction

Lorsque la fission a lieu dans un réacteur nucléaire, les réactions nucléaires conduisent à la génération de produits de fission, y compris des atomes de gaz stables, et à des défauts ponctuels tels que des lacunes, des auto-interstitiels et du gaz en substitution. Les gaz de fission (Xe, Kr) produits pendant l'irradiation ont ensemble un rendement de fission d'environ 0,3 et sont insolubles dans la matrice combustible et précipitent en bulles. Les défauts ponctuels interagissent avec ces bulles, ainsi qu'avec les pores (de fabrication) et les joints de grain, dans le combustible. Ces interactions entre les défauts ponctuels mobiles et les défauts étendus comme les bulles de gaz, les joints de grain ou les surfaces libres peuvent conduire à des phénomènes macroscopiques comme le relâchement de gaz de fission (RGF) et le gonflement du combustible. Ces phénomènes affectent le bon fonctionnement du crayon combustible et doivent être pris en compte dans tout code de comportement combustible. Les gaz relâchés provenant du combustible augmentent la pression dans le plénum du crayon combustible, ce qui soumet la gaine à des contraintes accrues et réduit également la conductivité thermique du jeu gaine combustible, ce qui fait augmenter la température de fonctionnement des pastilles. En raison de leur faible solubilité dans UO_2 , les gaz de fission précipitent également en bulles hautement pressurisées causant le gonflement du combustible. Le gonflement contribue à l'interaction pastille-gaine, exposant à nouveau la gaine à des contraintes plus élevées, ce qui peut limiter sa durée d'utilisation. Il est donc très important de comprendre le comportement des gaz de fission pour une utilisation optimale du combustible pendant l'exploitation du réacteur nucléaire.

Afin de comprendre le comportement des gaz de fission, des mesures en pile et hors pile sont effectuées dans le combustible nucléaire. Il est cependant difficile d'effectuer des mesures dans un combustible sous irradiation (en pile) en raison de variables environnementales incontrôlables. Des essais de recuit post-irradiation (hors pile) sont effectués pour obtenir des données sur le RGF dans un environnement contrôlé et surveillé. L'une des questions intéressantes lors des essais de recuit post-irradiation est le transport du gaz intra-granulaire vers la surface du grain, car il s'avère très rapide par rapport aux valeurs prédites par la théorie de la diffusion effective. Les bulles de gaz de fission peuvent être soit des nanobulles à l'intérieur du grain (intra-granulaire), soit des bulles plus grosses aux joints de grain (inter-granulaire). Le mécanisme de libération des gaz de fission hors du combustible peut être compris comme un processus en deux étapes : le transfert de gaz du grain au joints de grain, puis l'interconnexion des bulles au joints de grain qui ouvre des chemins vers l'extérieur du combustible. Alors que ce dernier phénomène est clairement observé à haute température ($T \geq 1400^\circ\text{C}$), la première étape du transfert des atomes de gaz dans le grain a fait l'objet de débats au cours des dernières décennies. Si les bulles de gaz sont considérées comme des pièges parfaits pour les atomes de gaz et selon la théorie de la diffusion effective, le gaz devrait être piégé dans le grand nombre de bulles intra-granulaires préexistantes pendant le recuit à haute température et ne devrait pas s'échapper du grain pendant la durée du recuit. Cependant, on observe que, dans la pratique, le relâchement de gaz de fission peut atteindre des valeurs élevées ($\sim 65\%$). Plusieurs mécanismes ont été proposés par le passé pour expliquer ce comportement. Depuis quelques années, des modèles ont été développés à l'échelle mésoscopique pour mieux représenter la microstructure en détail. L'avantage de l'utilisation de l'échelle mésoscopique est que les caractéristiques microstructurales des matériaux, telles que les joints de grain ou autres défauts, peuvent être représentées explicitement. De plus, l'échelle mésoscopique nous permet d'étudier l'évolution de la microstructure sur des échelles de temps et de longueur plus grandes que l'échelle atomistique. Dans le cadre de cette thèse, nous présentons un nouveau modèle spatialisé, appelé BEEP, dédié aux interactions entre les défauts ponctuels et les défauts étendus comme les bulles de gaz de fission et les surfaces libres. Le but de la thèse est de modéliser et d'analyser certains des mécanismes de transport intra-granulaire des bulles de gaz pendant le recuit post-irradiation et leur impact sur le RGF en utilisant le modèle BEEP. Les mécanismes discutés dans la thèse incluent :

- Le mouvement dirigé des bulles de gaz dans le gradient de concentration de lacune causé par l'arrivée des lacunes thermiques à partir des joints de grain.
- Mouvement brownien des bulles de gaz par des mécanismes de diffusion en volume et en surface.
- Mouvement des bulles de gaz avec les dislocations via le mécanisme de montée de dislocation.

Les deux premiers scénarios de mouvement de bulles et de RGF ont été réalisés en 2D, tandis que le troisième scénario, incluant les dislocations, a été réalisé en 3D.

Analyses 2-D

Le premier mécanisme de mouvement des bulles est le mouvement dirigé des bulles intra-granulaires dans un gradient de lacune. Lors d'un recuit à haute température, la surface libre - ou les joints de grain recouverts de grosses bulles déjà vidangées - génère des lacunes qui se déplacent vers les bulles de gaz en raison du gradient de lacune et qui sont piégées par les bulles de gaz. Ce gradient existe car les bulles intra-granulaires sont sur-pressurisées en raison de la présence d'atomes de gaz Xe, ce qui conduit à une valeur inférieure de la concentration d'équilibre de lacunes à la surface des bulles par rapport à la concentration d'équilibre de lacunes à la surface libre. De même, un flux de lacunes peut exister entre les bulles en fonction du rayon et de la pression interne de chaque bulle et les bulles de gaz peuvent, à leur tour, émettre des lacunes vers d'autres bulles plus pressurisées. Cet afflux de lacunes de la surface du grain vers le grain entraîne un mouvement dirigé de bulles de gaz intra-granulaires vers la surface, ce qui pourrait mener au relâchement du gaz.

Un autre mécanisme du mouvement intra-granulaire des bulles est le mouvement aléatoire de ces bulles par le transfert d'atomes autour d'elles. Les bulles peuvent se déplacer de façon aléatoire soit par le mécanisme de diffusion volumique, soit par le mécanisme de diffusion en surface. Le mécanisme de diffusion volumique est le transfert d'atomes cristallins par les lacunes dans le solide au hasard près de la bulle et en l'absence de toute force motrice. D'autre part, le mécanisme de diffusion en surface est le transfert d'atomes cristallins à la surface des bulles.

Pour analyser ces mécanismes pour le mouvement de la bulle et le RGF, nous avons effectué des simulations 2D. Le domaine utilisé pour les analyses est illustré à la Fig.FR1.

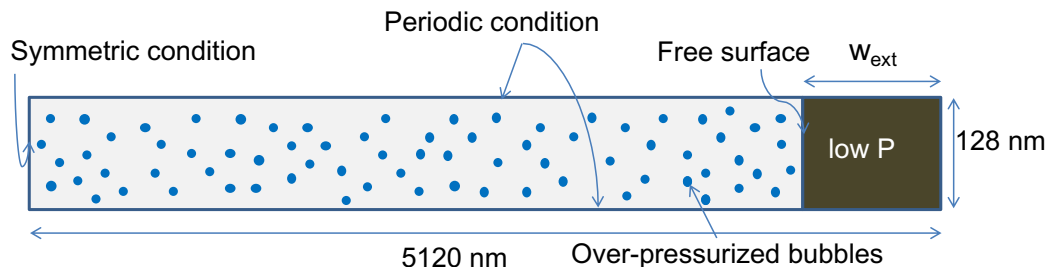


FIGURE FR1: Domaine utilisé pour les analyses en 2-D avec les différentes conditions.

Le domaine que nous considérons est un domaine rectangulaire de taille 5120nm*128nm avec une taille de grille de 4 nm (c'est-à-dire que le maillage

est de 1280×32 cellules). Cette taille de domaine est représentative d'un rayon de grain réel ($\sim 5\mu m$). Nous considérons une surface libre et une région extérieure à basse pression et un grand nombre de bulles sur pressurisées dans le grain. Nous essayons de respecter une distance entre les bulles compatibles avec une densité de bulles de l'ordre de $10^{23} - 10^{24}$ bulles/ m^3 comme observé dans les expériences, tout en générant les bulles au hasard dans le domaine. La taille des bulles est distribuée aléatoirement avec des rayons, $r \in (0.4 \text{ nm}, 1 \text{ nm})$. Nous imposons des conditions périodiques aux limites supérieures et inférieures et des conditions symétriques aux limites droites et gauches. Une température de recuit isotherme de 1600°C est utilisée pour l'analyse.

Nous comparons les valeurs de RGF obtenues par le calcul aux résultats des expériences. La fraction de RGF pour 3 heures de recuit isotherme à 1600°C était de $\sim 65\%$. Cette valeur de RGF est, cependant, la RGF global, à partir des bulles intra- et inter-granulaires. En utilisant des études antérieures réalisées à l'aide du modèle MARGARET pour discriminer le gaz retenu intra-granulaire et inter-granulaire et en passant de la géométrie sphérique réelle du combustible à une géométrie plane, nous obtenons une valeur RGF cible de $\sim 27\%$ pour le relâchement attendu dans notre simulation et qui serait compatible avec l'expérience.

Mouvement dirigé des bulles dans un gradient des lacunes

Le premier cas que nous avons réalisé était de tester le mouvement dirigé des bulles intra-granulaires dans un gradient de lacune et son impact sur le RGF lors des essais de recuit post-irradiation. La simulation est exécutée sur une durée simulée de 3 heures. Nous nous attendons à ce que les bulles à proximité de la surface extérieure grossissent en emprisonnant les lacunes émises par la surface et aussi à ce qu'elles se déplacent vers la surface extérieure dans le gradient de lacune. Cela a bien été observé. Cependant, le RGF après 3 heures de recuit s'est avéré être de 0.112% , ce qui est négligeable par rapport aux valeurs expérimentales, même si on compare à notre valeur de référence (27%). L'analyse a été poursuivie jusqu'à 110 heures de temps simulé afin de voir l'évolution des bulles et l'effet sur le relâchement global des gaz de fission. Les bulles ont continué à grossir et ont été modifiées jusqu'à une distance plus grande de la surface. Cependant, le RGF n'a atteint que 1.204% , ce qui est encore négligeable par rapport à la valeur cible.

Nous avons continué le calcul tant que le gradient de lacunes existe dans le solide. La simulation s'est arrêtée après un temps de simulation de $t = 8569$ h, avant que le profil de concentration de lacune ne devienne complètement plat car la région externe que nous considérons avait complètement disparu à cause du gonflement du grain (dû à la création de lacunes en surface). Pendant ce temps, les bulles ont encore grossi en emprisonnant les lacunes, non seulement à proximité de la surface libre, mais aussi plus loin dans le domaine. Même avec un grand nombre de bulles sorties du grain, le RGF calculé au temps $t = 8569$ h est seulement de $6,63\%$. Même si le nombre

de bulles dans le grain est diminué de 2/3, le RGF reste bas car la plupart des bulles ont simplement coalescé et ne sont pas sorties et par conséquent n'ont pas contribué au relâchement.

Ainsi, l'analyse réalisée montre que le seul mouvement des bulles dans un gradient de lacune ne peut expliquer le RGF observé dans notre expérience de référence. Même en continuant la simulation jusqu'à 8569 heures, il n'a pas été possible d'atteindre la valeur cible de RGF.

Le fait de continuer le calcul loin en temps est équivalent à faire une étude paramétrique sur D_v (coefficient de diffusion de lacune). Une étude paramétrique sur C_v^{eq} ($P_b=0$, $\kappa=0$) a aussi été menée en multipliant cette valeur par 10 et 100. Le RGF ne dépasse pas 9% même en prolongeant le calcul jusqu'à ce que $C_v(\text{center}) \approx 0,8C_v^{eq}$ (surface libre).

Mouvement aléatoire des bulles par volume et diffusion en surface

Ensuite, nous avons analysé l'influence du mouvement aléatoire des bulles par les mécanismes de diffusion en volume et en surface sur l'évolution des bulles à l'intérieur du grain. Afin de ne mettre l'accent que sur le mouvement aléatoire, nous n'avons pas considéré de force motrice (diffusion des lacunes) dans le solide. La simulation a été réalisée sur une durée simulée de 3 heures.

Tout d'abord, nous avons testé le mouvement aléatoire des bulles par mécanisme de diffusion volumique. L'analyse a permis d'observer que le mouvement des bulles par le mécanisme de diffusion volumique était négligeable. Après 3 heures de recuit, le nombre de bulles est resté le même qu'avant. La valeur moyenne du coefficient de diffusion des bulles est également restée inchangée à une valeur très faible. On peut donc noter qu'il n'y a pas eu de contribution significative du mécanisme de volume au mouvement aléatoire des bulles et, par conséquent, aucun impact supplémentaire sur le RGF.

Ensuite, le mouvement aléatoire des bulles dû au mécanisme de diffusion en surface a été testé. Comme le suggère Mikhlin, nous avons utilisé un terme multiplicatif d'atténuation de la diffusion qui devient quasiment nul pour des bulles très fortement pressurisées (diffusion des bulles empêchée). Les valeurs du coefficient de diffusion avec le facteur d'atténuation sont très faibles et il n'y a pas de mouvement de bulles en raison de ces faibles valeurs des coefficients de diffusion. Après 3 heures de recuit, le nombre de bulles est resté le même qu'avant. La valeur moyenne du coefficient de diffusion des bulles est également restée inchangée à une valeur très faible. Ainsi, nous pourrions conclure que le mécanisme de diffusion en surface avec le terme d'atténuation de Mikhlin ne peut pas expliquer le RGF observé.

Cependant, comme le terme d'atténuation de Mikhlin dans le coefficient de diffusion des bulles supprime la diffusion des petites bulles sur pressurisées, un scénario intéressant peut être envisagé si l'on considère à la fois la diffusion des lacunes dans le grain et le mouvement aléatoire des bulles par diffusion en surface incluant le terme d'atténuation de Mikhlin. Au fur et à mesure que les bulles piègent les lacunes et grossissent, l'atténuation de la

diffusion des petites bulles diminuerait. Cela permettrait à terme d'améliorer la diffusion de ces bulles et d'obtenir un RGF plus important.

Mouvement combiné par mouvement dirigé et diffusion de surface aléatoire

Nous avons donc testé le scénario ci-dessus. Le temps de simulation pour l'analyse était de 3 h et 110 h, comme pour l'analyse du mouvement dans le gradient de lacune. On a observé qu'au temps $t = 3$ h, les bulles à proximité de la surface libre s'étaient significativement déplacées. Le nombre de bulles dans le domaine a également diminué du temps $t = 0$ à $t = 3$ h. La diminution du nombre de bulles est due à la fois à la sortie des bulles et à leur coalescence.

Au fur et à mesure que les bulles commencent à piéger les lacunes provenant de la surface libre, elles grossissent, ce qui autorise la diffusion en surface et permet d'augmenter le coefficient de diffusion des bulles. Cependant, après un certain temps, le coefficient de diffusion des bulles cesse de croître à cause de l'effet de leur taille.

Le RGF atteint seulement 0,84% à 3 h et 2,32% à 110 h de recuit. La diffusion des bulles a été facilitée par l'apport des lacunes. Elle a entraîné une coalescence accrue des bulles, mais finalement peu de relâchement.

Finalement, nous avons essayé de poursuivre le calcul jusqu'à ce que la concentration des lacunes dans le solide atteigne la valeur d'équilibre. La simulation a été interrompue après un temps de simulation de $t = 3080$ h car les deux plus grandes bulles ont coalescé en donnant une bulle de diamètre supérieur à la largeur du domaine. A $t = 3080$ h, il ne restait plus que 20 bulles dans le domaine et le RGF du grain en 3080 heures était encore de 2,32%, comme à 110 heures. Les bulles ont grossi par apport de lacunes et coalescé, mais sans quitter le grain.

Etude paramétrique du terme d'atténuation de Mikhlin

Nous avons essayé d'évaluer l'influence du terme d'atténuation sur la migration des bulles. Pour ce faire, le terme multiplicatif d'atténuation de Mikhlin a été fixé à 1 (pas d'atténuation). La simulation a été réalisée pendant 3 heures de recuit. En raison de leur coefficient de diffusion élevé, les bulles se déplacent rapidement et coalescent les unes avec les autres. Leur nombre passe de 2647 à seulement 5 en 3 h, avec un rayon moyen de 16,33 nm et un RGF de 6,64%. Le phénomène de coalescence a été prépondérant sur le relâchement. Le calcul a été poursuivi. À 5500 h, il ne reste que 3 bulles dans le grain et le RGF est de 28,67% (stable depuis $t = 3366$ h).

Cette enquête montre que même sans atténuation de Mikhlin, le mouvement aléatoire des bulles n'explique pas le RGF observé obtenu après 3 heures de recuit. La valeur cible pour les RGF est atteinte en 3366 heures, ce qui implique que pour atteindre le RGF cible en 3 heures, la valeur de D_s requise devrait être de $\sim 10^3$ fois plus grande et sans atténuation de Mikhlin

de la diffusion en surface. À notre avis, cela nous éloignerait trop des recommandations de la littérature.

Conclusions des analyses 2-D

La migration intra-granulaire des bulles de gaz et la libération des gaz de fission ont été analysées en 2D par le mécanisme de mouvement dans un gradient de lacune ainsi que pour le mouvement aléatoire sans aucune force motrice. Un effet combiné de mouvement dirigé et aléatoire dû au mécanisme de surface a également été analysé. Les conclusions pour les différents cas utilisant ces deux mécanismes et leur combinaison sont les suivantes (Fig.FR2):

- Aucune des trois simulations ne conduit à un relâchement supérieur à 0.84% en 3 heures et 2.32% lorsque le profil de lacunes est presque plat, à comparer avec le RGF cible de 27%
- Continuer le calcul loin en temps revient à faire une étude paramétrique sur D_v . Une étude paramétrique sur $C_v^{eq}(P_b=0, \kappa=0)$ a aussi été menée dans le cas du mouvement sous gradient thermique seul. Le RGF reste toujours trop bas par rapport au RGF cible.
- Une étude paramétrique du terme d'atténuation de Mikhlín a été réalisée pour tester son influence sur l'ensemble du RGF. Ce terme a une influence importante. Cependant, même dans les conditions les plus favorables, le mouvement aléatoire des bulles ne peut pas expliquer le RGF.

Analyse 3-D

Nous avons mis en œuvre une modélisation incluant des dislocations dans le modèle BEEP prenant en compte le mécanisme de montée des dislocations et sa capacité à provoquer des mouvements de bulles et, en fin de compte, à conduire à une amélioration du RGF. Une approche 3D est obligatoire si les lignes de dislocation sont explicitement représentées et évoluent dans le modèle.

Nous considérons un scénario dans lequel les bulles épinglées sur la dislocation peuvent se déplacer avec elle. Les lacunes générées le long de la dislocation migrent vers la bulle et remplacent les atomes cristallins présents à la surface de la bulle. Après plusieurs échanges de ce type entre les lacunes et les atomes cristallins, une nouvelle couche d'atomes peut se former le long de la dislocation et provoquer son montée. La bulle épinglée à la dislocation grossit, relâxe sa pression et est supposée se déplacer avec la dislocation. Cette bulle peut finalement sortir du grain, ce qui améliore le RGF. Ainsi, dans ce scénario, les bulles sur-pressurisées épinglées sur les

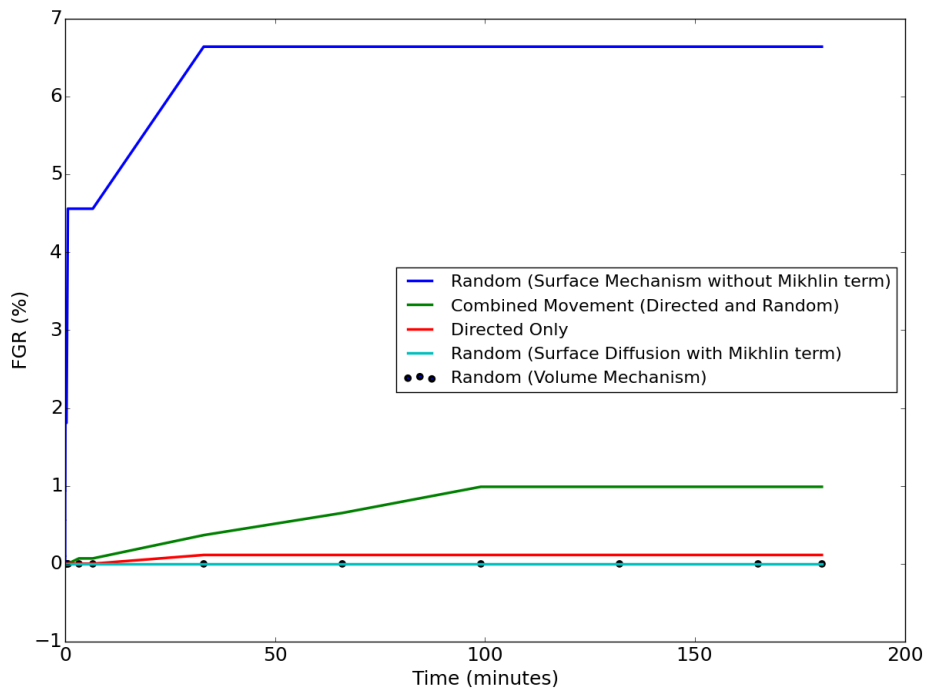


FIGURE FR2: RGF en 3 heures avec les différents mécanismes de mouvement des bulles adoptés dans les analyses 2D.

dislocations coin sont une force motrice pour le mécanisme de montée de la dislocation et se déplacent avec la dislocation quand elle monte.

En raison des coûts de calcul élevés des calculs 3D, nous considérons un domaine plus petit (plutôt que le grand domaine de $5 \mu\text{m}$ représentant le rayon d'un grain). Le domaine que nous utilisons pour l'analyse a des dimensions physiques de $1608\text{nm} \times 120\text{nm} \times 120\text{nm}$ incluant une région externe de longueur 98 nm . Une représentation schématique du domaine incluant les bulles et les conditions aux limites est illustrée dans la Fig. FR3.

Puisque nous effectuons des calculs tridimensionnels, nous pouvons obtenir la concentration de gaz en mol/m^3 créée pendant l'irradiation de base. Nous avons généré des bulles au hasard dans le domaine avec un rayon de bulle, $R_b \sim 1 \text{ nm}$ et le volume par atome de gaz dans les bulles égales au volume atomique d'un site UO_2 . On a pu obtenir une concentration de gaz égale à $139 \text{ mol}/\text{m}^3$ en début simulation en prenant la taille de la grille à 3 nm ce qui correspond à la quantité de gaz généré au taux de combustion de l'échantillon expérimental. Le nombre de bulles générées s'élève à 6136. Les conditions aux limites fournies sont périodiques sur les faces supérieures, inférieures, avant et arrière et symétriques sur les côtés droits et gauches du domaine.

Nous initialisons le domaine avec 20 dislocations parallèles à l'axe y ou z et ces dislocations sont réparties aléatoirement dans le domaine mais en épinglant chaque fois au moins une bulle. La valeur du coefficient de diffusion de lacune le long de la dislocation n'est pas connue et est considérée comme un paramètre pour l'analyse.

Nous avons fait un calcul sans diffusion de lacunes et sans atténuation de

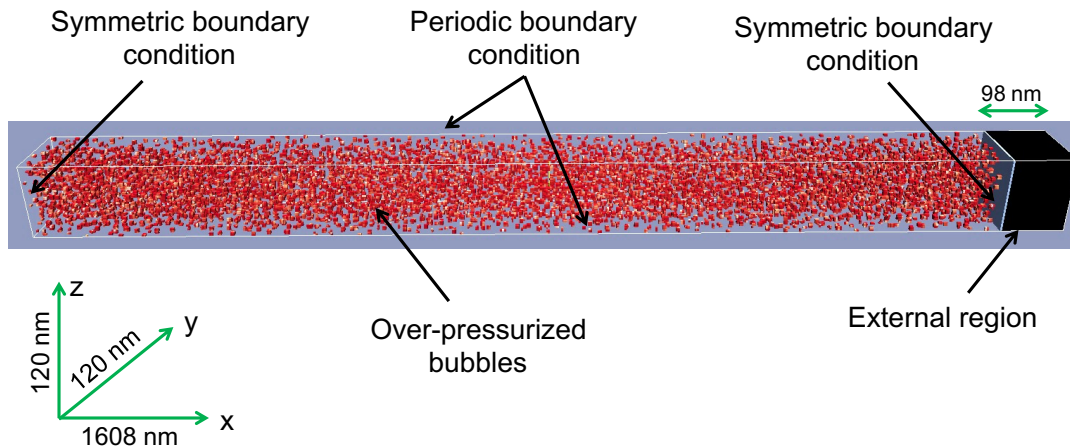


FIGURE FR3: Représentation schématique du domaine en 3-D avec conditions limites et initiales.

Mikhlin, pendant 3 h de recuit isotherme. Les bulles subissent une coalescence rapide dès le début de la simulation et sont réduites à seulement 100 bulles en l'espace de 5 secondes. Plusieurs bulles se sont épinglées sur les dislocations. Au temps $t = 5$ s, 59 bulles ont été épinglées sur les différentes dislocations. Au temps $t = 1122$ s, la plupart des bulles avaient coalescé en bulles plus grosses ou s'étaient déplacées avec les dislocations en mouvement. Il ne restait que 6 bulles chacune épinglée sur à une dislocation. Au temps $t = 7830$ s, il ne restait plus que 3 dislocations avec 3 bulles épinglées dans le domaine. A la fin de la simulation ($t = 10800$ s = 3 h), ces trois dislocations et bulles restent dans le domaine. Le RGF en 3 heures de simulation est de 93,76%.

Conclusion de l'analyse 3-D

D'après l'analyse, on constate que le mécanisme de montée de dislocation pourrait s'avérer être un mécanisme important pour provoquer le mouvement orienté de la bulle et le relâchement gazeux. Dans le cas testé ci-dessus, le RGF cible est atteint et même dépassé. Le domaine considéré ici était 32% ($\frac{1.608\mu m}{5\mu m}$) du domaine considéré pour le rayon réel du grain. Considérant que 93,76% du gaz de cette région est relâché, cela donne au moins 30% RGF pour le domaine d'origine (à comparer avec les 27% cible). Ainsi, ici, avec les dislocations, le RGF obtenu se situe dans l'ordre de grandeur attendu. Toutefois, on a supposé plusieurs conditions favorables, et ce mécanisme mérite d'être étudié en détail pour fournir un résultat plus précis. Le RGF en 3 heures de simulation de recuit par le mécanisme de montée de dislocation est représenté sur la Fig.FR4.

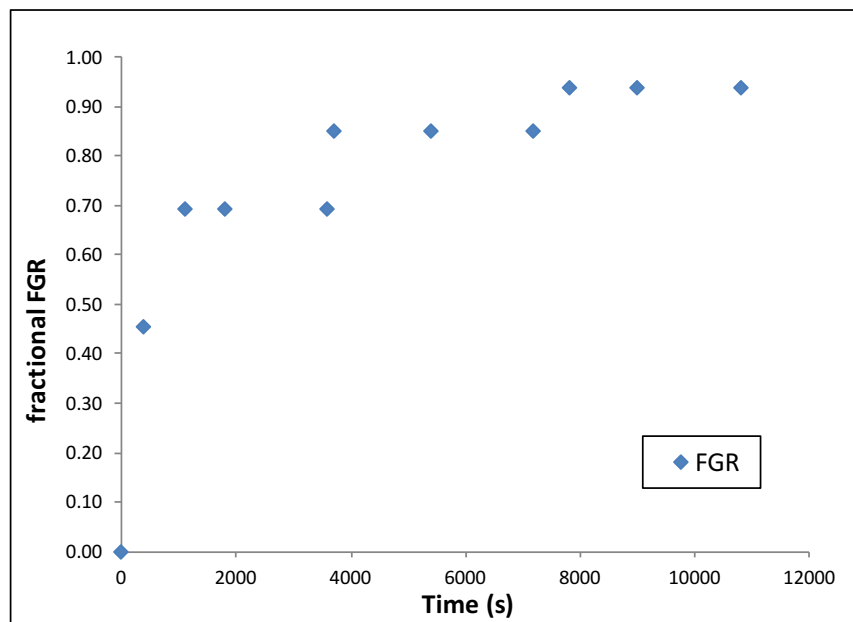


FIGURE FR4: RGF en 3h via un mécanisme de montée disloqué.

Conclusion générale et perspectives

Dans le cadre de cette thèse, l'impact du mouvement des bulles de gaz intra-granulaires sur le relâchement global de gaz a été analysé lors des essais de recuit post-irradiation à 1600°C. Un nouveau modèle spatialisé, appelé modèle BEEP, a été mis au point pour les interactions entre les bulles de gaz de fission et les lacunes à l'échelle mésoscopique. Ce type d'évaluation mécaniste faisait défaut, à notre connaissance. Le modèle BEEP a été vérifié pour divers aspects tels que les bilans atomiques, le calcul de la diffusion et le mouvement des bulles et il s'est avéré simuler les divers aspects avec une bonne précision.

La migration intra-granulaire des bulles de gaz et la libération des gaz de fission ont été analysées en 2D par le mécanisme de mouvement dans un gradient de lacune ainsi que pour le mouvement aléatoire sans aucune force motrice. Un effet combiné de mouvement dirigé et aléatoire dû au mécanisme de surface a également été analysé.

Les analyses ont montré que en prenant les paramètres disponibles dans la littérature, le mouvement des bulles dans un gradient de lacune ne peut expliquer l'important RGF qui est observé pendant le test de recuit post-irradiation de l'échantillon d'UO₂ pris comme référence, même si le mouvement dirigé est aidé par un mouvement aléatoire des bulles. Des études paramétriques sur D_v , C_v^{eq} ($P_b=0$, $\kappa=0$) et le coefficient de Mikhlin ont été effectuées. Dans tous les cas testés, le RGF reste bien dessous de la valeur cible.

Un autre scénario pour le RGF via un mouvement de bulle intra-granulaire a été testé. Ce scénario prend en compte les dislocations et leur mouvement via un mécanisme de montée induit par la surpressurisation des bulles. Les dislocations montent avec la ou les bulles de gaz qui y sont épinglées

parce que c'est un moyen pour les bulles de relaxer leur pression, offrant ainsi un mécanisme pour relâchement gazeux lors des essais de recuit post-irradiation.

Afin d'analyser ce scénario, les dislocations ont été incorporées dans le modèle BEEP et leur mouvement a été testé avec succès dans un domaine 3D plus petit. L'analyse 3D du RGF à l'aide de ce scénario a été effectuée à l'aide du modèle BEEP et a conduit à une prédiction du RGF compatible avec l'expérience. Toutefois, plusieurs hypothèses ont été utilisées dans l'analyse et la valeur, par exemple, du coefficient de diffusion des lacunes le long de la dislocation a été prise comme paramètre par manque d'information. Cette analyse pointe la nécessité d'études à l'échelle inférieure pour obtenir les grandeurs nécessaires aux modèles à l'échelle mésoscopique, tels que BEEP.

En perspective, des calculs de dynamique moléculaire sont prévus pour accéder à l'influence de la pression interne sur la mobilité de la bulle (équivalent du terme de Mikhlin). De plus, un calcul complet, incluant la montée de dislocation et la diffusion de lacune, devrait également être effectué. Le modèle BEEP devrait également être accéléré en termes de temps de calcul en utilisant à la fois la parallélisations MPI (pour le calcul de diffusion) et OpenMP pour paralléliser les boucles indépendantes sur les bulles.

Spatialized study of the coupling between extended defects and mobile species in the nuclear fuel

Fission gases (Xe, Kr) produced during irradiation in a nuclear fuel can contribute to significant effects such as swelling and fission gas release which may affect the overall performance of the fuel. The effective diffusion theory, which is generally used in the modelling of base-irradiation of nuclear fuel, cannot predict the intra-granular fission gas release during post-irradiation annealing tests. From the several scenarios proposed, we discuss and analyze three such mechanisms: the directed movement of pressurized intra-granular gas bubbles in a vacancy concentration gradient towards the grain surface, the Brownian movement of these intra-granular bubbles via volume and surface diffusion mechanisms, a scenario of gas bubble movement along with the dislocations via the mechanism of dislocation climb. A new spatially resolved model, BEEP Model, has been developed for gas bubble migration and its interaction with point defects. Analyses done using the BEEP model show that neither of the directed or random movement, nor their combination, could explain the large fission gas release obtained during post-irradiation annealing in our reference experiment. The dislocation climb mechanism has been demonstrated as a prominent gas release mechanism, however, the values for diffusion of vacancies on the dislocations are not known and were chosen to allow gas release. The work carried out in this thesis has provided a better insight to the transport of intra-granular gas bubbles and its impact on fission gas release. This work also emphasized the questions that need to be answered at the lower scales.

Keywords: Fission gas, Nuclear fuel, Modelling, Intra-granular bubbles, Mesoscale

Etude spatialisée du couplage entre défauts étendus et espèces mobiles dans le combustible nucléaire

Les gaz de fission (Xe, Kr) produits pendant l'irradiation d'un combustible nucléaire peuvent provoquer du gonflement et la libération de gaz de fission, qui peut affecter la performance globale du combustible. La théorie de la diffusion effective, qui est généralement utilisée dans la modélisation de l'irradiation de base du combustible nucléaire, ne permet pas de prédire le dégagement de gaz de fission intra-granulaire pendant les essais de recuit post-irradiation. Parmi les différents scénarios proposés, nous discutons et analysons trois des mécanismes possibles: le mouvement dirigé vers la surface du grain de bulles de gaz intra-granulaires pressurisées dans un gradient de concentration de lacunes, le mouvement brownien de ces bulles intra-granulaires via des mécanismes de diffusion en volume et en surface des bulles, un scénario de mouvement de bulles de gaz avec les dislocations via le mécanisme de montée de dislocation. Un nouveau modèle spatialisé, le modèle BEEP, a été mis au point pour la migration des bulles de gaz et leur interaction avec les défauts ponctuels. Les analyses effectuées à l'aide du modèle BEEP montrent que ni le mouvement dirigé ou aléatoire, ni leur combinaison ne peuvent expliquer le relâchement important de gaz de fission obtenu lors du recuit post-irradiation dans notre expérience de référence. Il a été démontré que le mécanisme de montée peut constituer un mécanisme de relâchement de gaz important, cependant, le coefficient de diffusion de lacunes le long d'une dislocation, non connu, a été pris comme paramètre ajustable. Les travaux menés dans le cadre de cette thèse ont permis de mieux comprendre le transport des bulles de gaz intra-granulaires et son impact sur le relâchement des gaz de fission. Ce travail permet aussi de mieux cerner les questions aux quelles il serait utile de répondre aux plus basses échelles.

Mots-clés: Gaz de fission, Combustible nucléaire, Modélisation, Bulles intra-granulaires, Méso-échelle

Auteur: Lokesh VERMA

Discipline: Physique et Sciences de la Matière

Lieu et date de soutenance: CEA Cadarache, le 11 décembre 2019
DEC/SESC/LM2C, CEA Cadarache, 13108 St Paul lez Durance
